CREATION OF 3-DIMENSIONAL MICRO-OPTICAL MATERIALS

BY

DANIEL BACON-BROWN

DISSERTATION

Submitted in partial fulfillment of the requirements
for the degree of Doctor of Philosophy in Materials Science and Engineering
in the Graduate College of the
University of Illinois at Urbana-Champaign, 2019

Urbana, Illinois

Doctoral Committee:

Professor Paul Braun, Chair
Professor Gary Eden
Professor Andre Schleife
Professor Moonsub Shim

ABSTRACT

Structure at or below the wavelength of light can greatly modify the optical properties of materials. Control over these aspects can introduce a variety of optical phenomena, such as photonic band gaps, negative refractive index, transformation optics, and sub-diffraction limit focusing, to name a few. These phenomena have great implications for our ability to control light, whether it is in its spectral emission and absorption, in directional control through waveguides, or in its ability to propagate through a material at all. This dissertation will cover a variety of topics in this domain.

Chapter 1 will be a brief overview of how light behaves in response to structures at different scales: features much larger than, comparable to, or smaller than the wavelength of the light. This will lay groundwork for more advanced concepts to be introduced later on, but if you are already familiar with the field of modern optics, you may wish to skip the basics introduced here.

Chapter 2 will be focused on multi-beam interference lithography, a technique whereby the interference pattern of beams of light is converted into a pattern of solid photoresist, often used to create photonic crystals. The mathematical relations between the interfering beams and the fabricated pattern are discussed in detail. The problem of reflectance at the interface between photoresist and substrate is shown to cause problems for interference lithography glancing angles of incidence, and a tunable polymer blend antireflection coating is proposed and demonstrated to eliminate this issue.

Chapter 3 discusses proximity-field nanopatterning, a variation of interference lithography where a diffractive mask generates the beams of light that create the interference pattern. The design space of this technique is examined for a cubic lattice and multilevel phase masks are shown to be greatly expand the possible design space compared to the more conventional binary phase mask.

Chapter 4 presents work on using proximity-field nanopatterning to create arrays of metallic helices to function as broadband circular polarizers. While this project was ultimately unsuccessful, a better understanding of the fabricability limits was developed. Concepts of

concentration fluctuations and shot noise were borrowed from EUV lithography and used to create more rigorous models of the interference lithography process.

Chapter 5 discusses our recent discovery that direct laser writing can be used inside the pores of porous silicon and porous silicon oxide, and that the local fill fraction of resist can be controlled. This method opens up great possibilities for a wide variety of micro-optics. Nearly arbitrary 3D structures can be defined with a refractive index over a wide range and with no direct connection to the substrate. A variety of focusing optics are created, including with a gradient refractive index. This method is used to shift the bandgap position of PSi DBR's across the visible spectrum, and is used to embed true-color images into PSi with pixel sizes on approximately a micron in width. The ability to combine 3D spatial control with gradient refractive index control on such fine scales shows great potential for new micro-optics.

ACKNOWLEDGEMENTS

First, I'd like to thank my family, who early on taught me the value of learning and unknowingly set me on this path so many years ago, throughout the years helping me in uncountable ways. My mother, father, and brother have helped me to maintain perspective while I toiled away in the ivory tower.

I'd like to thank my advisor Prof. Paul Braun for letting me join his research group so many years ago, and give me the opportunity to work on so many interesting projects and the tools to see them through. I'd also like to thank him for his patience when experiments obstinately refuse to work and clever ideas to cajole them into working. There's a mantra that as you move through academia you "know more and more about less and less". Something I admire in Paul is that he disproves this notion with his uncanny ability to always known more and more about more and more.

I'd like to thank everyone in the Braun group for providing a supportive environment in what can be a trying time. I've been helped by so many, in particular I'd like to thank (in alphabetical order: Ashish Kulkarni, Christian Ocier, Corey Richards, Eric Epstein, Erica Malloch, Hailong Ning, Julia Kohanek, Junjie Wang, Kaitlin Tyler, Kali Miller, Neil Krueger, Ozman Cifci, Runyu Zhang, Shuqi Lai, Sidhartha Gupta. Runyu Zhang and Hailong Ning deserve special thanks for the help in the interference lithography experiments, and Christian Ocier and Corey Richards for help in embedding optics in porous silicon. I thank William Goldschlag, Tom Galvin and their professor, Gary Eden, for their efforts to help with two-photon proximity field nanopatterning.

I'd like to thank the Light-Matter Interactions Energy Frontier Research Center for the funding necessary to pursue this work. Everyone in Beckman and MRL facilities deserves my thanks for doing the work necessary for me doing mine, especially Jeff Grau and Tao Shang. I thank my committee, Gary Eden, Andre Schleife, and Moonsub Shim.

Finally, I thank the giants whose shoulders I've been climbing to enable me to see a bit further and everyone in the past who has struggled to make life a little easier for those who followed.

TABLE OF CONTENTS

LIST OF ABBREVIATIONS

AFM	Atomic force microscopy
DBR	Distributed Bragg reflector
DiL	Dip-in lithography
DLW	Direct laser writing
DoS	Density of states
EBL	Electron-beam lithography
EMA	Effective medium approximation
FDTD	Finite-difference time-domain method
GRIN	Gradient refractive index
HF	Hydrofluoric acid
IP-dip	A liquid photoresist designed for Nanoscribe
LED	Light emitting diode
NIR	Near-infrared
NSOM	Near-field scanning optical microscopy
PAG	Photo-acid generator
PDMS	Polydimethylsiloxane
PETA	Pentaerythritol triacrylate
PGMEA	Propylene glycol monomethyl ether acetate
PR	Photoresist
PnP	Proximity-field nanopatterning
PS	Polystyrene
PSi	Porous silicon
$PSiO_2$	Porous silicon oxide
PVME	Poly(vinyl methyl ether)
RCWA	Rigorous coupled wave analysis
RIE	Reactive ion etching
S4	Stanford Stratified Structure Solver
SAM	Self-assembled monolayer

SEM	Scanning electron microscopy
STILUS	Shaped Tunable-Index Lithography Using Scaffolding
SU-8	A photoresist produced by Microchem
TMM	Transfer matrix method
UV	Ultraviolet
VASE	Variable-angle spectroscopic ellipsometer
VCSEL	Vertical cavity surface-emitting laser

CHAPTER 1

INTRODUCTION

Light seems to be something that humans find to be not only the most familiar but also the most mysterious. From the ancient humans that knew that sunlight gave warmth and growing crops and so worshipped the sun, the Hellenistic philosophers that considered vision to be a kind of "fire" that projects out from one's eyes, the wave and particle theories of the Renaissance and Enlightenment, to the quantum understanding we have today, we keep learning more about this mysterious "thing" that we know so intimately. In other words, we discover that there is more to light *than meets the eye*.

People going about their business today generally treat light as a kind of ray. That is to say, they use the "ray model of light".[1] In this model, light behaves familiarly, travelling in straight lines, bouncing off of objects, and forming shadows. But that is just one of the three models that we will need in this dissertation. On physical scales closer to the wavelength of light, we need the "wave model of light", where light is more like an ocean wave that can bend around corners and interfere with itself, giving rise to "photonic crystals" that perfectly reflect waves of a certain frequency and guide light along channels. Further still, on physical scales much smaller than the wavelength of light we reach the "long wavelength limit" where light, while still technically considered a wave, is treated more like a tide and interference effects disappear, allowing complex, varying structures to be treated as though it were entirely uniform. We will discuss each of these regimes in more detail.

1.1 Ray Model of Light

The ray optics model of light is the oldest and easiest to understand, so the basics will be glossed over here and only the bits important to understanding will be covered. When a ray of light propagating through air encounters an interface with a dielectric such as glass, a few things happen. First is refraction: light that transmits through the air is refracted, causing a

change in the angle of the relative to the interface.[1] The change in the angle is given by Snell's law:

$$n_i \sin(\theta_i) = n_t \sin(\theta_t) \tag{1.1}$$

Where n_i and n_t are the refractive indices of the incident and transmitted sides of the interface and θ_i and θ_t are the corresponding angles between the light ray and the line perpendicular to the substrate. Besides reflection and refraction, light can also change direction while passing through a gradient refractive index, where the refraction occurs not at a single interface, but continuously through the medium.

1.1.1. Gradient Index Optics

One aspect of the ray model of light that is often not included in regular classes is the concept of gradient index optics.[2] These are optics that are described not by a sudden transition between refractive indices, like between air and glass, but by a gradual shift.[3] The most common example of this is that of a desert mirage.[4] In a desert (and roads on a sunny day) the sun heats the ground to be hotter than the air around it. The road's heat slowly gets transferred to the air, so that there is a temperature gradient occurring through the air, creating a pressure gradient and thus a density gradient. The air closer to the ground has a lower density and thus a refractive index a little bit lower, closer to vacuum. As shown in **Figure 1.1**, the gradient refractive index causes the light path to slowly bend upwards. Note that the total change in the angle of the light ray is the same as if the light were totally internally reflected at a sudden interface between the hot and cold air.

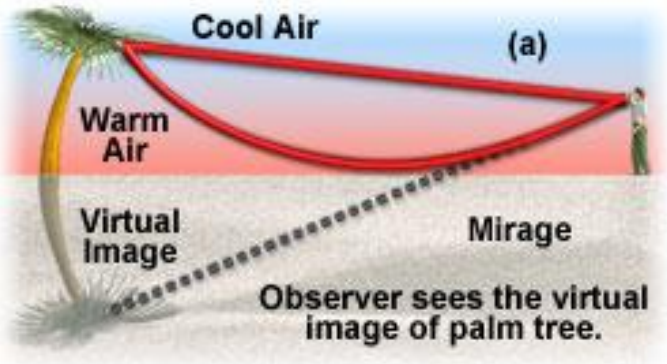

Figure 1.1. Cartoon of mirage formation due to gradient refractive index bending of the light path. Image by Michael Davidson.[3]

For mirages, the effect of the gradient refractive index is pretty low because the refractive index difference is quite small. However, we can manufacture much stronger refractive index gradients with a variety of methods, most commonly ion glass doping.[5] This enables us to create lenses that avoid aberrations found in conventional lenses.[6]

Another application of control over gradient refractive index is transformation optics, or optics that perform coordinate transformations of light, essentially stretching and deforming the "space" that the light travels through.[7] A couple of examples are shown in **Figure 1.2**, depicting a planar "carpet cloak" and a gradient refractive index lens with a transformed focal plane.

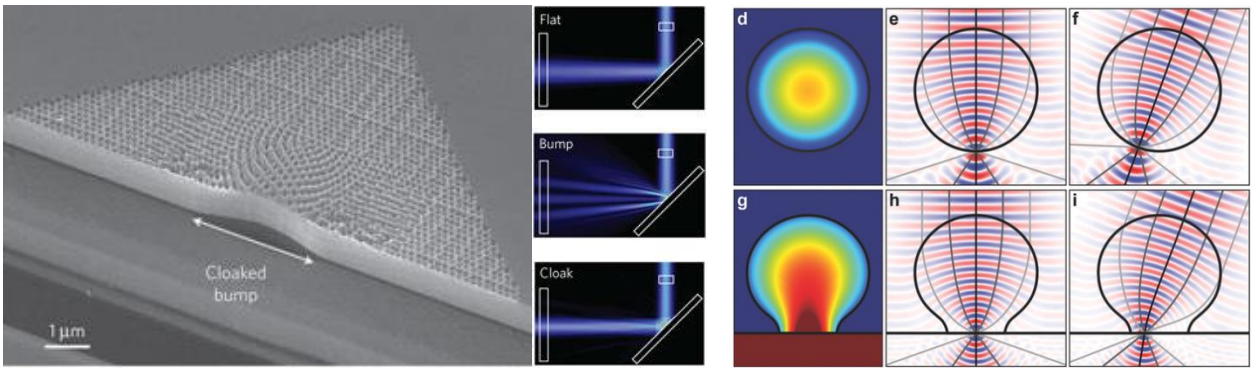

Figure 1.2. Left: An SEM image of a dielectric "carpet cloak" transformation optic that hides a bump on a flat surface, causing light to reflect off the surface as if there were no bump. From J. Valentine, et al.[8] Right: (d,e,f) show a gradient refractive index Luneburg lens that focuses light to a point on the surface of the spherical lens. In (g,h,i) the light paths have been transformed so that the focal surface is not a sphere but a flat plane. From F. Zhou, et al.[9]

1.2. Wave Optics

The ray model of light is not very accurate at smaller scales, near the wavelength of light.[10] At these scales, light is better modeled as waves in the electric and magnetic fields. The equations for the electric and magnetic fields for a propagating light wave at a single frequency are:

$$\tilde{E}(\vec{r},t) = \tilde{E}_0 e^{i(\vec{k}\cdot\vec{r}-\omega t+\delta)}, \quad \tilde{H}(\vec{r},t) = \tilde{H}_0 e^{i(\vec{k}\cdot\vec{r}-\omega t+\delta)} \tag{1.2}$$

where $\tilde{E}$ and $\tilde{H}$ are the complex electric and magnetic field vectors at position $\vec{r}$ and time t. $\vec{E}_0$ and $\vec{H}_0$ are the electric and magnetic field amplitude vectors describing the intensity and polarization of the electric field. ω is the angular frequency, describing the time interval

between wave crests, and $\vec{k}$ is the wave-vector, describing the space interval between wave crests with a magnitude inversely proportional to the wavelength. Finally δ is the phase shift, a constant that essentially shifts the wave forward or backward in space. In this work, the $\tilde{}$ accent is used to denote a complex vector and $\vec{}$ is used to denote a real vector. The imaginary components of the electric and magnetic fields could be thought of as a mathematical fiction that keeps track of the rate of change of the electric field (though there are other valid ways of thinking about it. Those unfamiliar with complex waves should make note of Euler's formula, $e^{ix} = \cos(x) + i\sin(x)$, which greatly simplifies the math. For light in a uniform, isotropic (non-birefringent) medium, the magnetic field is always perpendicular and directly proportional to the electric field, so it is common to focus on the electric field in explaining optics because the magnetic field will usually behave similarly.

Light interference is simply the overlap of the waves at the same space and time. The electric fields sum linearly: $\tilde{E}_{tot} = \tilde{E}_1 + \tilde{E}_2$.[11] When the waves are at the same frequency, the waves form regions that are stable in time, regions where the electric fields combine to create stronger fields (constructive interference) and regions where the electric fields cancel to create weaker fields (destructive interference). This interference is useful to control where light goes and we will discuss two common ways that it is used this way: antireflection coatings and photonic crystals.

As discussed in the ray optics section, light reflects when hitting a material with a different refractive index, such as air hitting glass. If we want to reduce or eliminate this reflection, we can create destructive interference for the reflected beam.[12] A diagram of an antireflection coating using this principle is shown in the left half of **Figure 1.3**. A thin coating is placed on the material with a refractive index such that the amplitude of the reflection between the air and coating is the same as between the coating and glass. The thickness of the coating is set at a quarter-wavelength thickness so that there is a half-wave path length difference between the two reflections, resulting the crests and troughs of each cancelling each other out. With total cancellation of those fields, reflection is completely eliminated and 100% of the light is transmitted.

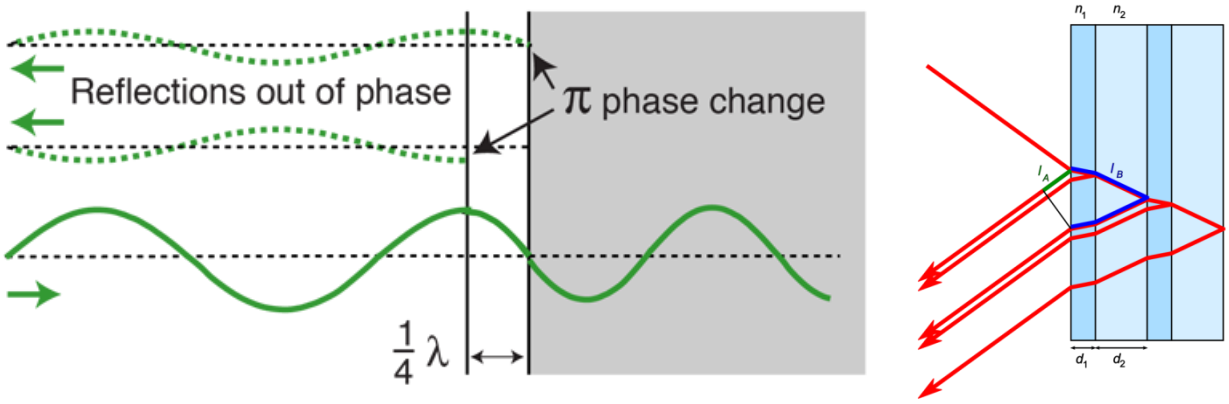

Figure 1.3. Left: cartoon of an anti-reflection coating based on destructive interference of reflected light. Image by Rod Nave.[13] Right: cartoon of a 1D photonic crystal based on constructive interference of reflected light. Image by Hank Wang.[14]

If we instead want to increase the reflectance, we can use constructive interference of the reflected light.[15] A Bragg stack (also known as a 1D photonic crystal) is a repeating set of high-index and low-index layers configured to increase reflectance, shown in the right half of **Figure 1.3**. In it each layer has a quarter-wave thickness, so that there is a full-wave phase shift on round trips for the entire unit cell. This results in constructive interference of the reflected waves. With higher number of pairs of layers, the reflectance gets closer and closer to 100%. This principle can be extended to higher dimensions, allowing the creation of 3D periodic media that reflect light in all directions.

These principles of constructive and destructive interference can be used to create multidimensional periodic patterns in a method called interference lithography.[16]–[18] In short, regions of constructive interference lead to enhanced absorption of light, causing local chemical changes of a photoresist. In regions with destructive interference there is reduced absorption and thus less chemical change. The chemical changes result in differences in solubility of the resist, leaving a solid structure with a 1D, 2D or 3D periodic pattern. This method is discussed in detail in chapter 2.

1.3. Effective Index Media

When physical scales are well below the wavelength of light, the wavelike interference effects are no longer seen.[19], [20] In this case, light can be thought of as being closer to a

'tide' than a wave. This is a regime where complex structures with a rapidly spatially varying refractive index can be treated as though it were a single material with a constant refractive index, called an effective index medium. For a far-subwavelength structure with dielectric constituents, the effective refractive index will be between the indices of the constituents. But the effective refractive index is not simply a weighted average: the effective index depends heavily on screening effects that occur based on the geometry of each constituent. Because of this geometrical dependence, screening can introduce a birefringence into the effective index.[21] An example of structure resulting in birefringence in an effective medium material is that of a wire-grid polarizer.[22] When the light is polarized parallel to the metallic ribs, charge builds up at the edges of the wires, screening the electric field from the wires, minimizing absorption. When light is parallel, there is no screening of the electric field, causing large attenuation of the light. An example we will discuss in chapter 5 is porous silicon, which is single-crystal silicon into which a high density of vertical pores have been etched.[23] The effective refractive index when the electric field is orthogonal to the pores is lower than when the electric field is parallel to the pores due to screening of the Si. This is discussed in more detail in chapter 5.

Effective index media is one way that we can control the refractive index to make the transformation optics in section 1.1. The example transformation optics in **Figure 1.2** are made with effective media with gradually changing porosities. Effective index media is one of the more common techniques for making transformation optics due to the high range of indices that can be achieved.[24]

A special kind of effective index medium is metamaterials, which has been given a great deal of research focus recently.[25]–[27] There is no single definition for the word 'metamaterial' but it is generally used to indicate an effective index medium that incorporates a coupling of the electric and magnetic field components. This field coupling can introduce new optical characteristics not found in natural materials, most notably a negative refractive index. Dielectric effective index media do not have these capabilities but also do not have the high losses commonly found in metamaterials.[28] In chapter 4 we will discuss a metallic helical

array that operates somewhat as an effective medium that exhibits circular dichroism, though it does not quite meet the characteristics of an effective medium.[29]

Effective index media are usually studied by sending light through the composite material (either in simulation or in the laboratory), measure that light leaves, and calculate what kind of effective index would yield the same results.[30] On warning I will give to those starting to work in the field is that these calculations will always give an answer, regardless of whether that answer has any real meaning.[31] So one must always check whether the effective medium model is appropriate in the first place. For example, one should check whether the effective index is stable across changes in the thickness of the element because if the effective index changes with the quantity of material you cannot actually treat it as an intrinsic property.

1.4. Photolithography

Photolithography is the process of turning a pattern of light into a pattern of a material.[32] A schematic of conventional lithography is shown in **Figure 1.4**. Light, usually in UV, is first sent through a plate covered with an opaque material (often chromium) in the desired pattern, called a mask. After the mask, the light hits a photoresist, which is a material whose solubility changes upon exposure to light and is resistant to desired etchants – i.e. it responds to *photons* and *resists* etching. In this dissertation only negative resists are discussed, meaning that the photoresist starts as soluble to the developer but resists development after sufficient exposure to light. After the film of photoresist is exposed, it is developed in a solvent, removing some of the resist in a pattern that is either a copy of the mask, or a negative of the mask. The pattern of photoresist can then be used to prevent etching of the material directly beneath it. A photoresist pattern on top of a layer of metal, for example, can be exposed to an etch of the metal so that the pattern of the mask is ultimately transferred to the metal. The photoresist can then be removed with a different solvent or etch process.

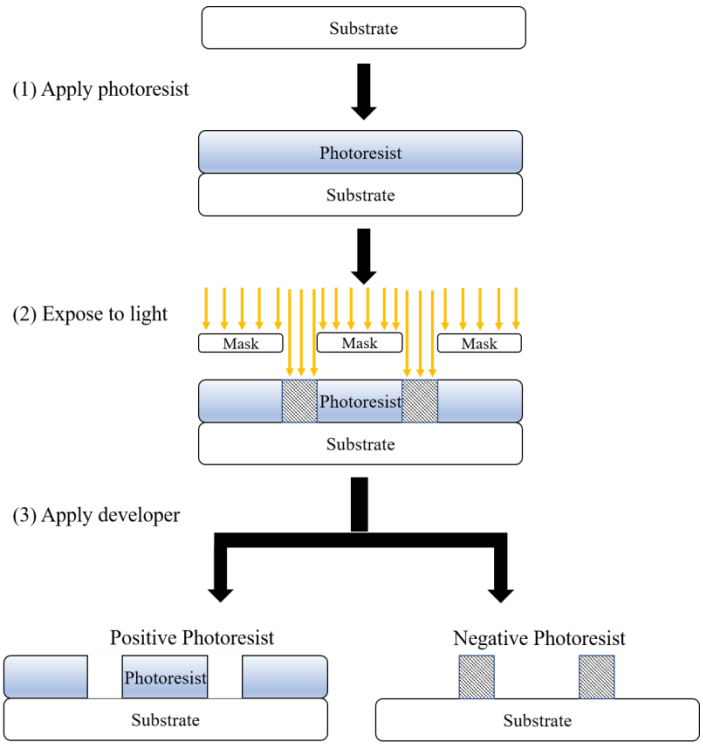

Figure 1.4. Schematic of conventional lithography process. Photoresist is applied to a substrate, then exposed to light in selective regions according to a mask. The photoresist is then selectively developed according to the exposure, leaving the remaining photoresist as either a copy of the mask or its opposite. Image by May Iam.[33]

This dissertation involves a couple of more unusual kinds of photolithography that do not use masks. The first is interference lithography, where the pattern is controlled by regions of constructive and destructive interference of lasers.[16], [34]–[36] This is discussed in detail in Chapter 2. The second is direct writing.[37], [38] We use two kinds of direct writing lithography: direct laser writing (DLW) and electron beam lithography (EBL). DLW works by focusing light to a tight focus so that a small portion of the beam is exposed. The focus is moved relative to the sample, rastering over the areas designated for exposure. In this way, the photoresist can be patterned without the need for a mask. If the system is set up for two-photon absorption, then absorption only occurs at the precise focus, enabling 3D structures to be written.[39] While EBL is not technically *photo*lithography, it operates on much the same principles, with the exception that electrons are used to expose the resist rather than photons, allowing much higher resolutions to be achieved.[40]

Two photoresists are particularly important for this work: SU-8 and IP-dip.[38], [41] Both photoresists are commonly used for their ability to maintain integrity with very high aspect ratios, making them especially useful for 3D photonic photonic crystals and other microscale 3D structures. Their mechanical stability is due in part to their high crosslink density. SU-8 contains (on average) 8 epoxide groups that can be a part of polymer chains, so each monomer can potentially bond with 16 other monomers.[41] The molecular structure is shown in **Figure 1.5**. SU-8 is spincoated onto a substrate and forms a solid film that is in the glassy state at room temperature. At temperatures above the glassy state, a relief pattern can be imprinted into the surface of SU8 and hold its shape at lower temperatures, which is useful for forming phase masks directly on the surface of the resist. SU-8 polymerization is initiated via a photoacid generator, continues as a cationic polymerization process, and terminates (usually) by reacting with the counter-ion of the photoacid generator.[41, p. 8] Polymerization only occurs above the glassy transition temperature, so the amount of crosslinking can be controlled using the temperature profile of the postbake.

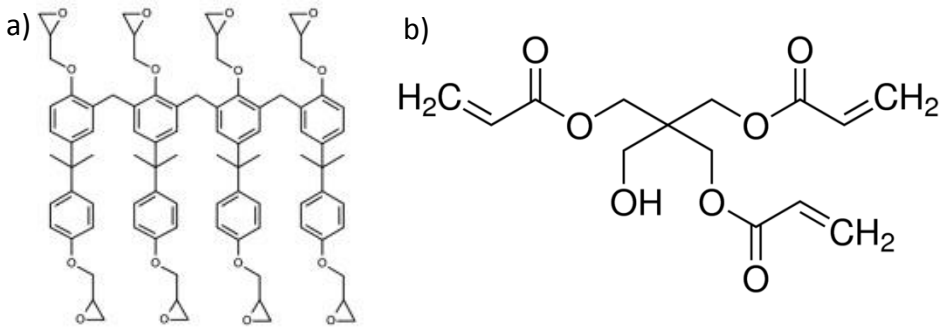

Figure 1.5. Chemical structures of (a) SU-8 photoresist monomer and (b) pentaerythritol triacrylate. Images from Krishnamurthy Nemani[42] and Sigma Aldrich.[43]

IP-dip has pentaerythritol triacrylate (PETA) as a resin, which has (as the name suggests) three acrylate groups, so each monomer can bond to 6 other monomers.[44], [45] With its small molecular size, the potential crosslink density of PETA is quite high. One unusual aspect of PETA is that it is liquid at room temperature, which makes it useful for immersion laser direct writing processes where the focusing lens moves through the resist.[38] IP-dip uses a two-photon photoinitiator, which enables the writing of dense 3D structures, as discussed above. IP-dip polymerization proceeds as a free radical vinyl polymerization and terminates upon reacting with diatomic oxygen dissolved in the resist. Polymerization in IP-dip occurs very

rapidly, but is quenched practically immediately by the oxygen, quite literally starting and stopping in the blink of an eye.

This chapter can only cover the basics, but each chapter begins with a short introduction that provides background information in more detail.

1.5. References

[1] E. Hecht, *Optics*, 4th ed. Addison-Wesley, 1998.

[2] J. Teichman, J. Holzer, B. Balko, B. Fisher, and L. Buckley, "Gradient index optics at DARPA," INSTITUTE FOR DEFENSE ANALYSES ALEXANDRIA VA, 2013.

[3] Michael W. Davidson, "Refraction of Light." Molecular Expressions, 13-Nov-2015.

[4] M. Berger, T. Trout, and N. Levit, "Ray tracing mirages," *IEEE Comput. Graph. Appl.*, vol. 10, no. 3, pp. 36–41, May 1990.

[5] S. N. Houde-Walter and B. L. McIntyre, "Dependence of refractive index on silver concentration in gradient-index glass," *J. Non-Cryst. Solids*, vol. 107, no. 2–3, pp. 316–322, Jan. 1989.

[6] H. Fujisaki and N. Nakagiri, "Design of a gradient refractive index phase zone plate for soft x-rays," *Appl. Opt.*, vol. 29, no. 4, p. 483, Feb. 1990.

[7] R. Foster, P. Grant, Y. Hao, A. Hibbins, T. Philbin, and R. Sambles, "Spatial transformations: from fundamentals to applications," *Philos. Trans. R. Soc. Math. Phys. Eng. Sci.*, vol. 373, no. 2049, p. 20140365, Aug. 2015.

[8] J. Valentine, J. Li, T. Zentgraf, G. Bartal, and X. Zhang, "An optical cloak made of dielectrics," *Nat. Mater.*, vol. 8, no. 7, pp. 568–571, Jul. 2009.

[9] F. Zhou, W. Cao, B. Dong, T. Reissman, W. Zhang, and C. Sun, "Additive Manufacturing of a 3D Terahertz Gradient-Refractive Index Lens," *Adv. Opt. Mater.*, vol. 4, no. 7, pp. 1034–1040, Jul. 2016.

[10] Bahaa E. A. Saleh and Malvin Carl Teich, *Fundamentals of Photonics*. New York: Wiley, 1991.

[11] M. Born and E. Wolf, *Principles of Optics*, 7th ed. Cambridge University Press, 1999.

[12] H. K. Raut, V. A. Ganesh, A. S. Nair, and S. Ramakrishna, "Anti-reflective coatings: A critical, in-depth review," *Energy Environ. Sci.*, vol. 4, no. 10, p. 3779, 2011.

[13] Rod Nave, *Antireflection coating*. .

[14] Hank Wang, *Bragg stack reflectance*. .

[15] J. D. Joannopoulos, S. G. Johnson, J. N. Winn, and R. D. Meade, "Photonic Crystals: Molding the Flow of Light." Princeton University Press, 13-Nov-2007.

[16] C. Lu and R. H. Lipson, "Interference lithography: a powerful tool for fabricating periodic structures," *Laser Photonics Rev.*, vol. 4, no. 4, pp. 568–580, May 2009.

[17] M. Miyake, Y.-C. Chen, P. V. Braun, and P. Wiltzius, "Fabrication of Three-Dimensional Photonic Crystals Using Multibeam Interference Lithography and Electrodeposition," *Adv. Mater.*, vol. 21, no. 29, pp. 3012–3015, Aug. 2009.

[18] D. A. Bacon-Brown and P. V. Braun, “Tunable Antireflection Coating to Remove Index-Matching Requirement for Interference Lithography,” *Adv. Opt. Mater.*, p. 1701049, Feb. 2018.
[19] D. E. Aspnes, “Local-field effects and effective-medium theory: A microscopic perspective,” *Am. J. Phys.*, vol. 50, no. 8, pp. 704–709, Aug. 1982.
[20] G. A. Niklasson, C. G. Granqvist, and O. Hunderi, “Effective medium models for the optical properties of inhomogeneous materials,” *Appl. Opt.*, vol. 20, no. 1, pp. 26–30, 1981.
[21] L. A. Golovan’, P. K. Kashkarov, and V. Y. Timoshenko, “Form birefringence in porous semiconductors and dielectrics: A review,” *Crystallogr. Rep.*, vol. 52, no. 4, pp. 672–685, Jul. 2007.
[22] G. R. Bird and M. Parrish, “The Wire Grid as a Near-Infrared Polarizer,” *J. Opt. Soc. Am.*, vol. 50, no. 9, p. 886, Sep. 1960.
[23] N. A. Krueger *et al.*, “Porous Silicon Gradient Refractive Index Micro-Optics,” *Nano Lett.*, vol. 16, no. 12, pp. 7402–7407, Dec. 2016.
[24] C. R. Ocier, N. A. Krueger, W. Zhou, and P. V. Braun, “Tunable Visibly Transparent Optics Derived from Porous Silicon,” *ACS Photonics*, vol. 4, no. 4, pp. 909–914, Apr. 2017.
[25] A. Boltasseva and V. M. Shalaev, “Fabrication of optical negative-index metamaterials: Recent advances and outlook,” *Metamaterials*, vol. 2, no. 1, pp. 1–17, May 2008.
[26] Y. Liu and X. Zhang, “Metamaterials: a new frontier of science and technology,” *Chem. Soc. Rev.*, vol. 40, no. 5, p. 2494, 2011.
[27] C. M. Soukoulis and M. Wegener, “Past achievements and future challenges in the development of three-dimensional photonic metamaterials,” *Nat. Photonics*, Jul. 2011.
[28] S. Jahani and Z. Jacob, “All-dielectric metamaterials,” *Nat. Nanotechnol.*, vol. 11, no. 1, pp. 23–36, Jan. 2016.
[29] J. K. Gansel *et al.*, “Gold Helix Photonic Metamaterial as Broadband Circular Polarizer,” *Science*, vol. 325, no. 5947, pp. 1513–1515, Aug. 2009.
[30] X. Chen, B.-I. Wu, J. Kong, and T. Grzegorczyk, “Retrieval of the effective constitutive parameters of bianisotropic metamaterials,” *Phys. Rev. E*, vol. 71, no. 4, Apr. 2005.
[31] D. R. Smith and J. B. Pendry, “Homogenization of metamaterials by field averaging (invited paper),” *J. Opt. Soc. Am. B*, vol. 23, no. 3, p. 391, Mar. 2006.
[32] M. Rothschild, “A review of excimer laser projection lithography,” *J. Vac. Sci. Technol. B Microelectron. Nanometer Struct.*, vol. 6, no. 1, p. 1, Jan. 1988.
[33] May Iam, *Photoresist of Photolithography*. .
[34] M. Miyake, Y.-C. Chen, P. V. Braun, and P. Wiltzius, “Fabrication of Three-Dimensional Photonic Crystals Using Multibeam Interference Lithography and Electrodeposition,” *Adv. Mater.*, vol. 21, no. 29, pp. 3012–3015, Aug. 2009.
[35] S. Yang, M. Megens, J. Aizenberg, P. Wiltzius, P. M. Chaikin, and W. B. Russel, “Creating Periodic Three-Dimensional Structures by Multibeam Interference of Visible Laser,” *Chem. Mater.*, vol. 14, no. 7, pp. 2831–2833, Jul. 2002.
[36] Q. Xie, M. H. Hong, H. L. Tan, G. X. Chen, L. P. Shi, and T. C. Chong, “Fabrication of nanostructures with laser interference lithography,” *J. Alloys Compd.*, vol. 449, no. 1–2, pp. 261–264, Jan. 2008.
[37] M. Beresna, M. Gecevičius, and P. G. Kazansky, “Ultrafast laser direct writing and nanostructuring in transparent materials,” *Adv. Opt. Photonics*, vol. 6, no. 3, p. 293, Sep. 2014.

[38] T. Bückmann *et al.*, “Tailored 3D Mechanical Metamaterials Made by Dip-in Direct-Laser-Writing Optical Lithography,” *Adv. Mater.*, vol. 24, no. 20, pp. 2710–2714, May 2012.
[39] T. Gissibl, S. Thiele, A. Herkommer, and H. Giessen, “Two-photon direct laser writing of ultracompact multi-lens objectives,” *Nat. Photonics*, vol. 10, no. 8, pp. 554–560, Jun. 2016.
[40] Y. Chen, “Nanofabrication by electron beam lithography and its applications: A review,” *Microelectron. Eng.*, vol. 135, pp. 57–72, Mar. 2015.
[41] A. del Campo and C. Greiner, “SU-8: a photoresist for high-aspect-ratio and 3D submicron lithography,” *J. Micromechanics Microengineering*, vol. 17, no. 6, pp. R81–R95, Jun. 2007.
[42] K. V. Nemani, K. L. Moodie, J. B. Brennick, A. Su, and B. Gimi, “In vitro and in vivo evaluation of SU-8 biocompatibility,” *Mater. Sci. Eng. C*, vol. 33, no. 7, pp. 4453–4459, Oct. 2013.
[43] Sigma-Aldrich, *Pentarythritol triacrylate*. .
[44] S. Dottermusch, D. Busko, M. Langenhorst, U. W. Paetzold, and B. S. Richards, “Exposure-dependent refractive index of Nanoscribe IP-Dip photoresist layers,” *Opt. Lett.*, vol. 44, no. 1, p. 29, Jan. 2019.
[45] J. Durisova, D. Pudis, M. Goraus, and P. Gaso, “IP-Dip photoresist surfaces for photonic applications prepared by laser lithography and studied by AFM,” *Appl. Surf. Sci.*, vol. 461, pp. 108–112, Dec. 2018.

CHAPTER 2

TUNABLE ANTIREFLECTION COATINGS FOR INTERFERENCE LITHOGRAPHY[1]

This chapter first covers the principles of interference lithography, then discusses the issue of backside reflections from the interface between the photoresist and substrate. A tunable refractive index antireflection coating is presented as a solution and demonstrated.

2.1. Introduction to Interference Lithography

Interference lithography is a maskless lithography technique whereby the interference of light waves defines the regions of photoresist that are exposed. Here we will only discuss interference patterns generated by plane waves, as they are the most common. The simplest way of generating an interference pattern is with a Lloyd's interferometer.[2] A diagram of this setup is shown in **Figure 2.1**. A laser beam is sent toward an assembly containing a mirror and a photoresist film. The mirror reflects part of the incident light so that the laser approaches the film in two directions, forming the simplest interference pattern. The interference pattern is driven by the difference in path length the two beams travel: when the path length difference is close to a multiple 2π, there is constructive interference and absorption of the light by the photoresist is inhanced; if not, there is destructive interference and absorption is diminished. The Lloyds mirror will lead to the simplest interference pattern: repeating planes that are oriented normal to the *difference* vector between the propagation directions of the incident beams. The spacing of the planes is controlled by the wavelength of the laser and the angles of incidence of the incoming beams.

[1] Parts of this chapter were previously published by the author and are included here with permission from WILEY-VCH Verlag GmbH.[1]

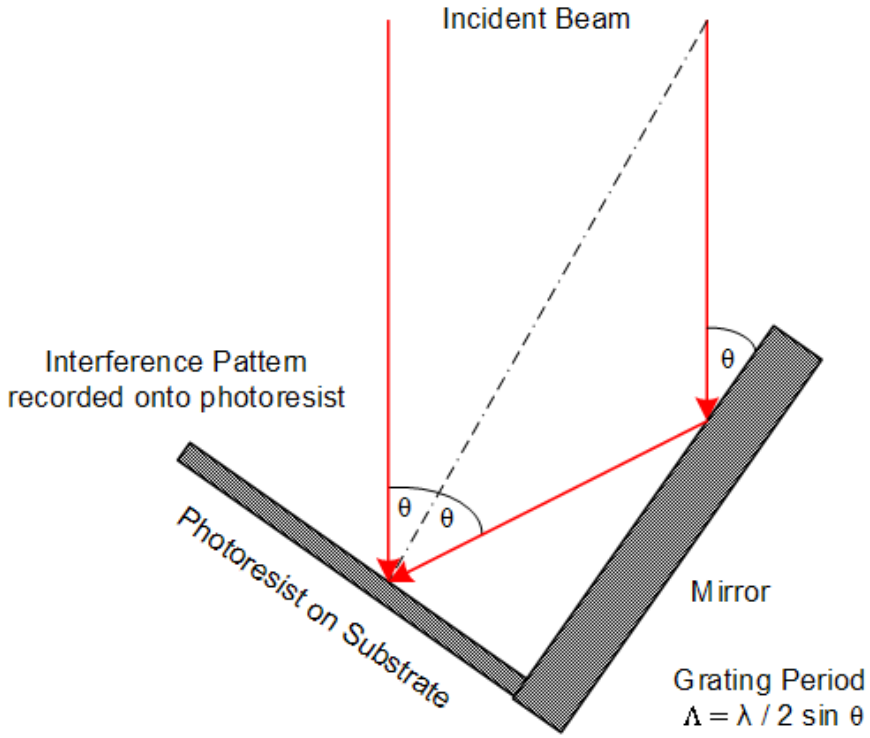

Figure 2.1. Diagram of Lloyd mirror interference lithography. Image by M.C. Marconi, et al.[3]

Interference lithography is attractive because it can write feature sizes below a quarter of the wavelength without requiring a mask,[4] but this also comes with real limitations. The pattern must be completely periodic, though that periodicity can include any Bravais lattice.[5] For this reason, interference lithography is used where the patterned layer is desired to be identical across the exposed region, commonly photonic crystals, polarizers, or graded antireflection coatings.[6]–[8]

One special characteristic of interference lithography is that it can create 3D patterns with a single exposure step. It is possible to define 3D lattices that have dozens of unit cells in the z-direction which would require an inordinate number of exposure steps with conventional lithography, which can only define a single plane at a time.

A common issue with interference lithography is that it can be difficult to determine the required amplitude and polarization parameters to generate a particular structure. It is easy to calculate the pattern generated by a set of interfering beams, but this calculation cannot be done backwards. This is known as the *inverse problem* of interference lithography. Solutions

can be found by performing optimizations of interference lithography designs, but this is no guarantee of a good solution.[9], [10]

2.2. Mathematics of Multibeam Interference Lithography

Here, I'll go into the calculation of the 3D intensity profiles generated in multibeam interference lithography (MIB), where the interference pattern is prepared by splitting a laser into distinct beams, individually controlling them, then interfering them at the photoresist. First, I'll go into the calculation of the periodicity of the lattice. This treatment is similar previous treatments, such as found in James Rinne's thesis,[10] but I've tried to make this brief and appeal to a somewhat broader audience.

2.2.1. Relating Incident Light to Bravais Lattice

Interference lithography is driven by the local electromagnetic intensity – the intensity controls the probability of a photochemical reaction occurring in any particular spot resist and thus governs the geometry of the fabricated structure. The local electromagnetic intensity, I, due to the overlap of plane waves in a uniform medium in the far field given by equation 2.1:[4]

$$\boldsymbol{I}(\vec{\boldsymbol{r}}) = \sqrt{\frac{\boldsymbol{\varepsilon}}{\boldsymbol{\mu}}} \sum_{\boldsymbol{i}} \sum_{\boldsymbol{j}} \overrightarrow{\boldsymbol{E_i}} \cdot \overrightarrow{\boldsymbol{E_j}}^{\dagger} \exp\left(\boldsymbol{i}\left[\left(\overrightarrow{\boldsymbol{k_i}} - \overrightarrow{\boldsymbol{k_j}}\right) \cdot \vec{\boldsymbol{r}} + \left(\boldsymbol{\delta_i} - \boldsymbol{\delta_j}\right)\right]\right) \tag{2.1}$$

where $\overrightarrow{E_i}$ is the complex electric field vector for each plane wave, $\vec{r}$ is the local position in space, δ is the phase of each plane wave, ε is the permittivity of the medium, and μ is the permeability of the medium.

We define the periodicity vectors, $\vec{R}$, as a set of vectors that show translation symmetry across the intensity of the lattice:

$$I(\vec{r}) = I\left(\vec{r} + \sum_{k} \overrightarrow{R_k}\, m_k\right) \tag{2.2}$$

for any set of integers, m.

Combining equation 2.2 into 2.1, we see that the periodicity condition is:

$$\exp\left(i \cdot \left(\overrightarrow{k_\iota} - \overrightarrow{k_\jmath}\right) \cdot \sum_k \overrightarrow{R_k}\, m_k\right) = 1 \tag{2.3}$$

or

$$\left(\overrightarrow{k_\iota} - \overrightarrow{k_\jmath}\right) \cdot \sum_k \overrightarrow{R_k}\, m_k = 2\pi m \tag{2.4}$$

for any integer m. By addition, this can be turned into:

$$\sum_{i,j} \left(\overrightarrow{k_\iota} - \overrightarrow{k_\jmath}\right) m_{i,j} \cdot \sum_k \overrightarrow{R_k}\, m_k = 2\pi m \tag{2.5}$$

In words, this means that the reciprocal of the real space lattice is equal to the lattice formed by the addition of the difference-vectors of the incident plane waves. We can use this to determine the periodicity of a lattice formed by a set of interfering waves, or to determine the required set of waves to create a desired lattice, as demonstrated in the next section.

2.2.2. Example of calculation of exposure conditions for simple cubic lattice

As an example, a set of beam angles will be calculated for the fabrication of a simple cubic lattice. It starts with a definition of the periodicity of the lattice:

$$\overrightarrow{R_1} = a[1\ 0\ 0], \qquad \overrightarrow{R_2} = a[0\ 1\ 0], \qquad \overrightarrow{R_3} = a[0\ 0\ 1] \tag{2.6}$$

The reciprocal lattice for a cubic lattice is simply another cubic lattice, giving a simple solution:

$$\left(\overrightarrow{k_1} - \overrightarrow{k_2}\right) = \frac{2\pi}{a}[1\ 0\ 0], \qquad \left(\overrightarrow{k_1} - \overrightarrow{k_3}\right) = \frac{2\pi}{a}[0\ 1\ 0], \qquad \left(\overrightarrow{k_1} - \overrightarrow{k_4}\right) = \frac{2\pi}{a}[0\ 0\ 1] \tag{2.7}$$

Unfortunately, direct fabrication of this lattice would require incident beams that propagate from both the top and bottom of the sample, which presents experimental challenges. Fortunately, this can be resolved by rotating the desired lattice so that the unit cell is standing corner on corner. This can be accomplished by rotating the lattice vectors around the x-axis 45°, and then around the y-axis 35.26°:

$$\begin{aligned} \overrightarrow{R_1} &= \left(\overrightarrow{k_1} - \overrightarrow{k_2}\right) = a[1, 0, \sin(35.26°)] \\ \overrightarrow{R_2} &= \left(\overrightarrow{k_1} - \overrightarrow{k_3}\right) = a[\cos(120°), \sin(120°), \sin(35.26°)] \\ \overrightarrow{R_3} &= \left(\overrightarrow{k_1} - \overrightarrow{k_4}\right) = a[\cos(240°), \sin(240°), \sin(35.26°)] \end{aligned} \tag{2.8}$$

This set of propagation vector difference matches the classic 'umbrella configuration' commonly used for 3D interference lithography of structures with a cubic Bravais lattice.[4],

[11]–[16] In this configuration, there is an incident beam that has a propagation vector normal to the substrate, and 3 beams propagating at the same azimuthal angle and at 0°, 120°, 240° polar angles. The umbrella configuration is experimentally convenient and relatively easily reconfigured for structures with useful symmetries, but many other configurations are possible – the reader is encouraged to experiment with beam configurations in order to obtain novel lattices.

2.2.3. Calculation of Unit Cell Basis

Thus far, we have covered lattice periodicity of interference lithography experiments and its relation to the incident beam angles, but we have not covered the *basis* of the unit cell. Here we will cover the calculation of the basis expected from a particular interference lithography experiment. The corresponding Matlab code for this calculation will be shown in Section 2.3.4.

The interference pattern is calculated by phasor addition of plane waves over a volume of space. Electromagnetic plane waves are defined by a complex electric field vector and a propagation vector. The volume of space is simply defined by a set of Cartesian coordinates. For convenience, we typically use a regular grid with axes aligned along the $\hat{x}$, $\hat{y}$, and $\hat{z}$ directions, but an arbitrary list of coordinates can be used with this technique. An example of a rotated and rhombohedral coordinate system will be shown in Section 2.3.5.

The intensity is well known to be equal to the dot product of the electric field vector and its own complex conjugate, equation 2.9. This is a convenient formulation for calculating the intensity, since this means we do not need to worry about the time variable, as this equation will yield the same result for every value of t.

$$I(\vec{r}) = \frac{\varepsilon}{2\mu}\vec{E}(\vec{r},t)\cdot\vec{E}^{\dagger}(\vec{r},t) \tag{2.9}$$

Thus, we merely need to calculate the sum of each electric field across a volume of space. We use the plane wave description of the electric field, equation 2.10, assuming t=0 for simplicity:

$$\overrightarrow{E_{tot}}(r,t=0) = \sum_n \overrightarrow{E_0}\mathrm{e}^{i\,(\vec{k}\cdot\vec{r}-\,\omega t)} = \sum_n \overrightarrow{E_0}\mathrm{e}^{i\,\vec{k}\cdot\vec{r}} \tag{2.10}$$

This calculation can be made relatively efficient by taking advantage of matrix multiplication. The following code was developed by the P.V. Braun group and is a useful tool for efficiently calculating the interference pattern. As written, this assumes that a uniformly spaced Cartesian grid is used, but it can be useful to use other grids. An example of a non-standard grid is shown in Appendix A. A more efficient but conceptual more complex calculation is shown in Appendix B.

Inputs:

- E: 3 x n complex matrix. Units of electric field. This defines the complex electric field vectors. Each column defines a beam as a 3 x 1 complex vector in the format $\left[\widetilde{E_x};\ \widetilde{E_y};\ \widetilde{E_z}\right]$. Note that the electric field is defined in 3D space, rather than s- and p-polarizations. Fields that are defined by s- and p-polarizations or a Jones vector can be easily converted to this coordinate system by following a short method described in Appendix A.
- k: 3 x n real matrix. Units of 2π/length. This defines the propagation vectors. Each row defines a beam as a 3 x 1 vector in the format $\left[k_x;\ k_y;\ k_z\right]$.
- dimx, dimy, dimz: 3 scalars. Units of length. These define the dimensions of the region for which the field should be calculated. The code presented here assumes that the simulation region is in the shape of a rectangular prism, but different coordinate systems can be calculated by multiplying the x, y, and z meshgrids by the appropriate transformation matrices.
- Nx, Ny, Nz: 3 scalars. Dimensionless. These define the number of voxels in each dimension of the grid for which the intensity is calculated
- Offset: 3 x 1 real matrix. Units of length. This translates the location of the unit cell

```
function IN = icalc(E,k,dimx,dimy,dimz,Nx,Ny,Nz,offset)

    %Get number of beams implicitly from input data
    Nb=size(E,2);
    %Calculate total number of coordinates to calculate
    N = Nx*Ny*Nz;

    %Calculate wavelength in the material from the first k-vector
    lambda = 2*pi/sqrt(sum(k(1,1:3).^2));
```

```
    %Create 3, 3D matrices that hold the x, y, and z index coordinates
    [y,x,z]=meshgrid(0:Ny-1,0:Nx-1,0:Nz-1);

    %Reshape the coordinate grid into a linear coordinate list, so that matrix operations can
        be performed on them
    x=reshape(x,1,N);
    y=reshape(y,1,N);
    z=reshape(z,1,N);

    %Combine the coordinate lists into a single matrix
    r=[x;y;z];

    %Convert coordinate indices into real-space coordinates and shift each coordinate by
        the offset vector
    r(1,:) = (r(1,:)/Nx + offset(1))*dimx;
    r(2,:) = (r(2,:)/Ny + offset(2))*dimy;
    r(3,:) = (r(3,:)/Nz + offset(3))*dimz;


    %These are the x,y,z components of the field to be multiplied by the plane wave at
        every point, r, in space (or specified volume).  This procedure makes a copy of
        the each E-field component so
    Ex=repmat(reshape(E(1,:),Nb,1),1,N);
    Ey=repmat(reshape(E(2,:),Nb,1),1,N);
    Ez=repmat(reshape(E(3,:),Nb,1),1,N);

    %Define matrix to create the phase shifts at each point in space for each beam.
        e^(i*k*r), where theta = k*r
    ei = exp(complex(0,1)*(k*r));

    %Apply phase shifts and sums the electric field contribution from each beam
    E_total=[sum(Ex.*ei,1);sum(Ey.*ei,1);sum(Ez.*ei,1)];

    %Calculate intensity from electric field sum
    IN=sum(E_total.*conj(E_total));

    %Convert the intensity data in 1-D format to a 3-D format
    IN = reshape(real(IN),Nx,Ny,Nz);
end
```

2.3. Embedding Functional Features in Interference Lithography

Recently, the Braun group has done a great deal of work on expanding the capabilities of 3D interference lithography.[1], [17]–[21] One of these expansions has focused on developing techniques to enable the addition of defect layers clad by thick regions of 3D patterned structures. The creation of a defect layer within a photonic crystal lattice is useful for

achieving a variety of optical properties.[22] For example, the photonic crystal can be used to control the optical density of states (DoS) for the defect layer, which affects the emission and absorption properties of an emitting or absorbing elements within the defect layer.[23] We showed that a photonic crystal stack with a defect layer can be fabricated by preparing a photoresist-defect-photoresist sandwich and exposing with interference lithography.[18] The emission spectra of emitters in the defect layer could be controlled by adjusting the position of the defect modes in the photonic crystal bandgap relative to the emission peak of the emitters.

Photonic crystals were discussed briefly section 1.2, but here we will discuss the properties of defects within photonic crystals. For now, we will discuss 1D photonic crystals, but this discussion also applies to higher dimensions. A defect in a photonic crystal is a local disruption of the translation symmetry of the photonic crystal, which can include a change in the complex refractive index or thickness of one of the layers.[24] A defect does not necessarily have a significant effect on the optics of the photonic crystal, but there can be major changes depending upon the interaction of the defect with light. If the defect is capable of strongly interacting with a wavelength of light that is normally blocked from propagating in the photonic crystal, this can cause a so-called defect mode to appear in the transmission spectrum, where there is high transmission near a peak surrounded by minimal transmission due to the usual photonic bandgap effect.[23] **Figure 2.4.1a** below shows a schematic of a 1D photonic crystal by increasing the refractive index of the lower refractive index layer.[24] The red line shows the electric field strength for light propagating through at a particular. In the bulk of the crystal, there is minimal electric field strength for that mode. The defect, however, is able to support a ½ wavelength standing wave. This leads to a greatly enhanced electric field in the vicinity of the defect and enhanced transmission at the defect wavelength; the defect functions as a high-Q cavity. As is usual with high-Q cavities, at slightly higher or lower wavelengths there is poor resonance with the defect and the photonic crystal reflects these wavelengths as usual.

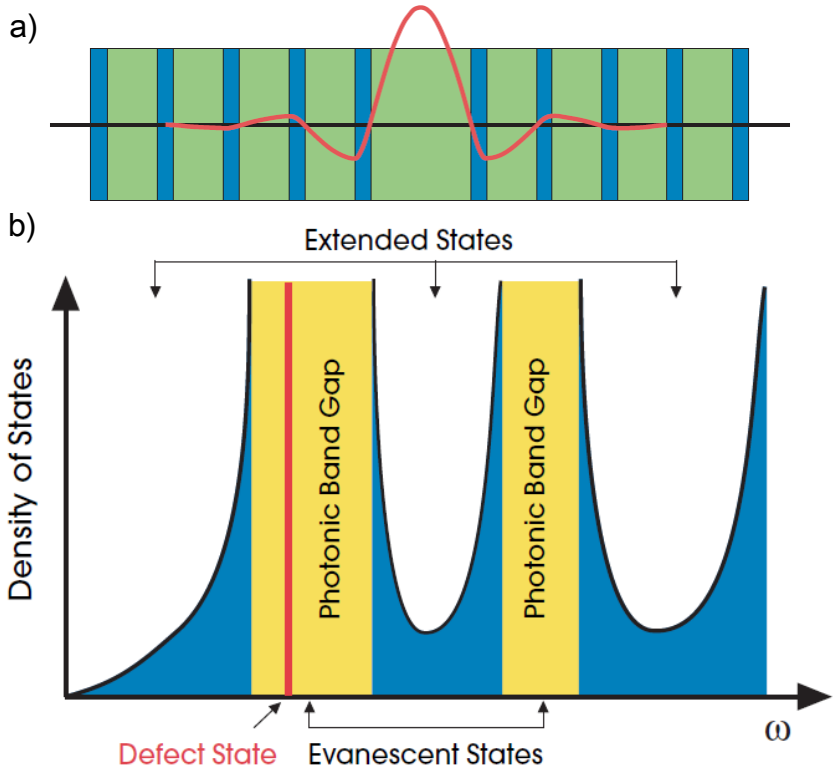

Figure 2.2. a) Schematic of a 1-D photonic crystal with a defect composed of a layer of material with extended thickness. The red line represents the electric field strength of the defect mode. b) Plot of the optical density of states against angular frequency for a photonic crystal with a defect within the bandgap. The red line indicates the defect mode in the presence of bandgap. Images are from Joannopoulos, et al, Molding the Flow of Light.[24]

Defect modes in photonic crystals have large effects on the local optical DoS.[23] The DoE is a description of the allowed wave-vectors of light with the energy of the light. Roughly speaking, it is the number of ways the light can propagate at a particular frequency. For a uniform 3D medium, the density of states increases with the square of the frequency. A plot of the DoE against energy is shown in **Figure 2.2b**. Within a photonic crystal the DoS must go to zero within the photonic bandgap, since there are no ways in which light can propagate at that frequency. When a photonic bandgap forms, the light lines of the bandstructure flatten, leading to an enhanced DoS near the bandgap. The defect mode can be thought of as being pushed from both sides, leading to an even greater enhancement of the DoE. This enhanced DoE can be used to maximize the interaction of light with the materials within the defect. For example, fluorophores that are spatially located within the defect and whose emission frequency is spectrally located within the defect mode, will show an enhanced emission.[25] If

the emission frequency is instead in the bandgap, then there will be greatly suppressed emission.[26] We demonstrated this by incorporating fluorescent defect layer into a photonic crystal fabricated by interference lithography and measuring the effect this had on the fluorescence.[18]

2.3.1. Interference Lithography of a 3D Photonic Crystal with a Built-In Defect Layer

One of the advantages of interference lithography is that a thick 3D lattice can be fabricated with a single exposure step.[4] However, one issue with this method is that lattices fabricated this way are often brittle and will crack when one tries to transfer this to a different substrate, damaging the optical quality. For this reason, it is preferable to have a way to make stacks of different materials without transferring a photonic crystal film. We accomplish this by making stacking materials, including unexposed SU8 films, into a 'sandwich' structure followed by exposing the sandwich all at once using interference lithography. A schematic of this procedure is shown in **Figure 2.3**.

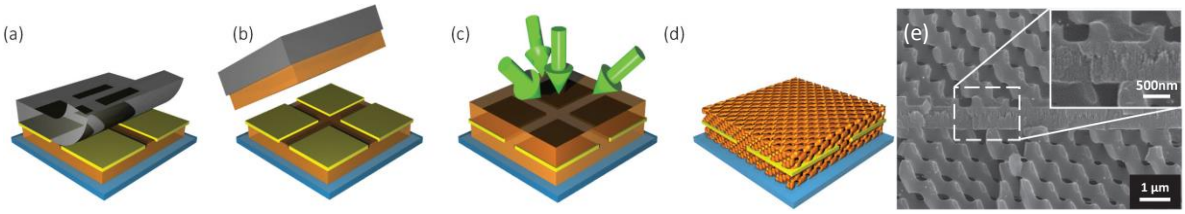

Figure 2.3. Schematic of fabrication of photonic crystal with embedded planar defect. a) The defect layer is placed onto a layer of SU8 using a PDMS transfer technique. b) Another layer is similarly placed on top of the defect layer. c) Conventional interference lithography is performed on the sandwich. d) After development of the SU8, the defect layer is left incorporated into a 3D photonic crystal. e) SEM cross-section of SU8 photonic crystal with embedded defect layer. Images from Runyu Zhang, et al.[17]

This technique has a few convenient symmetries. The top and bottom lattice are ensured to have registration (i.e. be 'lined up') in the x- and y-directions. The registration of the lattices in the z-direction depends upon the optical path length of the layer. For a defect layer that is sufficiently thin or has a refractive index very close to SU8, the top and bottom lattices will keep perfect translation symmetry. This feature is important for examining the optics of different films.

The modes that resonate with the defect layer depend upon both the properties of the defect as well as the properties of the lattice. **Figure 2.4** shows some of the effect of defect thickness, fill fraction of the photonic crystal, and the location of the defect within the unit cell. As mentioned, the defect acts as a cavity that holds an optical standing wave. The primary factor that governs the resonant frequency is the optical path length of the cavity: the longer the path length, the longer the wavelength that can be supported in the cavity. We see this in **Figure 2.4**, where the defect mode position increases monotonically with the defect thickness. For this sample, the left curve indicates the lowest-order mode, and this curve stops only when it reaches the end of the bandgap, after which it can no longer properly be called a defect mode. The defect mode position jumps back down to 1.34 μm because the right curve is a higher order mode that can support another half wavelength, but only for shorter wavelengths. Next, we examine the effect of the fill fraction of the photonic crystal. Here the fill fraction is defined as the fraction of the volume that is filled with SU8. As the fill fraction increases, the center wavelength position of the bandgap increases due to the greater quantity of a higher refractive index material, SU8, decreasing the effective wavelength of the light propagating through the lattice. Similarly, the mode position of the defect also increases due the greater effective index in the regions surrounding the defect, as any standing wave must penetrate partially into the surrounding medium. This effect is much greater for thin defects, like the 100nm mode shown below, where a large part of the mode profile exists in the surrounding medium. Lastly, we look at the effect of the defect position within the photonic crystal, **Figure 2.4c**. The photonic crystal lattice used here is similar to the cubic lattice discussed earlier in the chapter, just stretched in the z-direction. As mentioned the cavity modes depend upon the environment directly outside the lattice – this environment changes locally within the unit cell, with some regions having different shapes and differing amounts of the *local* fill fraction. We see that the defect position wobbles somewhat and repeats itself three times within each cell. We define the vertical lattice periodicity, a, as the distance for which the lattice repeats itself purely in the vertical direction. This lattice has other periodicity vectors with a z-component of a/3. Since the defect exists as a plane perpendicular to z, the modes ignore any of the x and y components of the lattice position. This results in the modes seeing the same environment

three times within a unit cell. If, however, the defect were a point or line defect, you would not see this kind of symmetry.

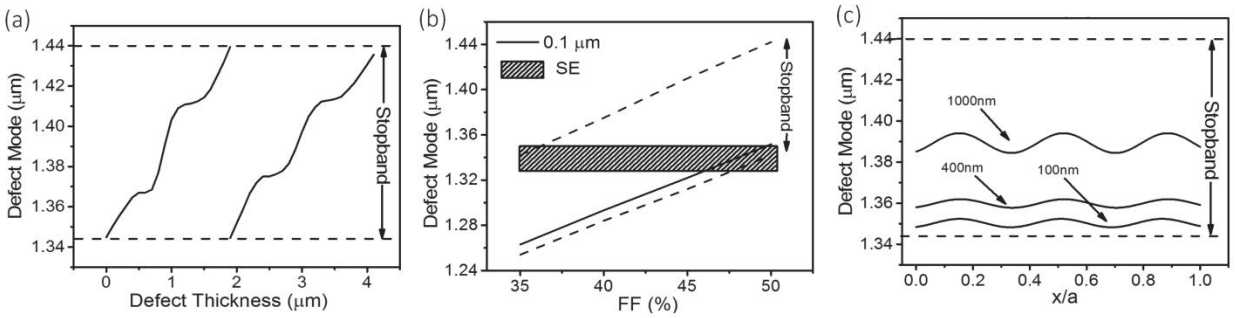

Figure 2.4. Plots of the simulated defect mode position according to variation in several parameters. The dashed lines denote the edge of the bandgap. Plot of the peak wavelength of the defect mode against the a) defect thickness, b) fill fraction (FF), and the position of the defect within the unit cell of the lattice for a few different thicknesses. From Runyu Zhang, et al.[17]

This last bit of variability, the effect of the defect position within a unit cell, does bode poorly for creating repeatable experiments. While the exact thicknesses of each film in the sample can be accurately controlled, the exact position of the photonic crystal structure cannot, due the impossibility of placing samples in the exact same location with an accuracy of below 100nm. However, in practice, the defect mode can be broadband enough that the exact placement of the defect becomes less important, and the desired mode can still be somewhat excited.

We demonstrate control of the defect mode to suppress and enhance emission from emitters held within the defect. **Figure 2.5** shows a photonic crystal with an embedded LaF_3:Nd^{3+} defect layer and the fluorescence spectra of two samples with different fill fractions, 35% and 50%. These different fill fractions have changed the position of the bandgap and of the defect mode. One can use the emission spectra to obtain information about the local optical DoS. These nanocrystals have a strong emission peak near 1.1μm, sufficiently far from the bandgap such that we can assume that there is no difference in the local DoS. We can thus normalize the fluorescence spectra here and then compare the relative intensities in the emission peaks. If we assume that any difference at 1.33μm is due to the optical effects of the defect and optical crystal, we can use the spectra to compare the optical densities of states. We see that there is suppressed emission in the red sample and enhanced emission in the blue

sample, relative the reference sample. This is expected because the emission peak is close to the center of the bandgap, which would reduce the local DoS (or reduce it to zero for an infinite perfect lattice). For the blue sample, the emission peak is close to the blue edge of the bandgap; as shown in **Figure 2.4**, a thin defect layer is expected to have a defect mode close to the blue edge of the bandgap. Thus, we expect overlap of the emission mode with the defect mode, causing an increase in the enhancement of the emission. However, it is clear that the photonic crystal is far from ideal, with fairly low reflectance. Thus, a great deal of broadening and scattering is likely playing a significant role in the optical characteristics of the photonic crystal, making it difficult to definitively establish the mechanism for the enhanced spontaneous emission. Phenomenologically, enhancement due to a defect mode increasing the local DoS is a plausible mechanism regardless.

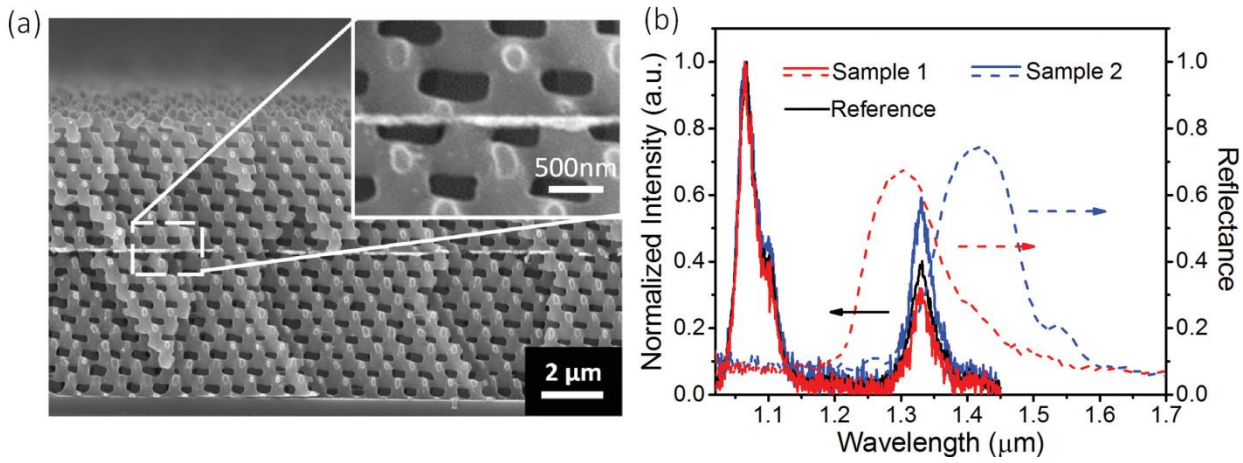

Figure 2.5. a) SEM cross-section of SU8 photonic crystal with $LaF_3:Nd^{3+}$ defect layer. b) Fluorescence spectra of an embedded $LaF_3:Nd^{3+}$ defect layers embedded in a 35% fill fraction(red) and a 50% fill fraction (blue) photonic crystal. The dashed lines show the reflectance spectra of the same photonic crystals. The black reference curve shows the fluorescence spectrum of a non-embedded layer of $LaF_3:Nd^{3+}$ nanocrystals. These curves have been normalized to an emission peak far from the bandgap so that the relative emissions near the bandgap can be compared.

2.4. Anti-Reflection Coatings in Interference Lithography

Backside reflections are common in interference lithography, whether as a problem to be eliminated[27]–[33] or as a useful design parameter.[32], [34], [35] These reflections from the photoresist-substrate interface interfere with the incident light, forming standing wave interference patterns that result in ripple-like features on the sidewalls of features. To reduce

these effects, BARCs are commonly placed between the photoresist and the substrate to minimize the power of the reflected light. The BARCs operate either through Fabry-Perot interference, reducing the power of the reflected mode or by using a material with a high absorption coefficient which absorbs light reflected from of the substrate.[36] Interference lithography has particularly stringent requirements, making these two approaches inadequate. Since the photoresist is exposed via a standing wave interference pattern, the effect of standing waves from reflections is much more significant.[37], [38] While reflections are only a problem in conventional lithography in cases of a very high index contrast, such as between photoresist and silicon, they present a problem in interference lithography between materials with similar refractive indices, such as ordinary borosilicate glass ($n \approx 1.52$) and SU-8 photoresist ($n \approx 1.59$). This refractive index range is a regime that work on anti-reflection coatings commonly ignores.[39] Tunable anti-reflection coatings relying on porous materials can cover this range, but scattering caused by the inhomogeneity of the pores and the photoresist infilling the pores could present problems.[40], [41] An absorbing antireflection coating results in heating issues, since interference lithography generally requires a high fluence and low level of absorption in the resist to provide a nearly uniform level of exposure through the entire depth of the resist).

2.4.1. Requirements of Suitable Antireflection Coating

There are several additional qualities to look for in a BARC for interference lithography. First, the BARC needs to exhibit very low scattering. Since even a small disturbance of the incident plane wave can cause formation of defects, a homogeneous BARC is preferable to a porous BARC.[22] Second, the material needs to be able to be deposited to a precise thickness. Lastly, it is desirable for the BARC to be suitable for a broad of a range of substrates. We identified PS/PVME homopolymer blends as good candidates for a BARC. PS and PVME are one of the few pairs of homopolymers that are completely miscible, ensuring no phase separation, which would lead to significant light scatter, over the full composition range.[42] Films of these blends can be made with precisely controlled compositions and thicknesses by spincoating from a solution of toluene.[43] These polymers also have very different refractive indices, $n \sim 1.47$ for PVME[44] and $n \sim 1.6$ for PS[45], which enables BARCs which provide near zero reflection for SU-

8 on substrates with refractive indices between 1.3 and 1.6, which includes even low refractive index materials such as CaF2 and NaF2, commonly used substrates for UV and IR optics due to their broad transmission range. While gradient index and multilayer antireflection coatings are necessary to provide the best antireflection for broadband and multi-angle illumination, e.g., as required for solar cells, for interference lithography, where low reflectances are required for only a single wavelength and a defined incidence angle, antireflection coatings can consist of a uniform film with the appropriate thickness and refractive index.[39]

2.4.2. PS:PVME Blends

The refractive index of PS/PVME blends can be varied over a broad range with composition. To select the blend composition needed for a particular photoresist, substrate, and wavelength, the relationship between the refractive index and composition of the PS/PVME blend needs to be known at the wavelength of interest. We find that for each blend composition a 3-variable Cauchy model provides a good fit to the ellipsometrically obtained refractive index over the range 450nm to 900nm.[46] **Figure 2.6** shows the wavelength-dependent refractive index of blends at approximately 10% composition intervals. Due to interactions between PS and PVME in blends the variation in refractive index due to composition cannot be modeled using methods that treat the components as distinct phases.[43] To enable selection of the appropriate blend for a given interference experiment, we fit the refractive index and composition through a linear interpolation of refractive index of the pure components and a 2nd order Redlich-Kister deviation,[47], [48] which can be written as:

$$n(f,\lambda_0) = n_{PS}(\lambda_0)\ f + n_{PVME}(\lambda_0)\ (1-f) + f(1-f)[a\,f^2 + b\,f + c]) \qquad (2.11)$$

where f is the fraction of the PS component, λ_0 is the vacuum wavelength, n_{PS} and n_{PVME} are the respective refractive indices of PS and PVME, $n(f, \lambda_0)$ is the refractive index of the blend, and a, b, c are fitting variables. We find optimum fitting with parameters: a =-0.0927, b = 0.264, and c = -0.188. We plot in **Figure 2.6b** the measured and modeled refractive index against composition at a series of wavelengths. The greatest deviation occurs at low concentrations of PVME and shorter wavelengths, with a maximum difference of 0.0056. This deviation is sufficiently small that equation 2.5.1 can be used to select a BARC composition for all of our interference experiments.

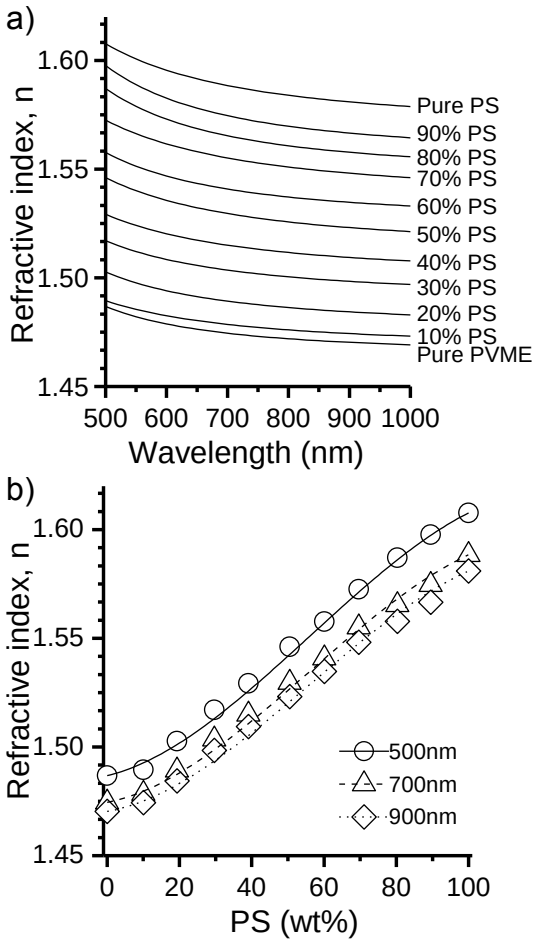

Figure 2.6. a) Refractive index vs. wavelength for a series of PS/PVME blends with varying compositions. b) Measured (circles) and fit (lines) refractive indices of the blends vs composition. The fit uses linear interpolation of refractive index with a 2nd-order Redlich-Kister deviation.

The ideal refractive index for the BARC, n2, assuming s-polarized light, for a given angle of incidence, photoresist refractive index n1, substrate n3, and propagation angles in photoresist, θ1, and substrate, θ3 can be calculated as:

$$n_2 = \sqrt{n_1 n_3 \cos(\theta_1)\cos(\theta_3) + {n_1}^2 \sin^2(\theta_1)} \quad (2.12)$$

The thickness of the BARC, d, is then calculated by:

$$d = \frac{\lambda_0}{4\, n_2 \cos(\theta_2)} \quad (2.13)$$

2.4.3. Demonstration of Backside Anti-reflection Coating

To demonstrate the effectiveness of this BARC for interference lithography, we fabricate periodic structures with three different geometries: hexagonal, face-centered cubic, and simple cubic. We use three-beam interference lithography to make a 2D hexagonal hole array pattern and four beams in the oft-used umbrella configuration to make the cubic structures (see **Figure 2.7**).[11], [13], [15], [16], [37], [49], [50] In the 3-beam system, a glass prism is placed on top of the substrate to outcouple light out of the substrate. Since the beam angles needed to form cubic structures are above the critical angle for SU-8 air interfaces, we use prism couplers above and below the photoresist. The front prism is n-BK7 glass or ITO-coated glass and the back prism is PDMS (n~1.41). The fact that the BARC works even with this low refractive index outcoupler demonstrates its utility.

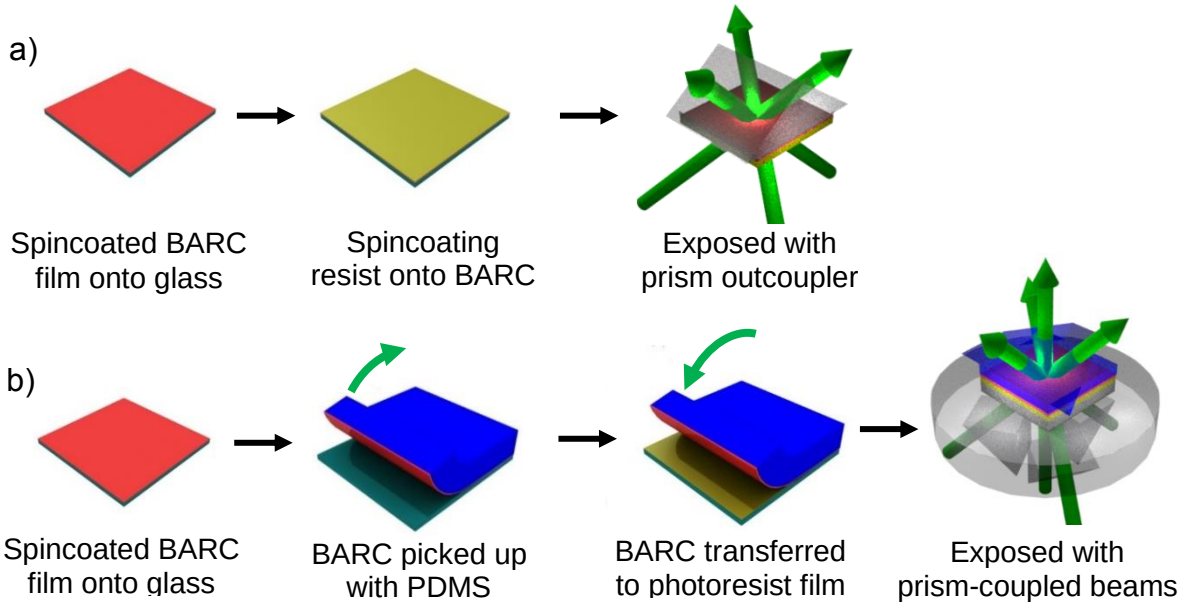

Figure 2.7. Diagrams of procedure for hexagonal (a) and cubic (b) patterns. a) Spincoating the PS/PVME BARC onto borosilicate glass, then spincoating SU-8, then exposing to 3beam interference pattern. b) Spincoating PS/PVME BARC onto glass, peeling PS/PVME BARC coating from substrate with PDMS stamp, rolling PDMS and film on top of SU-8, then placing into BK7-glass prism assembly for exposure.

PDMS is also used to apply the BARC to the substrate via a transfer printing process, enabled by PDMS's dynamic surface energy characteristics.[17], [32] Here we perform transfer printing of the BARC by using oxygen plasma to render the PDMS surface hydrophilic, allowing it to pick up the BARC from a glass slide and transfer it to the SU-8 photoresist. The elasticity and gas permeability of PDMS makes it easy to achieve bubble and defect-free conformal contact with SU-8. This technique avoids exposure of the photoresist to solvents and/or UV light as might be present if spincoating or vacuum deposition methods were used to place the BARC onto the photoresist. From our experience, spincoating or vacuum deposition of materials on sensitized SU-8 is problematic for these reasons. In this configuration light comes first through the substrate and then enters the SU-8, thus an antireflection coating is only required at the PDMS-SU-8 interface (light reflected at the substrate-photoresist interface is outcoupled through the same prism it entered, so the refractive index of the substrate is irrelevant so long as it is transparent). Thus a wide range of substrates can be used for a given BARC, provided the substrate is transparent and does not distort the laser wavefront.

Three different geometries, 2D hexagonal, FCC, and SC, were fabricated with and without a BARC. The conventional 'umbrella geometry' was used with azimuthal angles of the side beams set to 29°, 38°, and 52° in SU-8 respectively.[11], [17], [51] The 2D hexagonal and SC lattices were fabricated on a borosilicate glass substrate, whereas the FCC lattice is fabricated on an ITO substrate to demonstrate the use of this technique with a high-index substrate. Scanning electron microscopy (SEM) images of cross-sections were taken for each geometry and were compared to simulations of the cross-section profiles (see **Figure 2.8**). As expected, the cross-sections exhibit fringes normal to the substrate when a BARC is not used. These fringes disappear with the addition of the BARC, indicating that the polymer blend-based BARC is effective at reducing interference caused by undesirable reflections.

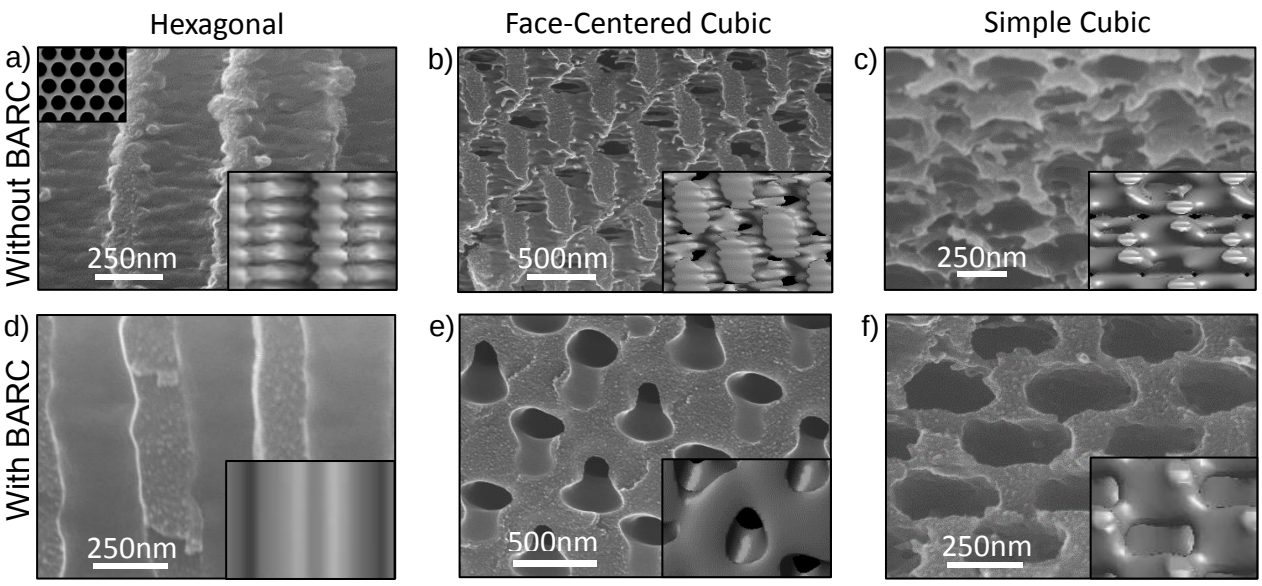

Figure 2.8. SEM cross-sections of hexagonal, FCC, and SC structures. a), b), and c) were fabricated without BARCs and d), e), and f) were fabricated with BARCs. Lower right insets are simulated cross-sections of the same plane. The hexagonal and SC structures were prepared on borosilicate glass, whereas the FCC lattice was prepared on ITO-coated glass. The upper left inset in a) is a top-view diagram of the honey-comb pattern of the hexagonal lattice.

We investigate the optical response of the FCC and SC 3D lattices formed through reflectance and transmission spectroscopy. In the beam configuration used, the lattices are oriented with each cubic unit cell standing on its corner, so that the Γ-R line corresponds to normal incidence. In this direction, there is not a bandgap due to the relatively low refractive index of SU-8, though reflection peaks and strong diffraction peaks are expected. We collect reflection and transmission spectra in the visible and near-IR, and compare it to finite-difference time-domain simulations (see **Figure 2.9**). Only the power of the 0,0-order transmitted and reflected modes are measured or calculated, leading to the reflectance and transmittance spectra not adding to unity. This can be seen at around 400nm and 600nm for the SC lattice and from 400nm to 700nm for the FCC lattice. The shrinkage of the FCC lattice led to blueshifting of the reflection peak so that it partially overlaps these regions of diffraction. The simulated transmission of the simple cubic has a drop-in transmission at 600nm due to strong diffraction at that wavelength, whereas the FCC lattice has broadband diffraction. Positions and heights of the main peaks in the fabricated samples closely match that of the

simulated spectra. Peak broadening in both reflection and transmission, particularly in regions of strong diffraction, is not unusual for interference lithography.[37,40]

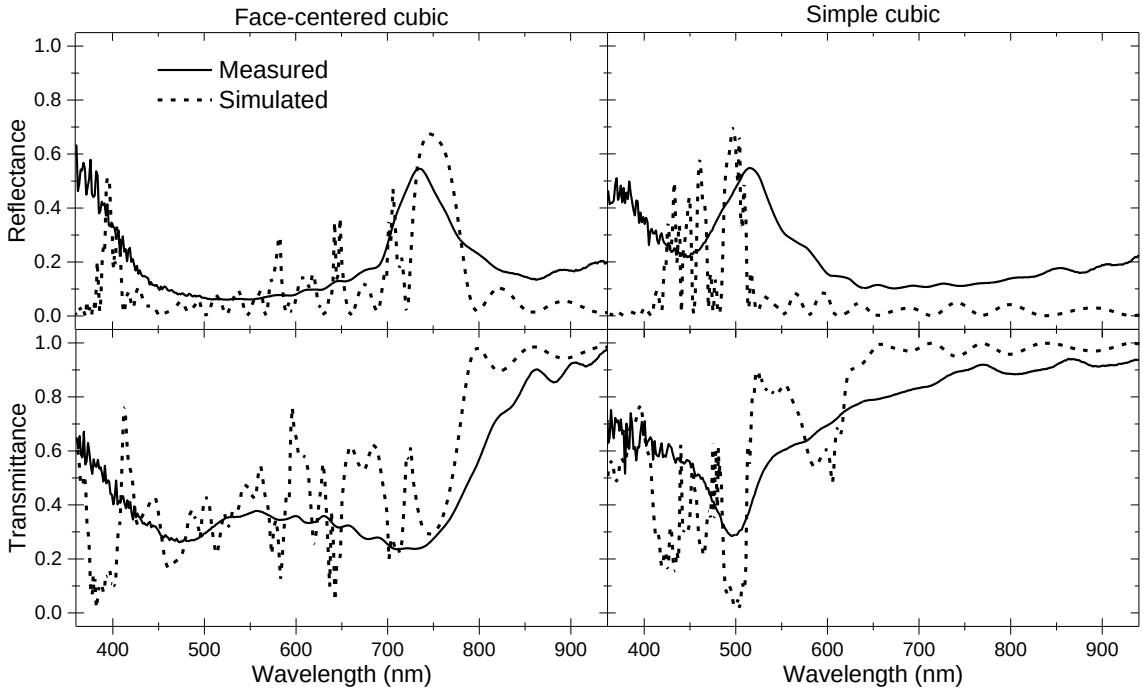

Figure 2.9. Measured (solid) and simulated (dashed) spectra of zero-order reflection (top) and transmission (bottom) spectra of the FCC lattice (left) and SC lattice (right) fabricated using BARCs.

The interference of reflected beams also introduces a quasiperiodicity to the lattice, due to mismatching z-components of the wavevectors. The periodicity of the lattice produced by interference lithography is determined by the wave-vector differences, according to $(\overrightarrow{k_i} - \overrightarrow{k_j}) \times \Delta\vec{R} = 2\pi m$, where $\overrightarrow{k_j}$ and $\overrightarrow{k_j}$ are the wave-vectors of each beam, $\vec{R}$ is the (infinite) set of lattice periodicity vectors, and m is an integer. In our four-beam when reflections are ignored, the side beams have the same azimuthal angle of incidence, so wave-vector component in the z-direction are the same, leading to a single value of Δk_z for all the beams, giving a single value for R_z (see **Table 2.1**).

Table 2.1. Wave-vector parameters for simple cubic configuration

Incident		Reflected		Δk_z for incident beams (μm^{-1})	Δk_z for incident + reflected beams (μm^{-1})
$\vec{k}$ [x,y,z] (μm^{-1})	$\vec{E}$ [s,p]	$\vec{k}$ [x,y,z] (μm^{-1})	$\vec{E}$ [s,p]		
[0, 0, -19.0]	[1, 1i]	[0, 0, 19.0]	[0.063, -0.063i]	7.2	7.2
[0, -14.9, -11.8]	[1, 0]	[0, -14.9, 11.8]	[0.21, 0]		23.6
[12.9, 7.4, -11.8]	[1,0]	[12.9, 7.4, 11.8]	[0.21, 0]		30.7
[-12.9, 7.4, -11.8]	[1,0]	[-12.9, 7.4, 11.8]	[0.21, 0]		38.0

The reflected beams have the same wave-vectors as the incident beams but reversed k_z. This leads to there being multiple distinct Δk_z, making the structure no longer periodic according to R_z. Instead, the lattice becomes quasi-periodic, forming a structure with roughly simple cubic periodicity, but with alternating layers of structure quality, depending on the phase difference between the incident and reflected beams. In **Figure 2.10a**, high fringe-effect layers, or regions where this phase difference leads to large defects in the fabricated structure, can be seen to alternate with low fringe-effect layers, where the phase difference leads to smaller deviations from the ideal structure. These bands occur with a repeating spacing of 1.5μm, as expected from simulations.

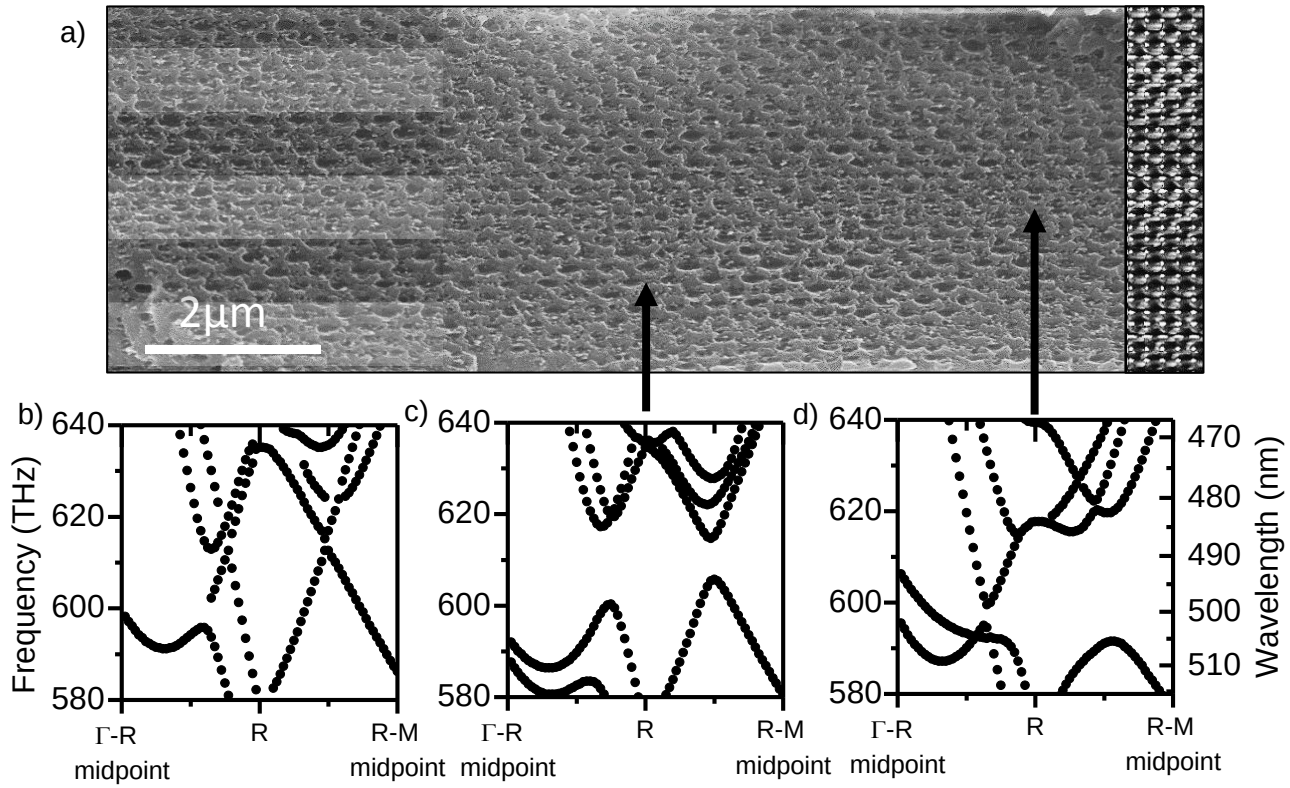

Figure 2.10. a) SEM cross-section of SC lattice fabricated without BARC and simulated cross-section (inset) showing quasiperiodic lattice with alternating layers of strong and weak reflection fringes. Highlighting of strong (emphasized by lightened area) and weak (emphasized by darkened area) reflection fringes on the left is a guide to the eye. Bandstructures near the R-point for b) ideal SC lattice, c) SC lattice with low fringe-effect, and d) SC lattice with high fringe-effect.

The fringes from reflected beams also change the optical bandstructure of the lattice. As seen, the presence of fringes result in a quasiperiodic lattice oscillating between layers of high fringe effect and low fringe effect. To better understand what effect this has on the overall optical properties, we calculate bandstructures for low, high, and no fringe effect, taking a simple cubic unit cell from the centers of the high fringe effect and low fringe effect layers. Full bandstructures are shown in **Figure 2.11**. At low frequencies, where the wavelength is much larger than the size of the fringes, there is little difference in the bandstructures, but as the frequency increases beyond about 500THz (600nm) there starts to be considerable divergence. Bandstructures near the R-point (corresponding to waves propagating normal to the substrate) and around 600THz (the peak reflectance for normal incidence) are shown in **Figure 2.10b-d**. In the no-reflection case, a band-crossing with linear dispersion can be seen at 610THz that is not present in either of the other bandstructure plots. Care must be taken when

interpreting the bandstructure results for the fringe-effect cases since the continually changing lattice violates the necessary assumption of infinite periodicity for bandstructure calculations. Nevertheless, this demonstrates that the presence of reflection fringes can lead to major alterations in the optical characteristics of photonic crystals.

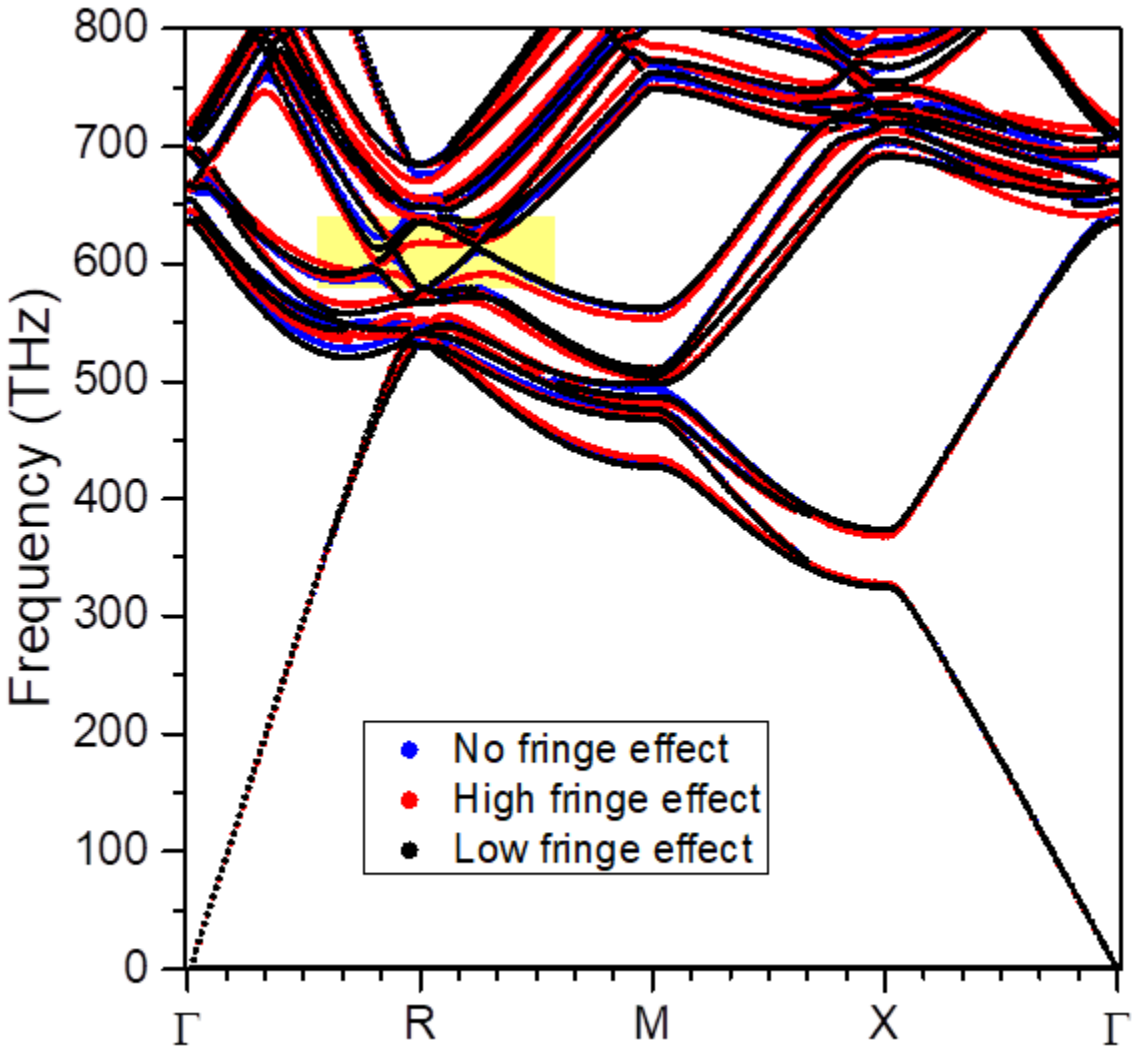

Figure 2.11. Bandstructure calculations of the ideal SC lattice (black), the low fringe effect SC lattice (blue), and high fringe effect lattice (red). The highlighted region shows the area that is plotted in Figure 5b-d.

2.5. Conclusion

This chapter has focused on interference lithography for the fabrication of photonic crystals. The underlying principles were discussed and a procedure for identifying the beam geometries needed for a particular lattice were discussed. Some of my recent work on extending the capabilities of the interference lithography were gone into in detail. The geometry of defects and photonic crystals control the properties of the defect mode formed and this was used to suppress and enhance spontaneous emission from fluorescent nanocrystals within the defect. The reflections from the interface between the photoresist and the substrate at steep incidence angles can introduce unwanted fringes in the structure of photonic crystals, even for substrates with a refractive index very close to that of the substrate. We developed a novel tunable-refractive index antireflection coating that eliminates these defects. These advancements increase the versatility of interference lithography, but the biggest challenges remain. 3D interference lithography still has difficulty in producing very high optical quality structures. Photonic crystals made using this technique still typically have reflectance peaks much lower than what is expected from simulation. In order for 3D interference lithography to become a viable mainstream technique, higher quality optics need to be demonstrated.

2.6. References

[1] D. A. Bacon-Brown and P. V. Braun, "Tunable Antireflection Coating to Remove Index-Matching Requirement for Interference Lithography," *Adv. Opt. Mater.*, p. 1701049, Feb. 2018.
[2] R. Kumar, "Diffraction Lloyd mirror interferometer," *J. Opt.*, vol. 39, no. 2, pp. 90–101, Jun. 2010.
[3] M. C. Marconi and P. W. Wachulak, "Extreme ultraviolet lithography with table top lasers," *Prog. Quantum Electron.*, vol. 34, no. 4, pp. 173–190, Jul. 2010.
[4] C. Lu and R. H. Lipson, "Interference lithography: a powerful tool for fabricating periodic structures," *Laser Photonics Rev.*, vol. 4, no. 4, pp. 568–580, May 2009.
[5] L. Z. Cai, X. L. Yang, and Y. R. Wang, "All fourteen Bravais lattices can be formed by interference of four noncoplanar beams," *Opt. Lett.*, vol. 27, no. 11, pp. 900–902, 2002.
[6] V. Ramanan, E. Nelson, A. Brzezinski, P. V. Braun, and P. Wiltzius, "Three dimensional silicon-air photonic crystals with controlled defects using interference lithography," *Appl. Phys. Lett.*, vol. 92, no. 17, p. 173304, 2008.

[7] J.-M. Park, K. S. Nalwa, W. Leung, K. Constant, S. Chaudhary, and K.-M. Ho, “Fabrication of metallic nanowires and nanoribbons using laser interference lithography and shadow lithography,” *Nanotechnology*, vol. 21, no. 21, p. 215301, May 2010.
[8] P. Spinelli, M. A. Verschuuren, and A. Polman, “Broadband omnidirectional antireflection coating based on subwavelength surface Mie resonators,” *Nat. Commun.*, vol. 3, no. 1, Jan. 2012.
[9] J. W. Rinne and P. Wiltzius, “Design of holographic structures using genetic algorithms,” *Opt. Express*, vol. 14, no. 21, pp. 9909–9916, 2006.
[10] J. W. Rinne, S. Gupta, and P. Wiltzius, “Inverse design for phase mask lithography,” *Opt. Express*, vol. 16, no. 2, pp. 663–670, 2008.
[11] Y. C. Chen, J. B. Geddes, J. T. Lee, P. V. Braun, and P. Wiltzius, “Holographically fabricated photonic crystals with large reflectance,” *Appl. Phys. Lett.*, vol. 91, no. 24, p. 241103, Dec. 2007.
[12] I. Divliansky, T. S. Mayer, K. S. Holliday, and V. H. Crespi, “Fabrication of three-dimensional polymer photonic crystal structures using single diffraction element interference lithography,” *Appl. Phys. Lett.*, vol. 82, no. 11, p. 1667, 2003.
[13] M. Miyake, Y.-C. Chen, P. V. Braun, and P. Wiltzius, “Fabrication of Three-Dimensional Photonic Crystals Using Multibeam Interference Lithography and Electrodeposition,” *Adv. Mater.*, vol. 21, no. 29, pp. 3012–3015, Aug. 2009.
[14] J. H. Moon, J. Ford, and S. Yang, “Fabricating three-dimensional polymeric photonic structures by multi-beam interference lithography,” *Polym. Adv. Technol.*, vol. 17, no. 2, pp. 83–93, Feb. 2006.
[15] O. Toader, T. Y. M. Chan, and S. John, “Diamond photonic band gap synthesis by umbrella holographic lithography,” *Appl. Phys. Lett.*, vol. 89, no. 10, p. 101117, 2006.
[16] X. Zhu, Y. Xu, and S. Yang, “Distortion of 3D SU8 photonic structures fabricated by four-beam holographic lithography withumbrella configuration,” *Opt. Express*, vol. 15, no. 25, pp. 16546–16560, 2007.
[17] R. Zhang, H. Ning, N. A. Krueger, D. Bacon-Brown, and P. V. Braun, “3D Holographic Photonic Crystals Containing Embedded Functional Features,” *Adv. Opt. Mater.*, vol. 4, no. 10, pp. 1533–1540, Oct. 2016.
[18] H. Ning, A. Mihi, J. B. Geddes, M. Miyake, and P. V. Braun, “Radiative Lifetime Modification of LaF_3 :Nd Nanoparticles Embedded in 3D Silicon Photonic Crystals,” *Adv. Mater.*, vol. 24, no. 23, pp. OP153–OP158, Jun. 2012.
[19] S.-G. Park, M. Miyake, S.-M. Yang, and P. V. Braun, “Cu2O Inverse Woodpile Photonic Crystals by Prism Holographic Lithography and Electrodeposition,” *Adv. Mater.*, vol. 23, no. 24, pp. 2749–2752, Jun. 2011.
[20] E. C. Nelson *et al.*, “Epitaxial growth of three-dimensionally architectured optoelectronic devices,” *Nat. Mater.*, vol. 10, no. 9, pp. 676–681, Jul. 2011.
[21] H. Ning *et al.*, “Holographic patterning of high-performance on-chip 3D lithium-ion microbatteries,” *Proc. Natl. Acad. Sci.*, vol. 112, no. 21, pp. 6573–6578, May 2015.
[22] J. Lutkenhaus, D. Lowell, D. George, H. Zhang, and Y. Lin, “Holographic Fabrication of Designed Functional Defect Lines in Photonic Crystal Lattice Using a Spatial Light Modulator,” *Micromachines*, vol. 7, no. 4, p. 59, Apr. 2016.

[23] S. Noda, M. Fujita, and T. Asano, “Spontaneous-emission control by photonic crystals and nanocavities,” *Nat. Photonics*, vol. 1, no. 8, pp. 449–458, Aug. 2007.
[24] J. D. Joannopoulos, S. G. Johnson, J. N. Winn, and R. D. Meade, “Photonic Crystals: Molding the Flow of Light.” Princeton University Press, 13-Nov-2007.
[25] A. Brzezinski, J.-T. Lee, J. D. Slinker, G. G. Malliaras, P. V. Braun, and P. Wiltzius, “Enhanced emission from fcc fluorescent photonic crystals,” *Phys. Rev. B*, vol. 77, no. 23, Jun. 2008.
[26] H. Ning *et al.*, “Transfer-Printing of Tunable Porous Silicon Microcavities with Embedded Emitters,” *ACS Photonics*, vol. 1, no. 11, pp. 1144–1150, Nov. 2014.
[27] T. A. Savas, “Large-area achromatic interferometric lithography for 100 nm period gratings and grids,” *J. Vac. Sci. Technol. B Microelectron. Nanometer Struct.*, vol. 14, no. 6, p. 4167, Nov. 1996.
[28] Y.-C. Lin, V. Marriott, K. Orvek, and G. Fuller, “Some aspects of anti-reflective coating for optical lithography,” in *1984 Microlithography Conferences*, 1984, pp. 30–37.
[29] N. J. Shirtcliffe *et al.*, “The use of high aspect ratio photoresist (SU-8) for super-hydrophobic pattern prototyping,” *J. Micromechanics Microengineering*, vol. 14, no. 10, pp. 1384–1389, Oct. 2004.
[30] S. S. Sethi, R. G. Distasio, D. H. Ziger, J. E. Lamb III, and T. D. Flaim, “Use of antireflective coatings in deep-UV lithography,” in *Optical/Laser Microlithography IV*, 1991, pp. 30–40.
[31] S. Jeon *et al.*, “Molded transparent photopolymers and phase shift optics for fabricating three dimensional nanostructures,” *Opt. Express*, vol. 15, no. 10, pp. 6358–6366, 2007.
[32] I. Wathuthanthri, Y. Liu, K. Du, W. Xu, and C.-H. Choi, “Simple Holographic Patterning for High-Aspect-Ratio Three-Dimensional Nanostructures with Large Coverage Area,” *Adv. Funct. Mater.*, vol. 23, no. 5, pp. 608–618, Feb. 2013.
[33] K. Du, Y. Liu, I. Wathuthanthri, and C.-H. Choi, “Dual applications of free-standing holographic nanopatterns for lift-off and stencil lithography,” *J. Vac. Sci. Technol. B Nanotechnol. Microelectron. Mater. Process. Meas. Phenom.*, vol. 30, no. 6, p. 06FF04, Nov. 2012.
[34] T. Y. Jeon, S.-G. Park, D.-H. Kim, and S.-H. Kim, “Standing-Wave-Assisted Creation of Nanopillar Arrays with Vertically Integrated Nanogaps for SERS-Active Substrates,” *Adv. Funct. Mater.*, vol. 25, no. 29, pp. 4681–4688, Aug. 2015.
[35] T. Y. Jeon, J. H. Kim, S.-G. Park, J.-D. Kwon, D.-H. Kim, and S.-H. Kim, “Stacked-Disk Nanotower Arrays for Use as Omniphobic Surface-Enhanced Raman Scattering Substrates,” *Adv. Opt. Mater.*, vol. 4, no. 11, pp. 1893–1900, Nov. 2016.
[36] E. K. Pavelchek *et al.*, “Highly absorbing ARC for DUV lithography,” in *SPIE’s 1996 International Symposium on Microlithography*, 1996, pp. 692–699.
[37] S. Lowrey and R. Blaikie, “Solid immersion optical lithography: index matching and resonant reflectors for large exposure field, high-aspect ratio imaging in the ultrahigh-numerical aperture regime,” *J. MicroNanolithography MEMS MOEMS*, vol. 14, no. 4, pp. 043510–043510, 2015.
[38] Y.-J. Hung, S.-L. Lee, Y.-T. Pan, B. J. Thibeault, and L. A. Coldren, “Holographic realization of hexagonal two dimensional photonic crystal structures with elliptical geometry,” *J. Vac. Sci. Technol. B Nanotechnol. Microelectron. Mater. Process. Meas. Phenom.*, vol. 28, no. 5, pp. 1030–1038, Sep. 2010.

[39] H. K. Raut, V. A. Ganesh, A. S. Nair, and S. Ramakrishna, “Anti-reflective coatings: A critical, in-depth review,” *Energy Environ. Sci.*, vol. 4, no. 10, p. 3779, 2011.
[40] M. B. de La Mora *et al.*, “Anomalous patterned scattering spectra of one-dimensional porous silicon photonic crystals,” *Opt. Express*, vol. 18, no. 22, pp. 22808–22816, 2010.
[41] P. Ferrand and R. Romestain, “Optical losses in porous silicon waveguides in the near-infrared: Effects of scattering,” *Appl. Phys. Lett.*, vol. 77, no. 22, pp. 3535–3537, 2000.
[42] E. Jabbari and N. A. Peppas, “Use of ATR-FTIR to study interdiffusion in polystyrene and poly (vinyl methyl ether),” *Macromolecules*, vol. 26, pp. 2175–2175, 1993.
[43] C. Lei, G. Li, Q. Yang, D. Chen, and S. Jiang, “Effect of shear flow on the phase-separation behavior in a blend of polystyrene and polyvinyl methyl ether,” *J. Polym. Sci. Part B Polym. Phys.*, vol. 41, no. 7, pp. 661–669, 2003.
[44] I. G. Voigt-Martin, K.-H. Leister, R. Rosenau, and R. Koningsveld, “Kinetics of phase separation in polymer blends for deep quenches,” *J. Polym. Sci. Part B Polym. Phys.*, vol. 24, no. 4, pp. 723–751, 1986.
[45] N. Sultanova, S. Kasarova, and I. Nikolov, “Dispersion Properties of Optical Polymers,” *Acta Phys. Pol.-Ser. Gen. Phys.*, vol. 116, no. 4, p. 585, 2009.
[46] M. Born and E. Wolf, *Principles of Optics*, 7th ed. Cambridge University Press, 1999.
[47] O. Redlich and A. T. Kister, “Algebraic representation of thermodynamic properties and the classification of solutions,” *Ind. Eng. Chem.*, vol. 40, no. 2, pp. 345–348, 1948.
[48] M. I. Aralaguppi, C. V. Jadar, and T. M. Aminabhavi, “Density, Viscosity, Refractive Index, and Speed of Sound in Binary Mixtures of 2-Chloroethanol with Methyl Acetate, Ethyl Acetate, *n* -Propyl Acetate, and *n* -Butyl Acetate,” *J. Chem. Eng. Data*, vol. 44, no. 3, pp. 441–445, May 1999.
[49] Y. V. Miklyaev *et al.*, “Three-dimensional face-centered-cubic photonic crystal templates by laser holography: fabrication, optical characterization, and band-structure calculations,” *Appl. Phys. Lett.*, vol. 82, no. 8, p. 1284, 2003.
[50] D. C. Meisel *et al.*, “Shrinkage Precompensation of Holographic Three-Dimensional Photonic-Crystal Templates,” *Adv. Mater.*, vol. 18, no. 22, pp. 2964–2968, Nov. 2006.
[51] M. J. Escuti and G. P. Crawford, “Holographic photonic crystals,” *Opt. Eng.*, vol. 43, no. 9, pp. 1973–1987, 2004.

CHAPTER 3

MULTILEVEL PHASE MASKS FOR PROXIMITY-FIELD NANOPATTERNING

Chapter 2 discussed the principles of conventional multibeam interference lithography and is recommended reading for those who are not familiar with the basics of interference lithography. This chapter will focus on a different variation of interference lithography called proximity-field nanopatterning.

3.1. Introduction to Proximity-Field Nanopatterning

Proximity-field nanopatterning (PnP) is a variation of interference lithography developed in a collaboration between the Paul Braun and John Rogers research groups. This method is different from more conventional techniques because the interfering laser is created not by the use of beamsplitters at a large distance, but the use of diffraction in close proximity to the surface. PnP is performed by exposing a diffractive optical element (DOE) in proximity with a photoresist film to collimated, coherent light.[1] The DOE diffracts the incident light beam into several coherent, propagating beams. The 3D interference pattern created by the superposition of these beams is recorded in the photoresist. The nanostructured photoresist can be used as a template for the deposition other materials with desired optical properties.[2] In this way, a complex periodic 3D structure can be fabricated on a large scale with a single exposure step. A schematic of this method is shown below in **Figure 3.1**.

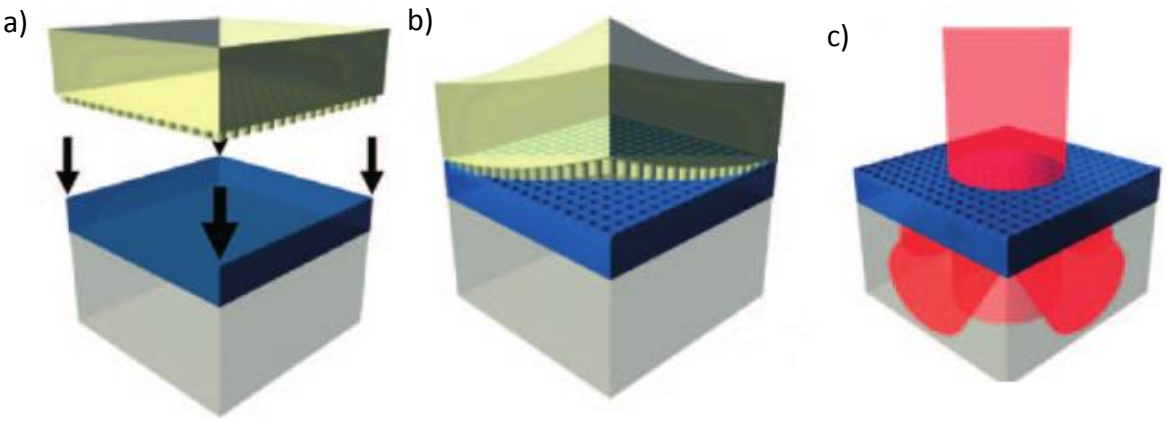

Figure 3.1. Schematic of proximity-field nanopatterning (PnP) process. a) A polydimethylsiloxane (PDMS) nanoimprint mask is fabricated with a diffractive relief pattern and pressed into a temporarily softened photoresist film. b) Once the film has hardened, the PDMS mask is peeled off, leaving the inverse relief pattern. c) An incident laser beam is diffracted into multiple interfering beams that create a 3D interference pattern that is recorded by the photoresist. Figure create by Matt George.[3]

There are some major advantages of PnP over more conventional interference lithography techniques. One important advantage is the control over the phase of the interfering beams. Multibeam interference lithography is generally limited to 4 or fewer beams since the dimensionality of the structure is one fewer than the number of non-coplanar beams.[4] With 4 beams creating a 3D structure any phase shift of a beam leads to a translation of the structure in space. If 5 non-coplanar beams are used, then a phase shift of one beam changes the geometry of the fabricated structure. Since the relative phase of each beam in a multibeam setup depends on the path length difference on the scale of hundreds of nanometers, control over this is practically impossible in an experimental setting. Some tricks can be played to avoid this, such as careful selection of polarizations to take advantage of the fact that orthogonally polarized beams will not interfere, but this limits the overall design space.[5] In proximity field nanopatterning, however, the beams are 'phase locked' meaning that the relative phase is set by the DOE, enabling the use of more than 4 diffracted orders without the risk of phase offsets distorting the structure.

An additional advantage lies in the fact that the constraints on temporal coherence are greatly reduce. Multi-beam interference lithography requires the total path length difference between the interfering beams is less than the coherence length of the incident laser, limiting

this process to laser sources with relatively long coherence lengths (a meter or more is typical). For PnP, coherence lengths on the order of tens of microns can be used. Since this is the approximate maximum phase difference one would typically see. This opens up the possibility of using pulsed lasers to enable non-linear affects, such as two-photon absorption. In two-photon absorption, the probability of photo-initiation of a molecule of the photo-resist is proportional to the square of the local light intensity, rather than directly proportional to the intensity. This enables much higher contrasts, relieving some design constraints and resulting in more mechanically stable photoresist templates.

A few challenges exist in the development of PnP for widespread use. One of these is that, as yet, a relatively low diversity of periodic structures has been demonstrated. Fabricated structures include woodpiles,[6] “interdigitated cylindrical structures”,[1] “stacks of sealed nanochannels”,[1] and penrose quasicrystals,[7] though demonstrations of PnP are overall dominated by DOE’s composed of a square array of cylindrical posts, because they are easy to fabricate in large areas. These demonstrations all use a binary phase shift DOE that necessarily limits the structures that can be fabricated. To develop a method with a broader design space, we developed multilevel phase masks that give greater control over the power and polarization of the diffracted orders.

3.2. Geometry of proximity-field nanopatterning

In chapter 2, the mathematics of multibeam interference lithography are described in detail. Here, that discussion is extended to the geometry of PnP. From the perspective of interference lithography as the addition multiple plane waves, PnP is identical to multibeam interference lithography, but there are important considerations with respect to the generation of these plane waves through the use of DOE.

The use of a diffractive optical element adds limitations to the k-vectors of the light. All beams must be generated by the DOE, instead of defined arbitrarily through the use of mirrors, prisms, or other optics. This means that the k-vectors of the interfering beams must have a

consistent set of difference vectors; the components of the propagation vectors parallel to the substrate, k_x and k_y, must be related to that of the propagation vector of central beam by:

$$k_{x,i} = k_{x,0} + m_{i,1}G_{x,1} + m_{i,2}G_{x,2} \tag{3.1}$$

$$k_{y,i} = k_{y,0} + m_{i,1}G_{y,1} + m_{i,2}G_{y,2} \tag{3.2}$$

where $G_{x,1}$ and $G_{x,2}$ are the x-components of each of the reciprocal grating vectors and $m_{i,1}$ and $m_{i,2}$ are the orders of diffraction for each beam. Not only must every beam be a diffracted mode, but every diffracted mode must be included in the calculation. This reduces some of the possibilities for designs. For example, if we tried to replicate the typical 4-beam umbrella geometry, we would run into an issue, namely that the three side beams in this geometry have orders of:

$$\begin{gathered}\left[k_{xy}\sin(\varphi), 0, k_z\cos(\varphi)\right], \\ \left[k_{xy}\sin(\varphi)\cos(120°), k_{xy}\sin(\varphi)\cos(120°), k_z\cos(\varphi)\right], \\ \left[k_{xy}\sin(\varphi)\cos(-120°), k_{xy}\sin(\varphi)\cos(-120°), k_z\cos(\varphi)\right]\end{gathered} \tag{3.3}$$

However, by symmetry, these modes must also be possible:

$$\begin{gathered}\left[-k_{xy}\sin(\varphi), 0, k_z\cos(\varphi)\right], \\ \left[-k_{xy}\sin(\varphi)\cos(120°), -k_{xy}\sin(\varphi)\cos(120°), k_z\cos(\varphi)\right], \\ \left[-k_{xy}\sin(\varphi)\cos(-120°), -k_{xy}\sin(\varphi)\cos(-120°), k_z\cos(\varphi)\right]\end{gathered} \tag{3.4}$$

These 3 additional modes will change the 4-beam geometry the rhombohedral to a 7-beam hexagonal planar lattice. It is theoretically possible to design a DOE such that these modes have zero diffractive power, enabling a lattice that would be equivalent to the 4-beam geometry, but this requires breaking some symmetries that are very difficult to strongly break using conventional DOE's. These symmetries will be discussed in detail later in the chapter. An additional, related constraint is that due to the symmetry between the x-,y- components of the k-vectors and the fact that the k-vector differences determine the periodicity of the lattice, is that the DOE and the lattice must have the same periodicity in the x-y plane. This can be intuited if one considers that there is nothing to break the x-y translation symmetry of the DOE; even an angular incident beam would not break this symmetry, as a plane wave has translation symmetry everywhere if one applies the proper phase-shift.

However, there are also ways that using a DOE can increase the capability of designing a lattice. Before, a 7-beam planar hexagonal lattice was mentioned. This structure would be nigh impossible to fabricate using a conventional multibeam setup, due to the need to precisely control the relative phases. A DOE will 'phase lock' the beams, making the relative phase precisely controlled by the optics of the DOE. With the 3-additional beams, there are additional parameters that can be adjusted to control the fabricated geometry, including the amplitude, polarization and phase, given 9 additional degrees of freedom in optic design. Later in the chapter, the use of this 7-beam setup for a helical pore design will be discusses.

3.3. Measurement of the design space of PnP

To examine the design space of PnP, we provide an analysis of the relationship between the grating geometry and the characteristics of the resulting structure. The intensity distribution generated during a PnP exposure is determined purely by the characteristics of the transmitted beams, namely the wave vectors, magnitude, relative phase, and polarization, according to equation 1.[8]

$$I(\boldsymbol{r}) = \sum_{i=1}^{N} \sum_{j=1}^{N} \widetilde{\boldsymbol{E}}_i^* \cdot \widetilde{\boldsymbol{E}}_j \exp i[(\boldsymbol{k}_i - \boldsymbol{k}_j) \cdot \boldsymbol{r} + (\delta_i - \delta_j)], \tag{3.5}$$

These variables are determined by the grating periodicity, the repeating grating motif, and by the incident polarization. The x-y periodicity of the interference pattern matches the x-y periodicity of the DOE; for periodicity in the z-direction, the z-component differences of the wave vectors must be integer multiples of one another. In this paper we will discuss only the popular 5-beam setup with normally incident exposure and square grating periodicity, which will always produce a 3-D periodic interference pattern.

The ellipticity and orientation of the polarization of the diffracted beams will adjust the fabricated structure, and is controlled by the incident polarization and the DOE motif. An experimental study of a 4-beam umbrella holographic lithography setup showed that changes in polarization small but clear effect on the fabricated structure.[9] The ellipticity and orientation of the polarization of each beam is another mode of control for design space of PnP, which could be expanded by the implementation of multilevel DOE's.

To investigate the limitations of beam magnitude and relative phase, we first construct a model of a DOE. We split a unit cell of the DOE into A stripes of varying thickness in the x-direction, and B stripes of varying thickness in the y-direction, so that the unit cell is split into $A \cdot B$ rectangles, which are each described by a phase shift. Assuming the DOE is thin, and using scalar diffraction theory, we describe the light transmission immediately through the DOE by:

$$T(x,y) = e^{i\,\phi(x,y)} \tag{3.6}$$

Where

$$\phi(x,y) = \begin{cases} \phi_{1,1}, & L_0 < x < L_1 \text{ and } M_0 < y < M_1 \\ & \vdots \\ \phi_{a,b}, & L_{(a-1)} < x < L_a \text{ and } M_{(b-1)} < y < M_b \\ & \vdots \\ \phi_{A,B}, & L_{(A-1)} < x < L_A \text{ and } M_{(B-1)} < y < M_B \end{cases}, \tag{3.7}$$

L_n describes the position of the left edge of the nth cell in the x-direction, and M_n describes the bottom edge of the nth cell in the y-direction.

3.3.1. Proof of symmetric diffraction efficiency

It can be shown using the above model that for a two-level DOE the diffraction efficiencies of opposite diffracted orders in a 5-beam setup, e.g. [1 0] and [-1 0], must be equal. This symmetry limits the kinds of designs that are possible conventionally, but use of a multilevel grating can break this symmetry, increasing the design space.

Here we prove that the diffraction efficiencies of opposite, first orders of two-level DOE's for a 5-beam configuration are equal. Using Fourier analysis, the transmission (eq 2) can be rewritten as

$$T(x,y) = \sum_{j,k \in \mathbb{Z}} c_{j,k}\, e^{i\, j\frac{2\pi}{L}} e^{i\, k\frac{2\pi}{M}} \tag{3.8}$$

where the Fourier coefficient is given by

$$c_{j,k} = \frac{1}{LM} \int_0^L \int_0^M e^{i\,\phi(x,y)}\; e^{-i\, j\frac{2\pi}{L}x} e^{-i\, j\frac{2\pi}{M}y} dx\, dy \tag{3.9}$$

And the diffraction efficiency is given by $\eta_{j,k} = \left|c_{j,k}\right|^2$. [10]

Using the discretization of the DOE, the diffraction efficiency can be rewritten as

$$\eta_{j,k} = \left| \frac{1}{4\pi^2 jk} \sum_{a=1,b=1}^{A,B} e^{i\,\phi_{a,b}} \left(e^{-i\,j\frac{2\pi}{L}L_a} - e^{-i\,j\frac{2\pi}{L}L_{a-1}} \right) \left(e^{-i\,k\frac{2\pi}{M}M_b} - e^{-i\,k\frac{2\pi}{M}M_{b-1}} \right) \right|^2 \quad (3.10)$$

Since we are interested in the 5-beam configuration, we need to know $\eta_{j,k}$ when $j = 0\ and\ k = \pm 1$ as well as when $j = \pm 1\ and\ k = 0$.

$$\eta_{0,k} = \left| \frac{1}{2\pi} \sum_{a=1}^{A} \frac{L_a - L_{a-1}}{L} \sum_{b=1}^{B} \left(e^{-i\,k\frac{2\pi}{M}M_b} - e^{-i\,k\frac{2\pi}{M}M_{b-1}} \right)\ e^{i\,\phi_{a,b}} \right|^2 \quad (3.11)$$

And by symmetry,

$$\eta_{0,j} = \left| \frac{1}{2\pi} \sum_{b=1}^{B} \frac{M_b - M_{b-1}}{M} \sum_{a=1}^{A} \left(e^{-i\,k\frac{2\pi}{L}L_a} - e^{-i\,k\frac{2\pi}{L}L_{a-1}} \right)\ e^{i\,\phi_{a,b}} \right|^2 \quad (3.12)$$

The diffraction efficiency of the [0 1] order can be rewritten as:

$$\eta_{0,1} = \left| \frac{1}{2\pi} \sum_{a=1}^{A} \frac{L_a - L_{a-1}}{L} \sum_{b=1}^{B} e^{-i\frac{2\pi}{M}M_b} \left(e^{i\,\phi_{a,b}} - e^{i\,\phi_{a,(b+1)}} \right) \right|^2 \quad (3.13)$$

And the [0 -1] order as:

$$\eta_{0,-1} = \left| \frac{1}{2\pi} \sum_{a=1}^{A} \frac{L_a - L_{a-1}}{L} \sum_{b=1}^{B} e^{i\frac{2\pi}{M}M_b} \left(e^{i\,\phi_{a,b}} - e^{i\,\phi_{a,(b+1)}} \right) \right|^2 \quad (3.14)$$

We replace the interior of the absolute value with its conjugate:

$$\eta_{0,1} = \left| \frac{1}{2\pi} \sum_{a=1}^{A} \frac{L_a - L_{a-1}}{L} \sum_{b=1}^{B} e^{i\frac{2\pi}{M}M_b} \left(e^{-i\,\phi_{a,b}} - e^{-i\,\phi_{a,(b+1)}} \right) \right|^2 \quad (3.15)$$

Looking at the special case of a DOE with two levels (as most demonstrated DOE's are), we declare that the phase shift of each block can have two possible values:

$$\phi_{a,b} = \begin{cases} 0 \\ \psi \end{cases} \quad (3.16)$$

So that

$$e^{i\,\phi_{a,b}} - e^{i\,\phi_{a,(b+1)}} = \begin{cases} e^{i\psi} - 1, & \phi_{a,b} = \psi\ and\ \phi_{a,(b+1)} = 0 \\ 0, & \phi_{a,b} = \phi_{a,(b+1)} \\ 1 - e^{i\psi}, & \phi_{a,b} = 0\ and\ \phi_{a,(b+1)} = \psi \end{cases} \quad (3.17)$$

Multiplying equation 5 by $\left|-e^{i\psi}\right|^2 = 1$,

$$\eta_{0,1} = \left| \frac{1}{2\pi} \sum_{a=1}^{A} \frac{L_a - L_{a-1}}{L} \sum_{b=1}^{B} e^{i\frac{2\pi}{M}M_b} \left(-e^{-i\,(\phi_{a,b}-\psi)} + e^{-i\,(\phi_{a,(b+1)}-\psi)} \right) \right|^2 \quad (3.18)$$

we see that the interior has the same values as above:

$$-e^{-i\,(\phi_{a,b}-\psi)} + e^{-i\,(\phi_{a,(b+1)}-\psi)} = \begin{cases} e^{i\psi}-1, & \phi_{a,b} = \psi \; and \; \phi_{a,(b+1)} = 0 \\ 0, & \phi_{a,b} = \phi_{a,(b+1)} \\ 1 - e^{i\psi}, & \phi_{a,b} = 0 \; and \; \phi_{a,(b+1)} = \psi \end{cases} \quad (3.19)$$

So,

$$\eta_{0,1} = \left| \frac{1}{2\pi} \sum_{a=1}^{A} \frac{L_a - L_{a-1}}{L} \sum_{b=1}^{B} e^{i\frac{2\pi}{M}M_b} \left(e^{i\,\phi_{a,b}} - e^{i\,\phi_{a,(b+1)}} \right) \right|^2 = \eta_{0,-1} \quad (3.20)$$

and by symmetry,

$$\eta_{1,0} = \eta_{-1,0} \quad (3.21)$$

This shows that the diffraction efficiencies of opposite orders of a thin, two-level phase mask must be equal, which limits the PnP design space.

3.3.2. Mapping the possible design spaces of multilevel gratings

To more fully understand the sets of diffraction efficiencies possible with DOE's with two or more levels, we do RCWA analysis of a diverse set of randomly generated DOE's. The DOE's here are defined using the same geometry as above, with experimentally realistic parameters. We assume a conformal phase mask DOE in air and SU-8 photoresist (refractive index n = 1.58); conformal phase masks eliminate the need for phase-matching fluid with steep diffraction angles.[3] We assume a periodicity of 772nm and an exposure wavelength 770nm, which will produce an interference pattern with cubic symmetry. The DOE is segmented into 4 stripes in the x and y dimensions, or 16 blocks. We allow blocks to have a maximum height of 8.34μm (equivalent to a 2π phase shift compared to air). We also check each DOE against a 'fabricability condition' as a heuristic for whether a DOE would be unduly difficult to fabricate; to meet the condition, each block must have a minimum width greater than 51.7nm and a maximum height lower than 500nm, so that no feature can have an aspect ratio greater than 10:1. The incident light has a wavelength of 532nm and is polarized with the electric field in the x-direction.

Figure 3.2a,b depict the sets of possible diffraction efficiencies of opposing first-orders of diffraction in the x-direction and y-direction, respectively. This shows that for 2-level fabricatable DOE's the opposing diffraction efficiencies must be nearly the same, corroborating the above thin element analysis. When the DOE's are allowed to have 3 levels, this symmetry is broken and more combinations of diffraction efficiencies are possible. Plots a and b are somewhat different due to the polarization of the incident light: p-polarized for plot a and s-polarized for plot b. Much higher diffraction efficiencies are possible with the s-polarized light and the breaking of the symmetry is somewhat stronger.

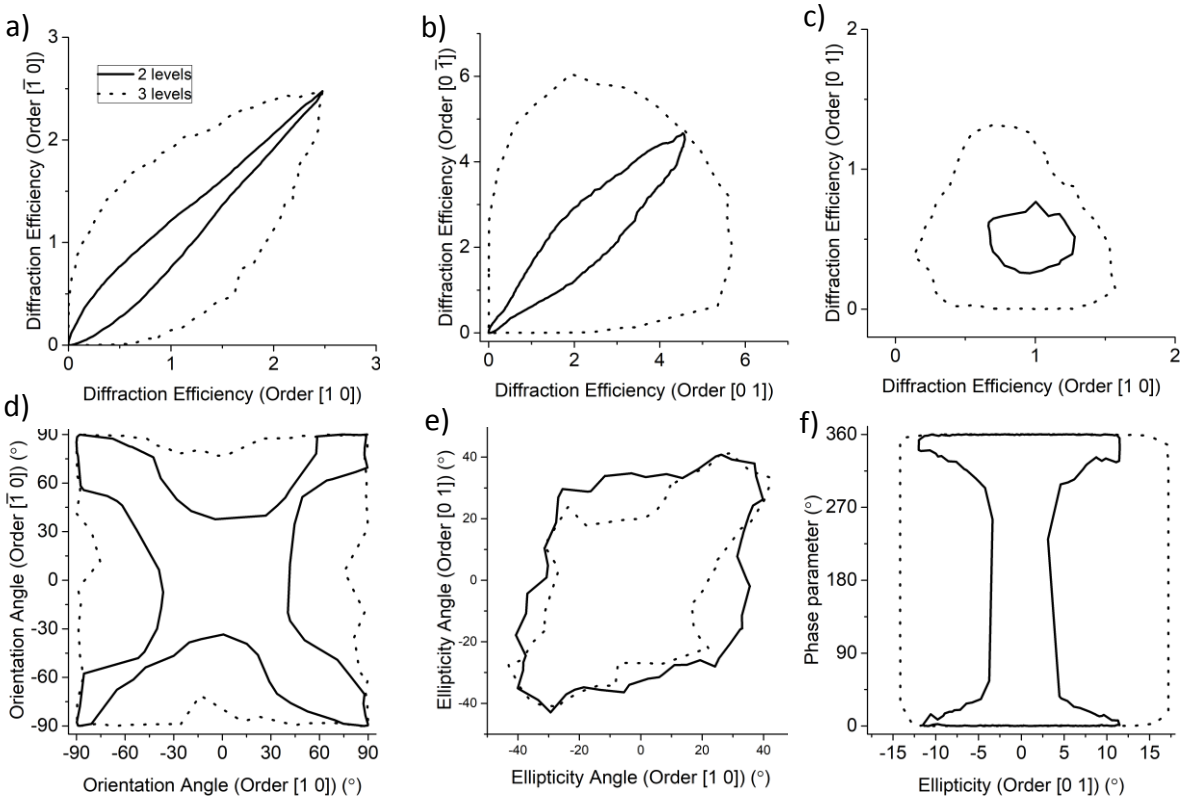

Figure 3.2. Hull plots showing the possible sets of diffracted order parameters for 2-level gratings (solid) and 3-level gratings (dashed). a) Diffraction efficiency of ±x diffracted orders. b) Diffraction efficiency of ±y diffracted orders. c) Diffraction efficiency of +x and +y diffracted orders when the –x and –y orders are held to diffraction efficiencies close to 1% and 0.5%, respectively. d) Orientation angles of the ±x diffracted orders. e) Ellipticity angles of the ±x diffracted orders. f) The phase parameter and the ellipticity of the +y order when the –x and –y orders are held to diffraction efficiencies close to 1% and 0.5%, respectively.

These designs show that some variation is allowed between the opposite diffraction efficiencies, though the analysis predicted a perfect math; this is due to the fact that the thin-element model only approximates the optics of a real, thick element. In a thick element, there is optical interaction between the blocks within a stratum, whereas in a thin element, the only interaction occurs after the light has propagated through the structure.

A similar expansion of sets of possible diffraction efficiencies for adjacent diffracted orders is evident in **Figure 3.2c**. To more clearly visualize the 4 dimensional design space with regard to diffraction efficiency, a slice of the dataset is depicted in Figure 1 c, where two adjacent diffraction efficiencies are held to within 10% (relative) of set values: $\eta_{-1,0} \approx 1\%$ and $\eta_{0,-1} \approx 0.5\%$; again, for a 2 level DOE, the diffraction efficiencies of the remaining diffracted orders can only be varied by a small amount.

The thin-film analysis above uses a scalar model of the electric field, meaning that we cannot glean any information regarding the direction of the electric field. In a real element, the electric field matters. With RCWA, the effects of the gratings on polarization can be computed. Here, we describe the polarization of light in terms of the orientation angle and ellipticity angle. The ellipticity angle describes how much of the light is linearly polarized and how much is circularly polarized. The orientation angle describes the orientation of the major linear-component of the light, shown in **Figure 3.3**. In **Figure 3.2d,e**, we see that there is an expanded design space for controlling the orientation angles of opposite orders. For a binary grating, orientations that are opposite seem to be preferred. This might make sense given that by analysis, mirror symmetry tends to be preferred. For ellipticity angles, however, the design space of the 2-level gratings seems to exceed that of the 3-level gratings. This is unexpected, since the set of all 2-level gratings must be included in the set of all 3-level gratings. Based on this and the jaggedness of the hulls – the difference is probably due to incomplete sampling of the design space. Unfortunately, many orders of magnitude greater computational power would be needed to clarify the effect of the number of levels on the ellipticity of the possible beams.

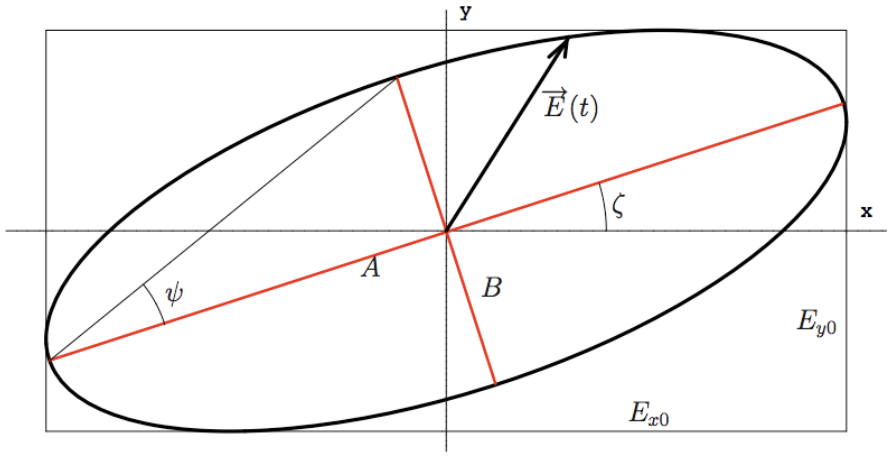

Figure 3.3. Plot the path of the electric field of elliptically polarized light, showing the definition of the ellipticity angle, ψ, and orientation angle,ζ. Image by Rodendo ,et al.[11]

The relative phase of the diffracted beams also impacts the generated interference pattern. For a 4-beam system, the relative phase does not effect the structure; phase shifts only translate the pattern in space. With a 5-beam system, however, there is one available degree of freedom. To find the phase shifts that will result in the same translated interference pattern, we apply $I(\vec{r},\delta) = I(\vec{r}+\vec{R},\delta+\Delta\delta)$ to equation 1, where $\vec{R}$ is the vector translation caused by the phase shift and $\Delta\delta$ is a sequence of phase shifts applied to each beam. We find that $\vec{R}$ exists (and the phase shift merely causes a translation in space) whenever the condition $\Delta\delta_{1,0} - \Delta\delta_{0,1} + \Delta\delta_{-1,0} - \Delta\delta_{0,-1} = 0$ is met;

$\vec{R} = \left(\frac{\Delta\delta_{1,0}-\Delta\delta_{-1,0}}{2k_p}, \frac{\Delta\delta_{0,1}-\Delta\delta_{0,-1}}{2k_p}, \frac{3\Delta\delta_{1,0}-\Delta\delta_{-1,0}-2\Delta\delta_{0,0}}{2(k_0-k_r)}\right)$, where k_p and k_r are the horizontal and vertical diffracted wavevector components, respectively, and k_0 is the magnitude of the wavevector. We define $\delta = \Delta\delta_{1,0} - \Delta\delta_{0,1} + \Delta\delta_{-1,0} - \Delta\delta_{0,-1}$ as a parameter identifying unique interference patterns among designs with similar diffraction efficiencies. Because the diffraction patterns are invariant on shifting the phase of a beam by 2π, and because δ and $-\delta$ are equivalent, δ can only be unique within $0 < \delta < \pi$. We use RCWA as before to determine the possible values of the diffraction efficiency and δ, taking the phase of the x-component of the polarization as the phase of the beam.

3.4. Process flow for multilevel diffractive optical elements

The procedure shown here for the fabrication of multilevel DOE's was developed by Sidhartha Gupta and Andrew Gardner, though this work was not published. Existing procedures for multilevel DOE's have relied on laser direct-write processes, combinations of linear gratings, or many steps of e-beam lithography, all of which either have only limited ability to control the DOE features, or require an expensive, time-consuming write-process.[12]–[15] We have also developed a procedure to produce multilevel DOE's with broad versatility. The procedure can be summarized as follows (**Figure 3.4**): 1) a diamond Berkovitch indentation tip is focused ion beam (FIB) milled into the inverse of the desired DOE pattern; 2) nanoindentation lithography is used to indent the desired pattern into film of SU8 photoresist, forming the conformal DOE; 3) the film is exposed to a laser with the desired wavelength and polarization; 4) ordinary SU8 baking and development is performed to reveal the SU8 nanostructure. The use of 3-D milling to fabricate the tip means that an arbitrary number of levels can be fabricated and is amenable to features that continuously change in the z-direction. Feature size that can be made on the DOE is limited only by the resolution of the FIB and by the mechanics of diamond tip with the indented photoresist.

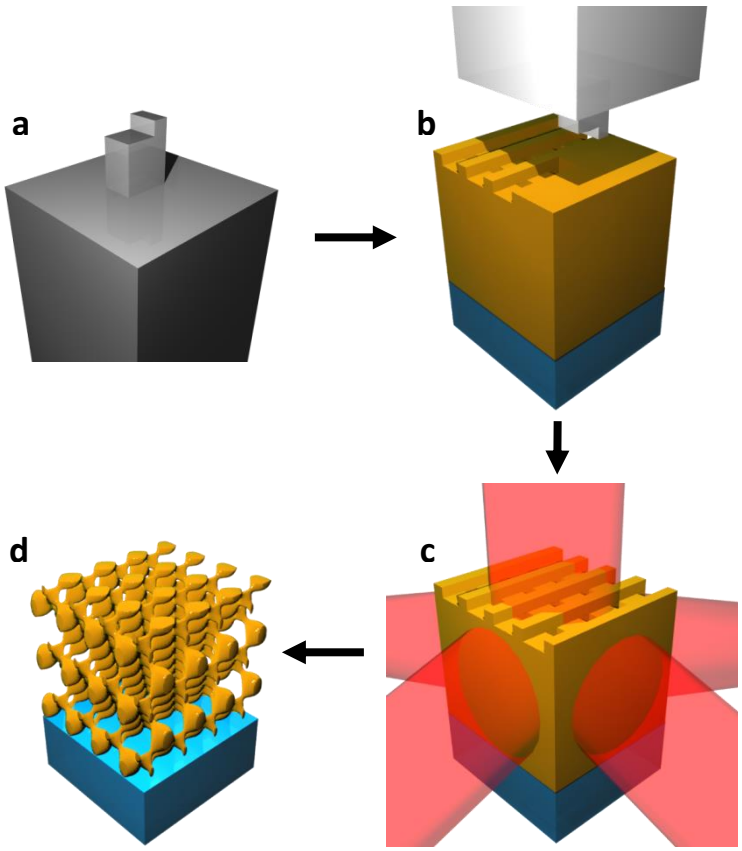

Figure 3.4. Diagram of process flow. a) An AFM tip is custom milled with a focused ion beam. b) The tip is indented into a film of SU8 photoresist. (c) The indented film is exposed with a laser. d) The photoresist is baked and developed to reveal the periodic structure.

For a demonstration of this technique, we first design a DOE that produces a desired complex nanostructure. Here, we choose a rod-connected diamond (RCD) structure (**Figure 3.5a**), a geometry known to exhibit the largest photonic bandgap,[16] and often chosen as a target for evolutionary design of holographic lithography procedures.[4], [17], [18] For a 770nm exposure wavelength, a cubic symmetry is achieved by a nm square periodic DOE. We assume a 3-level conformal DOE composed of SU-8 photoresist (n=1.58) and air. The DOE motif and exposure conditions were devised via an inverse design technique using evolutionary algorithms to minimize the volumetric mismatch between each candidate structure and the targeted RCD structure.[8] The optimized structure (**Figure 3.5b**) has a 79% volumetric overlap with the perfect RCD lattice. The corresponding DOE is shown in **Figure 3.5c**; light gray (α) indicating the bottom level, medium gray (β) indicating the middle level 160nm above α, and

dark gray (γ) indicating the highest level, 310nm above α. The diffraction efficiencies for design are 1.61% for the [0, 1] and [0, -1] orders and 1.58% for the [1, 0] and [-1, 0] orders. This design is qualitatively similar to a previously designed DOE to produce a diamond-like woodpile structure.[14]

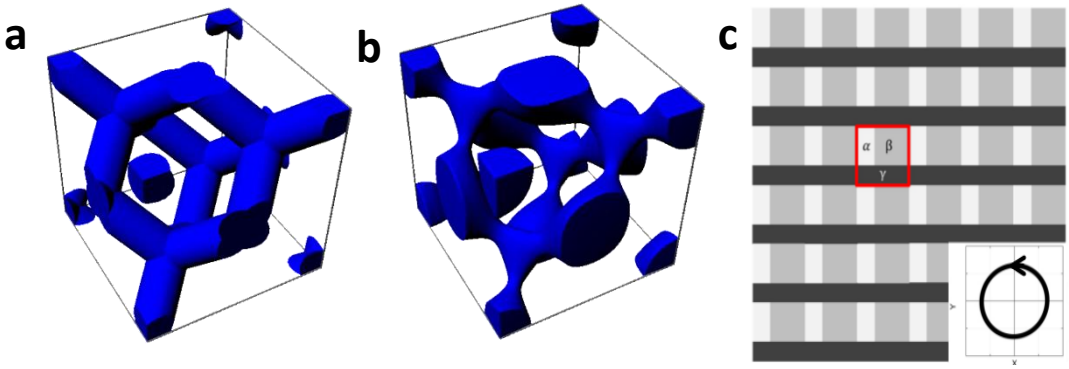

Figure 3.5. a) The rod-connected diamond structure used as a target for the evolutionary design of a DOE and exposure polarization to produce a similar model. b) The optimized simulated structure found to have the best match to (a). c) The DOE and (inset) incident polarization that yields the structure shown in (b). α denotes the lowest level, β denotes an elevation 160nm above α, and γ denotes an elevation 150nm above β. The inset in (c) describes the polarization, showing the change in the electric field vector as the wave propagates into the paper (nearly left-handed circular polarization). Plot c created by Sidhartha Gupta.

The indentation tip was milled into the desired shape (**Figure 3.6a**) from a commercial diamond Berkovitch nanoindentation tip using an FEI DB235 Dual-Beam Focus Ion Beam System. A deep nanoindentation with this tip into SU-8 (**Figure 3.6b**) shows good inversion of the tip shape into SU8; an inadvertent 30nm defect in the tip was also found in the resist, showing that very fine features are possible with a properly made indentation tip. The DOE was fabricated by more shallow, repeated indentations (**Figure 3.6c**). There is no feature on the tip corresponding to the γ level of the DOE – this feature is formed by mass transfer of polymer from the indented regions. The indentations do not exactly match the designed DOE; there is both a tilt to the tip and a shallow indentation depth, but this was found to not have an adverse effect on the fabricated structure. This conformal DOE was exposed to a femtosecond laser pulse centered at 770nm, exciting 2-photon absorption in the photoresist. The photoresist films were exposed using a regeneratively amplified Ti:Sapphire laser (Wyvern 1000; KM Labs).

An approximately 2.3W output was centered at 770nm with a 150-158ps pulse duration and operated at a 1000kHz pulse frequency. Exposure time was 2-3 minutes. Baking and developing of the exposed photoresist yielded the structure shown in **Figure 3.6d**. The structure shrunk approximately 27% in the vertical direction, consistent with past studies of holographic SU8 structures.[19] The shrinkage ratio and a slightly higher exposure level were incorporated into a simulation of the fabricated structure, shown in the inset of Figure 4d. The excellent match between the simulated and experimental structures indicates how robust this process is to minor defects in the tip milling and indentation processes.

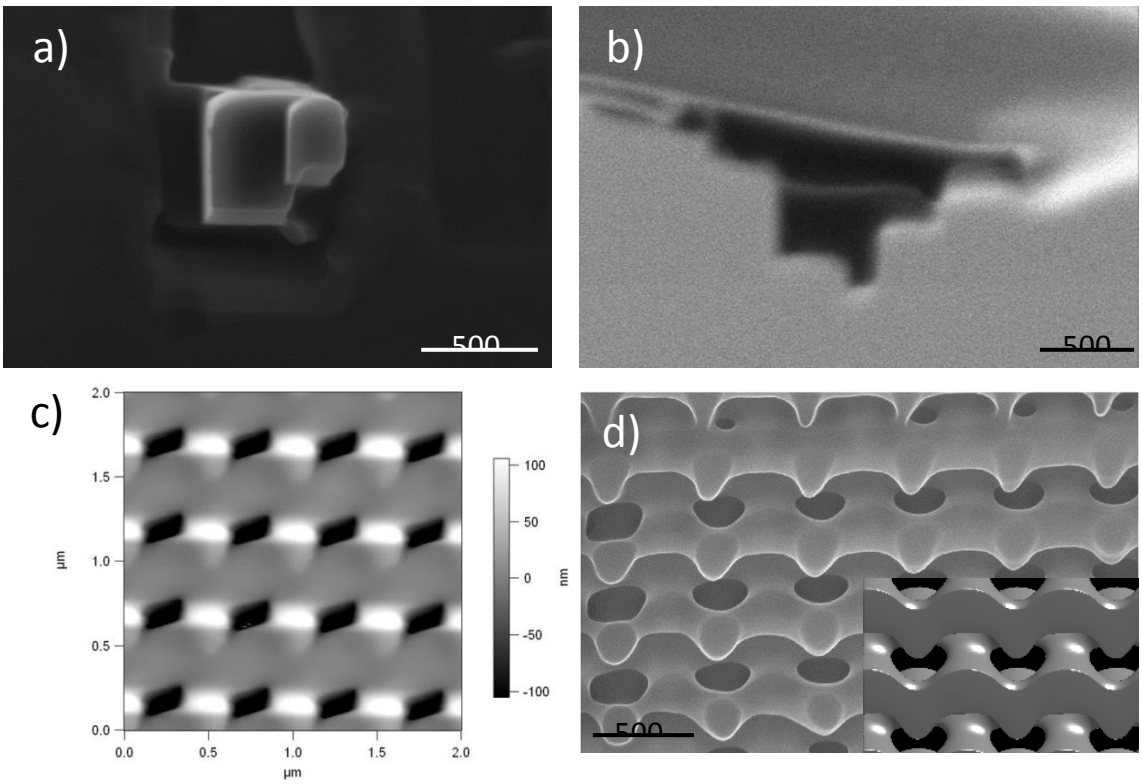

Figure 3.6. a) An custom AFM tip made using FIB milling. b) SEM of cross-section of an indentation with the tip. c) AFM of indented DOE. d) SEM of cross-section of developed nanostructure (main image) with simulated structure (inset). Images created by Sidhartha Gupta.

We have seen that we can fabricate an RCD structure using a multilevel phase mask. However, an astute reader will notice that the diffraction efficiencies of opposite orders of this design are equal. This RCD structure was designed and fabricated before the mathematical analysis of the design space was performed. Unfortunately, the design that was chosen to

demonstrate the efficacy of multilevel patterns was actually a design that could be replicated using a conventional, 2-layer diffraction grating! One example of such a binary mask that replicates the diffraction efficiency of the fabricated pattern is shown in **Figure 3.7**.

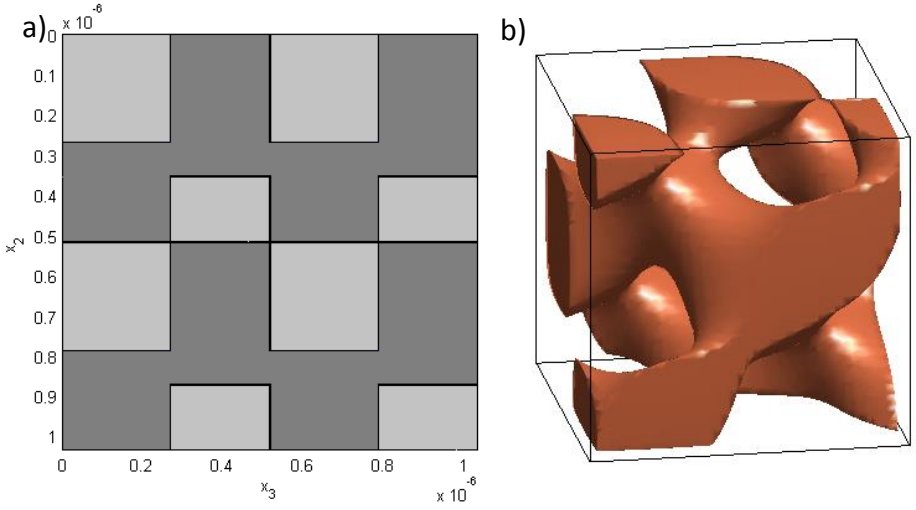

Figure 3.7. a) Schematic of two-level mask pattern to create RCD structure, with a period of 772nm. The light areas are raised and the dark areas are lowered, with a height difference of 250nm. b) The RCD unit cell that would be created using this mask.

3.5. Conclusion

In this work we have proven that the design space of PnP is greatly expanded by the use of DOE's with 3 or more levels over DOE's with two levels. We have also developed and demonstrated a DOE fabrication technique that enables use of an arbitrary number of levels, continuous changes in height, and feature sizes down to at least 30nm. Genetic algorithm optimization was used to devise a 3-level DOE to produce a rod-connected diamond nanostructure, an inverse design technique we believe is suitable for the design of many different desired nanostructures.

3.6. References

[1] S. Jeon *et al.*, "Fabricating complex three-dimensional nanostructures with high-resolution conformable phase masks," *Proc. Natl. Acad. Sci. U. S. A.*, vol. 101, no. 34, pp. 12428–12433, 2004.

[2] M. Miyake, Y.-C. Chen, P. V. Braun, and P. Wiltzius, “Fabrication of Three-Dimensional Photonic Crystals Using Multibeam Interference Lithography and Electrodeposition,” *Adv. Mater.*, vol. 21, no. 29, pp. 3012–3015, Aug. 2009.
[3] M. C. George, E. C. Nelson, J. A. Rogers, and P. V. Braun, “Direct Fabrication of 3D Periodic Inorganic Microstructures using Conformal Phase Masks,” *Angew. Chem.*, vol. 121, no. 1, pp. 150–154, Jan. 2009.
[4] C. K. Ullal, M. Maldovan, M. Wohlgemuth, E. L. Thomas, C. A. White, and S. Yang, “Triply periodic bicontinuous structures through interference lithography: a level-set approach,” *JOSA A*, vol. 20, no. 5, pp. 948–954, 2003.
[5] C. K. Ullal, M. Maldovan, E. L. Thomas, G. Chen, Y.-J. Han, and S. Yang, “Photonic crystals through holographic lithography: Simple cubic, diamond-like, and gyroid-like structures,” *Appl. Phys. Lett.*, vol. 84, no. 26, pp. 5434–5436, Jun. 2004.
[6] D. J. Shir *et al.*, “Dual exposure, two-photon, conformal phase mask lithography for three dimensional silicon inverse woodpile photonic crystals,” *J. Vac. Sci. Technol. B Microelectron. Nanometer Struct.*, vol. 28, no. 4, p. 783, 2010.
[7] D. Shir *et al.*, “Three-Dimensional Nanostructures Formed by Single Step, Two-Photon Exposures through Elastomeric Penrose Quasicrystal Phase Masks,” *Nano Lett.*, vol. 8, no. 8, pp. 2236–2244, Aug. 2008.
[8] J. W. Rinne, S. Gupta, and P. Wiltzius, “Inverse design for phase mask lithography,” *Opt. Express*, vol. 16, no. 2, pp. 663–670, 2008.
[9] X. Zhu, Y. Xu, and S. Yang, “Distortion of 3D SU8 photonic structures fabricated by four-beam holographic lithography withumbrella configuration,” *Opt. Express*, vol. 15, no. 25, pp. 16546–16560, 2007.
[10] I. Erteza, “Diffraction efficiency analysis for multi-level diffractive optical elements,” Sandia National Labs., Albuquerque, NM (United States), 1995.
[11] J. Redondo, “Can the PVLAS particle be compatible with the astrophysical bounds?,” PhD Thesis, Barcelona, Autonoma U., 2007.
[12] D. Chanda and P. R. Herman, “Phase tunable multilevel diffractive optical element based single laser exposure fabrication of three-dimensional photonic crystal templates,” *Appl. Phys. Lett.*, vol. 91, no. 6, p. 061122, 2007.
[13] D. Chanda, L. E. Abolghasemi, and P. R. Herman, “Single laser exposure fabrication of diamond-like 3-dimensional photonic crystal microstructures using circularly polarized light,” *Appl. Phys. A*, vol. 93, no. 1, pp. 33–37, Oct. 2008.
[14] D. Chanda, L. E. Abolghasemi, M. Haque, M. L. Ng, and P. R. Herman, “Multi-level diffractive optics for single laser exposure fabrication of telecom-band diamond-like 3-dimensional photonic crystals,” *Opt. Express*, vol. 16, no. 20, pp. 15402–15414, 2008.
[15] E. Pawlowski and H. Engel, “Multilevel diffractive optical elements fabricated with a single amplitude-phase mask,” *Pure Appl. Opt. J. Eur. Opt. Soc. Part A*, vol. 6, no. 6, p. 655, 1997.
[16] M. Maldovan and E. L. Thomas, “Diamond-structured photonic crystals,” *Nat. Mater.*, vol. 3, no. 9, pp. 593–600, 2004.
[17] J. W. Rinne and P. Wiltzius, “Design of holographic structures using genetic algorithms,” *Opt. Express*, vol. 14, no. 21, pp. 9909–9916, 2006.
[18] D. N. Sharp, A. J. Turberfield, and R. G. Denning, “Holographic photonic crystals with diamond symmetry,” *Phys. Rev. B*, vol. 68, no. 20, Nov. 2003.

[19] R. G. Denning, C. F. Blanford, H. Urban, H. Bharaj, D. N. Sharp, and A. J. Turberfield, “The Control of Shrinkage and Thermal Instability in SU-8 Photoresists for Holographic Lithography,” *Adv. Funct. Mater.*, vol. 21, no. 9, pp. 1593–1601, May 2011.
[20] K. A. Arpin *et al.*, “Multidimensional Architectures for Functional Optical Devices,” *Adv. Mater.*, vol. 22, no. 10, pp. 1084–1101, Feb. 2010.
[21] D. Chanda *et al.*, “Large-area flexible 3D optical negative index metamaterial formed by nanotransfer printing,” *Nat. Nanotechnol.*, vol. 6, no. 7, pp. 402–407, Jun. 2011.
[22] A. Brzezinski, J.-T. Lee, J. D. Slinker, G. G. Malliaras, P. V. Braun, and P. Wiltzius, “Enhanced emission from fcc fluorescent photonic crystals,” *Phys. Rev. B*, vol. 77, no. 23, Jun. 2008.
[23] C. Zhang, G. G. Cano, and P. V. Braun, “Linear and Fast Hydrogel Glucose Sensor Materials Enabled by Volume Resetting Agents,” *Adv. Mater.*, vol. 26, no. 32, pp. 5678–5683, Aug. 2014.

CHAPTER 4

PROXIMITY-FIELD NANOPATTERNING OF METALLIC HELIX ARRAY

In this section, we discuss the design of a two-level phase mask to create a template array of helical pores. This design was originally created by James Rinne and Sidhartha Gupta, though it has been modified in multiple ways to deal with fabrication issues. It should be made clear here that this project was fraught with challenges and was ultimately unsuccessful. It has been said that we learn more from failure than we do from success. As such, this project has been a fantastic learning experience.

While the attempts to fabricate a metallic helix with PnP lead to a dead end, in the process of reaching it we have developed a better understanding of the limits of what this technique is capable of. Through this understanding, we have methods of estimating the feasibility of interference lithography designs that may be considered in the future.

4.1. Broadband Circular Polarizers

First, let's discuss the primary motivation for creating a helical array: the creation of broadband circular polarizers.[1] Circular polarizers can be thought of as a circular analogue to a linear polarizer. Unpolarized light sent through this optic will have one handedness absorbed or reflected and have the other handedness transmitted. Right-handed circular polarizers will block left-handed light, and vice-versa. Unlike linear polarizers, these optics have a chirality, meaning that they have no mirror symmetry. Whereas a vertical polarizer can be turned into a horizontal polarizer by simply rotating it, a right-handed circular polarizer cannot operate as a left-handed polarizer without altering the polarizer itself (though one could include a half-wave plate after the circular polarizer to convert any circular polarized light to its opposite handedness).[2]

The simplest way of making a circular polarizer is to start with a linear polarizer to linearly polarize the light, and place a quarter-wave plate after it at 45° to convert the linear light to circularly polarized light.[3] However, this by itself could have some unwanted

behavior: unpolarized light will have half of its power blocked, but the transmission of linearly polarized light could vary from 0% to 100% depending on the orientation of the light relative to the polarizer. To resolve this, one can simply place another quarter-wave plate in front of the polarizer. The quarterwave plate will convert (depending on its orientation) any right-handed light into vertically polarized light and left-handed into horizontally polarized light. One of these can be selected by the linear polarizer. The selected orientation will be transformed back into circular polarized light with the second quarter-wave plate, as shown in **Figure 4.1**. This can be configured to transmit right-handed, transmit left-handed, convert right-handed light to left-handed, or perform more complex operations with elliptically polarized light.

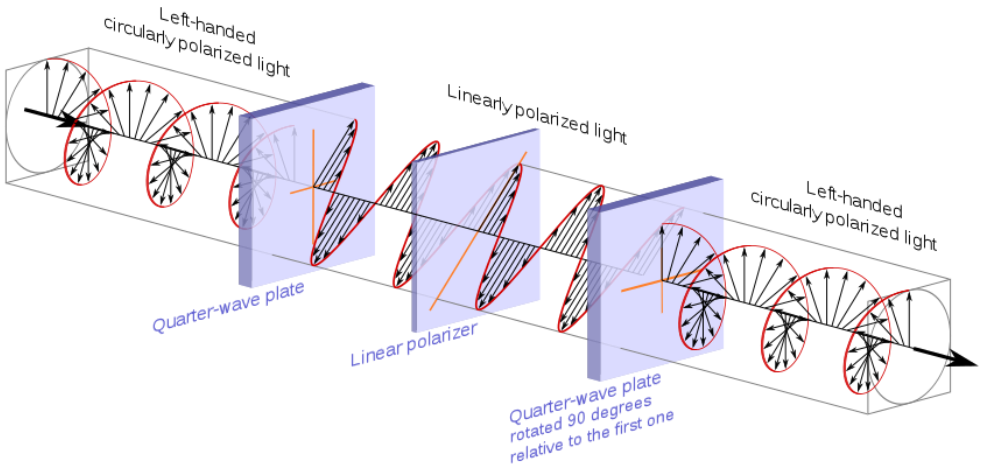

Figure 4.1. A cartoon of the electric field vector as light passes through a circular polarizer composed of a linear polarizer and two-quartwave plates. Image by David C Spratt.[4]

There are a few issues with circular polarizers made this way. One is that there is commonly issue with limited spectral bandwidth – the circular polarizer typically only operates over a narrow range of wavelengths. Linear polarizers made with a wire grid are ordinarily effective over a broad range of wavelengths, but quarter-wave plates are generally not. The birefringent materials waveplates are made of do not have the necessary dispersions in the ordinary and extraordinary refractive index for a waveplate to give a constant phase retardance across a broad spectrum of wavelengths. Thus, to make a broadband quarterwave plate, different birefringent materials are stacked at different orientations so that the phase

retardances of each layer will compensate eachother. This method works, but it results in a very bulky and expensive product.

Another issue with these kinds of circular polarizers is that they are difficult to integrate with certain kinds of devices.[5] These are useful for laboratory or manufacturing scale optical setups and photography, but they are difficult to miniaturize or incorporate into integrated photonics or lab-on-chip experiments. Thus, we need to look at non-conventional means to achieve our desired polarization control.

An alternative to the combination of linear optics is to use a material that intrinsically polarizes light, a circularly dichroic material.[5] Light passing through a circularly dichroic material will have one handedness absorbed, but not the other. Typically, this occurs in organic molecules and any material must have a chiral structure to exhibit circular dichroism. This phenomenon is often used in conjunction with FTIR to identify the handedness of enantiomers.[6] However, they commonly have narrow absorption bands, poor contrasts, and require large amounts of material to achieve a large reduction in the blocked polarization, making them poor solutions to the above applications.

If one could design a new material that has the requisite optical properties, these issues could be solved. A material with features well below the wavelength of light can function as an effective medium, affecting that light as though it were a region of uniform refractive index. This opens up a great deal of opportunities to tune the optical properties. Instead of being forced to rely on chemistry to control the effective optical properties, we can use subwavelength geometry. This is analogous to how wire-grid polarizers function.[7] Wiregrid polarizers, discussed briefly in section 1.3, can be thought of as an effective medium material. The metal is shaped into closely-packed lines at spacings below the operation wavelength, resulting anisotropic optical properties. The anisotropic property we care about most here is a linear dichroism, absorbing light with an electric field parallel to the lines. If, instead of an array of linear wires, we use an array of helical wires, the linear dichroism will be changed to a circular dichroism.[1] **Figure 4.2** shows how a conductive helix can result in circular dichroism. This involves the coupling of electric and magnetic fields. One can note that a metallic helix is very much like a solenoid in an open circuit, which results in magnetic fields when a current

flows though the wire, or inversely, generates a current when magnetic field lines pass through the wires. In AC, some frequencies strongly resonate, but only for one handedness of light. The frequencies that resonant primarily depend upon the period in z, and on the total height of the element. The element can be made to operate at higher frequencies by decreasing the period in z, and lower frequencies by increasing the total height.[8] Metallic helices have long been studied as a form of antenna that is useful for transmitting and receiving circularly polarized radio signals, helpful for being orientation insensitive. Until recently, these have been studied only in radio and microwave frequencies.

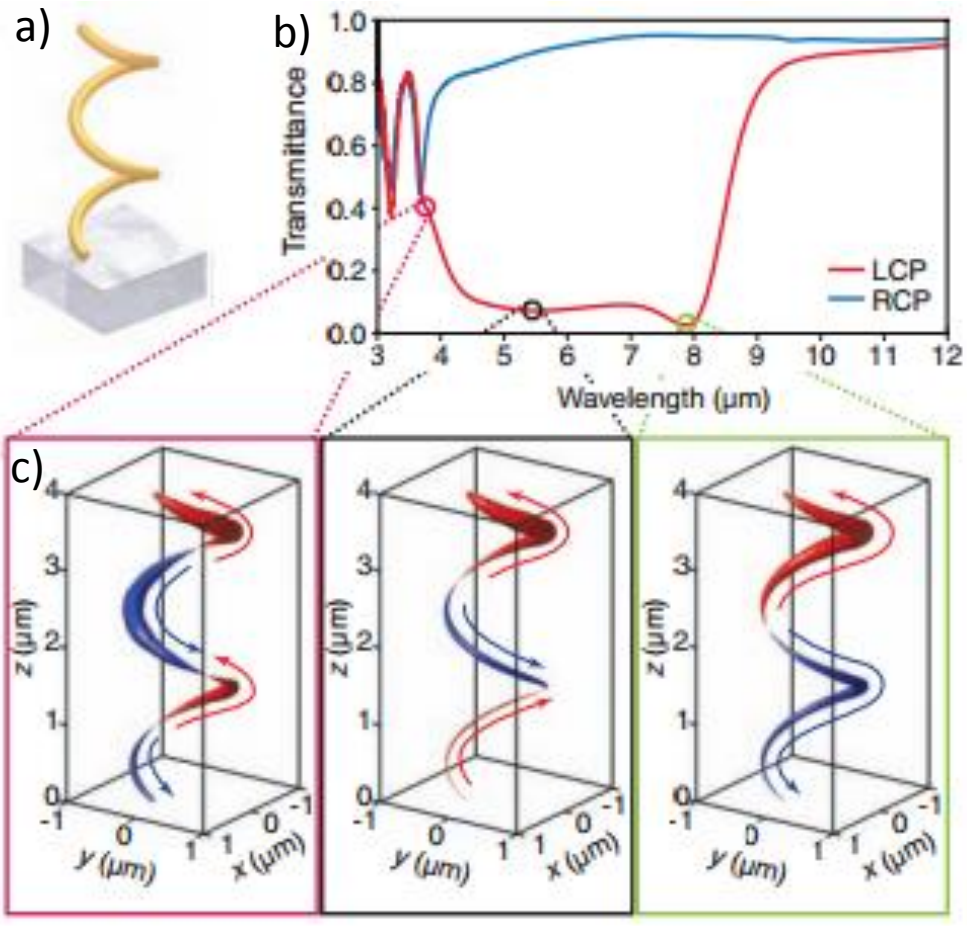

Figure 4.2. a) Cartoon of a metallic helix effective medium. b) Transmission spectrum of right-handed and left-handed circularly polarized light propagating vertically through the medium. c) Cartoon showing the induced electric current modes in the wire when exposed to three different wavelengths of left-handed circular polarized light. Adapted from Gansel, et al.[1]

This geometry has been recently been demonstrated in the NIR.[1], [8] Gold helices in a 2µm period square array were fabricated by DLW of an array of helical pores on an ITO substrate, then electrodeposition of gold into the pores. The results are shown in **Figure 4.3.** The experimental results are shown to accurately match the expected results. This has fabrication method has limitations, however. While DLW is effective at creating smaller arrays for experimentation and prototyping, it cannot be easily scaled up.[9] However, PnP is well posed to bridge the gap with its capability of scalably writing 3D periodic structures.

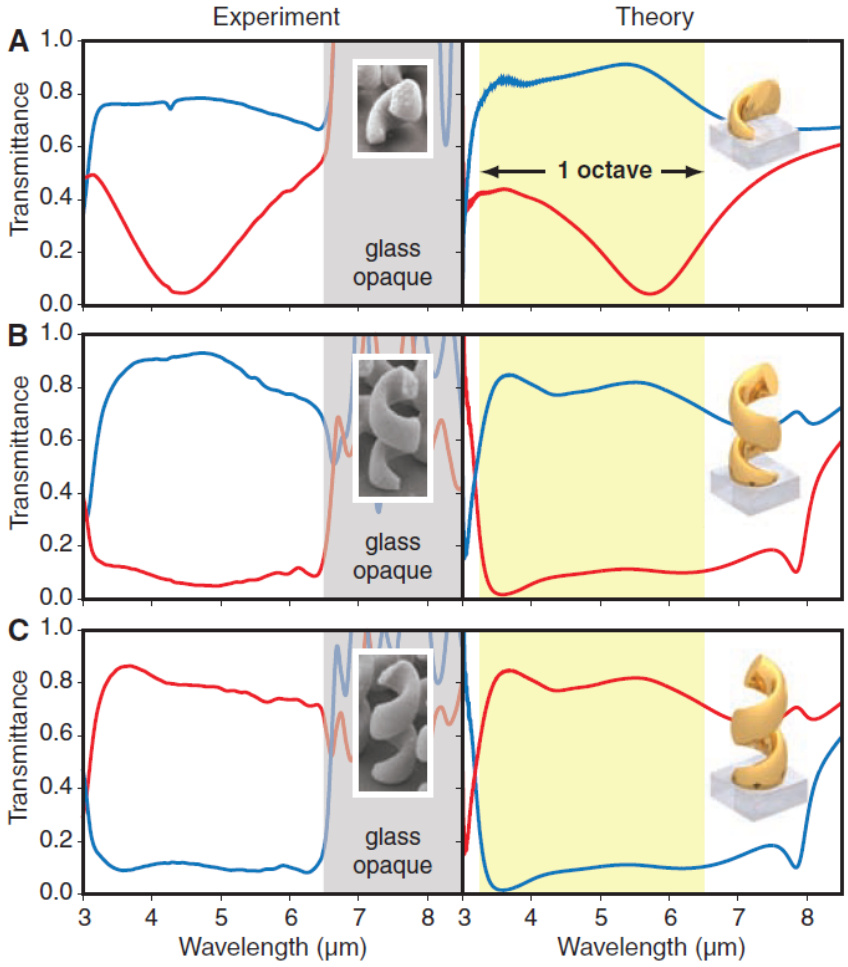

Figure 4.3. Experimental and simulated transmission spectra of RCP (blue) and LCP (red) light. A) Single pitch helix, b) 2-period left-handed helix, and c) 2-period right-handed helix. Above 6.5µm there is a large amount of noise due to the IR absorption bands of the glass substrate. Figure from Ganzel, et al.[1]

4.2. Design of Phase Mask for Helix Array

A design for the fabrication of a metal helix array was created by James Rinne and Siddhartha Gupta, and later optimized by the author. This design uses a hexagonal DOE with a period of 772nm, for exposure with 770nm light. The DOE and corresponding elliptical polarization is shown below in **Figure 4.4ab**. This pattern was designed to create a hexagonal array of helical pores that, once inverted with silver, will have greatly preferred transmission in one polarization, shown in **Figure 4.4cd**. The shape is of a wire with a highly variable thickness that goes down to 50nm, but has mostly the same properties of a helix of uniform wire thickness. However, the fine features lead to fabrication difficulties that will be discussed later this section 4.7.

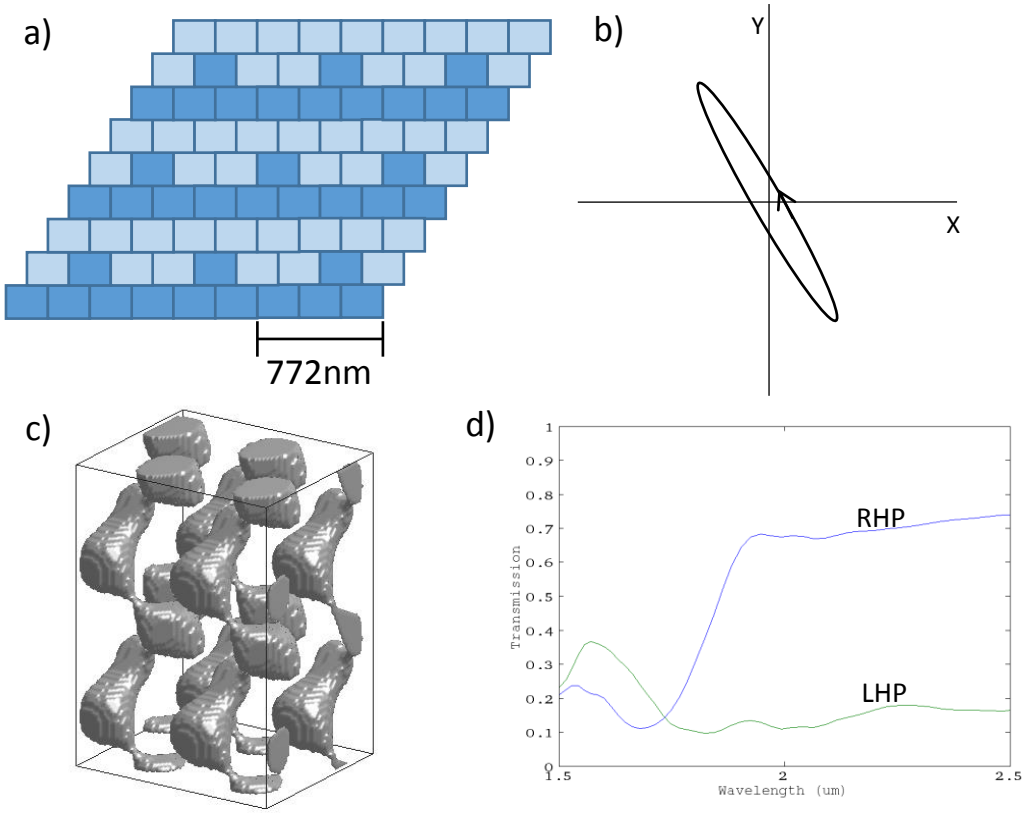

Figure 4.4. a) Plan-view diagram of the DOE for fabricating helices. Dark blue indicates raised regions and light blue indicates lowered regions. b) Plot of the electric field path for the elliptically polarized wave incident on the DOE. c) Iso-intensity surfaces of the interference pattern, depicting the expected shape of the pores in the structure after DOE. d) Simulated transmission spectra of planned metallic helix for right-handed (blue) and left-handed (green) circularly polarized light.

The pattern was optimized simply according to a volumetric match to an ideal helix pattern with a unit cell that has a period (a) of 772nm, an aspect ratio (c/a) of 2.2, a wire radius (r/a) of 1/10, and helix radius (r/a) of 1/4. The DOE was originally designed with a 3x3 array of pixels with uniform size. The free parameters were just which pixels were raised or not and the height difference. The contrast and feature size of this design was improved slightly by freeing the design to include pixels of variable dimension. More details of the optimization process are available in Sidhartha Gupta's and James Rinne's theses.[10], [11]

4.3. Fabrication of Phase Masks

As mentioned, the fabrication of the helix pattern was fraught with challenges and was ultimately unsuccessful. We will start with the initial plan, then go into each of the steps, the challenges that arised, as well as some solutions. The initial plan is shown in **Figure 4.5**.

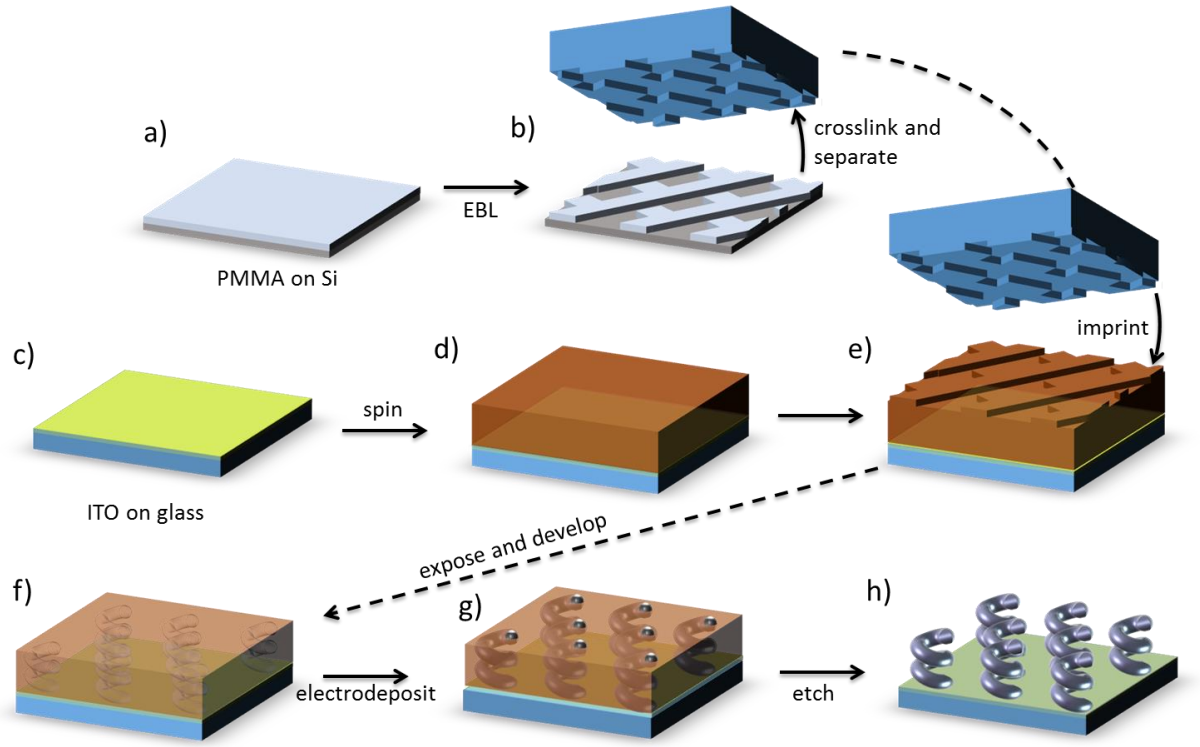

Figure 4.5. Overly optimistic initial plan for the fabrication of metallic helices. a) PMMA film spincoated on Si substrate. b) Electron-beam lithography to define the pattern geometry and making a PDMS mold of the pattern. c) O2 plasma treatment of ITO-coated glass. d) Spincoating and prebaking of SU8 on ITO substrate. e) Nanoimprint lithography of the PDMS mold to transfer the relief pattern to the top of the SU8. f) Exposure of the imprinted mask by a laser, followed by post-bake and development, leaving an array of helical pores. g) Electroless deposition using the ITO substrate inside the pores. h) Oxygen plasma etch of the SU8 matrix, leaving an array of freestanding helices.

4.3.1. Defining the Mask Pattern

The process begins with defining the geometry using EBL. A thin film of 950K molecular weight PMMA was spincoated onto a conductive Si wafer. The thickness of the film here must be equal to the relief depth of pattern and ellipsometry was used to verify the thickness. A useful note to make here is that the dimensions of the Si sample used for the spincoat are important for achieving a consistent thickness; variation in the sizes of the spincoating sample will lead to variations in the thickness of the film. As little as 20% wider samples would lead to an unacceptable deviation in thickness. The same is true of the cleaning process – this should be kept as consistent as possible to ensure that the resist solution wets the substrate equally well each time.

The e-beam exposure area is defined differently from the design, due to the proximity effect. This e-beam exposure has some different requirements compared to typical e-beam definition of devices: this requires a relatively larger amount of the resist to be removed and has much tighter tolerances on the areas defined. For these diffraction grating designs, approximately half of the area of the device must be developed, much higher than typical of e-beam lithography.[12] The dimensions need to be very precise as well, since any change in the device geometry will lead to different amplitude and polarization of the diffracted beams, distorting the structure.

The need to expose a large portion of the device area requires a higher average electron flux density. This leads to a proportionally higher density of scattered electrons that can lead to scissioning of the PMMA where there should be none, causing development of the structure that should be solid.[13] This can be ameliorated by using silicon with a 0.5-1µm oxide, which reduces the exposure from backscattered electrons: the electrons from the e-beam source have enough energy to travel through the oxide layer once, but rarely will they have enough to return to the resist after scattering on the silicon, which has a much higher scattering cross-section than SiO_2.[14]

This by itself is not enough to ensure a high quality pattern. One improvement is using a non-standard development process. Typically, PMMA is developed in mixture of MIBK:IPA for a set period of time, then transferred to pre IPA, then dried.[14] The IPA is commonly treated as a non-developer of IPA, and MIBK is used as the active developing component. However, this is not true – IPA is a developer for PMMA, but has a higher threshold dosage (and thus longer exposure times) than MIBK-IPA mixtures.[15] IPA is in fact a higher contrast developer, which makes it great for minimizing the effect of backscattered electron exposure. We found that using pure IPA as a developer with a development time of 45s lead to repeatable, sharp edges with consistent edges, as long as other factors were consistent.

Lastly, the exact dimensions of the pattern were defined in the e-beam process by performing a series of sweeps for the dimensions of the exposure area and of the dosage. Each step, the dimensions of the fabricated pattern were measured using SEM and the dimensions of the exposure area were readjusted. We found this to be very non-linear, making it difficult to

predict the amount by which to shift the exposure dimensions. This is also susceptible to drift of the e-beam lithography machine, so when optimal parameters are found, a dosage test, SEM measurement, and the final pattern fabrication needed to be performed in the same day to ensure that unacceptable drift did not occur. On a final note, one performing SEM measurements should be aware that the instrument scale bar can be inaccurate, but that the period of the pattern is likely accurate enough to use in place of scale bar if an accurate direct-write alignment was performed.

4.3.2. Creating the Mask Mold

Next, the PDMS mold must be prepared. Here, the mold requires a special combination of parameters. The mold must be very good at maintaining its shape even for nanoscale features under heat and pressure, requiring high rigidity. On the other hand, the mold must also be flexible enough to maintain conformal contact with a substrate with some tolerance for dust particles, as well as easily peeled from the mask without disturbing the relief pattern that was just formed in the nanoimprint process. We achieve this combination of parameters by having two-layers of PDMS with different properties. Within 10's of microns near the surface of the relief pattern, there is a very rigid layer, and further, there is a very flexible layer. The procedure has been modified since its original appearance,[16], [17] as the timing was found to be critical to achieve reliable results. The updated procedure is listed below:

Chemicals:

a. tridecafluoro 1,2,2–tetrahydrooctyl–1–trichloro Silane. This is the chemical we use to fluorinate the surfaces of our Masters. Any similar fluorinated chloro-silane should also work. This material is toxic. The vendor is United Chemical Technology.
b. VDT 731 – 100g from Gelest
c. 1,3,5,7 siloxane (Gelest part number SIT 7900.0 – 25 grams)
d. DiVinyl tetramethyl di-siloxane complex in Xylene with 2.1-2.4 wt.% Pt. Catalyst (PEPDC Platinum Catalyst). Keep this item refrigerated.
e. HMS-301 – 100g from Gelest
f. Slygard 184 and curing agent from Dow Corning (soft PDMS)

Procedure

1. Fluorinate the surface of Master (patterned PMMA on Si) with tridecafluoro 1,2,2–tetrahydrooctyl–1–trichlorosilane.

a. Put a few drops in the bottom of the vacuum jar.
b. Place the master inside the chamber, but away from the droplets.
c. Pull a good vacuum for 60 seconds.
d. Turn off (or turn down) vacuum level but leave sample in chamber for another 1.5 to 3.0 hours.
e. Test for good fluorosilane coverage. A drop of water on the side of the Master should have a large contact angle and roll off the Master when tilted.

2. Coat Master with thin layer of Hard-PDMS
a. Measure 3.4 grams of VDT-731 in plastic tray. Add 2 drops of the 1,3,5,7siloxane. Add one drop of the platinum catalyst.
b. Use the round glass stir bar to mix the above components for 5-10 minutes. Try not to generate too many bubbles.
c. Degas the mixture at room temp for several minutes (leave in fume hood or vacuum degas).
d. Place Master on spin coater and test for proper spin-up.

Spincoating recipe:
500 rpm for 30 seconds
1000 rpm for 40 seconds
500 rpm for 30 minutes

e. Start a timer. Add 1.0 grams of HMS-301 to the above mixture. Spread the drops over the surface of the previous mixture to improve mixing. Quickly mix without producing any bubbles. Pop bubbles with an N2 gas if necessary. Pour mixture onto wafer. This step should be completed within 4 minutes.
h. Wait until 12min mark on timer. Start spincoat.
i. Once spincoat is completed, bake the wafer in 65C oven for 4 minutes. Then allow wafer to cool.

3. Coat hard-PDMS layer with soft-PDMS
a. In plastic cup measure 30 grams of PDMS (Sylgard 184). Put in 2.5 grams of curing agent (use less curing agent for more flexibility of soft PDMS).
b. Mix vigorously for 5-10 minutes.
c. Pour PDMS onto H-PDMS coated master in a flat petri dish lined with aluminum foil.
d. De-gas for 30-60 minutes in the vacuum jar.
e. Let cure at room temperature overnight (8-24 hours) on a very level surface.
f. Cure at 55-70 degrees C for 2-5 hours to get rid of stickiness.

4. Remove PDMS mold from Master.
a. Lift the aluminum foil with mold and master out of the petri dish. Peel the foil from the backside of the mold.
b. Use razor blade to carefully cut through PDMS around master. Make sure not to delaminate the Master from the mold.

c. Use flat razor to get underneath the master and PDMS stamp. Remove from Petri dish.
d. Cut/clear away any PDMS from beneath Master that leaked underneath.
e. Slowly remove PDMS stamp from master.
f. Roll backside of mask onto a glass slide for mechanical support

Once the mask has been prepared, it can be used repeatedly without being replace, but the relief pattern will slowly decay over time. The sample begins as a piece of ITO coated glass, which is first cleaned with oxygen RIE to increase the adhesion of the SU8 photoresist to the ITO.[18] If a nonconductive substrate is acceptable, an adhesion layer of SU8 is prepared on the substrate by spincoating, pre-baking, flood exposing, post-baking, and short O_2 plasma ashing in order to prepare a surface with very good adhesion to the substrate.[19] Following substrate preparation, the SU8 photoresist is spincoated and prebaked to prepare for imprinting.

4.3.3. Nanoimprinting

The imprinting process involves pressing the mask into the photoresist until the photoresist flows into the shape of the relief pattern. SU8 is in the glassy state at room temperature, so it must be heated past the glass transition temperature, around 65°C, or treated with a plasticizer such as ethanol in order to flow.[20] The SU8 is warmed up in an oven set at 85°C and the PDMS mask is rolled onto the SU8. This assembly is compressed with two medium-sized binder clips and returned to the oven for 1 hour. The glass backing of the mask helps to spread out the compressive force and ensure more uniform pressure. After the 1 hour is done, the assembly is removed from the oven and allowed to cool for 30 minutes. After this point, the SU8 should be below its glass transition temperature, allowing the mask to be removed without distorting the pattern. The binder clips are removed first, followed by a gentle peeling of the PDMS from the SU8 surface.[2]

[2] In some select cases, it is necessary to perform transfer printing such that mold comes into contact with the substrate. Here, it is helpful to use ethanol as a plasticizer, as it allows greater mass transfer than heating to 85°C. One (1) drop of ethanol is dropped onto the center of the resist and it is allowed to spread out and dissolve in the substrate for a few seconds, then the mold is pressed into the resist. It is then allowed to rest overnight with a weight on top. The

To verify that the imprint process was working correctly, AFM was performed on the pattern, the e-beam pattern, the PDMS mold and on the imprinted SU8 sample. AFM image are shown in **Figure 4.6**. The PDMS relief pattern is the inverse of the e-beam and imprinted e-beam patterns. One can see that in this case, the height contrast between the upper and lower levels is diminishing in the mold-making process and the imprint process. The lateral dimensions are also visible reduced. This is a fairly common issue with the fabrication process. Later, only tests of the final imprint were occasional performed to test the sample.

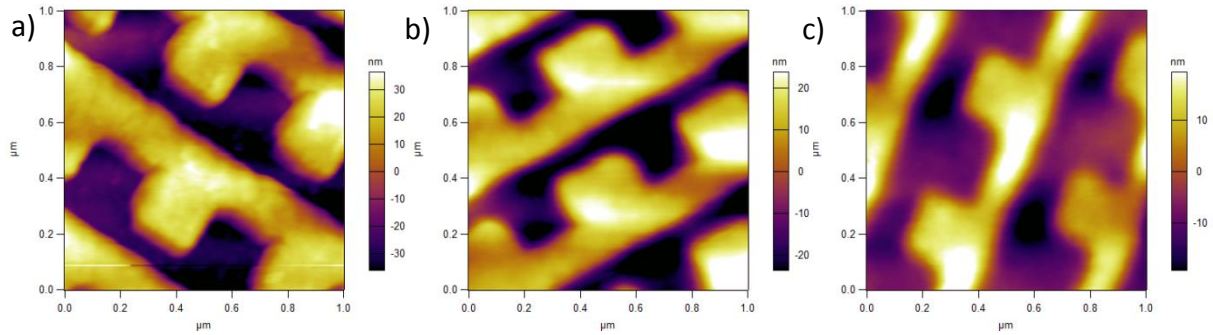

Figure 4.6. AFM plots of a) e-beam pattern, b) PDMS mold, and c) imprinted SU8 at different angles. These measurements were performed by Osman Cifci.

4.4. Exposure

Two sources of exposure were investigated: a 532nm Nd:YVO laser (Verdi V5) and a regeneratively amplified Ti:sapphire laser (KM-1000) centered at 770nm, which the Eden group graciously allowed to use and did a considerable amount of work to keep in good condition for our experiments. Special thanks goes to Tom Galvin and William Goldschlag for their help in this regard. Originally, the plan was to only use the Ti:sapphire laser, but due to difficulties in getting reliable output from this laser, the Nd:YVO laser started to be used. Maxwell's equations are scale-invariant, meaning that the absolute wavelength does not matter, only the ratios of the different length scales, involved, so a shift from 770nm to 532nm should require only decreasing the size of the optical element. However, dispersion means that the refractive index is slightly higher at 532nm compared to 770nm. In practice, this switch means only a

---

use of only a single drop is necessary to minimize thickness variation in the resist because the droplet with carry some resist with it as the dissolution front propagates through the resist.

slight change in the dimensions of the pattern and a new optimal set of dimensions could be quickly optimized for.

4.4.1. Including Reflection Fringes in the Simulation of Helical Interference Pattern

In chapter 2, we went into detail on the effect of backside reflections for interference lithography. This effect is also very important for helices fabricated via PnP. The effect of the backside reflections are amplified for two main reasons: the use of an ITO substrate and the low contrast of the structure. For the circular polarizer, the initial plan was to use ITO as a substrate so that silver could be electrodeposited into the pores.[21] ITO has a refractive index of about 1.9, much higher than typical glass substrates, which leads to much stronger reflections off of the SU8/ITO interface.[22] The low contrast of the helix design amplifies the appearance of the reflection fringes. In our design, there is only about a factor of 2 difference between the lowest intensity and the highest, whereas the contrast of the patterns described in chapter 2 are much larger. The low difference in intensity between different regions of the pattern means that the pattern is more susceptible to changes in intensity, such as interference from backside reflections. The simulated structure that results from the reflection is shown in **Figure 4.7**. One can see that the reflection fringes disconnect the helices vertically in some spots and connect the helices horizontally in others, which completely ruin the optics of the element as a continuous metallic wire is required for circular polarization.

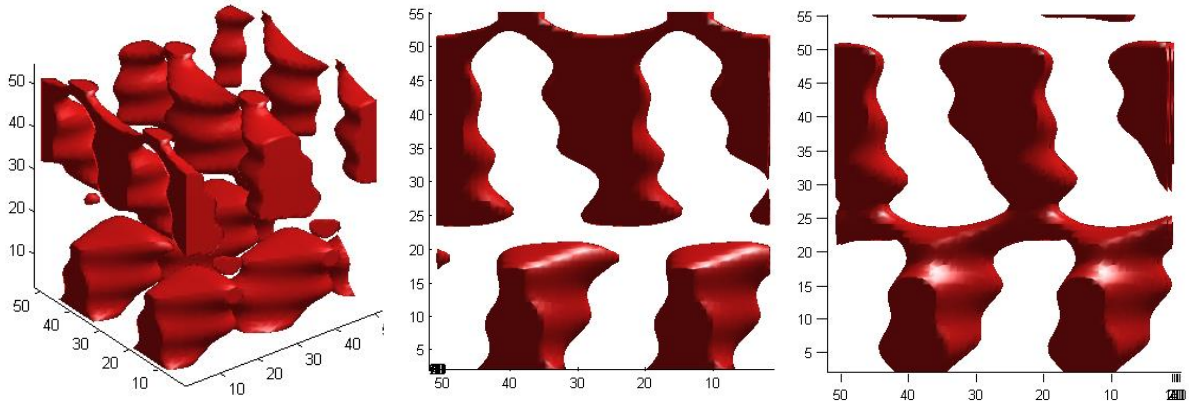

Figure 4.7. Simulated helix pore structures with 10nm ITO on an index-matched substrate. Each figure shows the structure from a different phase of the reflected beams due to different resist thicknesses.

Here, the main source of interference is from the reflection of the central beam, unlike the patterns in Chapter 2 where the reflections of the side beams were the major source of interference. In this design, the diffracted beams have powers of only 1-2%, so the reflections of these orders are low enough that they do not significantly affect the structure.

The solution that was described in chapter 2 cannot simply solve this problem, since the PS:PVME antireflection coating would block the electrodeposition of silver. The above figure shows the results for a 10nm ITO surface, so the reflections cannot be lowered by decreasing the thickness of the ITO while still having reasonable conductivity. The ITO layer needs to be removed from the stack in order to reduce the reflectance to an acceptable level. To deal with the lack of a conductive substrate, the plan was changed to depositing the silver electrochemically, a method that had its own issue and is discussed in detail in Section 4.6.

4.4.2. Two-Photon Exposure

Just as our experiments here began with a Ti:sapphire laser, we will discuss this source first. As mentioned in Chapter 1, two-photon exposure involves the absorption of two-photons in quick succession by a single photo-sensitive molecule.[2] This can cause chemical changes as though a photon with twice the energy were absorbed. SU-8 ordinarily responds only to UV light, being insensitive to light above 400nm.[23], [24] However, light at 770nm with high enough intensity will lead to 2-photon absorption and photo-initiation of the resist.

The 2-photon absorption process requires a *very* high intensity in order to get a high yield of initiation in SU-8, far above what is possible with a continuous wave laser.[24] An ultrafast pulse laser can achieve peak powers greater than gigawatts, more than ample for the initiating crosslinking in SU8. Not all ultrafast pulse lasers have the necessary powers necessary for this lithography process to work. Originally, we planned on using a regneratively amplified Ti:sapphire laser (K-M Labs Wyvern), but this particular system was remarkably unreliable. Briefly, a Tsunami Ti:sapphire laser oscillator was used while the amplifier system was down. Due to the lack of an amplifier system, the power output was much lower, so the beam was

focused to compensate. It was found that the beam focused to a spot size around 100µm diameter would become sufficiently exposed within 20 minutes, which initially seemed acceptable. However, since the beam was focused, it was sharply divergent. While at the precise position of the focal plane, the light may be propagating exactly on axis, the light also has a range of propagation vectors. This means that the light will not diffract into the simple 7-beam diffraction pattern desired, but into a continuum of beams, with each of the '7 orders' having power travelling at a range of directions, resulting in a distorted structure. There were additional issues with this system: the sample tended to overheat due to single-photon absorption from the ITO substrate that would be used for electrodeposition. The heat would cause premature baking of the resist. Fluorine doped tin oxide (FTO) was used as a replacement transparent conductive oxide, which has a lower absorptivity at 770nm. A sapphire substrate coated with ITO was used to more efficiently couple away heat from the surface. An optical chopper with an average duty of 10% was used to reduce the average power without affecting the peak power. This also increased the already long exposure time by 10x. Combined, this resolved the overheating issue.

Even with overheating resolved, creating a uniform enough exposure both in terms of power and phase would be infeasible with a focused beam. However, with a collimated source power limitations of an oscillator system become a problem. The rate of 2-photon absorption is proportional to the square of the peak power, which means that using fewer pulses with higher energy can dramatically improve the rate of exposure without requiring a higher average power.[25] Regeneratively amplified Ti:sapphire lasers select a single pulse once every ~1ms and repeatedly send it through a second gain medium, potentially millions of times.[26] At each pass, the energy of the pulse is increased and will be many orders of magnitude more powerful when it is released. With higher peak powers, a larger area can be exposed, eliminating the need for focusing, so the effect of beam divergence can be ignored. With the higher peak power of these systems, a spot-size of several millimeters can be exposed in ~30s, rather than the 100µm spot size that requires 15 minutes of exposure using a more conventional Ti:sapphire laser.

4.4.3. Theory of Pulses with Interference Lithography

There are a couple of major advantages for using pulses and 2-photon absorption for interference lithography. Foremost, 2-photon absorption increases the contrast.[24] In 2-photon absorption, the resist is exposed with a dosage proportional to $I^2 \cdot t$, where I is the intensity at a particular point in space and t is the exposure time, instead of $I \cdot t$ for 1-photon exposure. Having a high dosage contrast is important defining structures with high aspect ratios and fine features.[27] For any given interference pattern, the dosage contrast for 2-photon exposure will be greater than for the equivalent 1-photon exposure. The high-exposure areas will have a relatively more excitation of PAG's and low-exposure areas will have relatively lower excitation of PAG's using 2-photons. This results in more leeway with the exposure time, given that the pulses are consistent. Higher excitation of PAG's results in more rigid SU8, providing more support for high aspect ratio structures.[28]

Another important advantage is the typically low 2-photon absorptivity of the resist.[29] In interference lithography, it is important that the attenuation be quite low. As the light propagates through the resist, some of the light will be absorbed, leading to progressively lower and lower intensity, resulting in the dosage at the bottom of the structure being lower than at the top. This results in a smaller fill fraction at the bottom of the structure, potentially affecting its properties. Due to the low likelihood of two-photon absorption occurring in SU8 and the negligible absorptivity at NIR wavelengths, there is very low attenuation of the light for Ti:sapphire exposure.[24]

Lastly, the use of 2-photon absorption allows the use of longer exposure wavelengths.[29] Photoresists are typically designed to respond to UV light, so additional photoinitiators or photosensitizers are added to the resists to have them respond to longer wavelengths. However, using long wavelength photoinitiators add some experimental difficulties. Labs that use UV photoresists commonly light the room with yellow lights to avoid exposing the resist, and those that use resists sensitive to green light will use red light. For red light and longer, any light that a human can see has enough energy to activate the resist, making it difficult to work with. Nevertheless, single-photon IR-activated photoiniators have been developed.[30]

There are additional considerations and potential problems that should be taken into account when using pulsed lasers. Two important aspects of pulses are the frequency range and the duration.[2] Monochromatic plane waves, which have a single frequency and, in the theoretical limit, has the same amplitude at all positions in space and time. In contrast, pulses are localized spatio-temperally and have a finite wavelength range. One cannot have one of these characteristics without the other and their limits are related to eachother by Heisenberg's uncertainty principle:[31]

$$\Delta f \Delta t \geq \frac{1}{4\pi} \tag{4.1}$$

Both the range of frequencies and the range in time have important implications in interference lithography.

First we will discuss the range of frequency. In our originally analysis of interference lithography in chapter 2, we used plane waves of a single wavelength and the wavelength used is proportional to the linear size of the fabricated structure. With a range of wavelengths we get a range of periods, and the combination of structures will not be truly periodic for multibeam interference lithography. Once one takes into account dispersion of the SU8 photoresist, this gets worse. The period is not strictly proportional to the vacuum wavelength, but to the wavelength within the material. SU8 has positive dispersion at the wavelengths of the Ti:sapphire laser. The light with shorter vacuum-wavelengths have their wavelengths reduced even more, relative to the longer vacuum wavelengths, which increases the range of periods that are formed by this structure.

The above works fine for multibeam interference lithography, but it does not take into account the dispersion of the DOE. As a wavelength-scale optic, the ratio of the period of the DOE and the wavelength of incident light are very important. At different wavelengths, the DOE will send operate with different diffraction efficiencies, pulses, phases, and importantly, angles. **Figure 4.8a** is useful for explaining this phenomenon. The diffraction of the DOE introduces angular dispersion to the non-zero diffracted orders.[32] Light at slightly larger wavelengths will diffract at steeper angles, so that the k-vector is more lateral. The larger wavelengths will also have shorter k-vectors. Notably, for the x-y component of the k-vector, these two effects exactly cancel out so that all wavelengths will have the same x-y period. One

can also make a symmetry argument in this regard: as discussed, the fabricated structure must have the same lateral periodicity as the DOE, and this does not change by using a spectrum of incident wavelengths. This same phenomenon increases the range of z-periods, as the light with larger wavelengths diffract at steeper angles, further shortening the k_z's for modes with short k_0's.

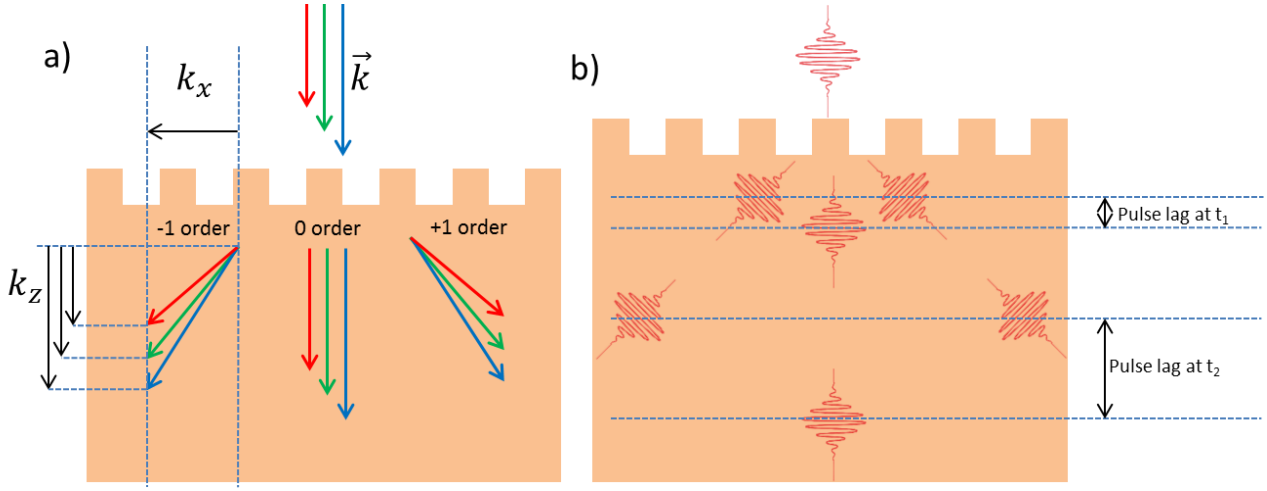

Figure 4.8. Cartoons of a 1D grating explaining (a) the angular dispersion of gratings and (b) the pulse lag that develops for pulses propagating at different angles in the medium. In (a), the red, green, and blue arrows represent the k-vectors of the light wavelengths on the longer, middle and shorter parts of the pulse spectrum, respectively. Due to the symmetry of the grating, all diffracted vectors for the same diffracted order must have the same kx, regardless of the wavelength, which results in changes in the propagation angle. These result in an inconsistent Δk_z, resulting in an inconsistent period in the z-direction. In (b), the red pulse profiles represent the z-positions of each pulse at two different time steps, t1 and t2. At t1, the pulses are at nearly the same position. However, the ±1 modes must propagate in both x and z, while the 0-order mode only propagates in z, so the ±1 modes will lag behind the 0-order mode at t2. Pulse image take from Sharma, et al.[33]

The temporal aspect of the pulse has a major effect on interference lithography as well. For exposures with Ti:sapphire lasers, pulse durations on the order of 100fs are common.[34] For a diffraction-limited pulse, 100fs pulse durations correspond to 30µm pulse durations in space.[31] For the interference lithography to work, each beam must overlap over the same space at the same time. This is what makes multibeam interference lithography so challenging to perform with pulses – it is very difficult to ensure the relative path length of each beam is accurate to within a few tens of microns. The use of a DOE ensures that the diffracted beams

are ‘phase-locked’, ensuring that the peaks of the diffracted pulses are overlapping at the position of the DOE.[27] However, these pulses will not stay in phase as they propagate through the resist. **Figure 4.8b** shows how the different modes develop a ‘pulse lag’, or a difference in position between pulses, as these modes propagate. The ±1 mode pulses travel through the resist at an angle θ with a velocity given by $v = \frac{c}{n}\sin(\theta)\,\hat{x} + \frac{c}{n}\cos(\theta)\,\hat{z}$ (note: this is only valid for a dispersionless medium, which is approximately true for SU-8 around 770nm), compared to the 0-order mode travelling at $\frac{c}{n}\hat{z}$. Over time, the 0-order mode will have practically no overlap with the diffracted orders, resulting in a completely different fabricated structure.

All of these effects can be controlled by controlling the parameters of the pulse: the spectral width and pulse duration. We want as short a spectral width as possible to minimize dispersion effects and a long pulse duration to minimize the effects of pulse lag. However, we also need to have a reasonable exposure time, which will get much longer if we decide to greatly extend the pulse duration. Thus, we need to balance these different parameters to make a sample that has low enough period-broadening and pulse lag, but which is also reasonable to achieve in the lab.

4.4.4. Calculations of the Expected Structure from Pulsed Interference Lithography

All of the above discussion is fairly qualitative but we need quantitative calculations to determine whether our experimental parameters are suitable enough to fabricate the structure we want. To achieve this we need to modify our calculation of the interference pattern, described as follows.

Pulses light can be viewed from the perspective of time-domain or frequency-domain. For this process, we will need both. At first, we will view the pulse as the interference of plane-waves traveling in the same direction, but at different frequencies. The pulse we use for exposure is continuum of wavelengths, but we will assume that it is a discrete array of wavelengths. This allows us to use RCWA, a frequency-domain method, to calculate the

diffraction of each wavelength (FDTD can calculate the diffraction of a continuum pulse, but this comes with its own difficulties).

We start with an incident plane-wave Gaussian pulse, with each frequency given by:[2]

$$\tilde{E}_i(\omega) = \tilde{E}_0 \exp\left(-\left(\frac{\omega - \omega_0}{\sigma^2}\right)^2 \right) \tag{4.2}$$

where ω the angular frequency, ω_0 is the center frequency, and σ describes the pulse width, $\sigma = \frac{FWHM}{2\sqrt{2\ln(2)}}$. We assume no phase variation, so the pulse is chirpless. A basic discussion of RCWA is in chapter 1, but we will assume that for any particular DOE, we can calculate the diffracted waves as a function of the input wave:

$$\tilde{E}_m(\omega) = f_{RCWA}\big(\tilde{E}_i(\omega)\big), \qquad \vec{k}_m(\omega) = f_{RCWA}\big(\tilde{E}_i(\omega)\big) \tag{4.3}$$

where the subscript m differentiates the diffracted orders. This gives a set of planewaves propagating with different wavelengths and directions. The 0,0 diffracted orders will propagate in the same direction and thus will be a planewave pulse. Though this pulse was completely in phase before the DOE, the transmitted orders of the DOE will have a phase shift that varies with wavelength. We have not seen major changes in the pulse due to this, however. The non-zero diffracted orders will exhibit angular dispersion but will still behave very pulse-like near the DOE.

Now we start from the opposite direction, a description of the total dosage from the interference of many pulses. We take the two-photon dosage, D_2, to be proportional to I^2 integrated over time, where I in this case refers to the *instantaneous* intensity, rather than the time-averaged intensity we used in previous chapters.[25] We let:

$$D_2(\vec{r}) \propto \int I^2(\vec{r}, t)dt \tag{4.4}$$

Substituting into equation 4.4 and performing a Riemann sum to make the calculation computable:

$$I(\vec{r}, t) = |E_{tot}(\vec{r}, t)|^2 \tag{4.5}$$

$$D_2(\vec{r}) \propto \int |E_{tot}(\vec{r}, t)|^4 dt \cong \sum_{t_0}^{t_1} |E_{tot}(\vec{r}, t)|^4 \Delta t \tag{4.6}$$

for a sufficiently small Δt. The total instantaneous electric field is simply the sum of each instantaneous electric field over all diffracted orders and wavelengths.

$$E(\vec{r},t) = \sum_{\omega}\sum_{m}\vec{E}_m(\omega,\vec{r},t) = \sum_{\omega}\sum_{m} Re\left(\tilde{E}_m(\omega,\vec{r},t)\right) \tag{4.7}$$

And finally:

$$D_2(\vec{r}) \propto \sum_{t_0}^{t_1}\left|\sum_{\omega}\sum_{m} Re\left(\tilde{E}_m(\omega)\exp\left[i\left(\vec{k}_m(\omega)\cdot\ \vec{r}-\omega t\right)\right]\right)\right|^4 \Delta t \tag{4.8}$$

Equation 4.8 gives use a trivial calculation of the 2-photon dosage in space. Next, we need only make the interior more easily computable. We calculate the interior of the sum in equation 4.8:

$$\tilde{E}_m(\omega)\exp\left[i\left(\vec{k}_m(\omega)\cdot\ \vec{r}-\omega t\right)\right] \tag{4.9}$$

for each m and ω to get the instantaneous electric field component of each frequency and order. We sum across m and ω to get a 4D matrix over space and time and then sum across time.

This procedure is much more computationally intensive than the procedure for CW waves that was shown in Chapter 2, due to the need to compute this over many time steps and to include another set of beams at every frequency. To save on computation time, we try to limit the number of redundant calculations. The most computationally intensive aspect is $\exp\left[i\left(\vec{k}_m(\omega)\cdot\ \vec{r}-\omega t\right)\right]$, which needs to be calculated $N_x\cdot N_y\cdot N_z\cdot N_t\cdot\omega\cdot m$ number of times (N_i is the number of positions along i dimension in the computation region). Fortunately, we can restructure this so it only needs to be calculated $\left(N_x+N_y+N_z+N_t\right)\cdot\omega\cdot m$ number of times.

$$\begin{aligned}&\exp\left[i\left(\vec{k}_m(\omega)\cdot\ \vec{r}-\omega t\right)\right]\\ &= \exp\left[i\left(k_{m,x}(\omega)\,r_x+\ k_{m,y}(\omega)\,r_y+\ k_{m,z}(\omega)\,r_z-\omega t\right)\right]\\ &= \exp\left[i\,k_{m,x}(\omega)\,r_x\right]\cdot\exp\left[i\,k_{m,y}(\omega)\,r_y\right]\cdot\exp\left[i\,k_{m,z}(\omega)\,r_z\right]\cdot\exp[i\,\omega\,t]\end{aligned} \tag{4.10}$$

In the final part of quation 4.10, each exponential function is dependent only on two-variables, either a k-vector component with a 1D position coordinate or a frequency with a time coordinate. This means that the exponential function can be calculated on four sets of linear coordinates and the result can be assembled into a 4D grid that is multiplied by $\tilde{E}_m(\omega)$ and then summed over each ω and m. As a result, a calculation that would naively take a day can be performed in a minute. The Matlab code for this procedure is shown below.

```
function D2_tot = icalc_pulse(E, k, r_limits, num_r_points, t_limits,
      num_t_points)

   %Arguments:
   %E and k contains k and E vectors for every wavelength and order
   %r_limits is the volume in which to do the calculation in microns (of
         the form [xlim-,xlim+; ylim-, ylim+; zlim-, zlim+])
   %num_r_points is the number of points in each dimension: [Nx,Ny,Nz]
   %t_limits is the time domain of the calculation in picoseconds  (pulse
         center is at r=[0,0,0] at t=0)
   %num_t_points is the number of time steps to integrate over

   %Parameters:
   %D2_tot is the two-photon dosage (with arbitrary units)

   c = 2.99e2; %Speed of light in um/ps
   omega = sqrt( sum( k.^2 ,2) ) * c;  %Calculate angular frequency for
         each beam

   %List of all r-coordinates
   xcoord = linspace(r_limits(1,1),r_limits(1,2),num_r_points(1));
   ycoord = linspace(r_limits(2,1),r_limits(2,2),num_r_points(2));
   zcoord = linspace(r_limits(3,1),r_limits(3,2),num_r_points(3));
   tcoord = linspace(t_limits(1),t_limits(2),num_t_points);

   %Allocate arrays for Ex, Ey, Ez values at each x, y, z, t
   E_x_rt_tot =
         zeros(num_r_points(1),num_r_points(2),num_r_points(3),num_t_point
         s);
   E_y_rt_tot =
         zeros(num_r_points(1),num_r_points(2),num_r_points(3),num_t_point
         s);
   E_z_rt_tot =
         zeros(num_r_points(1),num_r_points(2),num_r_points(3),num_t_point
         s);

   %Iterate through each beam
   for bi = 1:size(E,1)
      %Calculate the exp(kx * rx) etc. component for each 1D position
      expi_kx = exp(1i * k(bi,1) * xcoord);
      expi_ky = exp(1i * k(bi,2) * ycoord);
      expi_kz = exp(1i * k(bi,3) * zcoord);
      expi_wt = -1 * exp(1i * omega(bi) * tcoord);

      %Construct 4 grids corresponding to all x, y, z, t coordinates
      [expi_kx_mesh, expi_ky_mesh, expi_kz_mesh, expi_wt_mesh] = ndgrid(
            expi_kx, expi_ky, expi_kz, expi_wt);

      %Calculate exp(i*k*r - w*t) at each coordinate
      expi_rt = expi_kx_mesh .* expi_ky_mesh .* expi_kz_mesh .*
            expi_wt_mesh;

      %Calculate Ex, Ey, and Ez at each coordinate and add to the total
            for all beams
      E_x_rt_tot = E_x_rt_tot + E(bi,1) * expi_rt;
```

```
            E_y_rt_tot = E_y_rt_tot + E(bi,2) * expi_rt;
            E_z_rt_tot = E_z_rt_tot + E(bi,3) * expi_rt;
        end

        %Calculate I^2 at all coordinates
        I2_rt = (real(E_x_rt_tot).^2 + real(E_y_rt_tot).^2 +
              real(E_z_rt_tot).^2).^2;

        %Sum over time
        D2_tot = sum(I2_rt,4);

    end
```

4.4.5. Simulation of Helix Fabricated with Pulse

The code above was used for simulating the structure fabricated using the planned experimental design. Some of the parameters are left as free variables. Tuning of the pulse-length is commonly achieved in Ti:sapphire lasers.[35] In the cavity where the seed is generated, the pulse is sent through a pair of dispersive prisms with knife-edge apertures between them. By positioning the apertures, parts of the spectrum can be cutoff, allowing control over the center wavelength of the pulse and the bandwidth. By setting a smaller bandwidth, there are issues with dispersion of the DOE and pulse-lag, as discussed in section 4.4.4, are lessened. However, smaller bandwidth also means a lower peak power, considerably decreasing the rate of two-photon absorption, so a much longer exposure time is required two achieve the proper dosage.

Simulations that sweep the bandwidth reveal that a 7.5nm bandwidth is sufficiently low for defining the helix structure. The 7.5m bandwidth is quite low, but is achievable. Tests with this bandwidth required a long exposure time, on the order of 20min per sample, but not beyond the realm of practicality for research purposes. **Figure 4.9** below shows the simulated structure of the pore. The pore is seen to be much thinner at the top, indicating a higher fill fraction for the top unit cell at the top of the structure compared to the bottom. This is due to the pulse lag that develops between the zero-order and non-zero-order modes; when the pulse lag is smaller, there is a greater intensity due to the proximity of the pulses in the z-dimension. A helical pore pattern is created up to a depth of 6 unit cells; beyond this point, the fill-fraction is too low, causing undesired connections between adjacent helices to be formed. If the

threshold dosage is decreased to disconnect the pores, then the pores at the top of the helix will start to become closed off.

Figure 4.9. Simulated cross-section of helical pores created with the planned PnP design with a 7.5nm FWHM pulse proceeding from the left side. The simulation region is a single unit cell wide and 6 unit cells tall. The plotted surface is an isodose surface at a limit chosen to maximize the depth at which a helix structure is maintained.

4.5. Simulation of Optical Properties of Helical Structure

Just as more rigorous calculations of the exposure of helix pattern are helpful for finding the limitations and requirements of the fabrication method, it is helpful to perform a more rigorous simulation of the optical properties of the planned metallic helix. When the concept of a metallic helix was introduced at the beginning of Chapter 4, a plot of the transmission and reflection of circularly polarized light was shown in **Figure 4.3d**, but this was an oversimplification. Now let us dive into the details of the simulated optics of this helix structure.

A unit cell of a perfect helix array is shown in **Figure 4.10a**. This structure was used to optimize a DOE for the fabrication of an array of helices, of which the most successful pattern is shown in **Figure 4.10b**. Although these two patterns share the same connectivity, the designed helix shows major differences, notably wire thickness and outer radius. The designed helix breaks some of the symmetries of the perfect helix. To investigate the effect of this difference on their optical properties, we perform FDTD simulations of the circularly polarized transmission through each.[36] To ensure a realistic simulation, the designed helix pattern was broken into a fine grid of voxels and each voxel was individually added to Lumerical, an FDTD simulation application; this technique gave much more reasonable results than the standard "n,k import" procedure which assumes a non-dispersive medium. The results are shown in **Figure 4.10cd**. We see considerable differences between the two sets of transmission spectra. The designed helix has a considerably narrower band of circular dichroism and switches the direction of circular dichroism below 2μm. We also see that there is a difference between the direction of incidence for the designed helix but not the perfect helix. This is due the changes in

the shape of the wire breaking a rotational symmetry of the helix. The perfect helix has a 2-fold symmetry around the x and y axes, but the designed helix will have bumps and thin spots, etc. in the wrong order after this rotation. This results in a difference in transmission depending the direction of incidence.

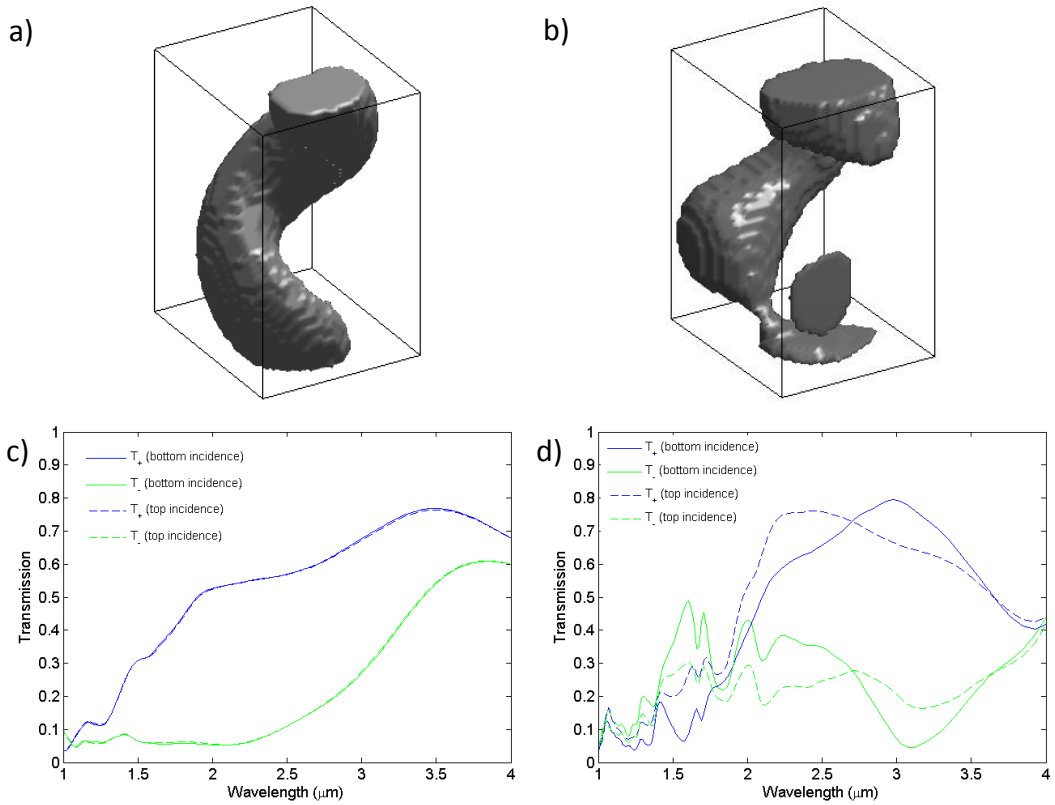

Figure 4.10. Simulation of perfect and designed helix patterns. a) Unit cell of perfect helix used for optimization and naïve simulations. b) Unit cell of helix expected from PnP design. c, d) Simulated transmission spectra of circular polarized light for a perfect helix array (5 unit cells deep) and expected helix array, respectively. Blue lines indicate transmission of RCP light and green indicated LCP light. Solids lines are for transmission from bottom to top and dashed lines are for transmission from top to bottom.

One might be inclined to be surprised by the transmission spectra varying depending on the direction of incidence. Lorentz reciprocity requires that a material transmit light equally in both directions and there has been significant recent work on non-reciprocal optical media.[37], [38] However, we should not get too excited by the idea that our defects have introduced non-reciprocity into our material. Time-reversal symmetry of electromagnetics tells us that any linear material must exhibit Lorentz reciprocity and our structure is composed only of linear media.[37] Our material, as it turns out is non-reciprocal only in the same way that a

combination of waveplate and polarizer is non-reciprocal, which is known to not violate time-reversal symmetry.[37] The common notion of a directionally variant transmission meaning non-reciprocity applies for certain symmetries. For a better understanding of the optics here, we investigate the Jones matrix description of the material.

In the FDTD transmission simulations, we decompose the transmitted and reflected light into its constituent right-handed and left-handed polarizations. The spectra for reflection and transmission of each polarization are plotted in **Figure 4.11**. These plots show that talking about these structures simply in terms of the transmission of circularly polarized light is an oversimplification. The designed helix array does not just absorb or transmit light of each polarization – it converts one polarization to another. This conversion is called 'cross-talk' and appears due to linear anisotropy in the structure which is not present in the perfect helix.[2] The existence of linear anisotropy was always clear due to the simulated structure lacking symmetry in the x and y directions, but it was not obvious how large of an effect it would be until calculated.

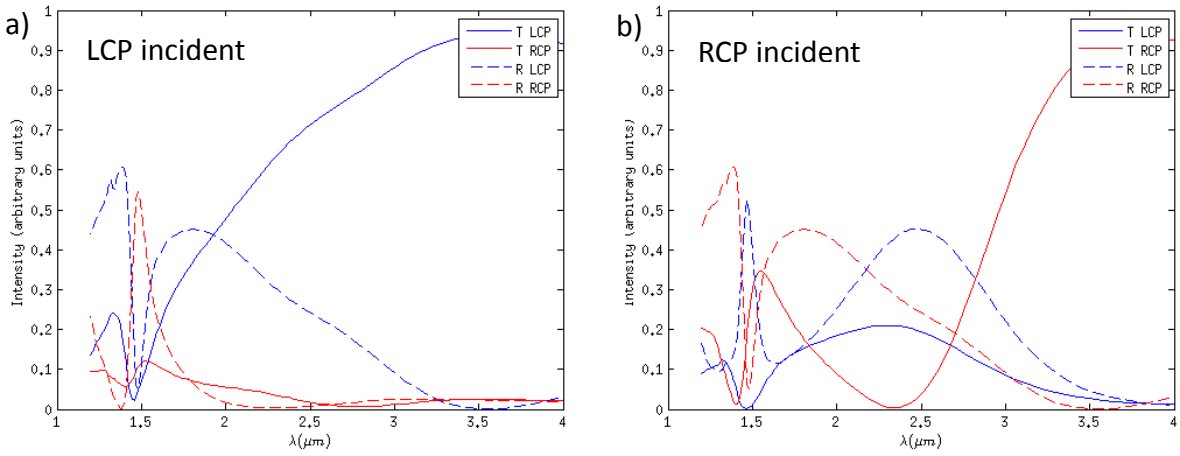

Figure 4.11. Reflection and transmission spectra of LCP and RCP light for the designed helical array with (a) LCP and (b) RCP light incident upon it.

This cross-talk is not purely beneficial or detrimental. In **Fig 4.11b**, on can see that that a considerable amount of RCP light converted into LCP light, which is additional efficiency when one wants max transmission of LCP and minimum transmission of RCP. However, if one instead

wants to use the circular polarizer to measure the magnitude of only the LCP component in a beam of light, conversion of RCP into LCP will increase the error of the result.

Another interesting characteristic is that the LCP reflectance for LCP incidence is identical to the RCP reflectance for RCP incidence. This is due to the polarization conversion of the light. Circularly polarized light reverses its polarization on reflection from a uniform medium.[2] Thus, the reflection of light with the same handedness is due to cross-talk. Due to time reversal symmetry and Green's theorem, conversion of the cross-talk of one mode into another mode in reflection must be equal to reverse case. If these spectra were not identical, this actually would indicate non-reciprocality. The lack of such a difference verifies that the material has Lorentz reciprocity.[37]

It has been said that these metallic helix arrays could become negative refractive index effective optical medium.[39] In fact, this was part of the motivation of this work. In this thesis we will not go into the question of whether there can be negative phase velocities in this material, due to the difficulty in defining phase for light propagating in such a medium.[40] However, it should be said that the metallic helix array causes some difficulties when modelling as an effective index medium. As discussed in section 1.4, an effective index medium denotes the counterfactual treatment of an optical composite structure as though it were a medium with a uniform refractive index. Recently, there has been a great deal of work on identifying structures that function as effective index media with a negative refractive index.[41] Many metal-dielectric composites have been found to have these properties. For the metallic helix structure, however, there are major problems with treating it as a negative refractive index model. If two films of effective index media are stacked on top of eachother, they should be able to be treated as a single block with the same index and twice the height.[2] However, for the metallic helix, this is simply not true. As explained in Section 4.2.1, if two metallic helix films are stacked, the spectrum of circular dichroism will expand because new, lower frequency modes can couple with the helix and become absorbed. This is distinct from the response expected from uniform media. Secondly, according to Lorentz reciprocity, a film with a uniform refractive index must have equal transmission in either direction.[37] As seen, this is not the

case with the designed helix; just as a combination of waveplate and polarizer with offset angles cannot be treated as an effective index medium,[37] neither can this helix.

4.5.1. Design of Circular Polarizer with Optical Objective Function

The above simulations of the optical response of the designed helix compared to an ideal helix bring to light some of the limitations inherent to the 'volumetric-match' objective function. The designed helix had an over 90% volumetric match with the ideal helix, but the simulated performance was not nearly as good. This motivates a different method for optimizing designs for broadband circular polarizers. Instead of optimizing PnP parameters in order to maximize the volumetric match with a targeted structure, we started optimizing according to the structure's simulated optical properties. The fitness function of the optimization procedure was changed so that for each candidate structure, RCWA would be performed for the candidate DOE and incident polarization to generate the resulting structure of a circular polarizer. Then, FDTD simulations would be performed for this candidate structure and the transmission of each polarization would be calculated and compared. The fitness was a combination of two factors: the ratio of integrated RCP to integrated LCP transmission over a broad spectrum, and the total RCP transmission. Without including the total RCP transmission, the optimized structures would have T_{LCP}/T_{RCP} as several orders of magnitude but with both transmissions being very low, e.g. 10^{-5} and 10^{-9}. The weight of these two factors was adjusted until the optimized structures had a good balance of contrast to total transmission. This fitness function requires two full-wave simulations for every structure and so is much slower compared to the volumetric match fitness function. However, it may uncover designs that are superior to the helix design.

An advantage of a method of optimizes for an optical parameter instead of a structural fit is that it can design highly effective structures that a human would not think of. The best circular polarizer that meets the fabricability requirements might not have the kind of symmetries that people may expect. We encountered this exact scenario. **Figure 4.12** shows the best design generated using this method. **Figure 4.12d** shows a unit cell of the structure, which we call 'pseudo-omega' due to the faint similarity with the repeated omega structure

previously studied as a circular polarizer.[42] It should be made clear that this pseudo-omega has a very different connectivity and operates very differently from the omega structure. The pseudo-omega structure you see below actually does not repeat in the z-dimension; the structure is actually just a piece of the unit cell of the PnP dimensions. Using the entire unit cell would greatly diminish the transmission through the structure.

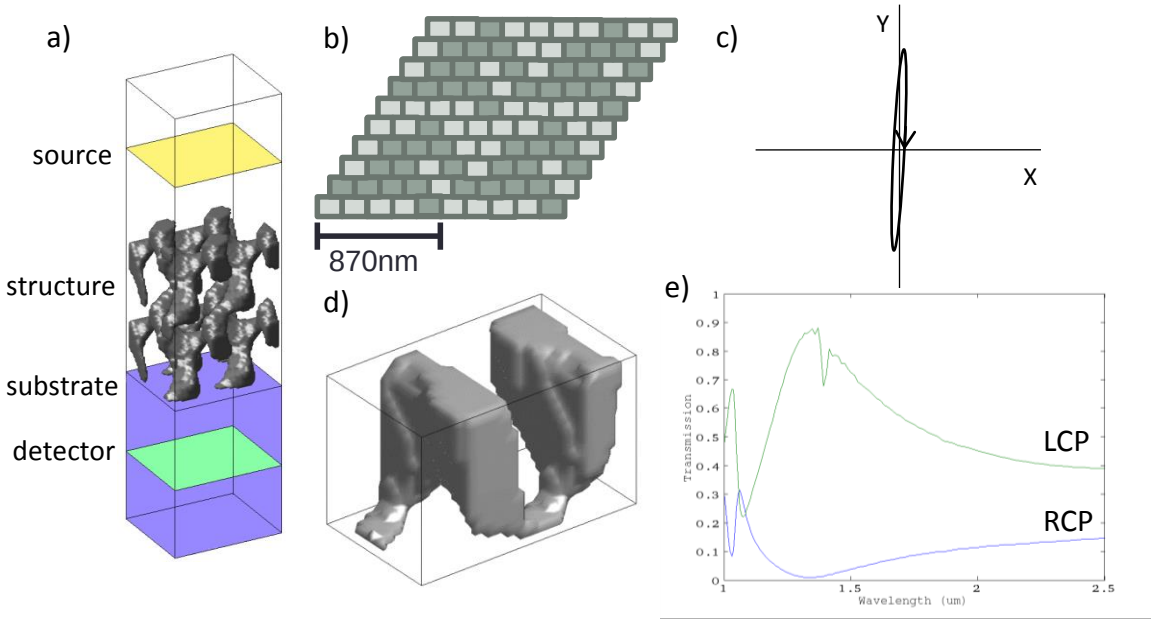

Figure 4.12. a) Cartoon of the FDTD simulation setup used in the fitness function with an example poorly polarizing structure. b) 4 unit cells of the DOE for the optimized pseudo-omega helix. c) The polarization of the light needed for the PnP process. d) Single unit cell of the pseudo-omega structure. e) IR transmission spectrum of LCP (green) and RCP (blue) light through the pseudo-omega structure.

The pseudo-omega structure adds a new fabrication challenge compared to the helix due to the fact that the structure does not repeat in z. The exact position in z needs to be precisely controlled. This position in z is determined by the relative phase of the central and side beams which is determined by the position of the DOE. The thickness of the photoresist between the substrate and DOE can be set by manipulating the spincoating and imprint processes, so the position of the lower boundary of the element can be feasibly controlled. The upper boundary is a dependent upon the electrodeposition process. As long is the electrodeposition process is highly repeatable, the optimum deposition conditions to achieve the exact deposition thickness should be achievable. Note that for this structure is more

resistant to the effects of backside reflection and would be amenable to fabrication on an ITO substrate, so it could be electrodeposited unlike the helix structure.

This new design also has some advantages in terms of fabricatability. One thing we have not yet discussed is our capability of tuning the dosage close enough to the ideal value to define the structure we want. How close do we need to be to the ideal exposure conditions? We find the highest and lowest doses that still achieve the appropriate connectivity in order to see how much leeway we have in dosage. Any real laser system is going to have some variation in its operation; if this variability exceeds the tolerance in the exposure process, the failure rate will become very high. **Figure 4.13** shows histograms of the intensity across the unit cell of each design. The acceptable values of the threshold intensity (represented by the red regions) is very small for the helix pattern. The tolerance for the threshold intensity is 2%, meaning that if our dosage is 1% too high or too low, the structure will be overexposed or underexposed. The pseudo-omega on the other hand has a much wider tolerance in dosage: the threshold can be off by over 6% before there is a problem.

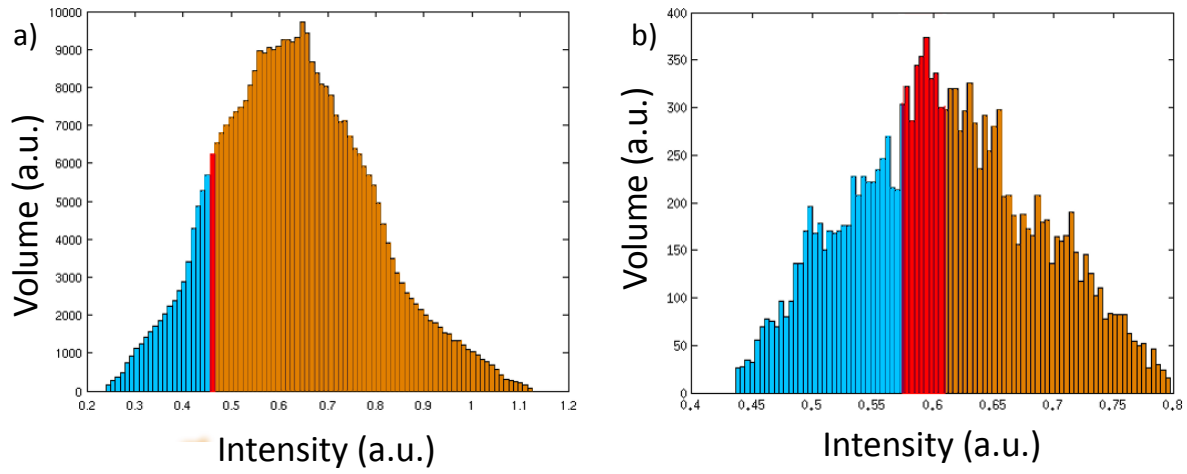

Figure 4.13. Histograms of the volume at each intensity for a) the helix design and b) the pseudo-omega design. The brown region on the right represents the volume of the unit cell that must be above the threshold intensity and the blue region on the left represents the volume that must be below the threshold intensity in order to create the designed structure. The red region in the middle represents the volume that is allowed to be filled or void and its width is the acceptable range of the threshold intensity.

4.6. Metallization of PnP templates

The exposure process creates a photoresist template with a complex structure, but in order to show circular dichroism we need to convert the photoresist-air structure into a silver-air structure. The plan to do this by depositing silver into the pores either by electrodeposition or electroless deposition followed ashing of the photoresist. Producing a uniform silver filling or conformal coating in the porous templates was challenging with conventional techniques. Here discuss the issues of metallization of these templates and how they were addressed.

4.6.1. Electrodeposition

Electrodeposition was performed using a silver succinimide-based electrodeposition solution (Silver Cyless II from Technic Inc.) using an Ag/AgCl reference electrode.[43] Pulses with a 1% duty cycle with a -1.7V on-state and 0V off-state were used to ensure uniform deposition.[44], [45]

Initially, there was difficulty in getting a dense nucleation on the ITO substrate. This could be resolved by depositing a thin film (2nm) of silver onto the ITO using electron-beam PVD before spincoating the resist. A film of silver, even this thin, does affect the interference pattern. Fortunately, the silver can be temporarily made transparent by oxidizing it in an O_2 plasma asher.[46] The silver oxide that forms is not entirely transparent, but a 2nm film has sufficiently low reflectance that it can be ignored. The silver oxide is simply reduced back into its metallic form during the electrodeposition process – no extra step is required.[47]

Cross-sections of the a 4-beam template infilled with silver are shown in **Figure 4.14**. Here, the SU-8 has not been removed, and is partially transparent under SEM. The electrodeposition can be seen to be uniform and absent of voids.

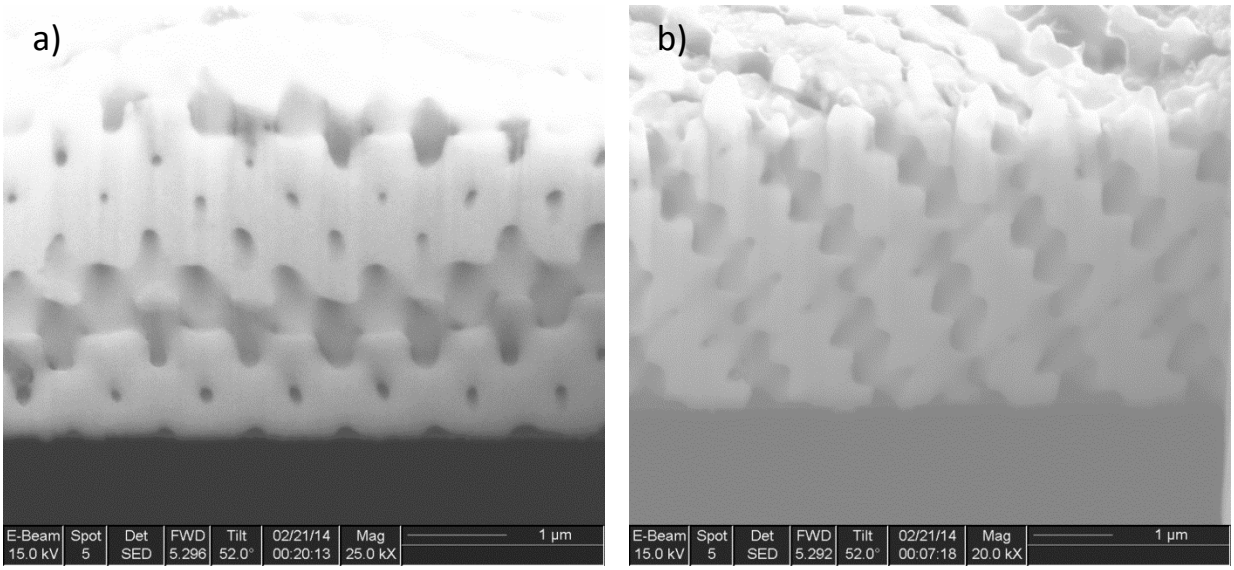

Figure 4.14. SEM cross-sections of silver electrodeposited in an SU-8 template defined with a 4-beam setup.

4.6.2. Electroless Deposition.

Due to the impossibility of using transparent conductive oxides for structure sensitive to backside reflections, we need to use change or silver deposition technique that does not require a current. Electroless deposition lets us deposit silver using a redox reaction without a current. The most studied method of silver electroless deposition is Tollen's method.[48] This consists of mixing $AgNO_3(NH_3)_2$, called Tollen's reagent, with a reducer which react to produce metallic silver. Tollen's method is famously used for determining whether a solution contains an aldehyde or similar functional groups and here we use glucose (an aldehyde) as the reducing agent.[49] While this method is widely used, it is not really well understood: many papers investigating reaction rates with Tollen's reagent contradict eachother.[43], [50], [51] Part of an issue is that the production method is not clearly defined. Frequently, the exact quantities or proportions used are not stated and when preparing Tollen's reagent, practitioners have the choice of using both ammonia and silver nitrate or just ammonia by itself, and also have the choice of not describing which method they used.[43], [52]

A saturated AgNO3 solution was prepared in a 1 to 2 ratio of saturated ammonia to deionized water solution. The supernatant was diluted by 1/30, making or "A" component of Tollen's reagent. 1.4mM α-D-glucose was used as a reducing agent, the "B" component. A pre-

treated SU-8 template (surface treatments will be described later in this section) was placed in a 1mL bath of the A component and held in an oven at 85°C. Every few hours a drop of the B solution was added and the solution was returned to the oven. It is believed that very slow adding of reducer improves the uniformity of the silver coating by ensuring that the reaction rate is slower than the diffusion of the silver ions through the pores of the template.

There are challenges in electroless deposition on polymer substrates.[51] We need to deposit on an SU8 surface which is not directly very amenable to silver, so modifying the chemistry of the SU8 surface was necessary. One successful method for depositing silver on SU8 involved using oxygen plasma on the SU8 structure to introduce aldehyde groups onto the surface of the SU8.[52] The aldehyde groups on the surface acted as reducing agents for Tollen's reagent, forming a dense seed layer for further deposition. They showed that this technique worked well enough to fabricate plasmonic optical elements that operate in the NIR, which suggests it to be a good starting point for our work on electroless deposition. We found this techniques works well for the top surface of our structure, but not within the pores. We believe this is due to difficulty in forming an energetic plasma within the pores; our patterns were highly tortuous with pore sizes of a few hundred nanometers or smaller, so considerable energy loss from the collisions with the template are expected, which would make it difficult to sustain a plasma. We primarily used 4-beam structures described in chapter 2 for these electroless deposition tests due to ease of fabrication. The designed helix template that we need the electroless deposition has much smaller pores, reaching 50nm at its narrowest, so any issues with pores size would be much worse for the helix design. Ozone was also attempted for treating the surface, but this yielded the same issues we found with plasma. This led us to pursue a wet chemical technique for surface treatment of the SU8.

One of the most critical aspects of electroless deposition in our templates is nucleation density, since conformal coating of the helix structure would reach pinch-off at only about 25nm of deposition due the pore diameter dropping to about 50nm at its narrowest. In this case, we need a conformal coating of the SU-8 structure before we reach 25nm of deposition. Most of our studies with electroless deposition included only a very short deposition time so that we can see the nucleation density.

We tried several methods for modifying the surface of the SU8 to make it amenable for silver deposition, but here we will only discuss the most successful two. The first is a 'gentle' piranha treatment. Piranha is a mixture of H_2O_2 and H_2SO_4 that is often used for cleaning glass substrates due to its aggressive breaking apart of a wide variety of organic materials. Piranha has been used for surface treatment of glass to encourage electroless deposition.[53] It is one of the few reliable methods of removing SU8. In this case, we attempt not to remove the organic template, but to chemically modify it. Piranha is known to be very effective at changing surface chemistry: for glass substrates, it leaves hydroxylated surfaces.[54] For polymers that it has not yet had the chance to completely remove, it leaves alcohols, ketones, and aldehydes.[55], [56] While we cannot precisely control the surface, a high density of reactive functional groups are expected. Due to the aggressive nature of the piranha etch, we need a very light touch in order to treat the surface of the SU8, but not to etch it. We used a solution of piranha with a lower concentration of H_2O_2 with the commercial name Nano-Strip. The temperature was tuned via hot plate so that SU8 samples could be held in the solution without deteriorating. The SU8 template was held in the Nano-Strip for 30s and immediately placed in water. Following this, the samples were well rinsed and electroless deposition was performed using the above technique. An example of results using this technique can be seen in seen in **Figure 4.15.** One can see that there is deposition throughout the depth of the lattice, indicating that wet chemical technique was successful in surface treating the SU8 deep within the pores. However, this treatment technique was very challenging to repeat. Frequently, the treatment did not lead to a high nucleation density or, on the other hand, led to the complete removal of the template, even with what appeared to be the exact same method. Given the difficulties in fabricating a helical template to begin with, we did not want to use a method that has a high risk of completely destroying templates. This led us to pursue more selective chemical treatments.

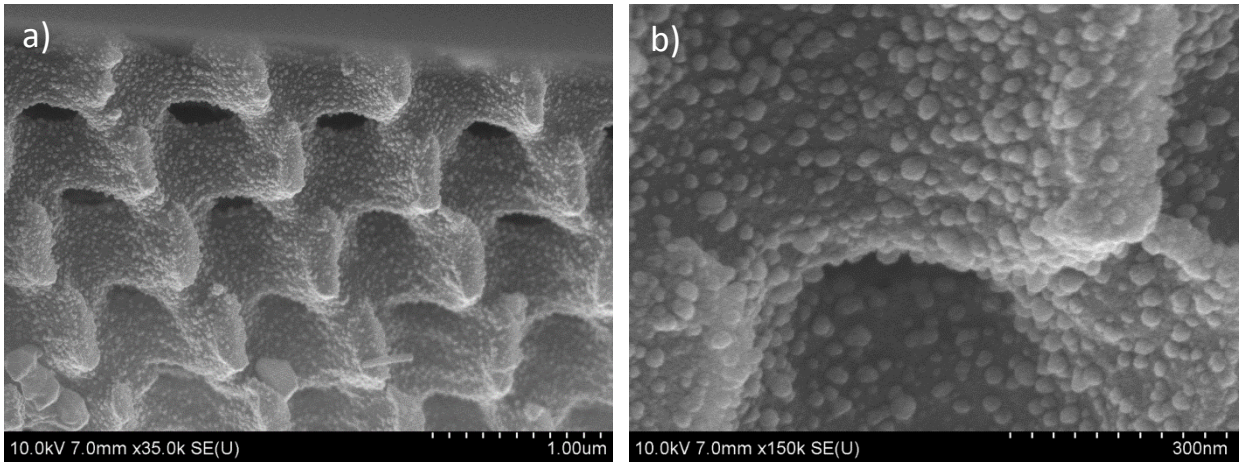

Figure 4.15. SEM cross-section of a 4-beam lattice treated with a low temperature piranha treatment followed by silver electroless deposition.

A method of introducing aldehyde groups onto the surface of SU8 without risking complete decay of the structure is Jones oxidation.[57] Jones oxidation is performed with Jones reagent, a solution of CrO2 and H2SO4 in acetone, and aggressively converts secondary alcohols into ketones and primary alcohols into aldehydes. A schematic of the full SU8 treatment process is shown in **Figure 4.16**. SU8 is an oligomer with approximately eight epoxide functional groups.[23] Each epoxide reacts with an acid to produce a radical that can form crosslinks with other epoxide groups. In water, and especially acid, the epoxide ring opens to form two alcohols, one primary and one secondary.[58] Jones reagent is then used to oxidize the primary and secondary alcohols into a carboxylic acid and a ketone respectively. Carboxylic acids are known to form bonds with silver ions.[59] Taken together, the ketone and acid group is very similar to oxalic acid, which forms the low solubility silver oxalate salt.[60] We believe this treatment to form a relatively high density of silver ions at the SU8 surface and create an effective seed layer for silver deposition.

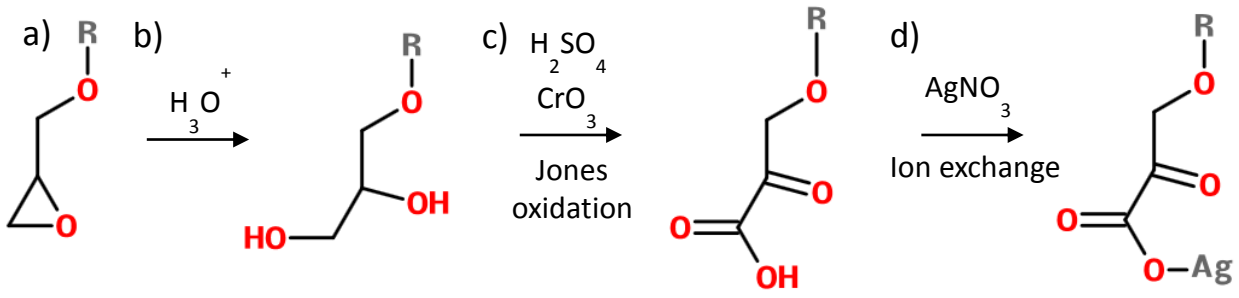

Figure 4.16. Schematic of the Jones oxidation-based surface treatment of SU8. a) One of the epoxide groups of uncrosslinked SU8. b) Ring-opening of the epoxide from exposure to acid. c) Jones oxidation of the primary and secondary alcohols. d) Ion exchange with silver nitrate and the carboxylic acid group.

The 4-beam SU8 templates were held in 1mM HCl to ensure complete ring-opening of the epoxide groups. After this treatment, the SU8 was found to be much more hydrophilic. It is likely that this particular step is unnecessary, as the Jones reagent has a very low pH and should open the rings, but it is unlikely to do any harm. Jones reagent was prepared with 2.67M CrO_3 and 3M H_2SO_4.[61] The SU8 templates were bathed in this solution overnight. Note that Jones Reagent is quite dangerous. You should ensure that you are well informed of the risks and proper safety procedures before working with it. The Jones oxidized templates were bathed in a saturated silver nitrate solution overnight at 85°C to form the seed layer. Afterwards, the template was treated with the same electroless deposition technique described before.

This method was successful in nucleating silver deposition on the surface of the SU-8 without risking degradation or destruction of the structure. SEM cross-sections are shown in **Figure 4.17**. In **Figure 4.17a** relatively high density of silver nucleation sites can be seen, but not as high of a density as was seen using the soft piranha etch. It was expected that a high nucleation density would lead to growth of a uniform film. **Figure 4.17b** shows that this is not necessarily the case. In this case, a higher concentration of glucose was used so that there would be faster growth of silver, so that it would not take weeks to create a substantial silver film. This has apparently led to a much more heterogeneous deposition. More work is needed to identify a method for uniform electroless deposition in a porous SU8 film.

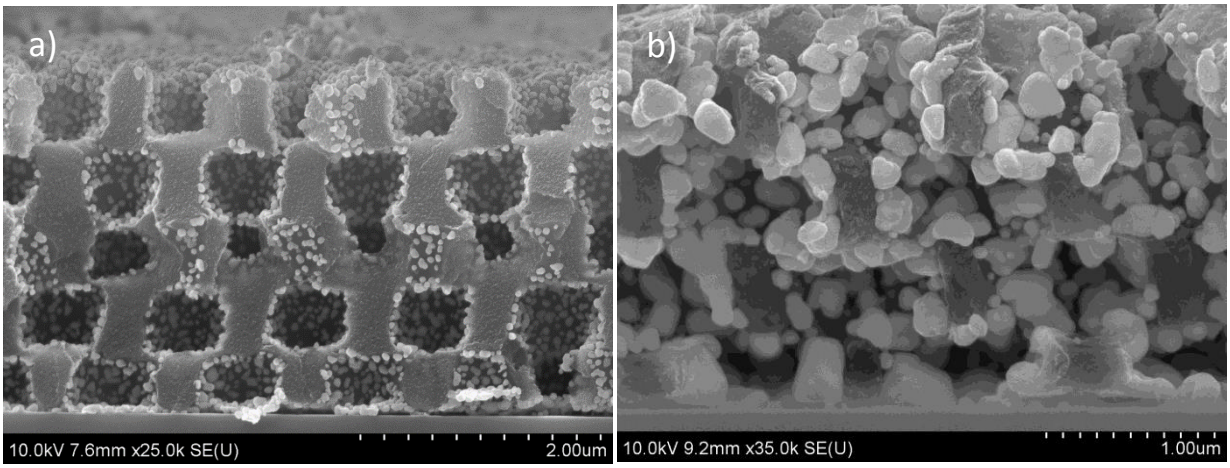

Figure 4.17. SEM cross-sections of silver electroless deposited samples following Jones oxidation treatment for a) low and b) high concentrations of glucose.

There was significant progress in identifying a silver electroless deposition for SU8 structures that are not amenable to O_2 plasma surface treatment. However, the nucleation deposition and uniformity is still too low to use this for the fabrication of the desired metallic helix. At this point, we will turn our focus to more fundamental problems with the helix design.

4.7. Stochastic Modeling of Interference Lithography

This section describes the development of a more rigorous model of the lithography process that we use to determine whether a particular design is reasonable. It is important that our simulations appropriately model important aspects of the lithography process, especially when dealing with structures that push the limitations of lithography. In particular we discuss concentration fluctuations and shot noise applied to the interference lithography process.

Our earlier model of interference lithography made major assumptions that we should look at in more detail. I have not seen an interference lithography paper has not implicitly made these same assumptions or has questioned whether they are appropriate to make, though there is some literature on these effects in EUV lithography.[62], [63] Essentially, the photoresist was assumed to be insoluble if the local light intensity is greater than a threshold intensity ($I(\vec{r}) > I_{threshold}$) and soluble otherwise ($I > I_{threshold}$). It turns out that this assumption is nearly always adequate for fabricating structure via interference lithography – the feature sizes are sufficiently large that these sources of noise are minimal. However, the

helix and pseudo-omega designs are exceptions to this rule. In these cases, the exposure is more complicated and is significantly affected by two sources of noise.

The first source of noise is concentration fluctuations of the photoacid generator. Conventionally, the photoresist is treated as a uniform, continuous medium. In the case of SU8 (and most other photoresists), the resist is actually a mixture of a photoacid generator and a resin (as well as some stabilizer, which will be ignored here). A common misconception is that a mixture that is well-mixed must have a uniform concentration of each component and concentration is treated as a continuous variable. The resin is in fact made of up of molecules with a discrete quantity and a particular position, and their actual distribution is governed by the laws of thermodynamics. The assumption of continuous, uniform concentration works well when dealing with high concentrations and volumes, but breaks down when dealing with low molecular counts for a particular component. In these cases, one must look at the local concentration for a particular volume of space rather than the average concentration of the whole solution. Different volumes will have different local concentrations at different positions in time and space; these are called concentration fluctuations and must exist at any non-zero temperature.[64] These concentration fluctuations in the photoacid generator will lead to "noise" in the local concentration of photoacid generators that are activated by light exposure. These, in turn, will lead to noise in the concentration of SU8 crosslinks and thus noise in the definition of the final structure.

The second source of noise is shot noise.[2] You'll most often hear shot noise in reference to electronics, where something we usually consider as a continuous quantity, current, shows stochastic behavior due to charge carriers being discrete: the charge carriers will arrive at intervals given by the Poisson distribution, giving rise to current fluctuations. Shot noise also refers to optical processes, such as photons being absorbed by a photon counter. Here, we can consider the PAG as a kind of photon counter with the limitation that it can count only a single photon and signals this by releasing a photoacid. Shot noise combines with the noise from the concentration fluctuations.

These kinds of noise have been studied before for EUV (extreme ultraviolet) lithography.[62], [63] However, these studies had a somewhat different goal in mind. In EUV

lithography, one of the biggest obstacles is reaching the threshold dosage in an economical way, since the process of making high power x-ray sources is very expensive and imaging optics that work with x-rays are very lossy. Researches developed these more rigorous exposure models in order to predict what is the minimum dosage required to sufficiently dose the resist. Here, we have a different goal. High power green sources are relatively cheap (though for a 2-photon process getting a high I^2 can be a challenge) and minimizing the exposure time for a technique that is far from being commercialized is not a high priority. The biggest obstacle is not power, but contrast. Even though high contrast resists like SU-8 are effective at resolving low contrast structures, there must be a limit to what can be resolved. We would like to determine whether a particular pattern is possible *at all*, and if it is, to provide us with estimates of the necessary PAG concentration and exposure dosage.

We find that our helix design is one such case in which we need to take into account these concentration fluctuations. We will first go through a revised model for interference lithography with concentration fluctuations and then apply it to our designs. The basic procedure for our model is to 1) create a trial distribution of photoacid generator within a unit cell of the pattern, 2) calculate the light intensity as usual, 3) create a trial distribution of photoactivated PAG based on the local intensity and local PAG concentration, and 4) simulate the kinetics of diffusion and the crosslinking reaction based on SU8 kinetics studies.

4.7.1. Calculation of Concentration Fluctuations

First, we need to calculate the local concentration of the photoacid generator. For a chemical dissolved in a solution (as the PAG is in SU8), each molecule will engage in something of a random walk. For SU-8 room temperature is below the glass transition temperature, so diffusivity of the large PAG molecules will be very low, leading the distribution to be in a "snapshot" state. To model this quantitatively, we need to make a few assumptions about how the PAG interacts with itself and the resist.

The first assumption is that there is no volume-exclusion for the PAG. That is to say, a PAG molecule takes up no space and thus does not inhibit the presence of more molecules. In reality, two molecules of PAG cannot exist in the same spot. This effect could be accounted for

by incorporating a hard-sphere model for the molecule, which provides a minimum distance that can separate the molecules. If molecules are thought to be added to a region one-by-one, each additional molecule would reduce the amount of places that another molecule could be placed. Such a model would have a lower entropy compared to volumeless model and would have a tendency to 'even out' the concentration fluctuations between regions of space. However, the volumetric density of the PAG in SU8 is approximately 1% and so we assume the mathematically simpler and computationally quicker volumeless model to be sufficient for estimating distributions of local concentrations.

The second assumption is that there is no enthalpy of mixing between the PAG and SU8. The enthalpy of the mixture is assumed to be simply the linear combination of its constituents. We know that this is inaccurate. We find that phase separation of the PAG-SU8 mixture occurs at around 5% w/w PAG. The phase separation is driven by the lower enthalpy of the PAG in proximity to other PAG and SU8 near SU8 relative to the enthalpy of the mixed species. This assumption has an effect in the opposite direction of the first assumption. If a single PAG molecule were added to the solution one at a time, each molecule would prefer being in a region in which there is a high number of PAG molecules already. Unfortunately, we were unable to find any literature that would let us develop a decent estimate of the strength of the intermolecular reactions. It was decided it would not be worth the work to develop even a rough estimate. So we assumed that the components would mix only according to positional entropy.

Combining these assumptions, we end up with a result much like an ideal gas, with each PAG molecule having a position completely independent of one another. This has the advantage of being easy to calculate. It is important that the distribution of PAG be computationally efficient, since there are millions of PAG molecules within a single unit cell of the lattice. We divide a unit cell into many tiny voxels and calculate a trial number of PAG within each voxel. The distribution of the number of PAG within each voxel is given by a binomial distribution with n as the number of PAG molecules to add to a large region and p is the probability of each molecule arriving in the voxel (equal the ratio of the volume of the voxel to the volume of the large region). This is a case of the binomial distribution where the

probability of each trial being a success is very small, but the number of trials is very small. The probability of a voxel having n molecules is given by:

$$P(n\ PAG\ molecules\ in\ volume\ v) = \frac{(\rho\ v)^n e^{-\rho\ v}}{n!} \tag{4.11}$$

In this case, we can approximate this distribution as a Poisson distribution. Here, the interval of the Poisson distribution is simply given by $\lambda = n\ p$. A rule of thumb for the accuracy of approximating a binomial with a Poisson distribution is that λ be less than 10. If, as sometimes happens, the simulation we wish to perform has $\lambda > 10$ then we can simply divide each voxel into smaller pieces when distributing the PAG to ensure a very low value of λ, then recombine them afterward. The Matlab code used to calculate a trial PAG concentration distribution is shown below.

```
function PAGcountReduced = distributePAG( numPAG, Nvoxels )
%Creates a trial Poisson distribution of PAG molecules within a unit cell of the
    simulated structure
%Arguments:
%numPAG is scalar.  The expected number of PAG molecules within a unit cell
%Nvoxels is an integer 3-vector, [Nx, Ny, Nz].  The number of cells that the unit
    cell is broken into in the x, y, and z dimensions
%Parameters:
%PAGdist is an integer matrix with size [Nx, Ny, Nz].  The value at each position is
    the trial number of PAG within the volume of the voxel represented by that
    position.

    %Divide into smaller cells
    %First calculate how many pieces to divide the cell into
    LambdaNaive = numPAG / prod(Nvoxels);
    NsubVoxels = ceil(lambdaNaive / 10);
    %Create a 4D matrix where the 4th dimension is the number of pieces to
        subdivie each voxel into.  If no subdivision is necessary, the size in this
        dimension is simply 1.
    NsubVoxels = [Nvoxels(1), Nvoxels(2), Nvoxels(3), Nsubvoxels];
    %Recalculate Lambda
    PoissonLambda = numPAG / prox(NsubVoxels);
    %Calculate trials of number of PAG within each sub-voxel
    PAGcount = poissrnd( PoissonLambda, NsubVoxels);
    %Combine sub-voxels into the original voxels
    PAGcountReduced = sum(PAGcount, 4);
end
```

Once the PAG distribution is calculated, we calculate the intensity of the interference pattern and create a trial distribution of the PAG that become activated and initiate polymerization of the SU8. During exposure, we assume no diffusion of the PAG because the SU8 is below its glassy transition temperature; during the post-bake process, however, this diffusion will be very important.

4.7.2. Calculation of Shot Noise

Next, we need to calculate the number of PAG molecules in each voxel that absorb a photon and release an acid during exposure. This is a stochastic process and the frequency of absorption events is strongly affected by shot noise when considering a low number of absorption events. The probability of absorption is linearly dependent on the optical intensity, but due to the nature of absorption being a stochastic process, a region with a high optical intensity can lead to a lower number of absorption events than a region with lower optical intensity.[62] The probability of any particular photon getting absorbed by a particular molecule is very low, so we can consider the probability of a particular PAG molecule absorbing a photon as given by the Poisson distribution. However, in order to calculate the number of PAG molecules that activate in a particular voxel, we need to use a binomial distribution, since the probability of a particular PAG molecule becoming activated should be quite large in regions that we want to crosslink and become solid.

The probability of a PAG molecule absorbing at least one photon is given in equation 4.12 below,

$$p_{activated} = 1 - e^{-\frac{\gamma \Phi I t_{exposure}}{E_{photon}}} \tag{4.12}$$

where γ is the absorption cross-section of the PAG, Φ is the quantum yield of the PAG, $t_{exposure}$ is the exposure time, and E_{photon} is the photon energy. The intensity and exposure time can be controlled with laser parameters and the photon energy predetermined by our choice of laser. The absorption cross-section and quantum yield are characteristics of the

absorbing medium, and will need to be measured in order to know what dose ($I\ t_{exposure}$) is optimum. This measurement will be discussed in Section 4.5.3.

Assuming that the all of the parameters are known, it is easy to calculate a trial of the number of activated PAG. First, we calculate the probability of a particular PAG being activated with each particular voxel, which is simply the repeated application of equation 4.12 for each voxel. From here, we perform a binomial experiment for each voxel, with the well known probability distribution given by:

$$P(n) = \binom{N}{n} p^k\ (1-p)^{N-n} \tag{4.13}$$

where N is the total number of PAG molecule within that voxel, p is the probability of any particular molecule become activated (given by equation 4.12), and n is the number of activated PAG. Matlab code for performing these calculations is shown below.

```
function excitedPAGcount = excitePAG(intensity, tExposure, PAGcount,
    gammaPhiProduct, Ephoton)
%Performs a trial exposure, calculating the number of activated PAG molecules
    within each voxel.
%Arguments:
%intensity is a real matrix with size [Nx, Ny, Nz].  The intensity at the the center
    of each voxel in units W/m^2
%tExposure is a real scalar.  The exposure time in seconds.
%PAGcount is an integer matrix with size [Nx, Ny, Nz].  The number of PAG
    molecules within each voxel.  Must be the same size as intensity.
%gammaPhiProduct is a real scalar.  The product of Phi, the quantum yield of the
    PAG (unitless),  and gamma, the absorption cross-section (nm^2/molecule).
%Ephoton is a real scalar.  The energy of the incident light in J/photon.
%Parameters:
%excitedPAGcount is an integer matrix with size [Nx, Ny, Nz].

    %Calculate the probability of activating a single PAG molecule for each voxel
    pActivation = 1 - exp( -1 .* gammaPhiProduct .* intensity .* tExposure ./
        (Ephoton.*1e-18) );

    %Initialize matrix holding the number of PAG with same size as intensity
    N = size(intensity);
    excitedPAGcount = zeros(N);

    for i_x = 1:N(1)
        for i_y = 1:N(2)
```

```
            for i_z = 1:N(3)
                %Binomial distribution to give # of excited acid in each volume
                excitedPAGcount(i_x,i_y,i_z) = binornd( PAGcount(i_x,i_y,i_z),
                    pActivation(i_x,i_y,i_z) );
            end
        end
    end
end
```

4.7.3. Example Simulation of Noise

Before we get into the reaction-diffusion aspects of this models, let's look a simple example of noise arising from concentration fluctuations. Below, in **Figure 4.18**, there is a series of plots going through different steps of the simulation. Below are 2 hypothetical 1D exposure patterns differing only in the amplitude of the intensity, one higher contrast (a) and one lower contrast (b). These two simulations have the same PAG distribution (c,d). The local concentration of the excited PAG (e,f) is a affected by both the intensity and local PAG concentration, where density of PAG acts as a kind of noise applied to the intensity 'signal'. If the signal is 'weak' (lower intensity contrast) then the final activated PAG distribution is harder to resolve. The brown lines below show the positions that have a local activated PAG concentration above a threshold, showing that the edges are less clear-cut. This toy-model is intended to intuitively demonstrate how concentrations fluctuations can lead to local areas of over- and under- crosslinking. Reaction-diffusion models that make for a more accurate simulation will be discussed in Section 4.5.

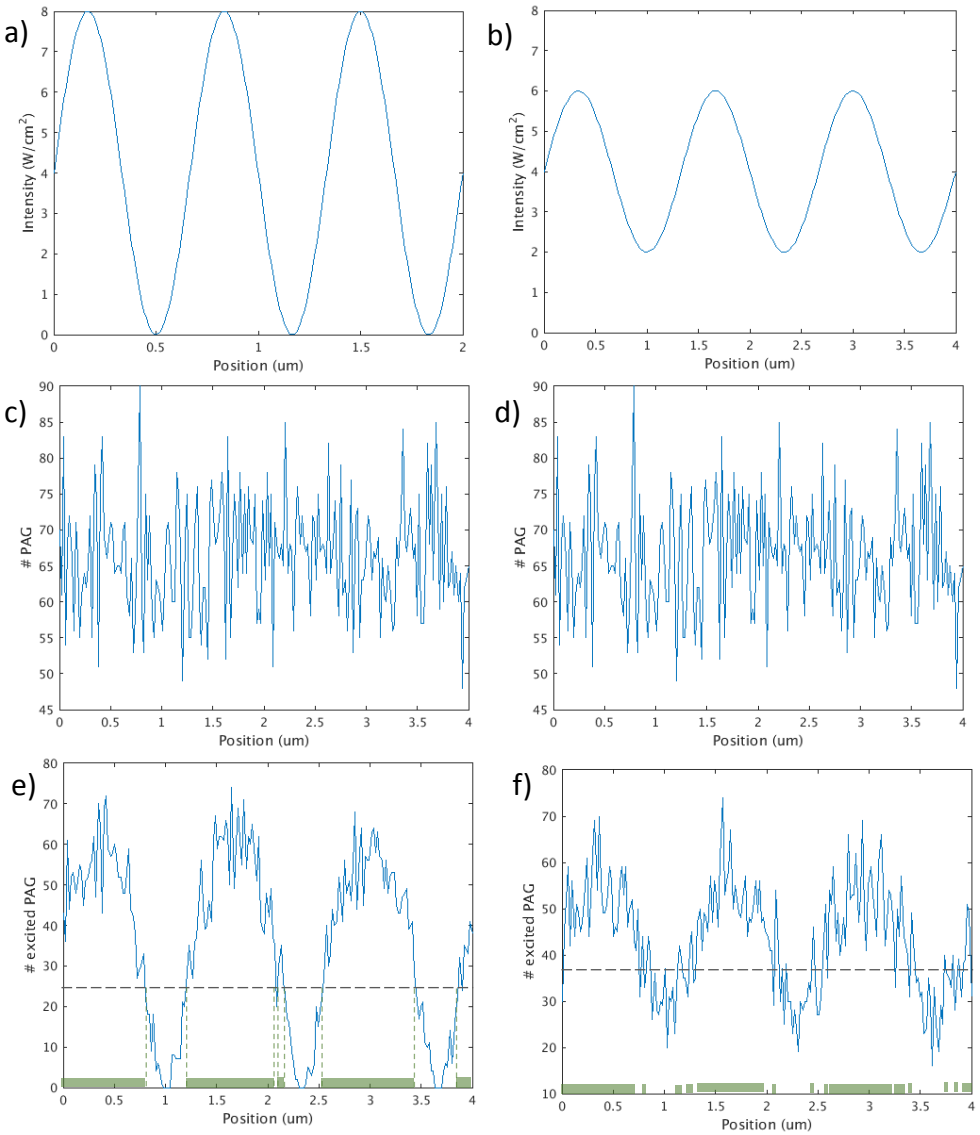

Figure 4.18. a,b) Plots of intensity vs position for a 1D interference pattern with higher (a) and lower (b) contrast. c,d) Local PAG concentration vs position, showing concentration fluctuations. e,f) Local concentration of activated PAG for lower (e) and higher (f) contrast, a convolution of the intensity distribution and the PAG distributions above. The orange line at the bottom indicate the regions that are above a threshold concentration (dashed line).

4.7.4. Measuring Quantum Yield and Absorptivity

In the above model we use two parameters whose values can be difficult to accurately measure, the quantum yield and absorptivity. Note that while absorptivity is easy to measure for a wide variety of materials, we purposefully use a PAG with a very low absorptivity at the exposure wavelength in order to ensure that the beams do not attenuate as they propagate through the resist. In practice, the measured attenuation of the light is less than the lowest

experimental noise we could achieve. The quantum yield, defined as the fraction of absorption events that actually lead to activation of the photoacid generator, could be found by measuring the concentration of activated PAG after an exposure with a known absorption, but this again requires knowledge of the number of absorption events.

Fortunately, we can avoid measuring each of these by redefining the key variables. In equation 4.12, the quantum yield and absorptivity can be replaced with a single variable equal to the product of the quantum yield and absorptivity. The quantum yield-absorptivity product is much easier to measure. The unactivated PAG during exposure can be thought of as exponentially decaying with a half-life that is constant for a particular kind of PAG and exposure condition. After the minus sign in equation 4.12 is the probability of non-activation (or equivalently, the probability of zero activation events), which we can write as a function of exposure time:

$$p_{unactivated}(t_{exposure}) = e^{-\frac{\gamma \Phi I}{E_{photon}} t_{exposure}} \quad (4.14)$$

The concentration of the unactivated PAG during a uniform exposure process is given by an exponential decay function. If we calculate the exponential decay constant, $\lambda = \frac{\gamma \Phi I}{E_{photon}}$, we can solve for the quantum yield-absorptivity product, $\gamma \Phi$.

To calculate the exponential decay constant, we prepare thick films (~40μm) of SU8 with a relatively high concentration of PAG (~4%). Thicker films were difficult to spincoat on the substrate with uniform thickness and without significant scatter. We perform a sweep of exposures with increasing exposure time and uniform intensities (prepared by greatly expanding the laser). Without a post-exposure bake, the transmission of the films is measured using an FTIR-microscope. At this step, care should be taken to ensure that the resist is not additionally exposed with light, since the resist is quite sensitive to blue light: computer monitors should be turned off, the focusing performed with visible light should not done on areas used for measurement. The films have an absorbance peak at ~3.1μm that changes with the level of exposure, plotted in **Figure 4.19**. The absorptivity of the film at different exposure doses is fit to the exponential decay model.

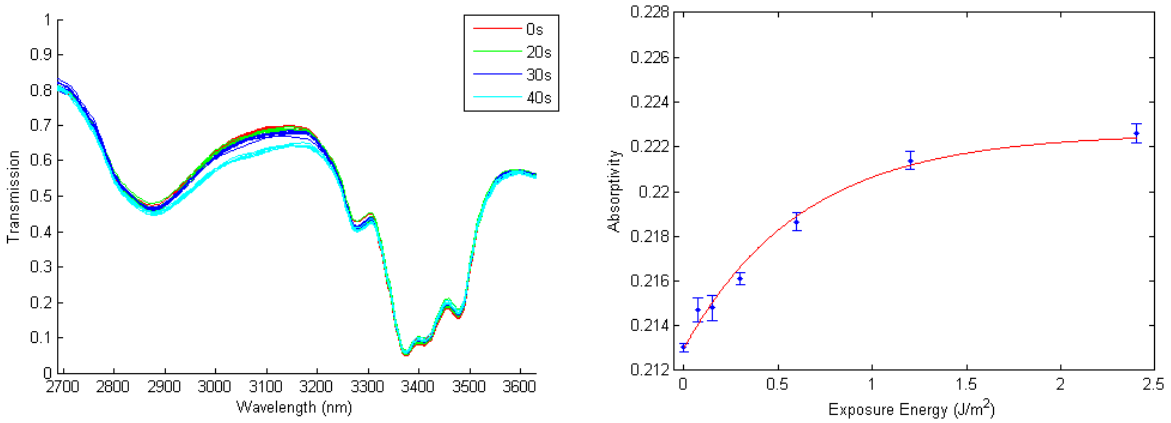

Figure 4.19. a) FTIR transmission spectrum of sensitized SU8 films after 0s, 20s, 30sm and 40s uniform exposures. Repeated lines of same color indicate different measurements. b) The absorptivity of the film at 3µm at a series of increasing dosages. The red line is a logarithmic fit of the absorptivity.

We made a few important assumptions in this measurement. We considered the change in absorptivity to be due to only the concentration of unactivated and activated PAG (or to components whose concentration is linearly proportional to the concentration of unactivated and activated PAG). Because the films are kept below he glassy transition temperature, we predict that polymerization of the resist is roughly linear to the concentration of activated PAG. If photoinitiated side-reactions are present, specifically reactions that remove PAG but do not initiate polymerization, then this will give an inaccurate estimate of the number of growing polymerization chains but will not affect the estimation of the optimum dosage.

4.7.5. Reaction kinetics simulations

The above should give us a trial distribution of initiations sites of SU-8 polymerization. However, we still need to go from this to the final structure of SU-8. To bridge this gap, we use a reaction diffusion model to simulate the polymerization of SU8 and treat the boundary between the solid and developed SU8 as an isoconcentration surface of the crosslink density. We base our model on previously published reaction-diffusion kinetic models of SU8

polymerization.[65], [66] This model includes three species: unreacted epoxides, crosslinks, and radical moities. The rate equations for these are:

$$-\frac{d[M]}{dt} = \frac{d[C]}{dt} = K_p[I][M] \tag{4.15}$$

$$\frac{d[I]}{dt} = K_t[I] + D\nabla^2[I] \tag{4.16}$$

where [I] is concentration of growing polymer chains, [M] is concentration of unreacted moieties, [C] is the concentration of crosslinks, D is diffusivity of the active site, K_t is rate constant of termination, K_p is rate constant of polymerization. There are a few caveats with our use of their data, such as our use of an additional PAG with its own hexafluoride phosphide component, which acts as a terminator in the polymerization process. Thus the termination rate is likely slightly underestimated. Secondly, there may be other differences in the process that may cause changes in the process, such as atmospheric contamination, that would make their rate constants not work for every process. Nevertheless, we consider these parameters the most accurate of what is available and far more accurate than the usual model that considers the crosslink threshold as given only by the local intensity.

To perform the simulation with quantized species concentrations, we break up the process into timesteps. The rate equations are adjusted accordingly:

$$-\frac{\Delta[M]}{\Delta t} = \frac{\Delta[C]}{\Delta t} = K_p[I][M] \tag{4.17}$$

$$\frac{\Delta[I]}{\Delta t} = K_t[I] \tag{4.18}$$

You'll notice the diffusion component is missing from these equations. Instead, we consider the diffusion as a random walk, whereby the sites of polymerization within a voxel have a small probability of moving to an adjacent voxel.

The Matlab code used for performing these calculations is shown below:

```
function crosslinkCount = reactionDiffusionSim( activeSiteCount, k_p, k_t,
    timeStepDuration, NepoxideVoxel, voxelVolume, numRandWalkSteps, probWalk,
    probCrosslink)
%Does reaction-diffusion simulation SU8 crosslinking
%Arguments:
% activeSiteCount is an integer 3D array with size [Nx, Ny, Nz]. The number of initiation
sites at beginning of simulation.
% k_p is a scalar. The rate constant of polymerization. (m^3/s)
```

```
% k_t is a scalar.  The rate constant of termination.  (1/s)
% timeStepDuration is a scalar.  The duration of each time step.  (s)
% NepoxideVoxel is a scalar.  The number of epoxide groups per voxel.  Can be
continuous.
% voxelVolume is a scalar.  The volume of the voxel. (m^3).
% numRandWalkSteps is an integer scalar.  The number of timesteps in the reaction-
diffusion model.
% probWalk is a scalar with values between [0,1].  The probability of an particular
molecule moving to an adjacent voxel per time step.
% probCrosslink is a scalar with values between [0,1].  The probability of a particular
molecule creating a crosslink in a time step.

%Parameters:
% crosslinkCount is 3D array with size [Nx, Ny, Nz].  The number of crosslink sites with
each voxel at the end of the simulation.

Nx = size(activeSiteCount, 1);
Ny = size(activeSiteCount, 2);
Nz = size(activeSiteCount, 3);

%Constants for diffusion calculation
prob_north = 1/6; %Probability of moving north given moving
prob_south = 1/5; %Probability of moving south given moving but not moving north
prob_east = 1/4;
prob_west = 1/3;
prob_up = 1/2;
prob_down = 1;
n_moving = zeros(Nx,Ny,Nz); %Holds the number of particles moving north from each
spot
n_north = zeros(Nx,Ny,Nz);
n_south = zeros(Nx,Ny,Nz);
n_east = zeros(Nx,Ny,Nz);
n_west = zeros(Nx,Ny,Nz);
n_up = zeros(Nx,Ny,Nz);
n_down = zeros(Nx,Ny,Nz);

%Initialize arrays
crosslinkCount = zeros(Nx, Ny, Nz);
epoxideCount = ones(Nx, Ny, Nz) * NepoxideVoxel;
crosslinkCount = zeros(Nx,Ny,Nz);

%Iterate through timesteps
for i_step = 1:numRandWalkSteps
```

```
%Calculate number of initiators within each cell that travel in this timestep
n_moving_tot = binornd( activeSiteCount, probWalk);

%Determine the direction of movement so that there is an equal chance of moving
    in each direction
n_moving = n_moving_tot; % Number of moving PAG left to assign to different
    directions
n_north = binornd(n_moving, prob_north);  %Number of PAG moving North
n_moving = n_moving - n_north;  %Update the number of PAG left to assign
n_south = binornd(n_moving, prob_south);
n_moving = n_moving - n_south;
n_east = binornd(n_moving, prob_east);
n_moving = n_moving - n_east;
n_west = binornd(n_moving, prob_west);
n_moving = n_moving - n_west;
n_up = binornd(n_moving, prob_up);
n_moving = n_moving - n_up;
n_down = n_moving;

%Remove particles that moved away
acidCount = acidCount - n_moving_tot;

%Add particles that arrived from each direction, including a wrap-around for PAG
    crossing unit cell edges.
%East
activeSiteCount(1,:,:) = activeSiteCount(1,:,:) + n_east(end,:,:);
activeSiteCount(2:end,:,:) = activeSiteCount(2:end,:,:) + n_east(1:(end-1),:,:);
%West
activeSiteCount(end,:,:) = activeSiteCount(end,:,:) + n_west(1,:,:);
activeSiteCount(1:(end-1),:,:) = activeSiteCount(1:(end-1),:,:) + n_west(2:end,:,:);
%North
activeSiteCount(:,1,:) = activeSiteCount(:,1,:) + n_north(:,end,:);
activeSiteCount(:,2:end,:) = activeSiteCount(:,2:end,:) + n_north(:,1:(end-1),:);
%South
activeSiteCount(:,end,:) = activeSiteCount(:,end,:) + n_south(:,1,:);
activeSiteCount(:,1:(end-1),:) = activeSiteCount(:,1:(end-1),:) + n_south(:,2:end,:);
%Up
activeSiteCount(:,:,1) = activeSiteCount(:,:,1) + n_up(:,:,end);
activeSiteCount(:,:,2:end) = activeSiteCount(:,:,2:end) + n_up(:,:,1:(end-1));
%Down
activeSiteCount(:,:,end) = activeSiteCount(:,:,end) + n_down(:,:,1);
activeSiteCount(:,:,1:(end-1)) = activeSiteCount(:,:,1:(end-1)) + n_south(:,:,2:end);

%Simulate reactions:
```

```
            %Exponential decay of unreacted epoxides
            epoxideCountNew = epoxideCount .* exp( -k_p .* activeSiteCount ./ voxelVolume .*
                timeStepDuration);

            %Increase crosslink count by the number of epoxides lost
            crosslinkCount = crosslinkCount + (epoxideCount - epoxideCountNew);

            %Set epoxide count to new value
            epoxideCount = epoxideCountNew;

            %Exponential decay of sites of polymerization due to termination
            activeSiteCount = activeSiteCount .* exp( -k_t .* activeSiteCount .*
                timeStepDuration );
        end
    end
```

4.7.6. Applying Models to Lithography Designs

First, we should apply this to well-established patterns. The simple model of defining the expected structure as resulting only from the intensity has worked well in a wide variety of cases. Our model should fallow the results of the simpler model in common cases. We choose to test our model using the 4-beam pattern introduced in section 2.3.1. It has been found experimentally that the 4-beam structures can be made with fairly low PAG concentrations (0.5%w/w is common, but concentrations down to 0.1%w/w also work) and has a wide tolerance for dosage. Results of simulations of the 4-beam exposure are shown in **Figure 4.20**, where we see that the two models are nearly identical in this case, as expected, with only a slight amount of roughness found in the second. For this case, the method chosen to simulate does not make a difference, which is expected since the intensity-only model is considered adequate for most cases.

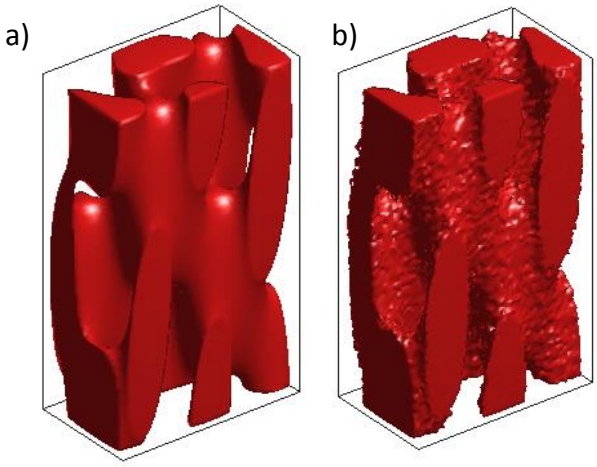

Figure 4.20. 3D isosurfaces estimating the regions that are exposed in a 4-beam pattern (a) assuming that only intensity matters and (b) using our more rigorous model.

Now we will apply this model to the helix and pseudo-omega patterns. **Figure 4.21** shows a trial simulation for the helix pattern at different steps in the simulations process. The intensity profiles for the two are the same, but one has a much higher starting concentration of PAG and thus less relative effect from to concentration fluctuations. The local concentration of excited PAG can be seen to be much closer to the intensity plot when the concentration of PAG is high. This has an effect on the expected 3D structure as well.

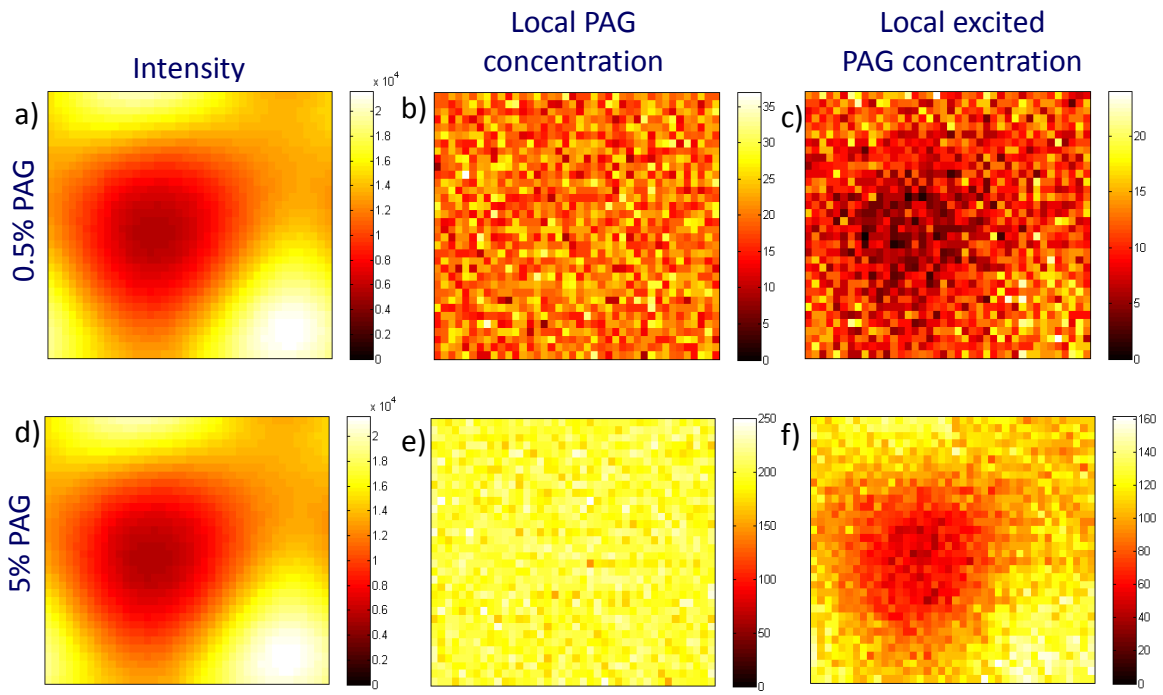

Figure 4.21. Heat maps of planar cross-sections of a unit cell at different steps in the simulation process. a,d) The local optical intensity during exposure. b,e) The local PAG concentration for (b) 0.5% and (c) 5%w/w average PAG concentrations, showing the local concentration fluctuations. c,f) The local concentration of activated PAG for the same concentrations.

The simulated 3D lattices for the helix design are shown below in **Figure 4.22**. In (a), adjacent helices are in close proximity (10's of nm apart) but not in contact at the location indicated by the black circle, but in (b) the two helices are connected at this spot. In the simulations, the presence or absence of this connection varies from trial to trial, depending on the concentration fluctuations and shot noise. This connection can be forced to be broken but lowering the dosage, but this in turn will cause the connection at the blue circle to only sporadically appear. We find that there is no feasible set of parameters that will ensure the proper connectivity of the structure needed for the necessary optical properties. If two-photon exposure is incorporated into the simulation, there is some improvement in the contrast, but it is not enough to enable fabrication. This is theoretical validation of the empirical challenges in fabricating this structure. However, this does not mean that fabricating 3D circular polarizers cannot be done – it simply cannot be done using the planned experimental design.

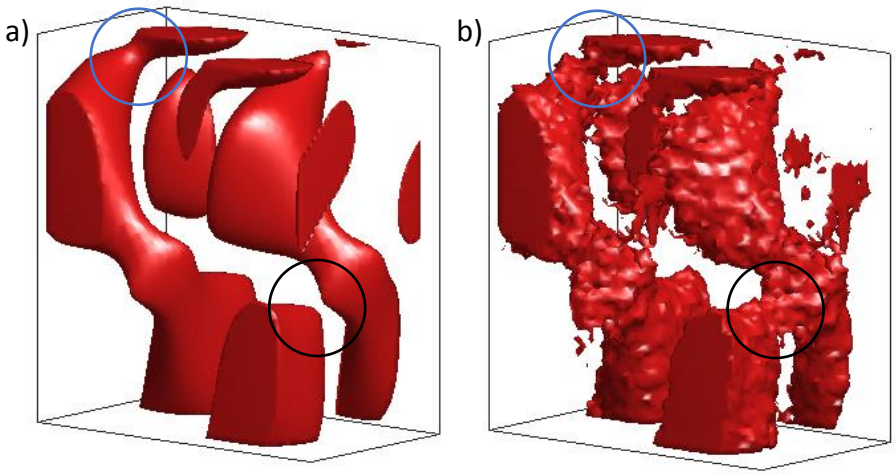

Figure 4.22. 3D isosurfaces showing expected fabricated structure using (a) only intensity and (b) our more rigorous model. The closed red regions represent the *pores* of the structure. The perspective is chosen to emphasize the proximity (in a) and connectedness (in b) between adjacent helices. The circles indicate critical locations where the connectivity of the pattern is very fragile; the black circles indicate a region where there *must not* be a connection, and blue circles indicate a region where there *must* be a connection, in order to ensure circular dichroism of the structure.

The pseudo-omega pattern is a design that avoids some of the design challenges of the helix pattern. There are no very fine features and, judging only by intensity, there is a much broader range of acceptable dosages (see section 4.3.6). However, it is still susceptible to concentration fluctuations and shot noise. In **Figure 4.23**, a side-view of the simulated pseudo-omega structure is shown alongside a SEM cross-section side-view. In both, we see a kind of 'spider webbing' of the SU8. Based on simulations, this noise will prevent fabrication of the structure until the PAG concentration is ~20%w/w, well above the solubility limit. This pattern is *consistent* with what would be expected from fundamental noise in the lithography process, but unfortunately we cannot be *certain* that this is the cause. Other issues, such as atmospheric contamination of the SU8 film by amines or humidity has been known to cause issues with the crosslinking of SU8.[67], [68]

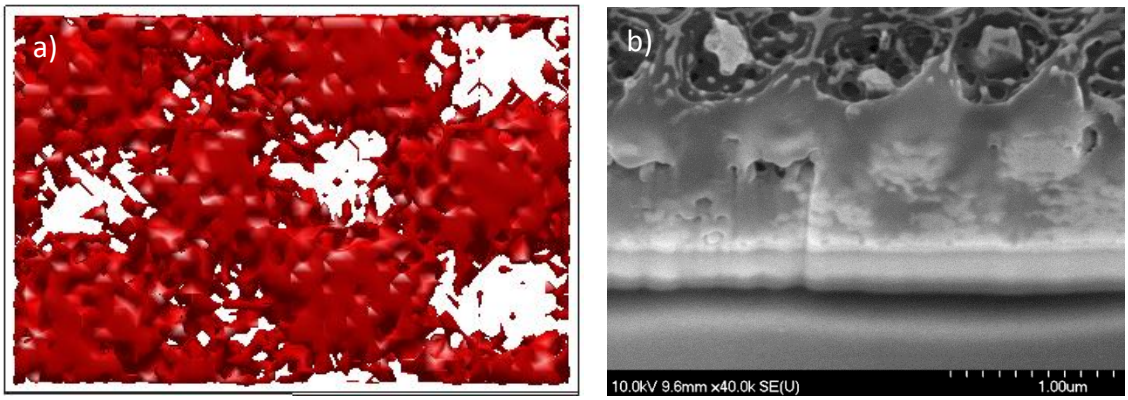

Figure 4.23. a) Crossection of simulated isosurface of crosslink density and b) SEM cross-section of silver electrodeposited pseudo-omega pattern.

4.8. Conclusion

This chapter represents a large amount of work proceeding down a collection of branches toward a particular goal: using proximity-field nanopatterning to scalably fabricate a 3D circularly-polarizing material. Though we have failed to reach this goal, we have made some useful discoveries along the way, such as methods to improve nucleation density in both silver electrodeposition on ITO and silver electroless deposition on the surface of SU8. We have developed a more rigorous model of the interference lithography process in the case of low intensity contrasts, which can be used to investigate the feasibility of interference lithography designs before experiment work is invested.

The helix and pseudo-omega designs that we proposed are infeasible barring major changes to the process. It is suggested that using a different kind of photoresist may support at a higher concentration of photo-initiators and thus reduce the effect of concentration fluctuations. However, few photoresists have been shown to be as high-contrast or as effective at forming self-standing 3D structures as SU8 has. Solving both problems is expected to be a significant challenge. We encourage others to keep in mind that there may be different interference lithography designs that can achieve the same result without the same challenges.

4.9. References

[1] J. K. Gansel *et al.*, "Gold Helix Photonic Metamaterial as Broadband Circular Polarizer," *Science*, vol. 325, no. 5947, pp. 1513–1515, Aug. 2009.

[2] Bahaa E. A. Saleh and Malvin Carl Teich, *Fundamentals of Photonics*. New York: Wiley, 1991.
[3] S. Trippe, "POLARIZATION AND POLARIMETRY: A REVIEW," *J. Korean Astron. Soc.*, vol. 47, no. 1, pp. 15–39, Feb. 2014.
[4] Dave3457, *Homogeneous circular polarizer left handed*. 2010.
[5] D.-H. Kwon, P. L. Werner, and D. H. Werner, "Optical planar chiral metamaterial designs for strong circular dichroism and polarization rotation," *Opt Express*, vol. 16, no. 16, pp. 11802–11807, 2008.
[6] B. Ranjbar and P. Gill, "Circular Dichroism Techniques: Biomolecular and Nanostructural Analyses- A Review," *Chem. Biol. Drug Des.*, vol. 74, no. 2, pp. 101–120, Aug. 2009.
[7] G. R. Bird and M. Parrish, "The Wire Grid as a Near-Infrared Polarizer," *J. Opt. Soc. Am.*, vol. 50, no. 9, p. 886, Sep. 1960.
[8] Justyna K Gansel, Martin Wegener, Sven Burger, and Stefan Linden, "Gold helix photonic metamaterials: a numerical parameter study." Optical.
[9] M. Vaezi, H. Seitz, and S. Yang, "A review on 3D micro-additive manufacturing technologies," *Int. J. Adv. Manuf. Technol.*, vol. 67, no. 5–8, pp. 1721–1754, Jul. 2013.
[10] J. Rinne, "COMPUTATIONAL DESIGN OF INTERFERENCE LITHOGRAPHY FOR THE FABRICATION OF 3D MICROSTRUCTURES," Ph.D., University of Illinois at Urbana-Champaign, Urbana, IL, 2009.
[11] G. Gupta Sidhartha, "DESIGN AND FABRICATION OF NOVEL AND FUNCTIONAL 3D STRUCTURES VIA PROXIMITY FIELD NANO-PATTERNING," Ph.D., University of Illinois at Urbana-Champaign, Urbana, IL, 2012.
[12] Y. Chen, "Nanofabrication by electron beam lithography and its applications: A review," *Microelectron. Eng.*, vol. 135, pp. 57–72, Mar. 2015.
[13] E. . Lee, G. . Rao, and L. . Mansur, "LET effect on cross-linking and scission mechanisms of PMMA during irradiation," *Radiat. Phys. Chem.*, vol. 55, no. 3, pp. 293–305, Jul. 1999.
[14] C. Vieu *et al.*, "Electron beam lithography: resolution limits and applications," *Appl. Surf. Sci.*, vol. 164, no. 1–4, pp. 111–117, Sep. 2000.
[15] S. Yasin, D. G. Hasko, and H. Ahmed, "Comparison of MIBK/IPA and water/IPA as PMMA developers for electron beam nanolithography," *Microelectron. Eng.*, vol. 61–62, pp. 745–753, Jul. 2002.
[16] S. Jeon *et al.*, "Fabricating complex three-dimensional nanostructures with high-resolution conformable phase masks," *Proc. Natl. Acad. Sci. U. S. A.*, vol. 101, no. 34, pp. 12428–12433, 2004.
[17] M. George, "NOVEL INORGANIC PHOTORESISTS FOR 3D MICROFABRICATION," Ph.D., University of Illinois at Urbana-Champaign, Urbana, IL, 2009.
[18] R. Zhang, H. Ning, N. A. Krueger, D. Bacon-Brown, and P. V. Braun, "3D Holographic Photonic Crystals Containing Embedded Functional Features," *Adv. Opt. Mater.*, vol. 4, no. 10, pp. 1533–1540, Oct. 2016.
[19] P. Abgrall, V. Conedera, H. Camon, A.-M. Gue, and N.-T. Nguyen, "SU-8 as a structural material for labs-on-chips and microelectromechanical systems," *ELECTROPHORESIS*, vol. 28, no. 24, pp. 4539–4551, Dec. 2007.

[20] S.-W. Youn, A. Ueno, M. Takahashi, and R. Maeda, “Microstructuring of SU-8 photoresist by UV-assisted thermal imprinting with non-transparent mold,” *Microelectron. Eng.*, vol. 85, no. 9, pp. 1924–1931, Sep. 2008.
[21] N. Perez, A. Huls, D. Puente, W. Gonzalezvinas, E. Castano, and S. Olaizola, “Fabrication and characterization of silver inverse opals,” *Sens. Actuators B Chem.*, vol. 126, no. 1, pp. 86–90, Sep. 2007.
[22] Y. Yang *et al.*, “Refractive indices of textured indium tin oxide and zinc oxide thin films,” *Thin Solid Films*, vol. 510, no. 1–2, pp. 95–101, Jul. 2006.
[23] A. del Campo and C. Greiner, “SU-8: a photoresist for high-aspect-ratio and 3D submicron lithography,” *J. Micromechanics Microengineering*, vol. 17, no. 6, pp. R81–R95, Jun. 2007.
[24] S. Juodkazis, V. Mizeikis, K. K. Seet, M. Miwa, and H. Misawa, “Two-photon lithography of nanorods in SU-8 photoresist,” *Nanotechnology*, vol. 16, no. 6, pp. 846–849, Jun. 2005.
[25] P. Zhao *et al.*, “Two-photon absorption coefficient in relation to the typical pulse models of laser,” *Opt. Commun.*, vol. 283, no. 9, pp. 1924–1928, May 2010.
[26] K. Wynne, G. D. Reid, and R. M. Hochstrasser, “Regenerative amplification of 30-fs pulses in Ti:sapphire at 5 kHz,” *Opt. Lett.*, vol. 19, no. 12, p. 895, Jun. 1994.
[27] M. C. George, E. C. Nelson, J. A. Rogers, and P. V. Braun, “Direct Fabrication of 3D Periodic Inorganic Microstructures using Conformal Phase Masks,” *Angew. Chem.*, vol. 121, no. 1, pp. 150–154, Jan. 2009.
[28] S.-H. Park, D.-Y. Yang, and K.-S. Lee, “Two-photon stereolithography for realizing ultraprecise three-dimensional nano/microdevices,” *Laser Photonics Rev.*, vol. 3, no. 1–2, pp. 1–11, Feb. 2009.
[29] D. Bratton, D. Yang, J. Dai, and C. K. Ober, “Recent progress in high resolution lithography,” *Polym. Adv. Technol.*, vol. 17, no. 2, pp. 94–103, Feb. 2006.
[30] S. Zhang, B. Li, L. Tang, X. Wang, D. Liu, and Q. Zhou, “Studies on the near infrared laser induced photopolymerization employing a cyanine dye–borate complex as the photoinitiator,” *Polymer*, vol. 42, no. 18, pp. 7575–7582, 2001.
[31] W. Heisenberg, “Uber den anschaulichen Inhalt der quantentheoretischen Kinematik und Mechanik,” *Z. Phys.*, vol. 43, no. 3–4, pp. 172–198, Mar. 1927.
[32] J. P. Torres, M. Hendrych, and A. Valencia, “Angular dispersion: an enabling tool in nonlinear and quantum optics,” *Adv. Opt. Photonics*, vol. 2, no. 3, p. 319, Sep. 2010.
[33] A. Sharma, Z. Tibai, J. Hebling, and J. A. Fülöp, “Quasi-monoenergetic proton acceleration from cryogenic hydrogen microjet by ultrashort ultraintense laser pulses,” *Phys. Plasmas*, vol. 25, no. 3, p. 033111, Mar. 2018.
[34] M. Beresna, M. Gecevičius, and P. G. Kazansky, “Ultrafast laser direct writing and nanostructuring in transparent materials,” *Adv. Opt. Photonics*, vol. 6, no. 3, p. 293, Sep. 2014.
[35] H. A. Haus, “Mode-locking of lasers,” *IEEE J. Sel. Top. Quantum Electron.*, vol. 6, no. 6, pp. 1173–1185, Nov. 2000.
[36] A. Taflove, “Review of the formulation and applications of the finite-difference time-domain method for numerical modeling of electromagnetic wave interactions with arbitrary structures,” *Wave Motion*, vol. 10, no. 6, pp. 547–582, 1988.
[37] R. J. Potton, “Reciprocity in optics,” *Rep. Prog. Phys.*, vol. 67, no. 5, pp. 717–754, May 2004.

[38] C. E. Rüter, K. G. Makris, R. El-Ganainy, D. N. Christodoulides, M. Segev, and D. Kip, "Observation of parity–time symmetry in optics," *Nat. Phys.*, vol. 6, no. 3, pp. 192–195, Mar. 2010.
[39] C. Wu, H. Li, Z. Wei, X. Yu, and C. T. Chan, "Theory and Experimental Realization of Negative Refraction in a Metallic Helix Array," *Phys. Rev. Lett.*, vol. 105, no. 24, Dec. 2010.
[40] Z. Li, M. Mutlu, and E. Ozbay, "Chiral metamaterials: from optical activity and negative refractive index to asymmetric transmission," *J. Opt.*, vol. 15, no. 2, p. 023001, Feb. 2013.
[41] A. Boltasseva and V. M. Shalaev, "Fabrication of optical negative-index metamaterials: Recent advances and outlook," *Metamaterials*, vol. 2, no. 1, pp. 1–17, May 2008.
[42] K. Aydin, Z. Li, S. Bilge, and E. Ozbay, "Experimental and numerical study of omega type bianisotropic metamaterials combined with a negative permittivity medium," *Photonics Nanostructures - Fundam. Appl.*, vol. 6, no. 1, pp. 116–121, Apr. 2008.
[43] M. Schlesinger, "Electroless and Electrodeposition of Silver," *Mod. Electroplat.*, vol. 52, p. 131, 2011.
[44] N. V. Mandich, "Pulse and pulse-reverse electroplating," *Met. Finish.*, vol. 97, no. 1, pp. 375–380, 1999.
[45] M. S. Chandrasekar and M. Pushpavanam, "Pulse and pulse reverse plating—Conceptual, advantages and applications," *Electrochimica Acta*, vol. 53, no. 8, pp. 3313–3322, Mar. 2008.
[46] L. A. A. Pettersson and P. G. Snyder, "Preparation and characterization of oxidized silver thin films," *Thin Solid Films*, vol. 270, no. 1–2, pp. 69–72, Dec. 1995.
[47] J. Droog, "Electrochemical formation and reduction of silver oxides in alkaline media," *J. Electroanal. Chem.*, vol. 115, no. 2, pp. 211–224, Dec. 1980.
[48] B. Tollens, "Ueber ammon-alkalische Silberlösung als Reagens auf Aldehyd," *Berichte Dtsch. Chem. Ges.*, vol. 15, no. 2, pp. 1635–1639, Jul. 1882.
[49] S. Iravani, H. Korbekandi, S. V. Mirmohammadi, and B. Zolfaghari, "Synthesis of silver nanoparticles: chemical, physical and biological methods," *Res. Pharm. Sci.*, vol. 9, no. 6, pp. 385–406, Dec. 2014.
[50] A. Antonello *et al.*, "Optimized Electroless Silver Coating for Optical and Plasmonic Applications," *Plasmonics*, vol. 7, no. 4, pp. 633–639, Dec. 2012.
[51] X. Wei and D. K. Roper, "Tin Sensitization for Electroless Plating Review," *J. Electrochem. Soc.*, vol. 161, no. 5, pp. D235–D242, Mar. 2014.
[52] Yanjun Yan, M. Ibnur Rashad, Ee Jin Teo, Hendrix Tanoto, Jinghua Teng, and Andrew Bettiol, "Selective electroless silver plating of three dimensional SU-8 microstructures on silicon for metamaterials applications," *Opt. Mater. Express*, vol. 1, no. 8, pp. 1548–1554, 2011.
[53] J. Hu, W. Li, J. Chen, X. Zhang, and X. Zhao, "Novel plating solution for electroless deposition of gold film onto glass surface," *Surf. Coat. Technol.*, vol. 202, no. 13, pp. 2922–2926, Mar. 2008.
[54] Y.-P. Wang, K. Yuan, Q.-L. Li, L.-P. Wang, S.-J. Gu, and X.-W. Pei, "Preparation and characterization of poly(N-isopropylacrylamide) films on a modified glass surface via surface initiated redox polymerization," *Mater. Lett.*, vol. 59, no. 14–15, pp. 1736–1740, Jun. 2005.
[55] D. Maji, S. K. Lahiri, and S. Das, "Study of hydrophilicity and stability of chemically modified PDMS surface using piranha and KOH solution," *Surf. Interface Anal.*, vol. 44, no. 1, pp. 62–69, Jan. 2012.

[56] L. Hallmann, A. Mehl, N. Sereno, and C. H. F. Hämmerle, “The improvement of adhesive properties of PEEK through different pre-treatments,” *Appl. Surf. Sci.*, vol. 258, no. 18, pp. 7213–7218, Jul. 2012.
[57] K. Bowden, I. M. Heilbron, E. R. H. Jones, and B. C. L. Weedon, “13. Researches on acetylenic compounds. Part I. The preparation of acetylenic ketones by oxidation of acetylenic carbinols and glycols,” *J. Chem. Soc. Resumed*, p. 39, 1946.
[58] I. Vilotijevic and T. F. Jamison, “Epoxide-Opening Cascades Promoted by Water,” *Science*, vol. 317, no. 5842, pp. 1189–1192, Aug. 2007.
[59] B. Y. Ahn and J. A. Lewis, “Amphiphilic silver particles for conductive inks with controlled wetting behavior,” *Mater. Chem. Phys.*, vol. 148, no. 3, pp. 686–691, Dec. 2014.
[60] S. Navaladian, B. Viswanathan, R. P. Viswanath, and T. K. Varadarajan, “Thermal decomposition as route for silver nanoparticles,” *Nanoscale Res. Lett.*, vol. 2, no. 1, pp. 44–48, Jan. 2007.
[61] A. Hagedorn, “Make Jones Reagent.” Not Voodoo X, 2018.
[62] R. L. Brainard *et al.*, “Shot noise, LER, and quantum efficiency of EUV photoresists,” 2004, pp. 74–85.
[63] E. Hassanein *et al.*, “Film quantum yields of EUV and ultra-high PAG photoresists,” in *SPIE Advanced Lithography*, 2008, pp. 69211I–69211I.
[64] R. M. Mazo, “Concentration fluctuations in fluid mixtures,” *J. Chem. Phys.*, vol. 129, no. 15, p. 154101, Oct. 2008.
[65] J.-D. Cho, H.-T. Ju, Y.-S. Park, and J.-W. Hong, “Kinetics of Cationic Photopolymerizations of UV-Curable Epoxy-Based SU8-Negative Photoresists With and Without Silica Nanoparticles,” *Macromol. Mater. Eng.*, vol. 291, no. 9, pp. 1155–1163, Sep. 2006.
[66] Y. Sensu, A. Sekiguchi, S. Mori, and N. Honda, “Profile simulation of SU-8 thick film resist,” 2005, pp. 1170–1185.
[67] S. Yang, M. Megens, J. Aizenberg, P. Wiltzius, P. M. Chaikin, and W. B. Russel, “Creating Periodic Three-Dimensional Structures by Multibeam Interference of Visible Laser,” *Chem. Mater.*, vol. 14, no. 7, pp. 2831–2833, Jul. 2002.
[68] D. A. Chang-Yen, R. K. Eich, and B. K. Gale, “A Monolithic PDMS Waveguide System Fabricated Using Soft-Lithography Techniques,” *J. Light. Technol.*, vol. 23, no. 6, p. 2088, Jun. 2005.

CHAPTER 5

GRADIENT REFRACTIVE INDEX OPTICS IN POROUS SILICON AND POROUS SILICON OXIDE

This chapter concerns a recent discovery that direct laser writing (DLW) can be performed inside the pores of porous silicon (PSi) and porous silicon oxide ($PSiO_2$). A photoresist-PSi composite is formed where the fraction of photoresist can be controlled with optical dosage, allowing 3D gradient index optics to be created. This technique is demonstrated to fabricate a variety of optics taking advantage of these new capabilities.

5.1. Background on porous silicon

Porous silicon is, as could be guessed by the name, silicon with pores incorporated into it.[1] These pores are typically on the order of 10's of nm, though they can be made narrower or wider depending on the characteristics of the fabrication process. The pores follow the [1 0 0] direction of the atomic lattice of the silicon. Usually, the porous silicon is made on a [0 0 1] silicon wafer, so that the pores are formed normal to the silicon surface, but sometimes they are formed on a [0 1 1] direction, so that two sets of pores form at 45° angles from the surface.[2]

The pores are formed by electrochemically etching silicon using a solution of HF.[3] A schematic of a common electrochemical cell to achieve this is shown in **Figure 5.1**.[4] The porosification process is driven by holes in the silicon that react with HF according to the chemical reaction shown in the figure. Due to the importance of holes in this reaction, the process is very dependent upon the doping of the silicon wafer. Higher concentrations of p-dopants in silicon will increase hole concentration and lead more rapid etch rates and higher porosities.[5] Neutral or n-doped silicon will have little to no etching due to minimal hole concentration.

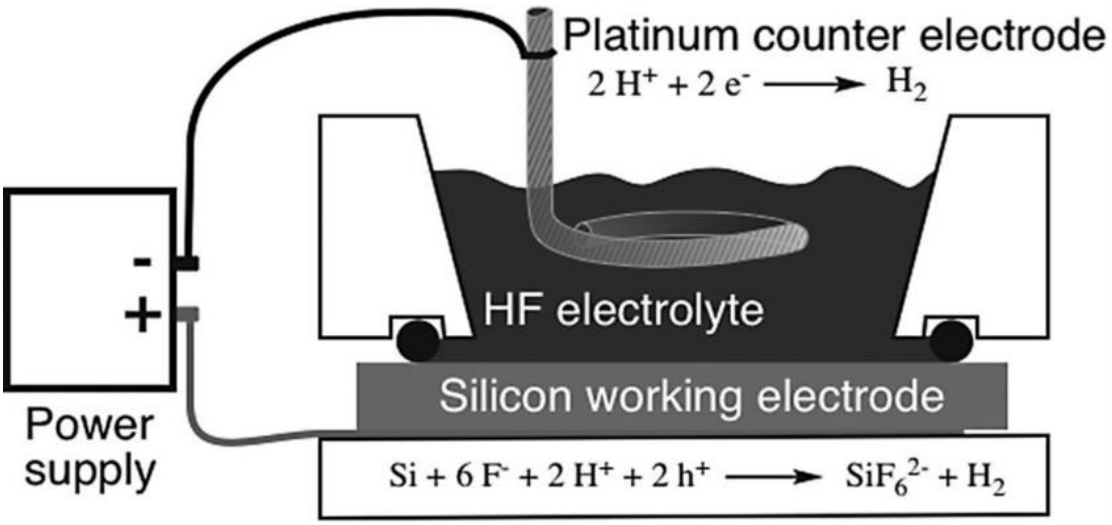

Figure 5.1. Schematic of the silicon porosification process. Image from Binoy Bera.[4]

The hole concentration can be controlled not only by the wafer's dopants, but also by the electrical potential applied to the wafer.[5] Higher voltages lead to higher etch rates and higher porosities. This leads to one great advantage of PSi: it is possible to create films with varying porosities at varying depths. Higher and lower porosity PSi have higher and lower refractive indices and since silicon has such a high refractive index, a very broad range of refractive indices are possible. Figure 5.1.2a shows the range of refractive indices possible. Note that very high and very low porosities (below 10% and above 90%) are not possible but that still leaves an incredibly broad range of possible refractive indices. One of the most common uses of PSi for optics is for the creation of Bragg stacks (discussed in section 1.2) an example of which is shown in **Figure 5.2b**.[1]

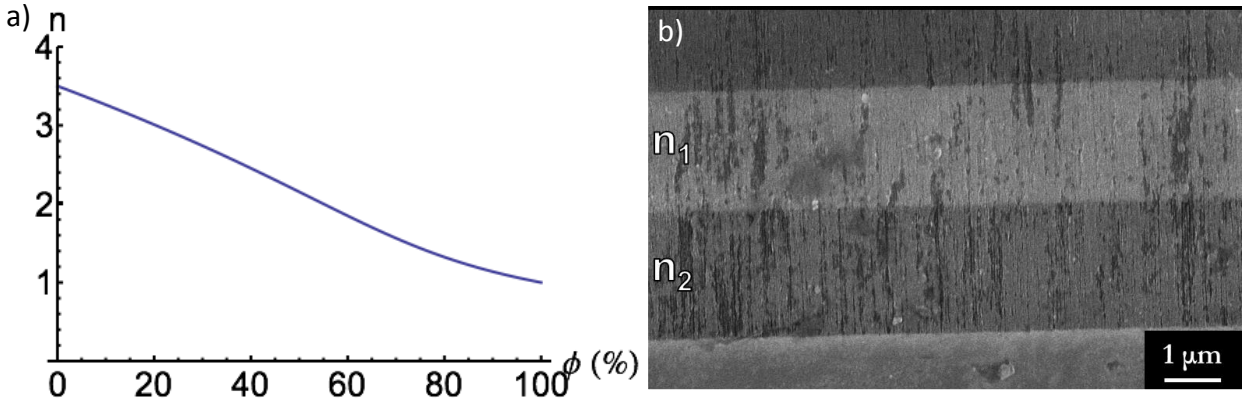

Figure 5.2. a) Plot of effective refractive index (n) at different porosities (ϕ) of PSi calculated using an EMA. b) SEM cross-section of PSi Bragg stack. Images by Neil Kreuger.

This method is not the only method by which Bragg stacks can be fabricated but it allows gradient refractive index (GRIN) with a single step. From any desired refractive index profile, the necessary waveform of the applied potential can be calculated and the entire process of etching complex Bragg stacks can be automated.[6]

PSi has some disadvantages for creating optical devices. One of these is absorptivity.[1] In the visible spectrum silicon is highly absorptive, especially for blue light. Porosification can greatly reduce this absorptivity, depending on the porosity, but often zero absorptivity is desired. This can be achieved by oxidizing the PSi into $PSiO_2$. Films of PSi can be oxidized by plasma or ozone treatment, but these can be very slow and only oxidize PSi close to the surface. Dry oxidation of PSi using oxygen gas at temperatures above 900°C is effective at oxidizing thick films. However, the material expands when oxidized: the volume per mol of Si increases from $12\frac{cm^3}{mol}$ to $26\frac{cm^3}{mol}$. The expansion tends to proceed into the pores, considerably reducing the porosity. The oxidation process tends to make films brittle due to the higher molar volume of SiO_2 relative to Si. The PSiO2 maintains the relative level of porosity present in the original PSi, but the refractive indices possible are within a much smaller range. The lower absorptivity of the PSi is met with a tradeoff of reduced index contrast.

5.2. Porous silicon optics using birefringence

This section focuses on work that has been submitted to Physical Review Materials with the title “Structural Birefringence as a Design Parameter for In-Plane Porous Silicon Micro-Optic Devices”.

The pores in PSi and $PSiO_2$ are highly aligned, which leads to a birefringence of the effective refractive index, where the ordinary axis is orthogonal to the pores and the extraordinary axis is parallel to the pores.[7] Different parts of the pores are These parameters have been studied surprisingly little. This is likely due a couple of reasons: the magnitude of the birefringence depends upon the size and density of the pores, which vary considerably with processing conditions; and the tendency of the optical characteristics PSi to be used only with normal incidence, where only the ordinary refractive index has an effect on the optics.

There are cases, however, where the extraordinary refractive index is important: anytime that there is a considerable component of the electric field parallel to the pores. If the optics are designed such that pores are perpendicular to the direction of propagation, strong polarization selectivity can be introduced into the optics since one polarization will experience the ordinary refractive index and the other polarization will experience the extraordinary refractive index.

Typically, the etch process is restricted to 1-dimension with variation only in direction normal to the surface, so that only films that are uniform in the x- and y- directions can be made. However, recent work in our group has demonstrated optics that have variations of refractive index in more dimensions.[6] This is made possible by first etching the silicon substrate using conventional methods, such as Bosch etch, to define a relief pattern. Porosification proceeds everywhere that the silicon is in contact with the etchant and is connected by a conductive path to the current generator. These pores still follow the [1 0 0] directions, so along etched sidewalls of a [0 0 1] silicon wafer, pores will propagate lateral to the surface, introducing a birefringence between the x- and y-directions. This technique could be used to introduce a birefringence and a lateral gradient refractive index in silicon on the scale of microns, greatly opening up the design space of silicon micro-optics.

In practice, attempts at developing optics using this method had a recurrent challenge: while the patterned silicon geometries were etched as desired, we also etched the substrate in ways that interfered with the optics of our designed geometries. **Figure 5.3** shows the formation of a pointed structure immediately beneath the rib, which leads to scattering at a position where the wavefront of light is most critical.

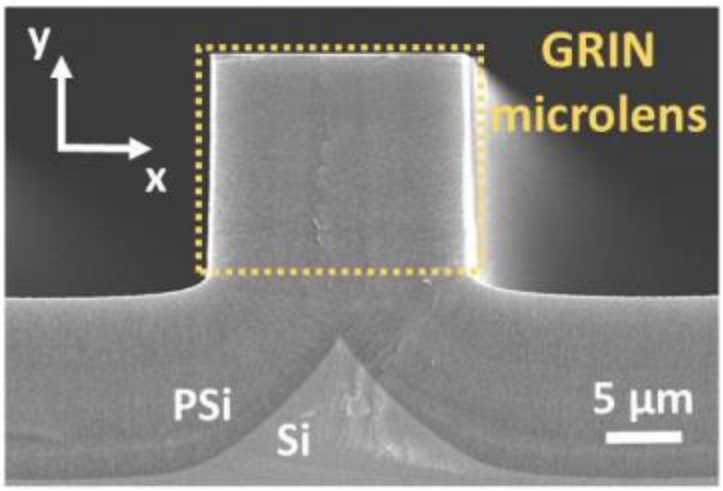

Figure 5.3. SEM cross-section of porosification of patterned silicon. Image by Neil Krueger.

To deal with this issue, we developed a new process for creating porous silicon optics and separating them from the substrate. The process is described in **Figure 5.4**. We start by defining a tall structure, usually square pillars, in the silicon using conventional lithography and reactive ion etching. That structure is porosified and released from the substrate by applying mechanical stresses (the silicon was gently tapped with a tweezer while being held above the receiving substrate). The porosified silicon pillars lie on the receiving substrate at random positions and orientations, but typically parallel to the surface. The optic could then be characterized without the scattering from the silicon substrate.

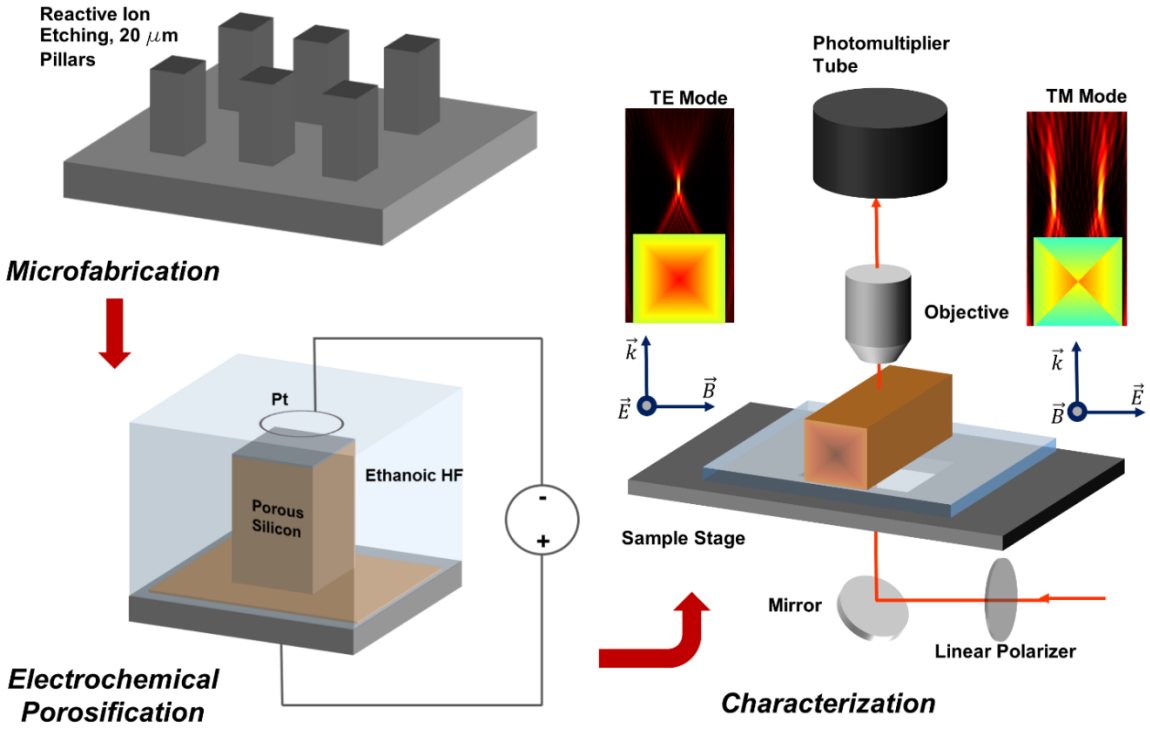

Figure 5.4. Schematic of the preparation of birefringent silicon optics. Silicon pillars are prepared by conventional lithography and reactive ion etching. These pillars are then etched using electrochemical HF porosification with a predefined wavefunction to create gradient porosities. The etched pillars are aligned sideways on a transparent substrate and then characterized using laser confocal microscopy.

To understand how these optics will behave we need to first understand the birefringent properties of PSi and $PSiO_2$. Due to the high alignment of the pores in PSi and the high refractive index contrast between Si and air, there is a strong birefringence.[7] This is called a "structural" birefringence as the birefringence is due to the nanostructuring of the film introduced by the etching, rather than from an inherent chemical property. As the diameters of the pores we use (10's of nm) are much smaller than the size of the wavelengths of light we are interested in (100's of nm), an effective medium approximation (EMA) is well suited to use to characterize the substrate; we are able to treat the PSi as an single material with uniform optical characteristics in place of a complex combination of Si and air.

There are a few options for birefringent EMA models, but we have found that the Bruggeman EMA provides the best fit to our data.[8] The Bruggeman EMA is defined by the equation:

$$\phi_{Si/SiO_2}\frac{n_{Si/SiO_2}-n_{eff}}{n_{eff}+L_{\perp,\parallel}(n_{Si/SiO_2}-n_{eff})}+\phi_{air}\frac{n_{air}-n_{eff}}{n_{eff}+L_{\perp,\parallel}(n_{air}-n_{eff})}=0 \qquad (5.1)$$

where $\phi_{Si/SiO_2}$is the volume fraction of Si or SiO2, ϕ_{air} is the remaining volume fraction, $n_{Si/SiO_2}$is the refractive index of the Si or SiO2 at the wavelength of interest, n_{air} is refractive index of air (≈1), $L_{\perp,\parallel}$ are the depolarization factors ($L_\perp$ and $L_\parallel$ should be used for electric field polarized perpendicular to and parallel to the pores, respectively), and finally n_{eff} is the effective refractive index we're interested in calculating.

Unfortunately, this equation is not analytically solvable, but the solution for n_{eff} can be calculated numerically with little work or time; one can simply calculate the left side of equation 1 at many different values of $n_{eff}$and use the value for n_{eff}that yields the result closest to zero. The values for the depolarization factors $L_\perp$ and $L_\parallel$ we use are from a published fits.[9], [10] All of this of course assumes that we know the volume fraction of the medium that is Si or SiO2 vs air. Given the small sizes size and nanoscale roughness inside the pores, getting an direct measure of the porosity is difficult. Instead, we take a different approach: we start with uniform films of PSi on a silicon substrate, perform ellipsometry on the films and fit the results to an anisotropic Bruggemann model built into the ellipsometer software, which allows us to fit the pore fraction of the material. If we repeat this across a sweep of etch conditions, we develop a library that tells us what etch conditions we need to achieve any given refractive index.

The ellipsometry was performed using a variable angle spectroscopy ellispometer (VASE) made by Woolam with angles of 45°, 60°, and 75° and a wavelength range of 400nm to 1100nm. Reflectance spectra was also recorded at these angles and incorporated into the fitting of the model. In order to achieve better fits, thin mixing layers at the boundary of PSi and air, and the boundary of PSi and Si were added. Without these mixing layers, the model greatly overestimated the magnitude to of the Fabry-Perot fringes in reflectance.

5.3. Simulations of porous silicon birefringence

Simulations were performed to better understand the origin of the birefringence. Is the birefringence purely due to the structure? Does the remaining, unetched silicon have essentially the same local refractive index as bulk silicon, or are there important chemical

changes? We perform finite-difference time domain (FDTD) simulations of the nanoporous silicon structure to determine the refractive index in each direction.[11]

5.3.1. Principles of Effective Refractive Index Calculations Using FDTD

FDTD is an electromagnetic simulation method favored for the high versatility and applicability to a wide variety of studies.[11] FDTD operates using a lattice of discrete steps in both space and time. A Yee-cell is used, where space is split into two grids, one where the complex electric field is tracked and one where the complex magnetic field is tracked, such that the vertices of one grid are in the cell-centers of the other and vice versa. Time is similar split, with alternating time steps where discretized versions of Maxwell's equations are used to either update the magnetic fields based on the electric fields of adjacent vertices, or update the electric fields based on the magnetic fields of adjacent vertices.

In contrast with frequency domain simulations such as RCWA, FDTD calculations are time-domain (as the name implies) so that many different frequencies can be calculated in a single simulation. At time step t=0, the structure is initialized with zero electric and magnetic fields. A pulse of light is directed toward the structure from a plane near the edge of the simulation region, where there are no nearby structures that could lead to near-field interference. A t=0, the electric and magnetic field magnitude is approximately zero, preventing discontinuities in the electric field. The pulse is propagated by the repeated calculation of discretized Maxwell's equation from cell to cell (the time interval must be chosen such that the rate of update between adjacent cells is faster than the speed of light). At a particular plane of cells, denoted a 'monitor plane', the electric field is recorded at every time-step. Some of the amplitude of the light is reduced due to absorption in the silicon, but most is lost at contact with a phase matched layer (PML) at the ends of the simulation region that efficiently absorbs light with a minimal reflectance. Once the amplitude of the light is reduced to a sufficiently low amount (commonly 1e-10 of the input light), the simulation ends and a Fourier transform of the electric field with time is performed to yield the electric field over a spectrum.

The above description of the simulation process is fairly common for FDTD simulations. For calculating the refractive index, we need to do perform so-called 'parameter extraction' to get the effective optical parameters.[12], [13] 'Parameter extraction' as a concept has exploded in recent years alongside the study of metamaterials, optical composites that are designed to achieve a particular effective refractive index, especially a negative refractive index.[14] Parameter extraction is performed to calculate the effective refractive index of the simulated metamaterials to see if they have the desired effective optical properties. There are many different publications that outline new techniques for extracting the optical parameters, but are mostly variations on a few major techniques.

One of the more common methods is based on power and phase of reflected and transmitted light, commonly referred to as the "s-parameter method", the seminal paper of which is written by Smith.[12], [14] Electric field monitors are placed in front of and behind the structure to collect the reflected and transmitted electric field information and these are used to calculate the s-parameters, parameters that relate the transmitted and reflected light to the input light for a particular structure, effectively treating the optical structure as a 2-port system. These s-parameters are then used to calculate the effective refractive index. For birefringent media, one need only start with polarized light parallel to one of the axes and then repeat the simulation using an orthogonal polarization. We had an issue with this technique is that the results significantly depended on the way the simulation was setup. In our porous silicon structure, the geometry of the 'bulk' PSi (the shape we use will be discussed in detail in the next section) and the geometry of empty space are well defined, but the interface between the two is not. At the interface we must define a planar boundary where the PSi stops and empty space begins. If we define this boundary to go through the middle of pores, we reach a different effective refractive index than if we define the boundary to go between the pores. The actual effective refractive index of PSi cannot depend upon the precise location of the boundaries, so we must look elsewhere for an effective technique for parameter extraction that does not rely as much on the reflection and transmission at interfaces.

Another method of parameter extraction based on field averaging was also developed by Smith.[13] In this method, the reflections and transmissions at the interface are ignored. In

short, a unit cell of the structure is treated as an individual Yee-cell, where the average fields are calculated at the corresponding corners and surfaces of the cell and the effective index is calculated using the constitutive relations of the Yee-cell in what is essentially the inverse of the FDTD method. The fields at the points of the Yee cell are actually surface averages of those fields. These surface-averages are calculated using Stokes theorem to convert line integrals into surface integrals – the main advantage of this is that a line integral can be chosen to avoid any metal-air interface that can create very sudden jumps in the electric field due to the sudden jump in permittivity between metal and air. Unfortunately, we still find that there is a dependence of the calculated refractive index based on the location of the boundaries of the cell. The origin of this dependence is not clear, but it is suspected to be related to the relatively high 'filling' of the simulation region for our PSi. A common characteristic we have noticed for examples of this kind of field averaging is that the unit cells of the medium are very sparse and the points where the fields are calculated are far from the structure;[15]–[19] we cannot achieve this for PSi due to the relatively high filling of the unit cell.

Lastly, we consider a method that is little mentioned in the literature despite being much simpler: field-averaging that relies on averaging over the whole unit cell.[20] This actually predates Smith's field-averaging method discussed above. This kind of field averaging is much simpler to numerically implement: the local index and electric and magnetic fields are recorded at every point in space within the cell. The local D and B fields are calculated from the local refractive index and the E and H fields. The complex E, H, D, and B fields are averaged across the unit cell, and then used to calculate the effective permittivity and permeability. These calculations were performed using the scripting capabilities of Lumerical FDTD software. The code for these calculations is shown below, collecting information from two monitors called 'EHfield' and 'indexMonitor' over the same region of space that collect the electric and magnetic fields and the local refractive index, respectively:

```
#Get frequencies used in simulation
f = getdata('EHfield','f'); #frequencies

#Get the number of spatial positions and frequencies
nX = length(getdata('EHfield','x'));
nY = length(getdata('EHfield','y'));
```

```
        nZ = length(getdata('EHfield','z'));
        nF = length(getdata('EHfield','f'));

        #Get the electric and magnetic fields
        E_x = pinch(getdata('EHfield','Ex'));
        E_y = pinch(getdata('EHfield','Ey'));
        E_z = pinch(getdata('EHfield','Ez'));
        H_x = pinch(getdata('EHfield','Hx'));
        H_y = pinch(getdata('EHfield','Hy'));
        H_z = pinch(getdata('EHfield','Hz'));

        #Get local complex refractive index data
        index_x = getdata('indexMonitor','index_x');
        index_y = getdata('indexMonitor','index_y');
        index_z = getdata('indexMonitor','index_z');
        index_x = pinch(index_x(1:nX,1:nY,1:nZ,1:nF));
        index_y = pinch(index_y(1:nX,1:nY,1:nZ,1:nF));
        index_z = pinch(index_z(1:nX,1:nY,1:nZ,1:nF));

        #Calculate complex relative permittivity from complex refractive index
        epsilon_x_rel = (real(index_x)^2 - imag(index_x)^2) +
1i*(2*real(index_x)*imag(index_x));
        epsilon_y_rel = (real(index_y)^2 - imag(index_y)^2) +
1i*(2*real(index_y)*imag(index_y));
        epsilon_z_rel = (real(index_z)^2 - imag(index_z)^2) +
1i*(2*real(index_z)*imag(index_z));

        #Calculate relative permeability by the definition of refractive index
n=sqrt(mu*eps/m0/eps0)
        mu_x_rel = index_x^2/epsilon_x_rel;
        mu_y_rel = index_y^2/epsilon_y_rel;
        mu_z_rel = index_z^2/epsilon_z_rel;

        #Calculate displacement field from local E and permittivity
        D_x = eps0*epsilon_x_rel*E_x;
        D_y = eps0*epsilon_y_rel*E_y;
        D_z = eps0*epsilon_z_rel*E_z;
        #Calc mag induction field from local H and mu
        B_x = mu0*mu_x_rel*H_x;
        B_y = mu0*mu_y_rel*H_y;
        B_z = mu0*mu_z_rel*H_z;

        #Calculate the average E, H, D, B fields
        #mean() function removes complex component
```

```
E_x_avg = sum( pinch(E_x(1:nX,1:nY,testF_i)))/(nX*nY);
E_y_avg = sum( pinch(E_y(1:nX,1:nY,testF_i)))/(nX*nY);
E_z_avg = sum( pinch(E_z(1:nX,1:nY,testF_i)))/(nX*nY);

H_x_avg = sum( pinch(H_x(1:nX,1:nY,testF_i)))/(nX*nY);
H_y_avg = sum( pinch(H_y(1:nX,1:nY,testF_i)))/(nX*nY);
H_z_avg = sum( pinch(H_z(1:nX,1:nY,testF_i)))/(nX*nY);

D_x_avg = sum( pinch(D_x(1:nX,1:nY,testF_i)))/(nX*nY);
D_y_avg = sum( pinch(D_y(1:nX,1:nY,testF_i)))/(nX*nY);
D_z_avg = sum( pinch(D_z(1:nX,1:nY,testF_i)))/(nX*nY);

B_x_avg = sum( pinch(B_x(1:nX,1:nY,testF_i)))/(nX*nY);
B_y_avg = sum( pinch(B_y(1:nX,1:nY,testF_i)))/(nX*nY);
B_z_avg = sum( pinch(B_z(1:nX,1:nY,testF_i)))/(nX*nY);

#Calc average permittivity from average D and E
eps_x_avg = D_x_avg/E_x_avg;
eps_y_avg = D_y_avg/E_y_avg;
eps_z_avg = D_z_avg/E_z_avg;

#Calc average permeability from average H and B
mu_x_avg = B_x_avg/H_x_avg;
mu_y_avg = B_y_avg/H_y_avg;
mu_z_avg = B_z_avg/H_z_avg;

#Calculate refractive index from permittivity and permeability
n_x = sqrt((eps_x_avg*mu_x_avg)/(eps0*mu0));
n_y = sqrt((eps_y_avg*mu_y_avg)/(eps0*mu0));
n_z = sqrt((eps_z_avg*mu_z_avg)/(eps0*mu0));

#Calculate complex refractive index from real index and permittivity
k_x = sqrt(n_x^2-eps_x_avg);
k_y = sqrt(n_y^2-eps_y_avg);
k_z = sqrt(n_z^2-eps_z_avg);
```

The above method is what we settled on for using simulations for estimating the effective refractive index of PSi and PSiO2, as it gave consistent results while changing conditions of the simulation and gave results similar to what was found in experiment.

One should be aware of a few of limitations of this technique. One is that because the whole unit cell is averaged, a few 'artifact' points of field data could have an outsized effect on

the average. Avoiding this problem was the motivation of Smith's use of Stoke's equations for calculating field averages discussed above.[13] We test for this effect by repeating the same experiment at different resolutions. Field artifacts will appear in different numbers and magnitudes pseudorandomly depending on the resolution; the fact we see that the effective refractive index converges well suggests that these artifacts are not an issue in our model. However, if one were to use materials with negative permittivities, such as metals, we expect this problem to be much worse. Secondly, this method does not account for the phase difference at different parts of the unit cell. Our unit cell depth is much smaller than the wavelengths of interest and the effect is roughly proportional between the E and D, as well as H and B, so the effect on the effective index is quite small. However, one is encouraged to keep a close eye on this when using larger unit cells. One more thing to keep in mind in setting up these simulations is that back-reflections from the end of the PSi structure or beginning PML can cause interference with the incident pulse, creating crests and troughs in the electric field. We avoid this by creating a long simulation region and time the end to simulation so that the backwards propagating pulse does not have time to reach the monitor region.

5.3.2. Origin of structural birefringence in PSi

The precise geometry of PSi and PSiO2 is difficult to quantify, but we need to declare a definite structure to consistently simulate their optical properties. The pores of PSi tend to be arranged in a roughly hexagonal lattice, though with little long-range order.[3] For our simulations we assume that pores are arranged in perfect hexagonal lattice. The pores of PSi tend to be roughly circular, though there are local variations in geometry. If we were to use perfect spheres, we run into a problem: at a porosity of 90.69% the pores will be touching and at higher porosities, they will be overlapping. PSi can be made to have porosities higher than 91% and the PSi does not transition from an array of pores into an array of Si pillars, so we cannot treat the porous silicon as hexagonal arrays of circles across the whole range of reachable porosities. Instead, we treat the pores as hexagonal, which allows use to use porosities from 0%-100% without leading to interconnection of pores. **Figure 5.5a** shows a plan-view of the geometry we use in our simulation. Here, the unit cell is oriented so that the

wave is propagating in the 'armchair' direction. This direction was found to give results slightly closer to the experimental data, so this is what we used; using a stochastic geometry, like what is seen experimentally, would likely yield more accurate results, but is much more difficult to set up.

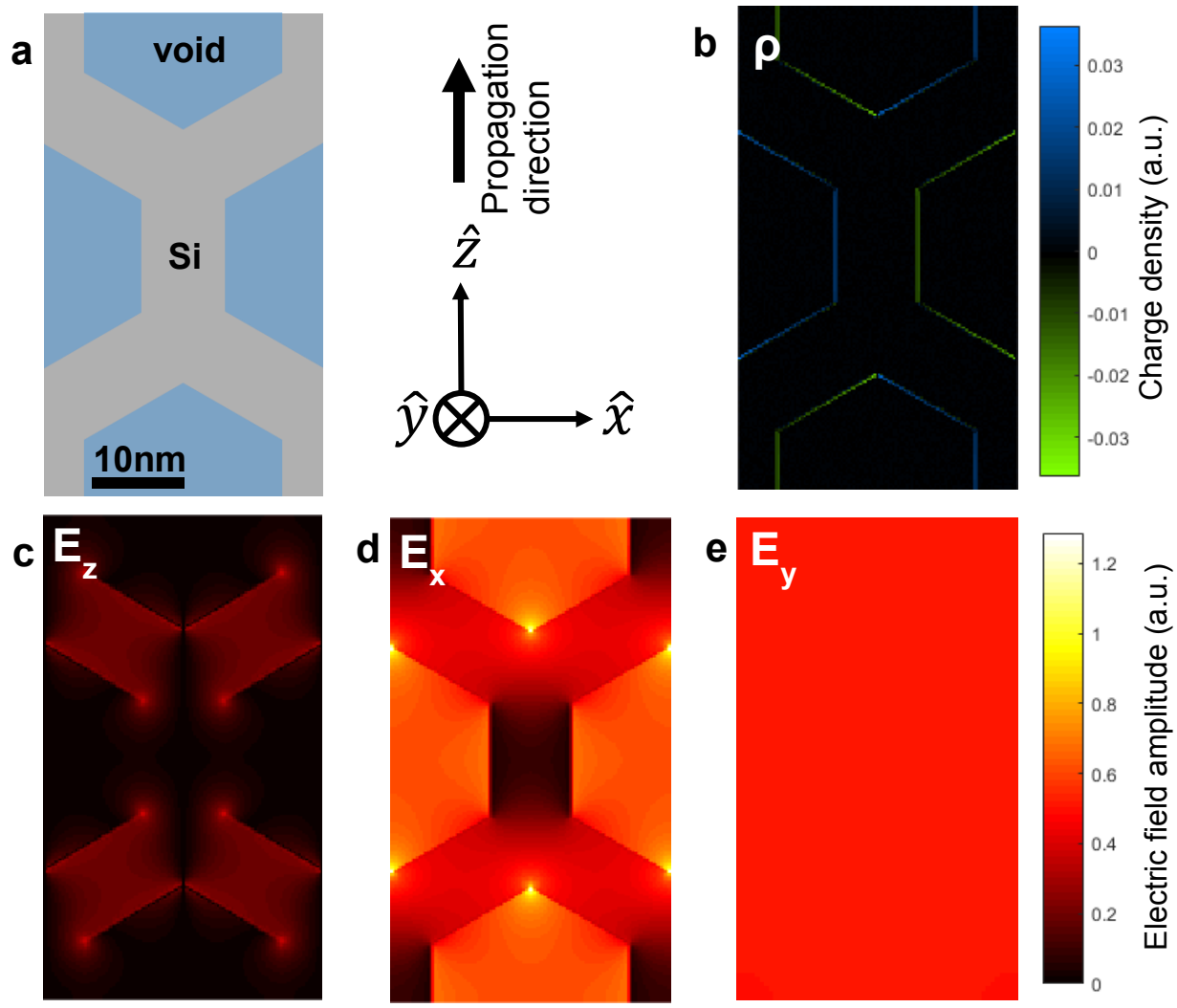

Figure 5.5. Plan view cross-sections unit cell in PSi lattice. a) Schematic of pore geometry. b) Amplitude of the oscillating charge density under x-polarized light wave propagating in the z-direction. c,d,e) Local electric field components in the x, y, and z-directions, respectively, under unpolarized light.

The birefringence of this structure was simulated using the direct field averaging method described at the end of section 5.3.1. The local electric field amplitudes used to calculate the birefringence are shown in **Figure 5.5cde**. The electric field in the x-direction, E_x,

has an increased amplitude in the void regions and a decreased amplitude in the Si regions, which causes the average refractive index to be greatly reduced compared to a volume-averaging of the refractive index. For the electric field in the y-direction, E_y, the amplitude is practically uniform (there is some variation, but is too small to be seen in the plot), which leads to the field-averaging to being essentially equal to the volume-averaging. In essence, the optical wave interacts with the Si and voids proportionally in the y-direction, but prefers the voids in the x-direction, leading to a relatively lower refractive index.

This phenomenon is due to screening of the electric field. Under an x-polarized oscillating electric field, there is an oscillating charge at the interface of Si and void, as plotted in **Figure 5.5b**. This charge creates an electric field the opposite direction of the incident field, screening the electric field from the silicon. When planes of silicon are perpendicular to the electric field, there is maximum screening, reducing the strength of the electric field in the silicon. Conversely, the charges create an electric field in the voids that are in the opposite direction, which happens to be the direction of the original incident electric field, causing a buildup of the electric field in the voids. Combined, the light wave 'sees' less of the Si and more of the void, lowering the effective refractive index in that direction. When the light is polarized parallel to the pores, the electric field is parallel to the silicon-void interface, making charge buildup impossible.

The charge buildup also explains the electric field in the propagation direction, which cannot occur in uniform films. When the silicon plane is at an angle to the electric field, there is some charge buildup, which leads to an induced electric field normal to the direction of the silicon plane. This induced field has a component parallel to the propagation direction, leading to what you see in **Figure 5.5c**.

5.3.3. Comparison of simulated and experimental birefringence

The refractive indices of PSi and PSiO2 were simulated across a wide range of porosities and compared to the indices of PSi films measured using ellipsometry. A comparison of the birefringence is shown below in **Figure5.6c,d**. There is excellent agreement between the measured and simulated birefringence for $PSiO_2$, suggesting that our model is fairly accurate.

For PSi, there are similar trends, including a slight skewness, but the simulated birefringence is much higher than what was measured in actual PSi films. There are many possible explanations for this discrepancy. One is that nanoscale features in the PSi not accounted for in the model cause the screening effect to be less than what they would be otherwise, and that these features become relaxed during the oxidation process, so that $PSiO_2$ has roughly the same features as the model used in the simulation. Another is that the Si surface has a slightly different local refractive index compared to bulk silicon due to disruption by the chemical etch. Regardless of the reasons for this particular discrepancy, we can see that we have confirmed that structural birefringence is the predominant source of the birefringence found in PSi and $PSiO_2$ and that this birefringence can be simulated fairly accurately with a relatively simple model.

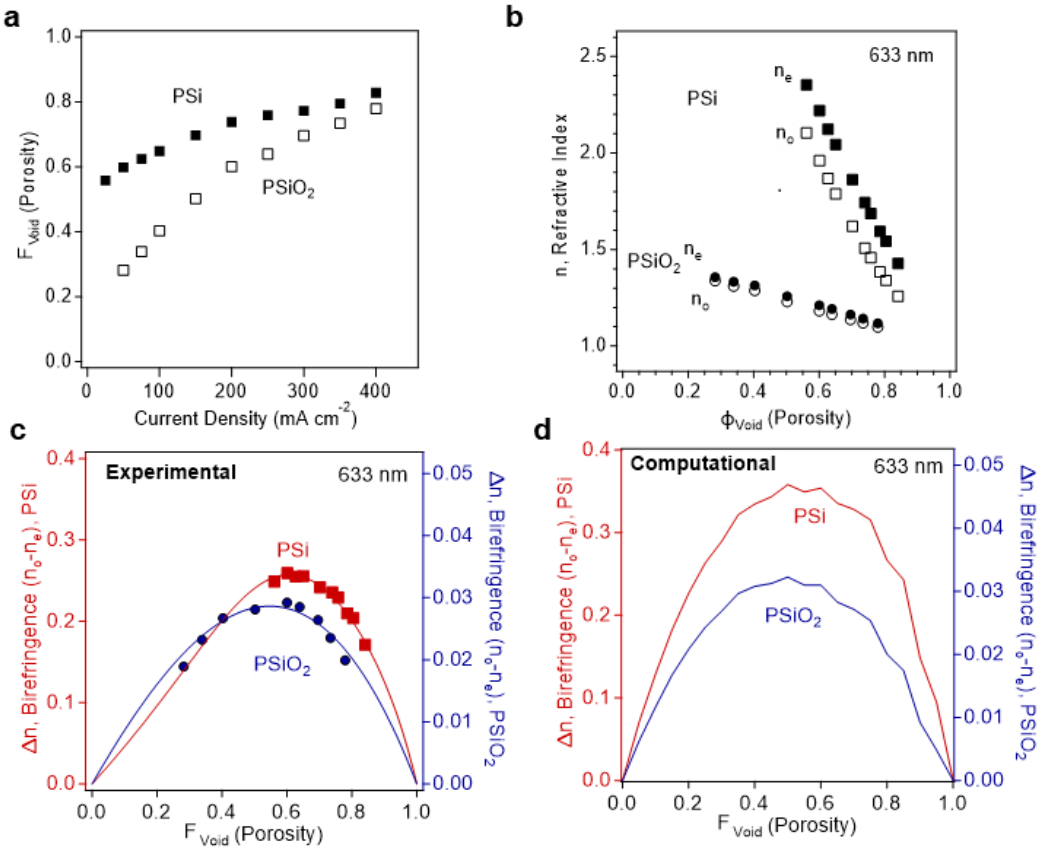

Figure 5.6. a) Porosity of the porous film for a range of current densities, before and after oxidation. b) Ordinary and extraordinary refractive indices of PSi and $PSiO_2$ for a range of porosities. Magnitude of the (c) experimental and (d) computational birefringence as a function of porosity for PSi and PSiO2. Plots created by Christian Ocier.

5.3.4. Optical PSi elements with engineered birefringence

PSi optics with gradient refractive indices (GRIN) are a common design, but these typically use only the ordinary index.[1] However, with a deeper understanding of how PSi birefringence changes with porosity, we can not only better predict how our optics will behave, but also use the birefringence as a design feature that lead to categorically new optical behavior. We fabricate square pillars using the above-described procedure with an etch profiles that are designed to give strong polarization-dependent optical characteristics.

Here we will discuss only one such optic, shown in **Figure 5.7**. This optic is designed to focus TM-polarized light to a single point and focus TE-polarized light to two adjacent points.[3] How these gradient refractive indices result in this particular pattern can be difficult to intuit, so we have prepared optical thickness curves for each polarization in **Figure 5.7c**. These optical thickness curves can intuitively be thought of as the shape of the lens that would lead to the same phase shift as this element if we used the thin element approximation. They are calculated by integrating the refractive index each polarization 'experiences' over a vertical line going through the structure. For TM polarization (electric field pointing into the paper) the light only ever sees the ordinary index so the integrated index has an approximately quadratic profile that causes focusing. For TE polarization, the side-regions of the element have a higher refractive index than the top and bottom, so the length of the optical path inside the side-regions has a large effect on the optical thickness. Instead of a single quadratic profile, there are two adjacent quadratic profiles, leading to two focal points.

[3] Note that language used in this paragraph could be slightly misleading, as the element is extended in one direction, so that it actually focuses to a line or lines rather than a point or points

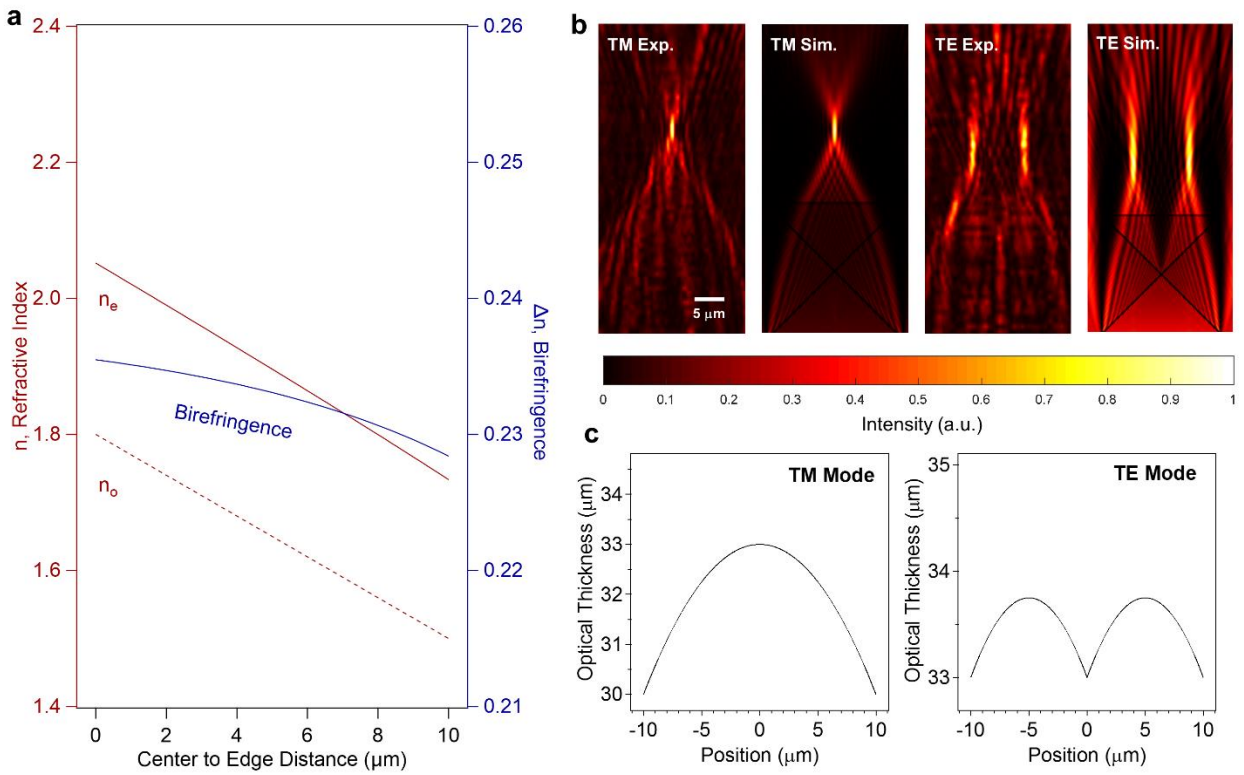

Figure 5.7. Optics of a square PSi element with engineered birefringence profile. a) Designed anisotropic refractive index of the element from the center of the element to the edge. b) Experimental and simulated intensity maps showing focusing of normally incident laser light for TM and TE polarizations. The black box indicates the boundaries of the simulated element. c) Vertically-integrated optical thickness profiles across x-position.

This element demonstrates the capability of using birefringence of PSi as a design parameter to achieve unique optical behavior. The current biggest obstacle lies in the separation of the elements from the substrate. In our current fabrication method there is no control over the position and orientation of the elements and damage of the elements is a common concern. We invite others to introduce more reliable techniques at this crucial step.

5.4. Introduction to Shaped Tunable-Index Lithography Using Scaffolding (STILUS)

It has been shown that PSi and PSi oxide can be filled with other materials in order to raise the refractive index and change optical properties. For instance, ALD of TiO2 inside a PSi DBR can cause a large shift in the bandgap.[21] But this does not address the biggest limitation of PSi, that, by and large, control over the optical properties exists in only one dimension. The

above described process of performing lithography on Si to define a relief pattern and then porosifying the film is one way of adding control in additional dimensions.[6] Still, the etching of a relief structure must occur conformally, limiting the kinds of designs that can be made. But what if we were to reverse these steps – to define a PSi film, and then use lithography to add lateral control over the optics?

We have recently developed a new technique, called Shaped Tunable-Index Lithography Using Scaffolding, or STILUS,[4] that uses direct laser writing (DLW) inside of a film of PSi or $PSiO_2$. Not only can we lithographically define optical elements in 3D space inside PSi, but we can do so while also using gradient refractive indices.

As a quick introduction to STILUS, an SEM cross-section of a STILUS element is shown in **Figure 5.8**. This is simply a PSi film whose pores have been filled with a photoresist. Regions have been selectively exposed to a laser and crosslinked. Development washes the unexposed photoresist away, leading to adjacent regions of PSi with different filling and refractive indices.

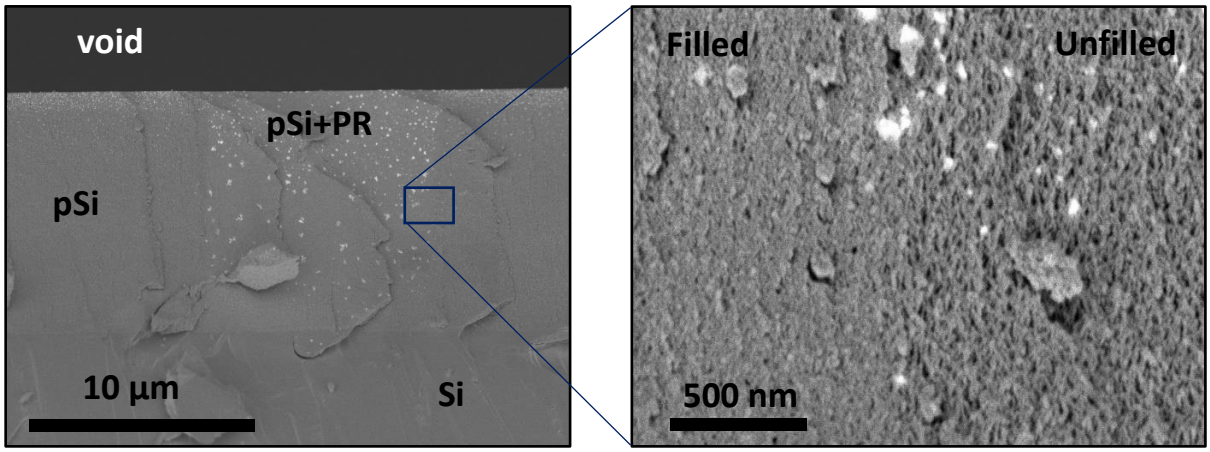

Figure 5.8. SEM cross-section of a region of PSi uniformly exposed via STILUS.

5.4.1. Background of Gradient Refractive Index Optics with Direct Laser Writing

DLW has been used before to create GRIN optics. These have been performed in three ways: creating a 3D microlattice that functions as an effective medium at sufficiently large wavelengths[22], [23], controlling the dosage to control the amount of reaction at a nanoscale level,[24], [25] and the induction of localized damage directly in glass.[26]–[28]

[4] STILUS was chose as a name to emphasize the spatial control that can be achieved with this technique, the elements are fabricated just as one would write with a pen

The first one of these, the fabrication of a microlattice, has seen the most recent attention.[22], [23], [29] Examples of this technique are shown in **Figure 5.9ab**. With the advent of commercial DLW tools, the creation of very complex shapes with extreme aspect ratios has become easily achievable. 3D lattices are written by rastering the beam back and forth with regular spacing and adjusting the laser power to change the porosity of the lattice. At wavelengths far above the lattice spacing, it functions as an effective medium with a gradient refractive index. At wavelengths close to the lattice spacing, it functions like a photonic crystal. The outside boundary of the lattice is given a particular shape to incorporate geometric optics. The biggest limitation of this technique is the size at which gradients can be created. The smallest lattice that, to my knowledge, has been demonstrated has a spacing of 2µm, which makes an EMA work well at wavelengths about 20µm and above. Bringing this technique to visible wavelengths would require lattices <100nm, well below the capability of conventional DLW. Secondly, it reach the refractive index of the background material, air; there is a lower limit of the fill-fraction of the lattice, below which the lattice is not mechanically stable. The Luneburg lens in **Figure 5.9b** does not include the outer edges of the lens due to this issue, so it cannot perform as well as it ideally should.

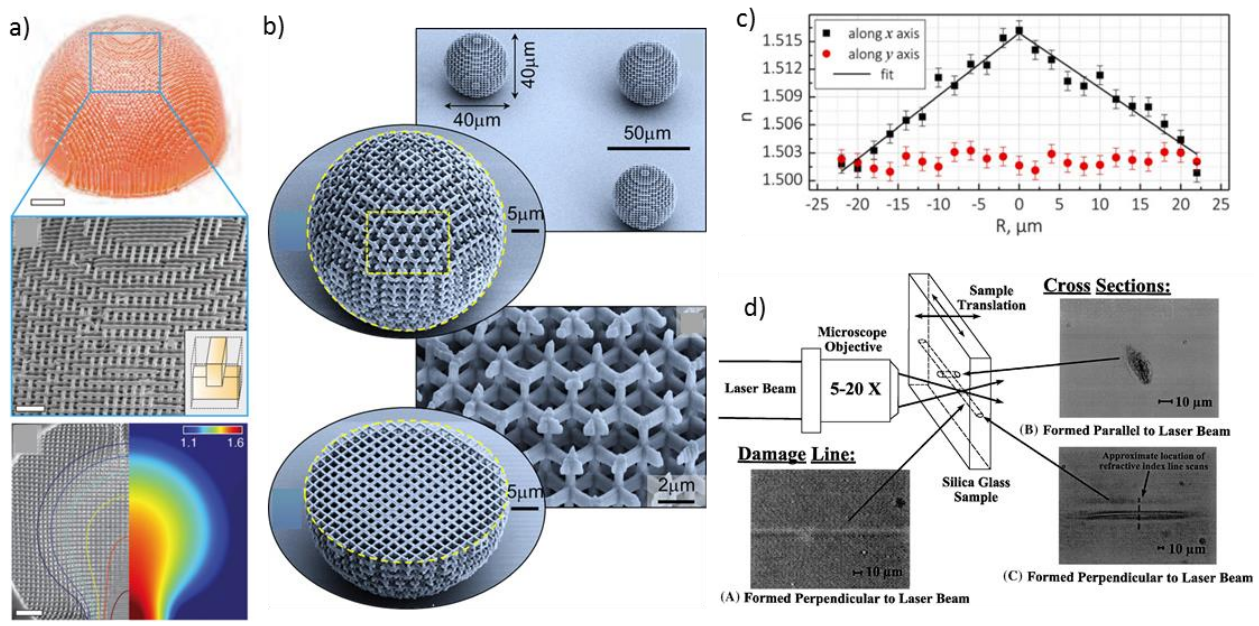

Figure 5.9. Examples of gradient refractive index lenses with DLW. a) THz-frequency lens designed to have zero Petzval curvature based on subwavelength 85µm woodpile lattice.[22] b) Mid-IR Luneburg lens with 2µm lattice spacing.[23] c) Visible-wavelength flat-lens based on controlling the crosslink density of SZ2080 photoresist.[24] d) Schematic and cross-sections of a waveguide written into glass based on localized laser damage.[26]

The second method, directly controlling the amount of chemical change in a photoresist, is the least common technique. Here, a laser focus is rastered through a photoresist while controlling the laser power, but there is a continuous solid film.[24] The gradient in refractive index is controlled by the density of the photoresist after development, which is controlled by the local dosage. Unlike the previous technique, this method is suitable for visible wavelengths but cannot be patterned in complex 3D shapes due to low mechanical stability of the resist at low crosslink densities.

The third method, using glass damage, is commonly used for etching waveguides in glass.[28] Two explanations for this method are that 1) the intense light causes the formation of trapped excitons in the glass which introduce optical absorption transitions at UV wavelengths and thus a small refractive index increase in the visible, or 2) localized heating leads to densification of the glass matrix. Variations of this technique have led to the creation of more complex structures such as nanogratings smaller than the focus of the laser.[30] Unfortunately, I have been unable to find any examples of this technique used for the creation

of more complex optics such as those demonstrated using the first technique; there may be some limitations with this method that makes more complex structures more difficult.

5.4.2. Using PSi and $PSiO_2$ Scaffolding

The method we are introducing, STILUS, conceptually close to second technique described above. It works not by fabricating a subwavelength lattice or creating localized damage, but by controlling the local quantity of crosslinked resist. The biggest limitations of that method are that there is little capability for 3D geometric control since lower crosslink density resist has less structural integrity, and that there is only a small range over which the refractive index can be tuned since lower crosslink densities also lead to less resistance to development. STILUS avoids these issues because the PSi and $PSiO_2$ work as a scaffold that supports the resist, preventing both mechanical collapse of the structure and complete development of the low crosslink density resist.

A cartoon of our explanation of this support compared to conventional lithography is shown below in **Figure 5.10**. In both, the focus of the laser beam has a roughly Gaussian profile, leading to a roughly Gaussian distribution polymer chains.[24] In conventional lithography, a necessary density of these chains is necessary to form a solid. During development, unconnected chains polymer chains are removed and the resist shrinks due to removal of shorter chains in the solid part of the resist, leaving only a binary of solid resist, and void. In STILUS, polymer chains that are not sufficiently connected to the main piece of resist can still avoid removal during development if it is sufficiently attached to the PSi scaffold, leading to a slight increase in the refractive index in regions with low density of remaining resist.

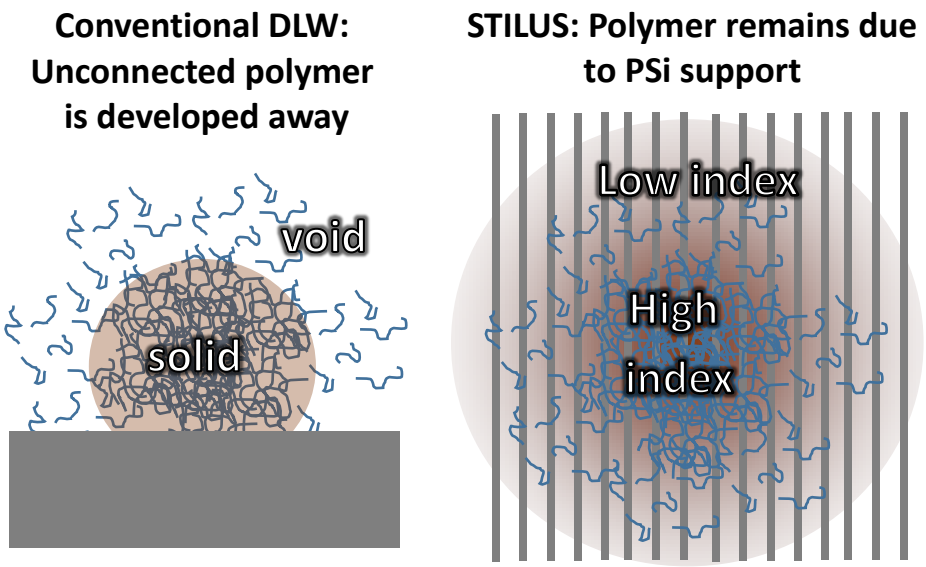

Figure 5.10. Cartoon comparison between conventional DLW and STILUS. Both are exposed to a Gaussian intensity distribution and approximately Gaussian densities of polymer chains (blue squiggles). When DLW is performed on a flat substrate, the polymer chains resist development if they are connected to a large enough mass (pink circle), leading to a binary solid/void structure. When performed inside a PSi, polymer chains can be supported by the scaffold, leading to gradients in refractive index.

Why does the resist stick to the PSi? We believe this is due to chemical grafting of the resist monomer onto the surface of the PSi or $PSiO_2$. It has been shown that primary alcohol groups on a dissolved molecule can react with silanol groups on the surface of silicon oxide via alcohol decondensation, forming a self-assembled monolayer (see **Figure 5.11a**).[31] In our DLW process, we use pentaerythritol triacrylate (PETA) which has three acrylates and one primary alcohol group. Silanols appear on the surface of native silicon oxide which provide a grafting site.[32]

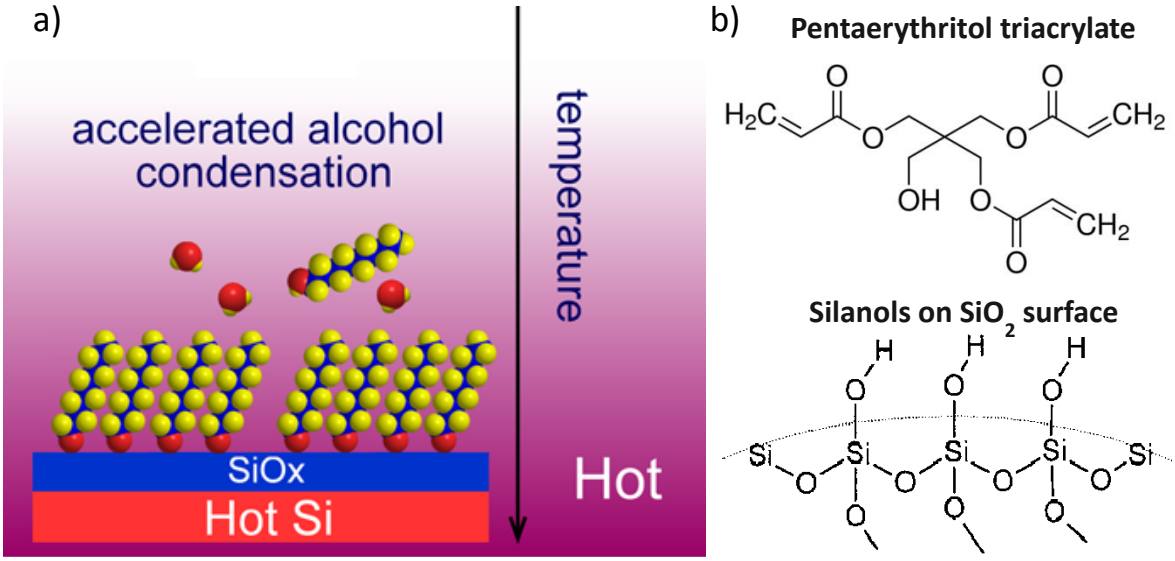

Figure 5.11. Expectation of grafting of monomer onto the surface via dehydration reaction. a) Cartoon of alcohol condensation technique onto silica surface.[31] b) Chemical structures of the resist resin monomer, pentaerythritol triacrylate (PETA),[33] and silanols on the surface of SiO_2.[34]

In order to see whether a self-assembled monolayer (SAM) of PETA could be forming on the silicon surface, we try to perform the same alcohol decondensation reaction[31]: we place a piece of silicon wafer with a native oxide in a solution of PETA overnight in an oven at 85°C, then develop and rinse PGMEA to remove the PETA. This wafer and an untreated wafer are measured with ellipsometry. We find that there is a significant change in the ϕ and Δ parameters that is explained by a thin (~1.5nm) film with a refractive index of n~1.48, consistent with our explanation. This lead us to repeat the experiment with the flat silicon wafer replaced by a film of PSi. This time, we increase the development time and temperature to overnight at 85°C to ensure that the PETA was able to fully develop. Ellipsometry was used to extract the effective refractive index of the film, shown below in **Figure 5.12**. A small increase in the refractive index can be seen, consistent with our explanation of the formation of a PETA self-assembled monolayer on the silicon oxide surface. We would like to see further study to verify the mechanism, but for the time being we will move on to studying other characteristics of this process.

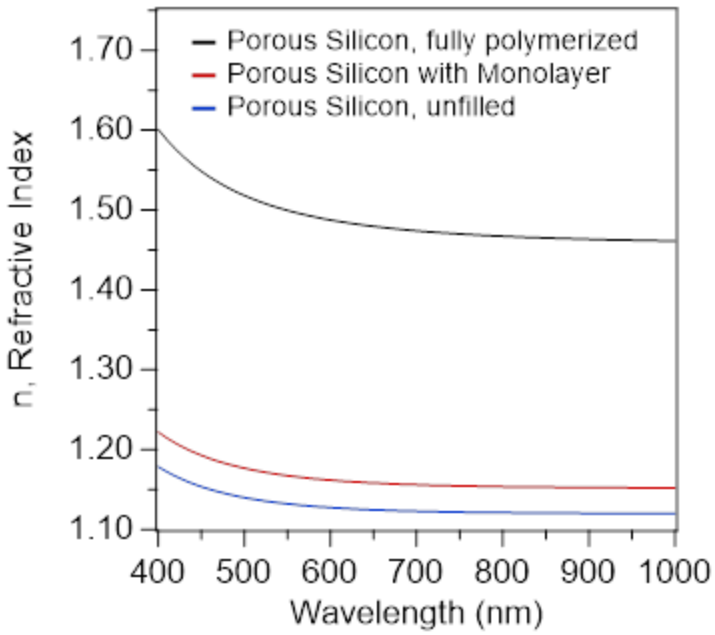

Figure 5.12. Refractive index spectra of a PSi film before (blue) and after (red) heated PETA treatment, and a PSi film that was fully crosslinked using DLW for comparison).

5.4.3. Experimental Process of STILUS

In this section we will discuss the experimental process of creating an optic using STILUS. A broad overview is presented in **Figure 5.13**. In short: a PSi film is etched, moved to a transparent substrate, vacuum casted with photoresist, exposed via DLW, and developed. First, a silicon wafer is electrochemically etched using the method discussed in Section 5.1. Constant current density is used for etching PSi for micro-optics such as lenses, and alternating high and low current densities are used for creating Bragg stacks.[35] After defining the PSi, a more concentrated HF solution is prepared and the electrochemical etch is continued such that the PSi film is nearly completely detached from the substrate.

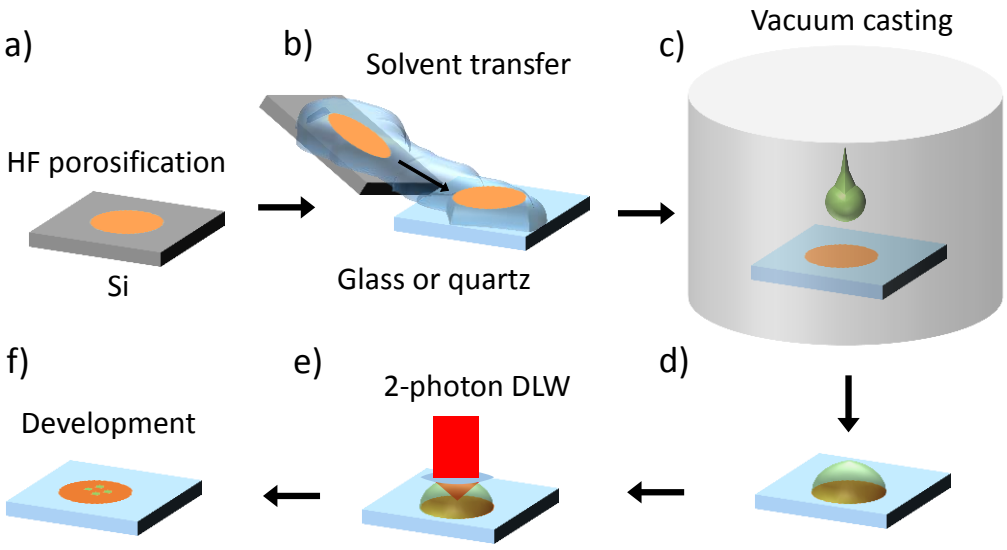

Figure 5.13. Schematic of process to create a micro-optic using STILUS. a) A PSi film is prepared by electrochemical etching. b) The PSi film is moved to a transparent substrate by solvent transfer. c) A droplet of PETA is dropped onto the PSi while held under vacuum. d) The vacuum jar is quickly vented to infiltrate the pores. e) Two-photon DLW is performed on the film. f) The film is developed in PGMEA and rinsed.

Possibly the most finicky step in this process is the transfer of the PSi to a transparent substrate. DLW cannot be performed on a reflective substrate like Si due to backside reflections at the interface of PSi and bulk Si (much like the backside interference discussed in section 2.3). We transfer to either glass or quartz substrates: glass because it is cheap, and quartz because it can withstand the temperatures needed to oxidize the PSi. We move the film via a solvent transfer technique using ethanol.[21] The nearly detached PSi film is removed from the substrate due to solvent stresses and the PSi film is floated on the ethanol and flowed toward the target substrate. The ethanol quickly evaporates, leaving the PSi weakly stuck to the substrate. Cracking and breaking of the PSi is common as the PSi dries. We have found that spraying hexane vapor at the PSi while the ethanol is drying is effective at minimizing cracking in the substrate, possibly due to lowering of the surface tension of the ethanol. Oxidation, if desired, is performed after transferring. Oxidation is performed in a tube furnace with pure oxygen using a slow ramp to 925°C. Oxidation also has a tendency to introduce defects into the film.

Vacuum casting is used to impregnate the pores of the PSi with photoresist for DLW.[36] The photoresist we use is IP-dip, a liquid, chemically amplified resist made for the Nanoscribe whose main component is PETA (IP-S also works with this method). The photoresist must not be exposed to white light, so this part of the procedure is performed in a darkroom. The PSi or $PSiO_2$ is placed in a vacuum jar along with an apparatus to apply resist onto the film. Vacuum is pulled to evacuate the pores of the PSi and a few seconds after the pressure is stabilized a droplet of resist is dropped onto the porous film. Our low tech but functional apparatus to control the resist is simply an inverted glass vial on a ramp; to time the application of drops, the flow rate of the resist can be controlled using the slope of the ramp and the quantity of resist. Once the drop is applied, we wait for the drop to spread to cover the PSi film, which is sometimes encouraged by tilting the jar. The vacuum jar is then quickly vented. We suspect that slow ventilation of the jar can lead to incomplete filling of the porous film, though we are unsure of what the mechanism for that could be. After casting, the film covered in resist is stored in the dark and allowed to rest overnight. We have encountered highly variable results if the exposure is performed shortly the casting. This may be due to the vacuum lowering the concentration of O_2, or other volatile compounds dissolved in the resist, that have important effects on the DLW process; the 'resting' period may allow the concentration of these compounds to normalize.

A Photonic Professional by Nanoscribe is used to expose the resist with 2-photon DLW. This instrument contains a Ti:sapphire laser that is focused through an objective lens onto a sample stage. It uses dip-in lithography (DiL), where the tip of objective lens is immersed in a liquid photoresist, which enables tighter focuses.[29] Typically, the focus rastered at a high speed across the sample back and forth, proceeding line by line and then layer by layer from the substrate to the top of the structure. There is no post-bake step in this process since any photoinitiators would diffuse in the liquid resist before baking could be started. Instead, the resist is locally baked from absorption of the laser and crosslinking occurs practically instantaneously and terminates quickly. This makes the process a little sensitive than might be assumed: we have found that the dosage of a particular area depends on what has been written nearby, possibly from the buildup of heat.

Development is simple. Samples are removed from the Nanoscribe, returned to the darkroom, and developed overnight in PGMEA. They are placed in a fresh bath of PGMEA for a few minutes, then in IPA, and finally blow dried with N_2.

5.5. Effective refractive index of STILUS films

To measure the relationship between the dosage and the optical properties, we measure the effective refractive index of PSi films treated with STILUS. For measuring the effective refractive index of clean PSi and PSiO2 films, we perform variable angle ellipsometry (VASE), usually on a Si substrate. Unfortunately, the ellipsometry tools readily available to use have spot sizes larger than a millimeter and the largest spot we can make with STILUS is about 100µm. This lead us to use microspectroscopy and later, confocal microscopy in order to measure the refractive index.

5.5.1. Measuring Refractive Index with Microspectroscopy

In order to measure the effective refractive index of the film, we combine ellipsometry measurements with microspectroscopy measurements.[37] In microspectroscopy, a white light source is focused onto a sample on a slide and the reflected and transmitted light is measured in a spectrometer so that optical information of only the small spot (10's to 100's of µm) is collected. By itself, microscopy returns only spectral transmission and reflection amplitudes, not enough to determine the thickness and refractive index of a film, unlike ellipsometry. To measure the effective refractive index of the exposed areas, we first perform ellipsometry on the unexposed areas, which tells us the effective refractive index. Cylindrical shapes with approximately 100µm diameter are written with a sweep of laser powers through the full depth of the porous films. Microspectroscopy reflection and transmission measurements are performed on these cylinders and on regions close to the cylinders. There is variation in the thickness of the porous silicon, but this difference is minimal for spots just 100's of µm apart.

After these measurements, transfer matrix method (TMM) models are used to fit the local thickness of the PSi or $PSiO_2$ film based on the microspectroscopy spectra of the clean film

the ellipsometry-measured refractive index spectra of the clean film. Then, once the thickness of the film is established, the same FFM fits are performed on the exposed regions of the film, giving the effective refractive index. In these calculations, the effective refractive index is modeled as a Cauchy material with an Urbach absorption tale.[38] This model is more effective at longer wavelengths – the Cauchy model is not very effective for Si at blue or NIR wavelengths, but performs reasonably well at the red end of the visible spectrum. In the TMM calculations of transmission and reflection spectra, the PSi and PSiO2 films are treated as isotropic, since in the microspectroscopy measurements the propagation direction is nearly parallel to the pores so only the ordinary index affects the light (some of the light has a lateral component due to focusing, which can also limit the strength of the interference fringes).

One issue with this method for refractive index measurement is that sometimes the microspectroscopy spectra of the exposed regions do not clearly follow a Fabry-Perot fringe pattern. This makes fitting of the refractive index impossible. This can happen when the depth of the exposure does not exactly match the thickness of the porous film, shown in **figure 5.14a**. Clean Fabry-Perot fringes are seen when there are reflections at exactly two interfaces, but if the DLW stops too early or too late as it progresses upward through the film, there can be additional interfaces that cause interference. The existence of IP-dip crosslinked above the structure or PSi that has not been exposed view DLW will cause complications in the transmission and reflection spectra.

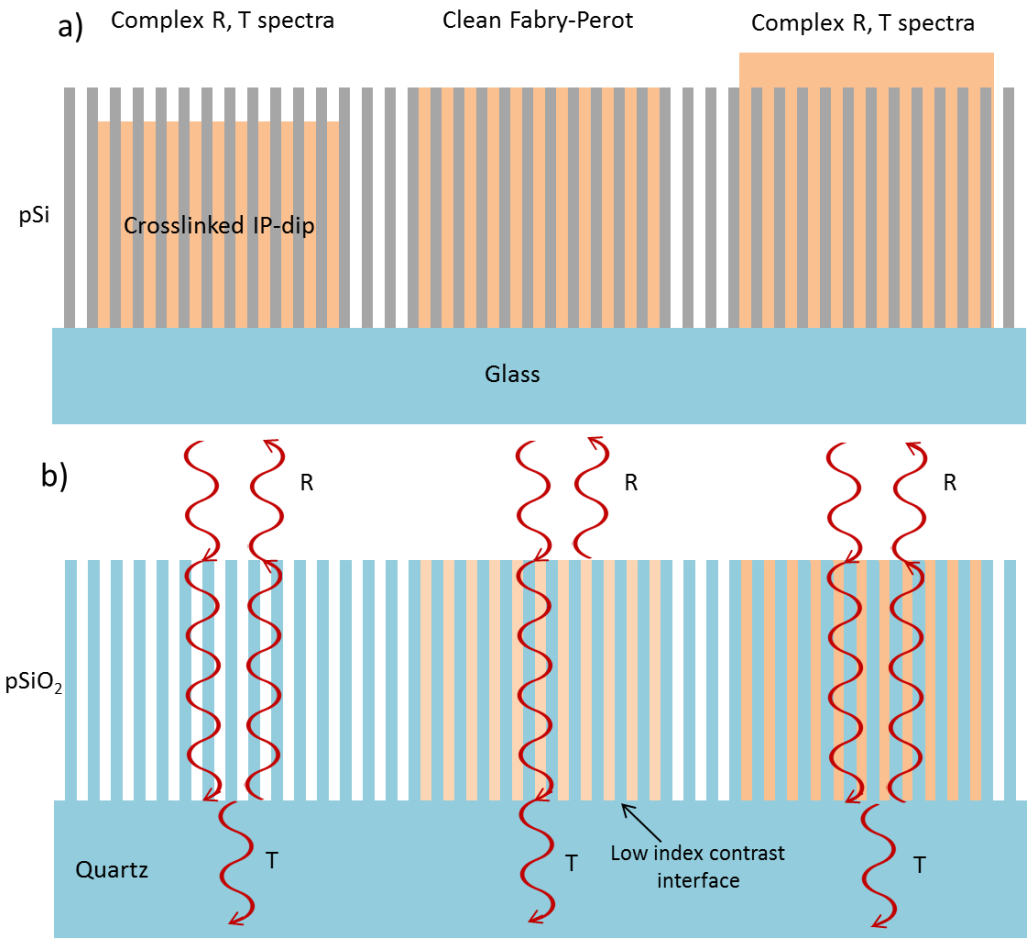

Figure 5.14. Cartoons of a) the results of underestimating (left) and overestimating (right) the depth of a PSi film, and b) the disappearance of Fabry-Perot fringes when a PSiO2-IPdip film has a similar effective refractive index as glass.

Another issue that we encountered in this method is that the Fabry-Perot fringes disappeared for a range of dosages for $PSiO_2$. This is due to the index matching of $PSiO_2$/IP-dip to the quartz substrate. The Fabry-Perot fringes appear to the interference between the reflections from the interfaces at the top and bottom of the $PSiO_2$ film, as shown in **Figure 5.14b**. In a plain $PSiO_2$ film or a fully exposed $PSiO_2$/IP-dip film (IP-dip has a significantly higher refractive index than quartz), the film has a refractive index much different from either the quartz substrate or air superstrate, so there are significant reflections at both the top and bottom of the film. In between these cases, however, there is a dosage where the effective index of the film matches the index of the quartz, which means there is no reflection from this surface and thus no Fabry-Perot fringes. To measure this we will need to look at other methods.

One solution is to use a different substrate. A convenient solution would be to leave it on the silicon to take advantage of the strong reflections from the silicon surface. However, strong reflections also lead to issues with the interference fringes during the exposure process. **Figure 5.15** shows the formation of fringes in the photoresist due to substrate reflections. The fringes are weaker at the top of the film due to the reflected light being more out of focus as the focal spot becomes further from the reflective substrate. At a high enough dosage, these fringes cannot be seen since everything becomes fully filled with polymer. As these fringes will greatly change the effective refractive index, less reflective substrates must be used to for effective refractive index measurements. It may be possible to create a built-in antireflection coating for the interface between Si and Si/IP-dip by creating a lower porosity layer of PSi at the end of the porosification process.

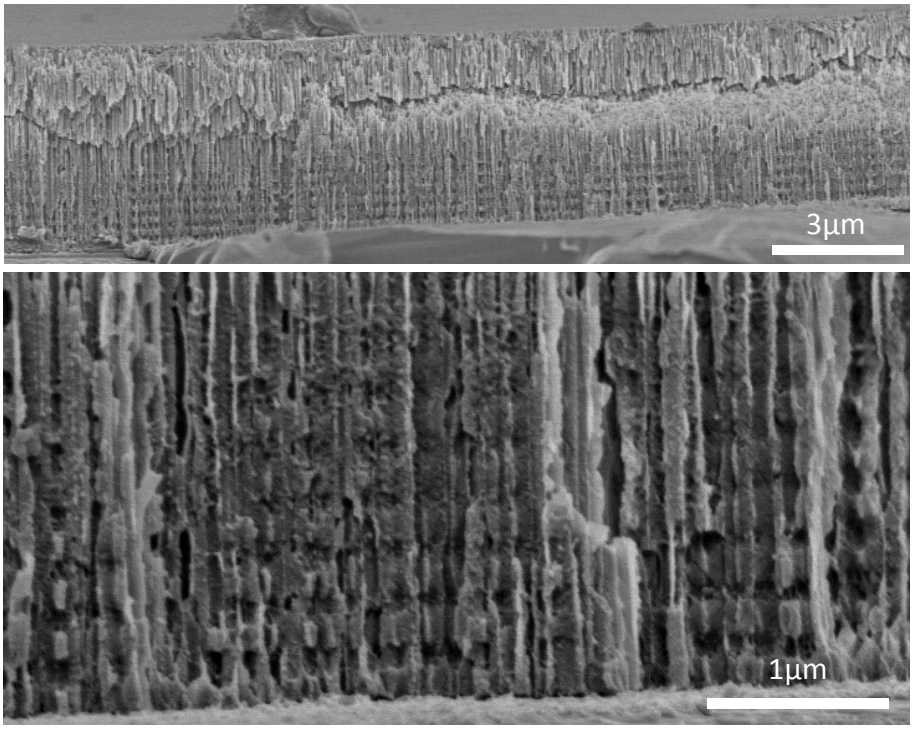

Figure 5.15. SEM cross-section of PSi on Si substrate with IP-dip crosslinking in layers due to backside reflections from Si substrate.

Aluminum oxide was used to introduce a reflective interface that is sufficient for creating Fabry-Perot fringes for refractive index measurement without causing much interference during the DLW. Al_2O_3 was deposited on quartz substrates before PSi was transferred on top of the substrate. Just a few nanometers of Al_2O_3 is sufficient to cause

reflectance and the short distance between the top and bottom of the film means that the interference pattern can be approximated as being due to just 2 interfaces. Extracted refractive index data is shown in **Figure 5.16**.

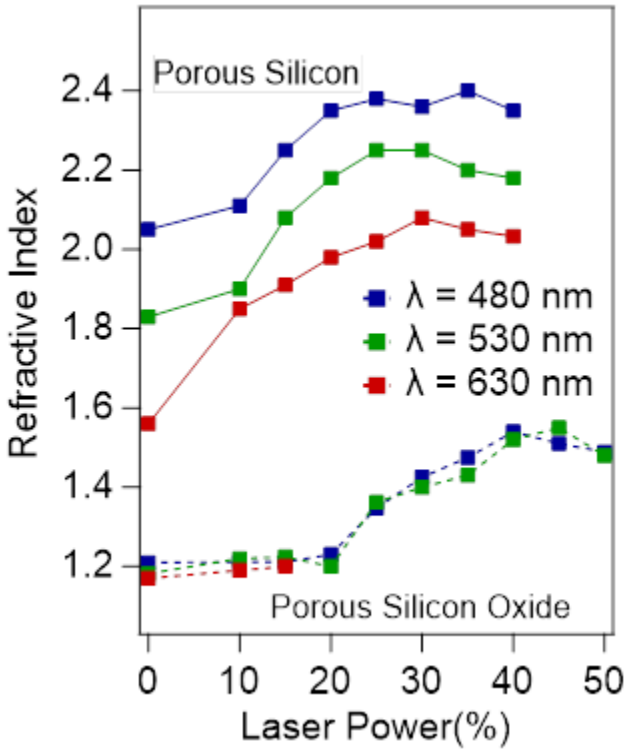

Figure 5.16. Refractive index of PSi/IP-dip and $PSiO_2$/IP-dip for sweep of dosages. Refractive indices are calculated at three wavelengths 480nm, 530nm, and 630nm (red, green, and blue) based on Cauchy fits. The laser power is displayed as a percentage of the maximum laser power (50mW).

There are a few issues with this technique that remain. Writing cylinders 100µm in diameter and approximately 10µm tall is a very time consuming exposure for DLW and this sweep of measurements needs to be repeated for each change in the porosification conditions. Studying how the refractive index changes with both dosage and porosity would be very slow and expensive. We have also found that there is a non-linear component to the writing: larger and denser elements tend to be somewhat different from smaller and sparser elements. Unfortunately, our equipment cannot measure much smaller elements. The high rate of error in write-depth, as shown in Figure 5.4.4.1.1a, also remains a problem.

5.5.2. Measuring Refractive Index with Confocal Microscopy

The above issues led us to pursue an alternate technique for measuring the effective refractive index: measuring the refraction of light through prism structures. Refractometry is a common technique whereby the angles of refraction of light passing through a prism are used to precisely measure the refractive index.[39] Specifically we measure the refractive index with a variation of a Fresnel biprism. A Fresnel biprism is a prism that creates a linear interference pattern when light is directed onto it, an alternate form of Young's double slit experiment that doesn't require the second pair of slits.[40] Fresnel biprisms are often used to measure wavelengths of optical sources, as well as the refractive index or thickness of films. We have not seen, however, use of this technique to measure the refractive index of the biprism itself; which is what we do here to determine the effective refractive index our PSi/IP-dip composites.

A prism about 20-30μm across, oriented as shown in **Figure 5.17**, is written into the PSi or PSiO2 with a set dosage. This prism is placed inside a confocal microscope with a laser directed upwards through the substrate. The laser light refracts through the prism, so that two plane waves are diverted toward each other at angles depending on the refractive index of the light. These two plane waves have a well-defined interference pattern: alternating planes of constructive and destructive interference. The spacing of these fringes is equal to inverse of the propagation-vector difference of the planewaves as shown in **Figure 5.17b,c**, causing low refractive index values to yield broadly spaced fringes and high refractive index values to yield finely spaced fringes (an explanation of the math of plane wave interference is presented in section 2.2), which is a result of only the angle and refractive index of the prism.

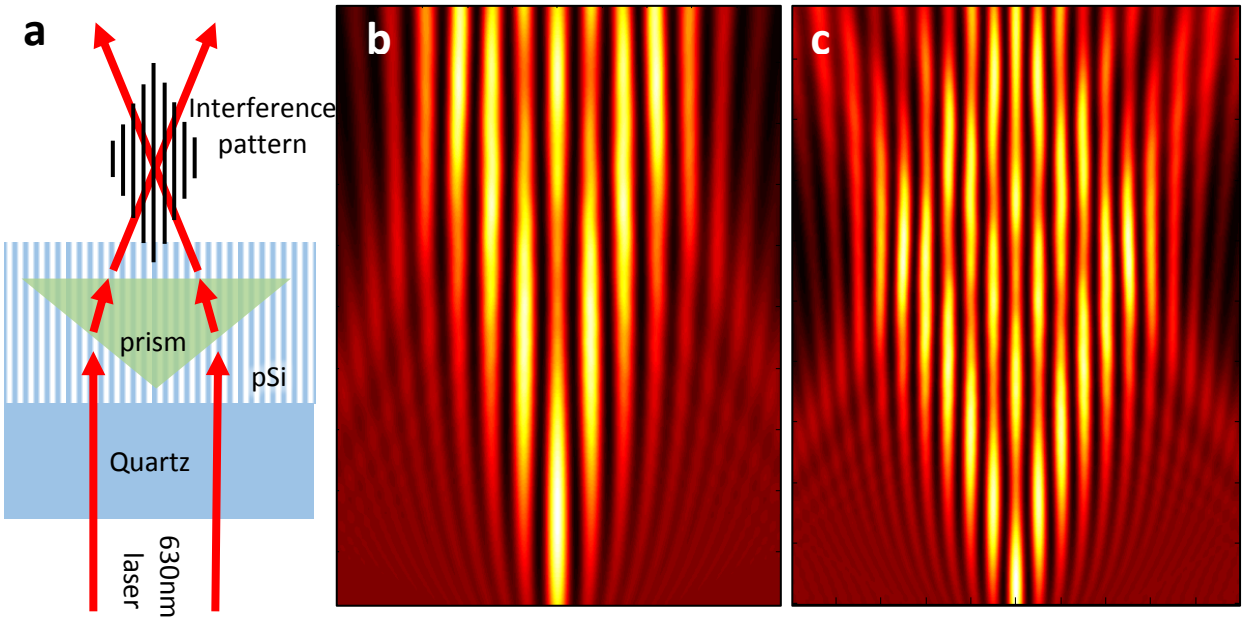

Figure 5.17. Refractive index measurements by interference from prism refraction. A) Cartoon of the interference pattern generation: the prism causes refraction of the incident light toward each so that they overlap causing interference fringes with a period that depends on the refractive index of the prism. b,c) Depth scans in confocal microscopy showing local intensity of the interference pattern.

The written prisms have an interference pattern that closely matches the simulated interference (**Figure 5.18a,b**). The spacings of the interference pattern are quantified by finding the peaks of the 2D Fourier transform (**Figure 5.18c,d**). Simulations are used to generate tables of the fringe spacing across a range of refractive indices, which lets us tie the fringe spacings found at each dosage to a refractive index.

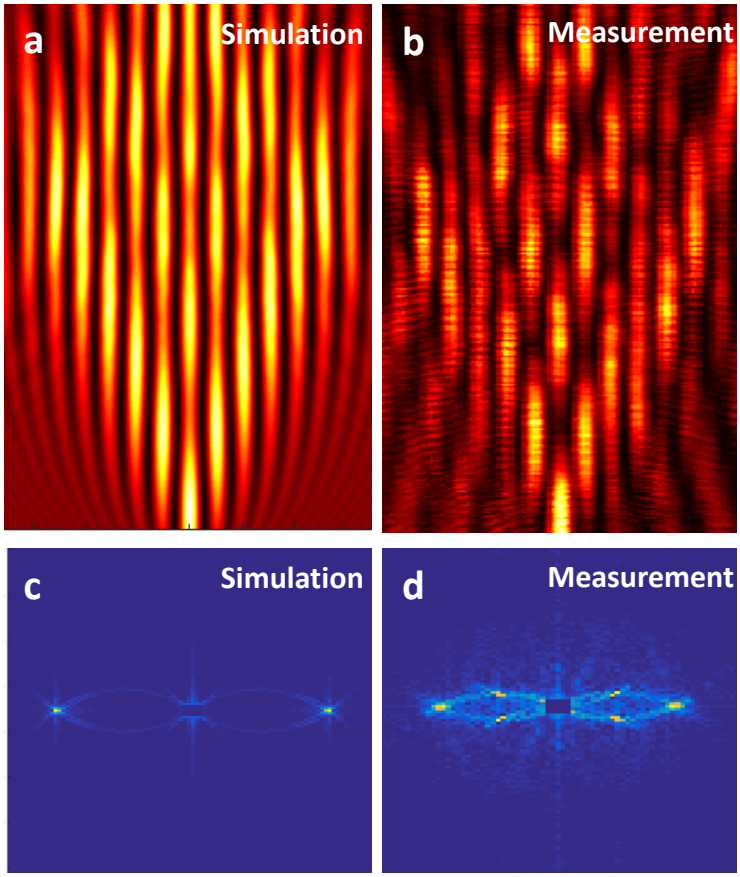

Figure 5.18. Simulated (a) and measured (b) confocal depth scans of birprism interference pattern. (d,e) 2D Fourier transforms of the interference patterns, where the peaks are used to quantify fringe spacing.

This method of refractive index measurement has useful advantages as well as serious limitations. One is that it takes very little time to fabricate the prism, since it is much smaller than the disks necessary for microspectroscopy. However, this is balanced by the need to perform confocal microscopy, requiring a time-consuming scan. Since the interference is only lateral, the fringe spacing does not depend on the distance from the top or bottom of the porous film, so precise registration is not necessary. Unfortunately, the STILUS process is also susceptible to refraction: the focusing laser will have its working distance changed due to refraction between the immersion IP-dip and the PSi/IP-dip. This will cause the slope of the actually prism to be different from the design if the refractive index change is not accounted for in the design. Correcting this involves knowing the refractive index of the porous film filled with unexposed IP-dip. We assume this value is given by the measured refractive index of the fully exposed film found using the microspectroscopy method. Additionally, there appears to be a

temperature sensitivity causing large or densily spaced elements to give different results from small or sparse elements; the prism can be made in a variety of sizes to adjust for this, though this issue is not well understood. There are also a few issues that we don't know how to solve: occasionally the prisms don't create a clean interference pattern and sometimes the fringes occur at an angle instead of orthogonal to the surface. Nevertheless, we consider this method to be mostly reliable.

The refractive index spectra measured using this method is shown below in **Figure 5.19.** This data has similar trends as **Figure 5.16**. The extracted refractive index of the $PSiO_2$ prisms is much higher than expected, to the point we cannot believe the data; there must be some issue with how these elements were made or measured. We speculate that the differences in PSi are due to the different sizes of the elements. The larger elements used in the microspectroscopy measurement require much longer exposures and so an increase in the temperature of the film is expected, leading to more rapid crosslinking. Unfortunately we currently do not have a method of finding the local temperature of the film during the writing process so we have not been able to test this.

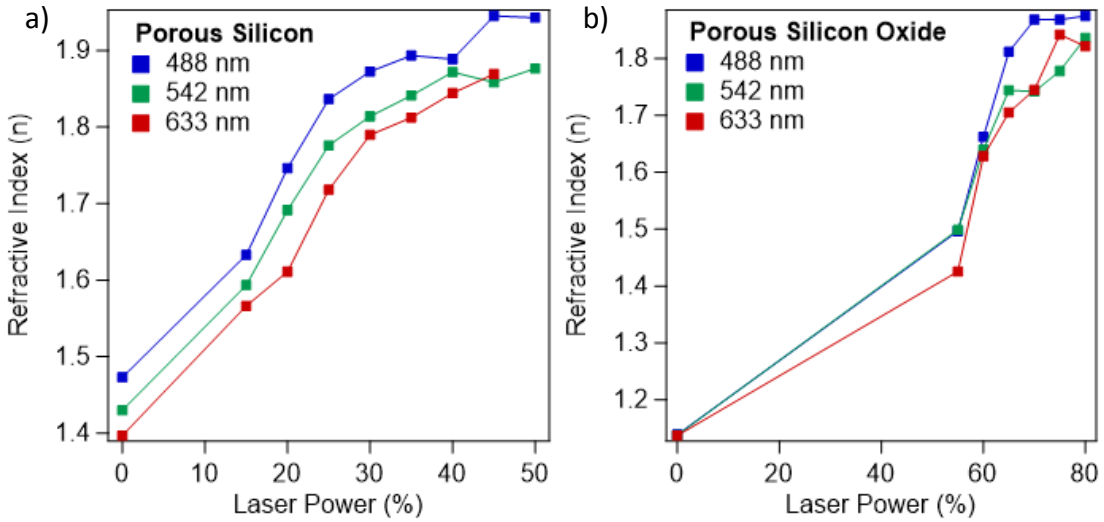

Figure 5.19. Refractive index spectra of STILUS-treated (a) PSi and (b) PSiO2 at varying laser powers using confocal microscopy at 3 different wavelengths. Figures created by Christian Ocier.

Another trend noticed in both **Figure 5.16** and **Figure 5.19** is that $PSiO_2$ requires a longer exposure time than PSi. There are a few explanations for this. One is that there is local field enhancement and diminishment in PSi and $PSiO_2$ respectively. As the photoresist is activated

by 2-photon absorption an enhancement or diminishment of the electric field has a major effect on the effective dosage. **Figure 5.20** shows the effect of field enhancement/diminishment due to the refractive index profile. Due to screening effects of the Si, the photoresist in PSi is exposed to a more intense electric field. In $PSiO_2$, the opposite happens since the SiO_2 has a lower refractive index than the photoresist. Based on this screening effect, photoresist in $PSiO_2$ would need 16% more power than in PSi to achieve the same effective dosage. However, 16% is not enough to explain the difference in the power at which crosslinking occurs.

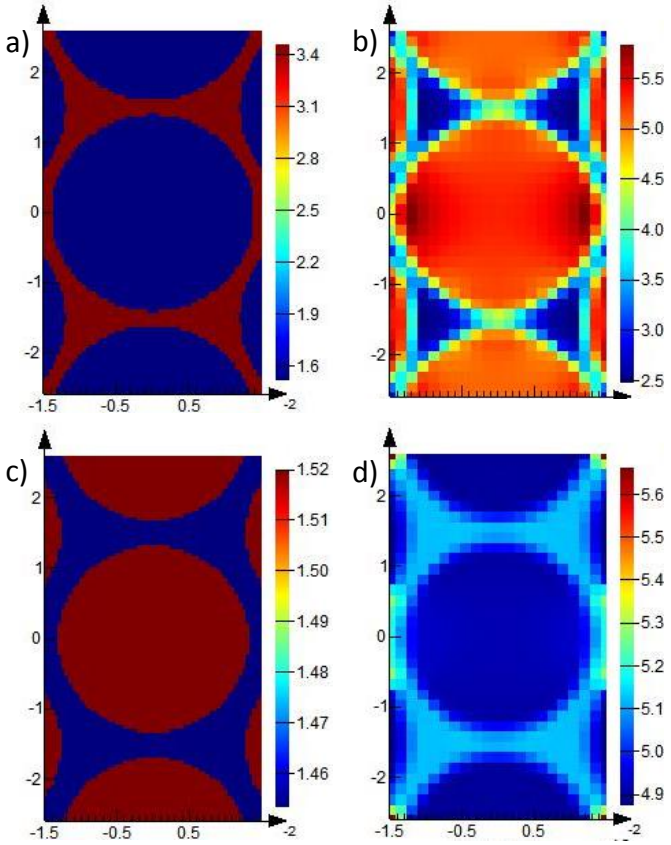

Figure 5.20. Refractive index profiles (a,c) and local electric field intensity (b,d) for PSi (a,b) and $PSiO_2$ (c,d) films. There is field enhancement for the photoresist for PSi and field diminishment for the photoresist for $PSiO_2$.

Another explanation for the difference in power needed to expose photoresist in PSi or $PSiO_2$ is that there is a second exposure mechanism in PSi. We have found that the photoresist can be exposed in ways that are unexpected. **Figure 5.21** shows PSi that was exposed with squares using a sweep of powers. In the figure, each square is surrounded by a circle with

rainbow coloration. These circles are always the same size and appear only on PSi films. The circles appear to be caused by exposure from the LED used in the nanoscribe for camera inspection, since they appear only on locations wherever the stage of the Photonic Professional is held for extended periods of time. The LED is near 700nm, well above the wavelengths at which IP-dip absorbs using single-photon absorption and the power is far too low to cause 2-photon absorption. This indicates that there is an additional mechanism for the exposure of IP-dip in PSi besides 2-photon absorption. We speculate that it is due to absorption in the silicon causing excitation of electrons that transfer energy to the IP-dip photoresist which initiates crosslinking. We find that performing oxygen plasma oxidation of the PSi prior to DLW diminishes the appearance of the circles, which is consistent with this idea since a thin oxide layer would inhibit energy transfer from the silicon to the resist. To completely eliminate the appearance of these circles, the inspection LED should be turned off during DLW and the samples should not be examined under microscope until after development.

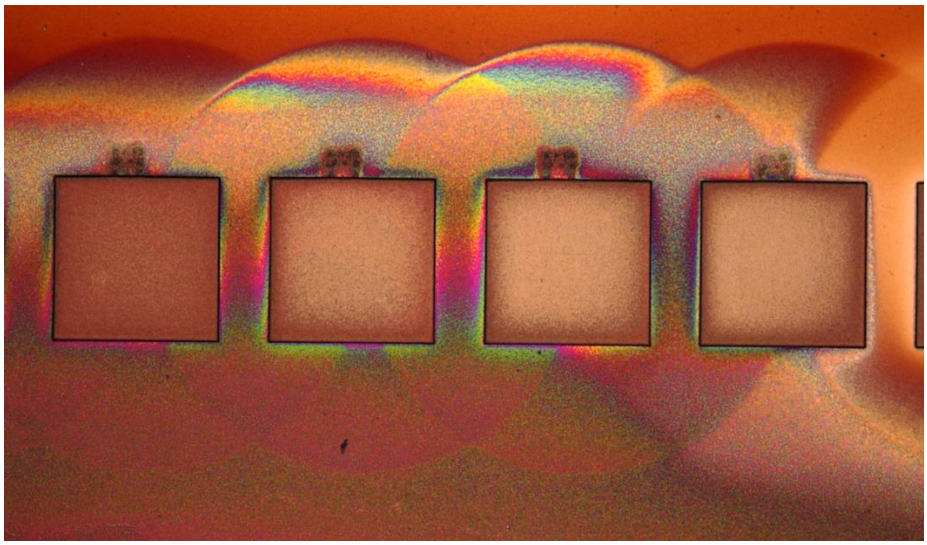

Figure 5.21. Optical microscopy of PSi exposed with 80µm squares. The circle around each square corresponds to exposure from the inspection LED.

5.6. 3D optical elements in porous silicon

Knowing how the refractive index of STILUS elements changes with a laser power, one can design a 3D exposure profile to create optical elements with a target refractive index or a gradient refractive index. We will start with simple cylindrical lenses, then move to GRIN Luneburg lenses and end with photonic nanojets.

5.6.1. Focusing with 2D Cylinders

First we will show a demonstration of simple 1D cylinders with the axis parallel to the substrate. This is a very simple focusing element and shows the shift in focal position as the refractive index is increased. 1D cylinders are experimentally easier to characterize, since for spherical elements the scan must be precisely at the center of the sphere, which is finicky to achieve with our instruments. A confocal depth scan of a spherical element is shown in **Figure 5.22a**, showing strong focusing. The expected focusing pattern expected for this element is simulated and the intensities of a linear intensity scan (along a line going through the center of the element in the direction of propagation) are compared with measurement, which is plotted in **Figure 5.22b**. The overall shapes of these intensity scans are similar, but the measured elements have additional fringes, possibly due to distortions in shape or refractive index. Simulated and experimental linear intensity scans were repeated for a variety of laser powers, based on the measured refractive index-power relations discussed in the section 5.4. The results of this sweep are shown in **Figure 5.22c**, which again have very similar shapes. Finally, a few select linear intensity scans for simulated elements are in **Figure 5.22d**.

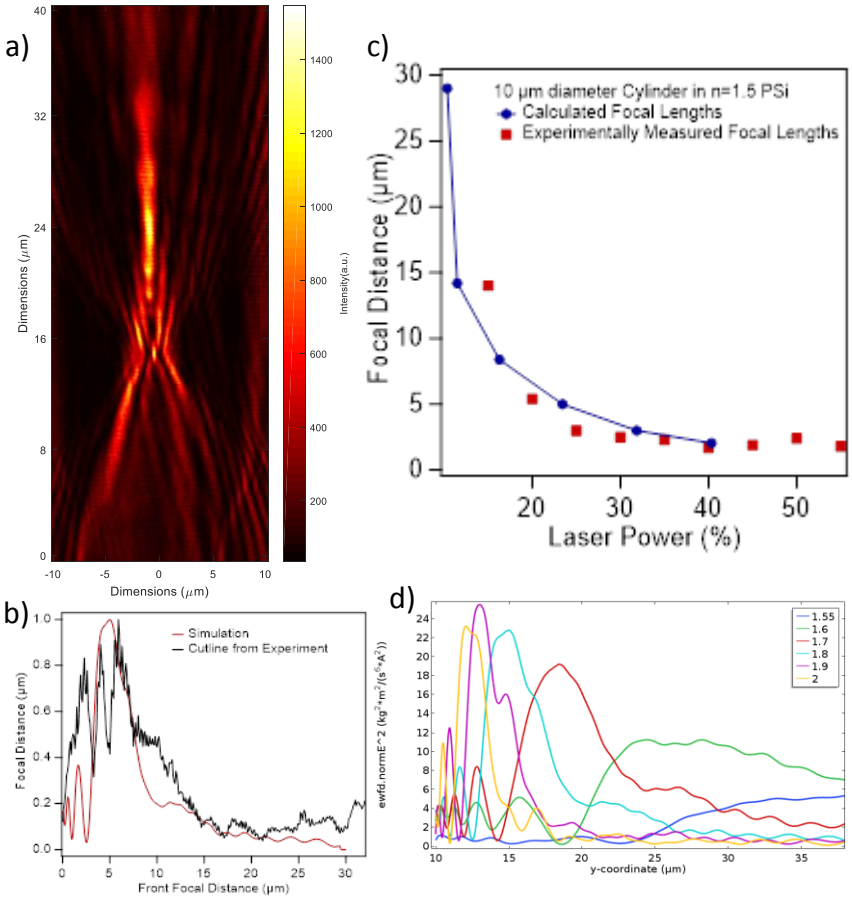

Figure 5.22. Focusing of light through cylindrical elements written in PSi at different laser powers. (a) Confocal microscopy depth scan of focusing by cylindrical element. (b) Simulated (red) and experimental (black) light intensity on a line passing through the center of the element. (c) Plot of simulated (blue) and measured (red) focal lengths at a sweep of laser powers. (d) Plot of simulated intensities along a vertical line through the element for a sweep of element refractive index.

5.6.2. Gradient Refractive Index Lenses.

One of the big advantages of STILUS is the ability to create 3D microscale GRIN optics in visible wavelengths, which to our knowledge has never been demonstrated before. One interesting gradient refractive index optic is the Luneburg lens,[41] which is a spherically symmetric GRIN lens with a refractive index profile, n, given by:

$$n(r) = \sqrt{2 - \left(\frac{r}{R}\right)^2} \tag{5.2}$$

Where r is the radial coordinate in space and R is the radius of the lens. It was proposed as a solution to Maxwell's question of what spherical index profiles will image a sphere onto

concentric sphere inside of it: in this solution the inner circle is the surface of the lens and the outer circle is at infinity. Though the Luneburg lens has been used in antennae for decades and in IR optics more recently, a visible wavelength Luneburg lens has not been demonstrated.

Traditionally, the Luneburg lens has a refractive index max of $\sqrt{2}$ and a refractive index min of 1. PSi is not capable of forming an effective refractive index equal to one, but we can linearly scale the refractive index profile of the lens without changing the unique optical characteristics. We scale by a ratio of $\frac{n_{max}}{\sqrt{2}}$ so that the maximum refractive index of the lens is equal to the maximum achievable refractive index for a particular PSi film. This results in a minimum refractive index just barely below the baseline refractive index of the film, so we are forced to cut a thin shell off the outer rim of the element, resulting in an index profile shown in **Figure 5.23a**. This refractive index profile was written into the PSi using the measured refractive index-power relations found in Section 5.4.4.1.

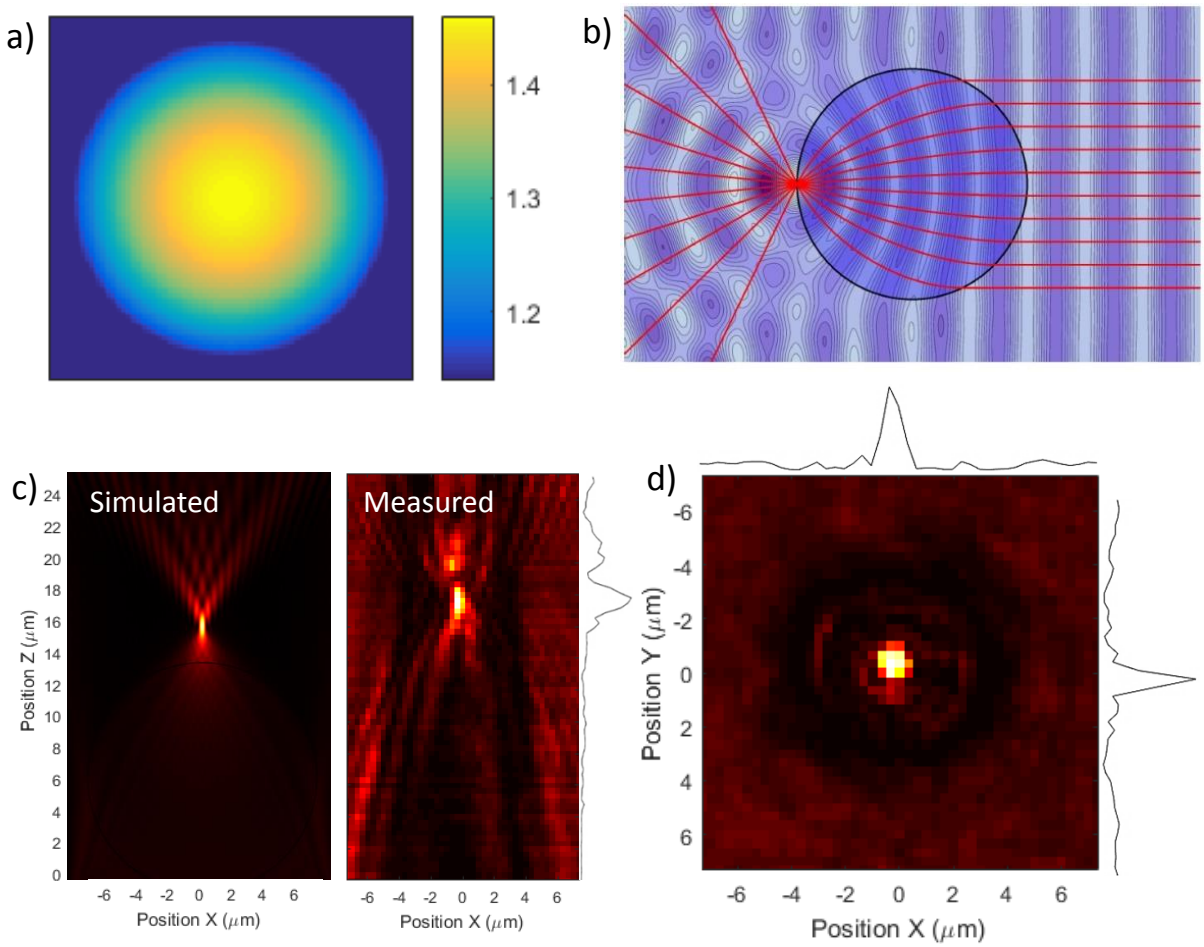

Figure 5.23. Optics of a Luneburg lens. a) Heatmap of the 2D refractive index profile for creating a Luneburg lens in PSi. b) Diagram of the focusing of a planewave to a point on the edge of the lens, made by Di Falco, et al.[42] c) Simulated and measured confocal microscopy depth scans of laser light being focused by a Luneburg lens. d) Lateral confocal microscopy scans of the focal plane of a Luneburg lens in PSi. Measured line intensity profiles are shown at the side of (c) and the top and side of (d).

Lenses written into the PSi were measured with confocal microscopy, as in Section 5.5.1. One confocal depth scan is shown in **Figure 5.23c** along with a simulation of the expected focusing properties of the lens. While the lens for the most part focuses as expected, there are some apparent distortions in the transmitted light. Unfortunately, properly characterizing the Luneburg lens is not a trivial task. With just a confocal microscope we were not able to rigorously measure the focal position relative to the lens itself, so an estimate of the focal length would not be accurate. The locations of the focal points in **Figure 5.23c** do not match because we do not know whether they actually match or not. We see that there are distortions in the focus of the lens, but even if it were perfect it would not prove the optics of the lens: the

ideal Luneburg lens has a higher numerical aperture than the lens of the confocal microscope so some information cannot be collected with just confocal microscopy. Lastly, even without the resolution limitations of the microscope, there are an infinite number of solutions for a 3D refractive index distribution for a particular transmitted light intensity profile. In short, we know we have deviations from the ideal Luneburg lens, but characterizing these deviations is a huge obstacle.

5.6.3. Photonic Nanojets

STILUS is also capable of creating more complex optical elements. Here we demonstrate a photonic nanojet, which is a long, narrow beam of high-intensity light.[43], [44] These beams can be much longer than focal points from conventional lenses and can be capable of narrower foci than allowed by the diffraction limit (but only in the near-field regime). Photonic nanojets can be created using a simple constant-refractive index sphere to focus light,[43] but photonic nanojets should not be confused with the lensing afforded by geometrical optics – the size of the element must be similar to the wavelength of the light. Nevertheless, the photonic nanojets do not rely on resonance, and broadband photonic nanojets are possible.[43] One interesting aspect of photonic nanojets is that they can work better with a smaller refractive index contrast. This makes STILUS an attractive method for the fabrication of these elements with its ability to slightly shift the refractive index with micron scale spatial control.

The Goddard group has experience with photonic nanojets and has made designs implementing a cascade of focusing elements that promise a greatly elongated photonic nanojet.[44] A few such elements are shown below in **Figure 5.24**. The second element in particular shows an elongation of the nanojet more than 7 times the wavelength of the light and a minimum focus of 0.42λ, below the diffraction limit.

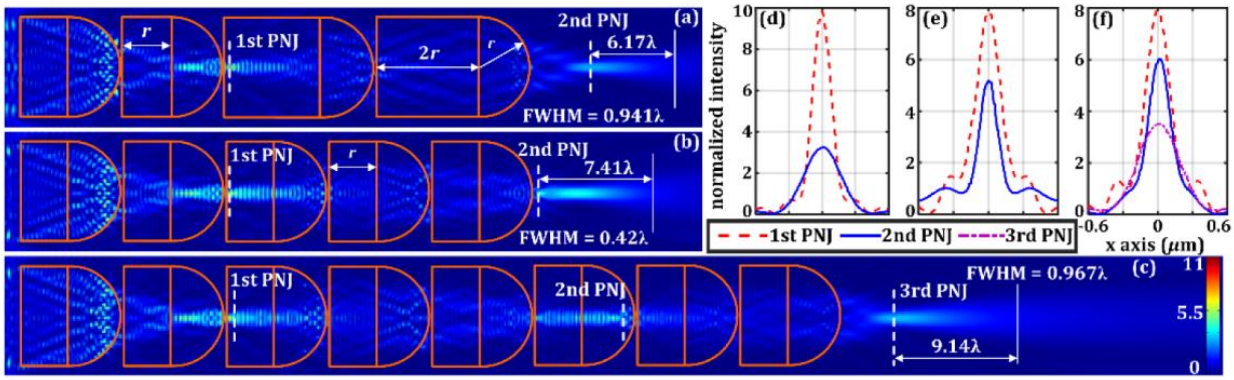

Figure 5.24. a,b,c) COMSOL-simulated optical intensity distribution maps for photonic nanojet elements (outlined in red). Plane waves are sent from the left edge and focused repeatedly inside the element. Intensity profiles at the focal plane are shown in (d,e,f). Figure by Zhu, et al.[44]

These kinds of elements are difficult to fabricate with conventional methods due to the tight requirements in dimensions and refractive index. Fabrication of these elements was first attempted using RIE of a porous silicon surface, but we could not achieve steep enough sidewalls. Instead, we focused on creating these elements with STILUS. We made these elements using a sweep of laser powers. The nanojets were measured using confocal microscopy. One example of the nanojets is shown below in **Figure 5.25**. As was done with the conventional lenses, these elements were cylindrical, forming about 50μm wide nanojet in the x-direction to make measurement easier.

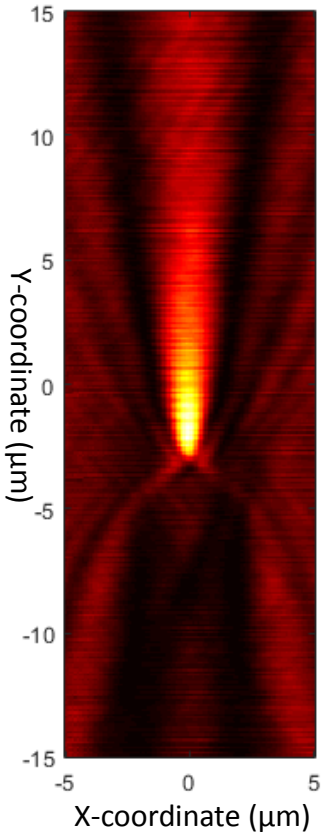

Figure 5.25. Confocal depth scan of photonic nanojet with 3µm width, 13µm top cylinder height, and 1µm bottom cylinder height.

Proper characterization of these elements presents a new challenge. We would like to directly measure the minimum resolution of the elements, as these can beat the diffraction limit. However, in order to measure whether the nanojet beats the diffraction limit, the measuring tool itself has to beat the diffraction limit. Confocal microscopy is insufficient. There are tools that may be used for this, such as NSOM, though this requires the focus (and thus the tip of the element) to be in the top few nanometers of the porous surface.

5.6.4. 3D Optical Circuitry

In addition to focusing elements, STILUS can be used for waveguiding elements. As optoelectronics and quantum optics demand more complex optical circuitry, the ability to write in 3D space is greatly desired. 3D optical waveguides have been demonstrated by rastering femtosecond lasers to locally shift the refractive index of the glass, as discussed in section 5.4.1.

A few particular advantages of STILUS is the much higher refractive index contrast that is achievable compared to writing waveguides in glass, the ability to stack a layer of PSi on top of an active material (such as a VCSEL array), and the ability to make the background material have low background refractive index along with giving different layers different background refractive indices. Having a high refractive index contrast is attractive because it allows the waveguide to make tighter turns without leading to leakage. **Figure 5.26** shows some possible optoelectronic designs using this.

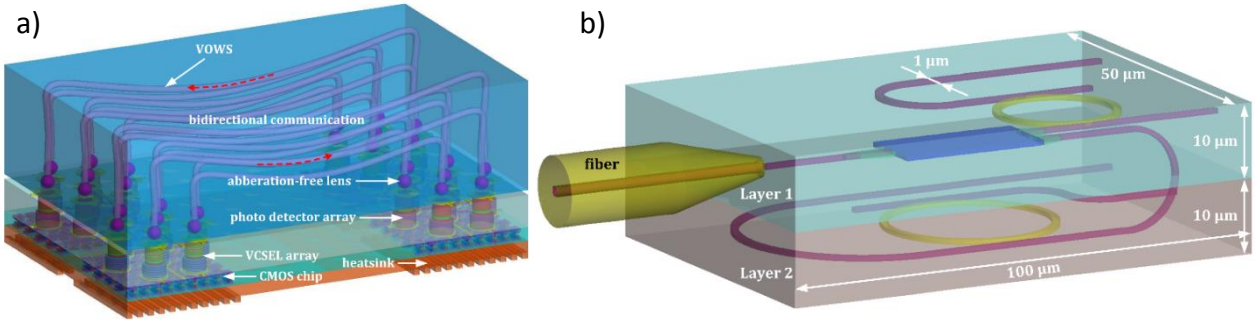

Figure 5.26. Cartoons of proposed STILUS optical interconnect designs. a) On-chip optical interconnect between arrays of VCSEL's and optical detector. b) Optical ring-resonator demultiplexer with two layers of different background refractive indices. Images by Jinlong Zhu.

To prove the principle of this technique, we start with a much simpler pattern, a single split ring resonator. **Figure 5.27b** shows a ring resonator written embedded in PSi. While the formation of the ring occurs as expected, a close examination shows a stitching error in the linear waveguide, which would result in high losses. This is due to the low repeatability of stage movements in the Nanoscribe. Our temporary solution is to use a very wide diameter waveguide whenever the stage needs to be moved, which unfortunately drastically increases write-time and limits the size of more complex elements such as ring resonators.

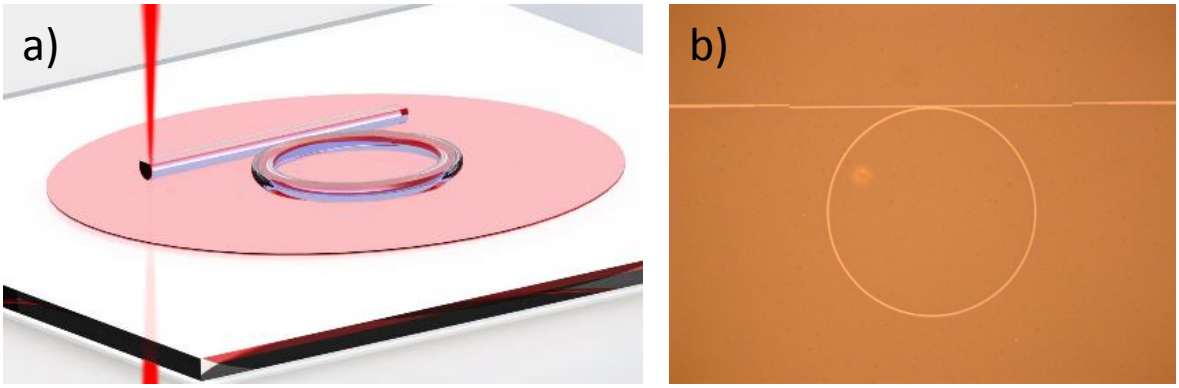

Figure 5.27. a) Cartoon of writing a ring resonator with STILUS. Image by Corey Richards. b) Optical microscopy image of a 80um diameter ring-resonator written in a PSi film.

Additionally, there is the recurring problem of how to characterize these elements. Initially, we intended to cleave the PSi and substrate and butt couple the light from and to optical fibers. Unfortunately, we were not able to cleanly cleave or cut the PSi, resulting in a rough surface that was highly scattering and difficult to couple. We are currently working on alternative methods to couple light into and out of embedded waveguides.

5.7. Shifting Bragg-stack band-gap

Thus far, we have only discussed the writing of new elements within a uniform PSi or $PSiO_2$ film. Here, we will introduce the concept of instead using STILUS to *modify* a pre-existing optical element using a uniform exposure. In particular, we discuss creating a DBR (distributed Bragg reflector) using conventional silicon porosification methods, then writing inside the DBR to shift its bandgap.

As mentioned in Section 5.1, DBR's can be created by etching porous silicon with a current density alternating between high and low values, yielding low and high refractive indices. In DBR's, the bandgap position is determined by the optical path length corresponding to one period of the DBR. The Bragg wavelength occurs when the optical path length of one period is equal to half-wave. As the optical path length of a period in a DBR is simply the sum of the products of thickness and refractive index for each layer (assuming normal incidence), the Bragg wavelength is simply:

$$\lambda_{Bragg} = 2\sum_i d_i\, n_i \tag{5.3}$$

where d_i and n_i are thickness and refractive index of the ith layer in a unit cell of the DBR. Thus, the Bragg reflectance increases linearly with the refractive indices of its constituent layers.

As demonstrated in previous sections, STILUS can be used to locally shift the refractive index. This enables us to increase the refractive index and thus redshift the resonant wavelength of a DBR. Further, the spatial control of STILUS means that the redshift can be localized to a particular domain in the x-y plane, so that a blue DBR can be next to a red DBR next to a green DBR. **Figure 5.28** shows a cartoon cross-section of this principle. These DBRs can have thicknesses that approach a micron, so a very fine array of DBR's at different colors can be made. Fabricating adjacent vertically-oriented DBR's with different bandgap frequencies is very difficult with conventional methods, but we have seen that creating these with STILUS is actually quite easy.

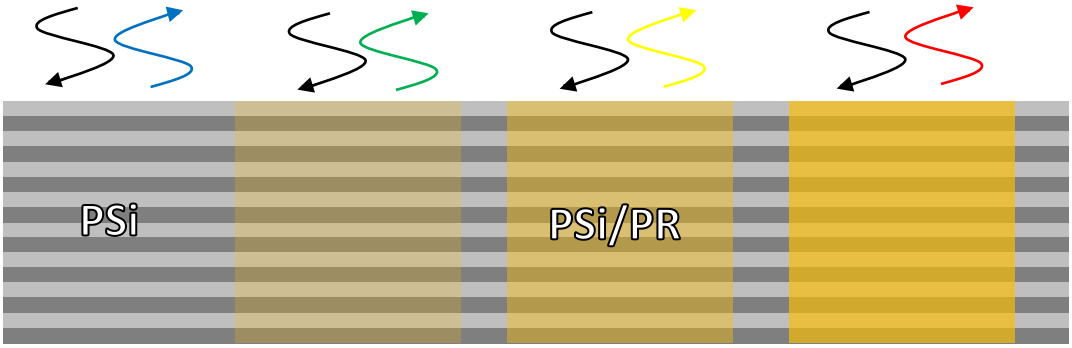

Figure 5.28. Cartoon of spectral shifting of a Bragg stack. On the left there is a side view of a PSi DBR tuned to reflect blue light. In regions exposed to progressively higher dosage (orange squares), the peak reflectance wavelength is red shifted.

We first demonstrated the principle of shifting the reflectance wavelength of large regions. The PSi DBR is created using high current densities since higher porosities yield a greater maximum refractive index shift. The DBR is initially centered at blue wavelengths to maximize the available coverage of the visible spectrum. After a uniform exposure through the depth of the DBR, the color shift is striking (**Figure 5.29a**). Microspectroscopy shows a shift in the center wavelength from 500nm to 620nm (**Figure 5.29b**).

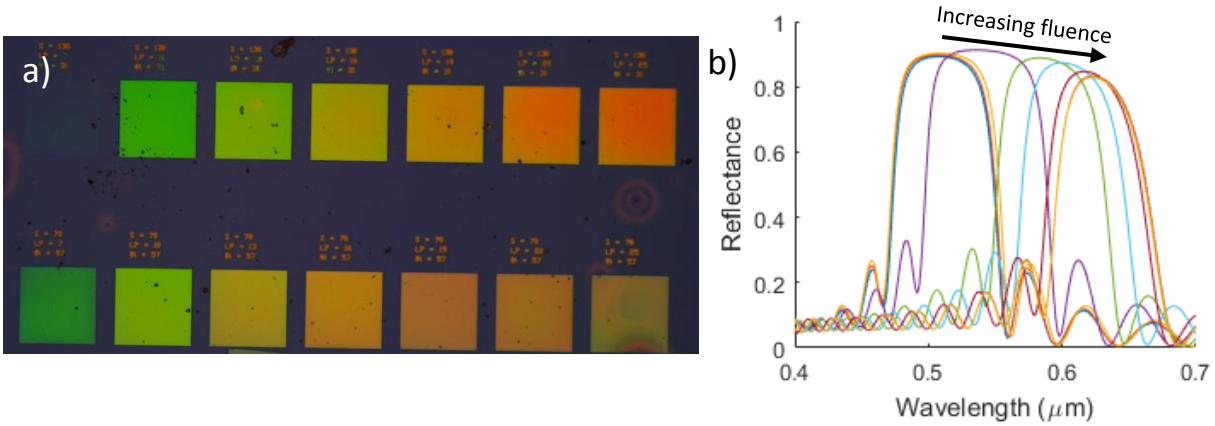

Figure 5.29. Shifting of reflectance spectra of PSi DBR's. a) Microscopy image of PSi DBR exposed to a sweep of dosages over 80µm squares. b) Reflection microspectroscopy of a PSi DBR with shifted bandgap.

5.7.1. Creating Images with Band-gap Shifting

Given how striking (and, admittedly, pretty) the colors created by band-gap shifting were, we investigated our ability to embed colorful images in PSi DBR's with this technique.

The simplest method for creating a colored image is to take a binary color image and use that as a map of regions to expose. The seal of the University of Illinois was extruded into a 3D geometry and imported into DeScribe (the built-in pattern generator for the Nanoscribe) and used to expose a film of PSi, and this was repeated for a sweep of laser powers. One of these is shown in **Figure 5.30a**. We estimate that the smallest visible feature is approximately 1µm, far smaller than our wildest expectations for resolution with this technique.

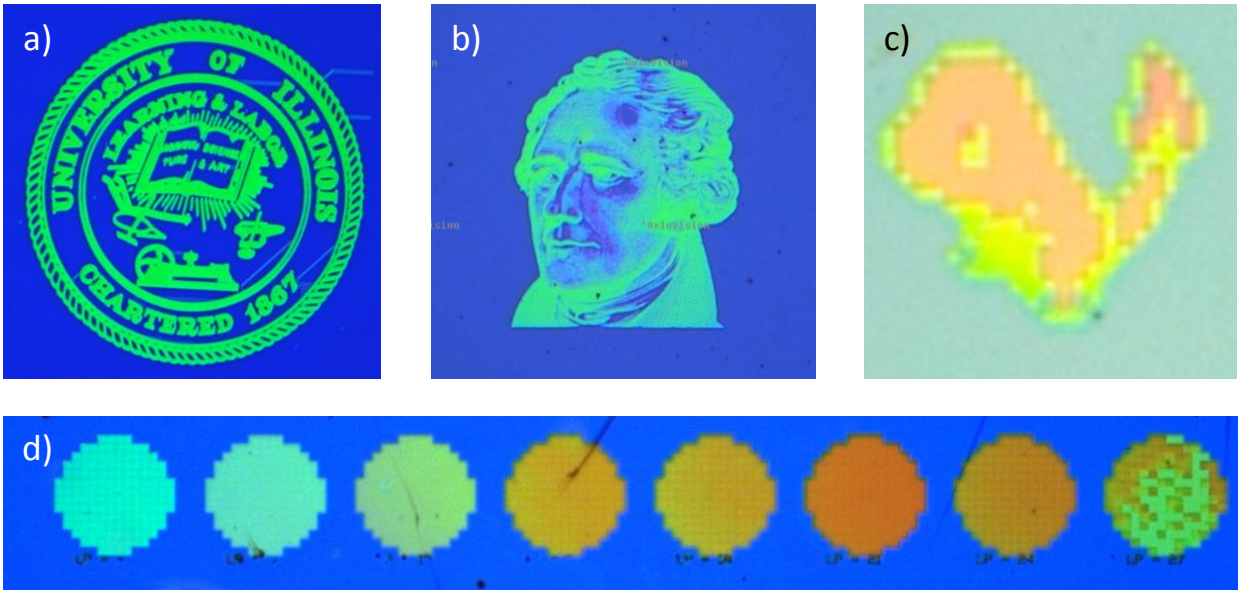

Figure 5.30. Optical microscopy images embedded into PSi DBR's by locally shifting band-gap wavelength. a) Seal of the University of Illinois made by rastering image with constant laser power (approximately 80µm in diameter). b) George Washington portrait made by linearly scaling laser power according to value of image (100µm across). c) Pixelated Charmander made by creating a pixelated color scale to convert between color and laser power. The Charmander image used a more greenish DBR so that more red colors could be achieved. d) An example of a pixelated color scale. The circles are written pixel-by-pixel (5µm pixels) with sweep of laser power increasing from left to right.

The next step in complexity is to take a greyscale image and convert the value channel linearly into dosage. In the lithography step, the laser was raster across a rectangular shape, line-by-line and layer-by-layer, with the color defined by changing the laser power as the focus is rastered. A micron scale portrait of George Washington was made using this method and shown in **Figure 5.30b**.

Another step in complexity is making an image with pre-defined target colors. The image is broken up into pixels and each pixel is written separately at a different laser power. We have found that writing pixel-by-pixel gives a different color-power relation than larger areas, so we expose large areas pixel-by-pixel (**Figure 5.30d**) in order to get the appropriate relation between color and power. One can see in this image that there are some oddities, such as higher laser powers sometimes causing a smaller change in DBR bandgap, or causing pixel to pixel variability. This is typically repeatable, but we have not been able to identify the cause. This kind of color scale was still enough to create colorful images, such as the Charmander in **Figure 5.30c**.

There are continuing difficulties in creating images with STILUS. The first and most obvious is that there is control over the hue but not the value or saturation. As such, this technique is incapable of creating black, white or gray. Simple DBR's can only produce colors found in the rainbow so brown and purple cannot be made (though we cannot rule out more complex DBR designs that can create reflectance peaks in multiple parts of the spectrum that could produce brown and purple). However, just as conventional LED displays can produce images excellent color control just from red, blue, and green phosphors, better color control could be achieved for band-gap shifted images for low-acuity imaging systems (such as the human eye).

Unlike STILUS performed within a uniform refractive index film, it would be difficult to create a 'library' of porosification conditions and exposure conditions for a DBR. A uniform film would have porosity and laser power as the only free parameters (assuming that line spacing, raster speed, etc. have been decided on), whereas with a DBR, the porosities of each layer along with the thickness of each layer are free variables, so a library of results would have too many dimensions. Thus it is probably best to measure the relation of dosage and band-gap shift on a case by case basis.

Another issue that remains is sample to sample variability. We found that we get the most consistent results when using the exact same film for both the dosage sweep and the final element. The results of the dosage sweep do not transfer very well to other samples, even when using identical porosification conditions. We have also noted that there can be significant differences between sweeps done at the center and near the edges of the film.

5.8. Conclusions

In this chapter, we looked at optics made using PSi and $PSiO_2$. Whereas most optical elements made using PSi control the refractive index only in a single direction, creating a 1D stack, we demonstrated sideways porosification of lithographical define Si pillars, enabling refractive index control in multiple directions. We showed how these elements could be used to take advantage of the birefringence of PSi, an aspect usually ignored.

We introduced a new method, which we are for now calling STILUS (Shaped Tunable-Index Lithography Using Scaffolding), whereby the refractive index of a PSi or $PSiO_2$ film can be controlled over 3D space. DLW is used to crosslink a photoresist inside the pores of PSi or PSiO2 and the porous nanostructure supports low crosslink densities that would be developed away with conventional DLW. The elements created can be given nearly arbitrary 3D forms and the refractive index can be continuously tuned from the base refractive index of the film up to 0.4 more than the base refractive index. The refractive index range achievable is much higher than similar techniques that work in the visible.

With his technique we have demonstrated that a variety of focusing optics embedded in PSi and $PSiO_2$, including a cylindrical lens, a gradient refractive index Luneburg lens (the first of its kind in the visible regime), and a photonic nanojet. These elements demonstrate the broad capabilities of STILUS for creating 3D micro-optical elements.

Band-gap shifting of PSi and PSiO2 DBR's was demonstrated with uniform DLW exposure. Shifting of the bandgap from blue to red wavelengths, and the continuum between, was demonstrated with relatively high porosity films. Band-gap shifting was controlled to create colored images, including a two-color blue-green image, a gradient index blue-green image, and a pixelated red-green-blue image.

We expect this method to be used to create a wide variety of optics that we have yet to consider. It is our hope that much work will be done to more fully understand the process and create effective design tools to make 3D gradient refractive index optics a common, effective research tool.

5.9. References

[1] V. Torres-Costa and R. J. Martín-Palma, "Application of nanostructured porous silicon in the field of optics. A review," *J. Mater. Sci.*, vol. 45, no. 11, pp. 2823–2838, Jun. 2010.
[2] S. Shichi, M. Fujii, T. Nishida, H. Yasuda, K. Imakita, and S. Hayashi, "Three-dimensional structure of (110) porous silicon with in-plane optical birefringence," *J. Appl. Phys.*, vol. 111, no. 8, p. 084303, Apr. 2012.
[3] Y. Watanabe, "Formation and Properties of Porous Silicon and Its Application," *J. Electrochem. Soc.*, vol. 122, no. 10, p. 1351, 1975.

[4] B. Bera, “Porous silicon nanoparticle prepared by Vapour phase strain etch and sacrificial technique,” West Bengal University of Technology, Kolkata, India, 2015.
[5] R. L. Smith and S. D. Collins, “Porous silicon formation mechanisms,” *J. Appl. Phys.*, vol. 71, no. 8, pp. R1–R22, Apr. 1992.
[6] N. A. Krueger *et al.*, “Porous Silicon Gradient Refractive Index Micro-Optics,” *Nano Lett.*, vol. 16, no. 12, pp. 7402–7407, Dec. 2016.
[7] L. A. Golovan’, P. K. Kashkarov, and V. Y. Timoshenko, “Form birefringence in porous semiconductors and dielectrics: A review,” *Crystallogr. Rep.*, vol. 52, no. 4, pp. 672–685, Jul. 2007.
[8] G. A. Niklasson, C. G. Granqvist, and O. Hunderi, “Effective medium models for the optical properties of inhomogeneous materials,” *Appl. Opt.*, vol. 20, no. 1, pp. 26–30, 1981.
[9] J. Álvarez *et al.*, “Birefringent porous silicon membranes for optical sensing,” *Opt. Express*, vol. 19, no. 27, p. 26106, Dec. 2011.
[10] V. Y. Timoshenko *et al.*, “Anisotropy of optical absorption in birefringent porous silicon,” *Phys. Rev. B*, vol. 67, no. 11, Mar. 2003.
[11] A. Taflove, “Review of the formulation and applications of the finite-difference time-domain method for numerical modeling of electromagnetic wave interactions with arbitrary structures,” *Wave Motion*, vol. 10, no. 6, pp. 547–582, 1988.
[12] Z. Szabo, G.-H. Park, R. Hedge, and E.-P. Li, “A Unique Extraction of Metamaterial Parameters Based on Kramers-Kronig Relationship,” *IEEE Trans. Microw. Theory Tech.*, vol. 58, no. 10, pp. 2646–2653, Oct. 2010.
[13] D. R. Smith and J. B. Pendry, “Homogenization of metamaterials by field averaging (invited paper),” *J. Opt. Soc. Am. B*, vol. 23, no. 3, p. 391, Mar. 2006.
[14] D. R. Smith, D. C. Vier, T. Koschny, and C. M. Soukoulis, “Electromagnetic parameter retrieval from inhomogeneous metamaterials,” *Phys. Rev. E*, vol. 71, no. 3, Mar. 2005.
[15] X. Chen, B.-I. Wu, J. Kong, and T. Grzegorczyk, “Retrieval of the effective constitutive parameters of bianisotropic metamaterials,” *Phys. Rev. E*, vol. 71, no. 4, Apr. 2005.
[16] P. Chılek and G. Videen, “Scattering by a composite sphere and effective medium approximations,” *Opt. Commun.*, vol. 146, no. 1–6, pp. 15–20, 1998.
[17] R. Zhao, T. Koschny, and C. M. Soukoulis, “Chiral metamaterials: retrieval of the effective parameters with and without substrate,” *Opt. Express*, vol. 18, no. 14, pp. 14553–14567, 2010.
[18] J. T. Costa, M. G. Silveirinha, and S. I. Maslovski, “Application of the Finite-Difference Frequency-Domain Method to the Extraction of the Effective Parameters of Metamaterials.”
[19] P. Ikonen, E. Saenz, R. Gonzalo, C. Simovski, and S. Tretyakov, “Mesoscopic effective material parameters for thin layers modeled as single and double grids of interacting loaded wires,” *Metamaterials*, vol. 1, no. 2, pp. 89–105, 2007.
[20] D. E. Aspnes, “Local-field effects and effective-medium theory: A microscopic perspective,” *Am. J. Phys.*, vol. 50, no. 8, pp. 704–709, Aug. 1982.
[21] C. R. Ocier, N. A. Krueger, W. Zhou, and P. V. Braun, “Tunable Visibly Transparent Optics Derived from Porous Silicon,” *ACS Photonics*, vol. 4, no. 4, pp. 909–914, Apr. 2017.
[22] F. Zhou, W. Cao, B. Dong, T. Reissman, W. Zhang, and C. Sun, “Additive Manufacturing of a 3D Terahertz Gradient-Refractive Index Lens,” *Adv. Opt. Mater.*, vol. 4, no. 7, pp. 1034–1040, Jul. 2016.

[23] Y.-Y. Zhao, Y.-L. Zhang, M.-L. Zheng, X.-Z. Dong, X.-M. Duan, and Z.-S. Zhao, “Three-dimensional Luneburg lens at optical frequencies (Laser Photonics Rev. 10(4)/2016),” *Laser Photonics Rev.*, vol. 10, no. 4, pp. 533–533, Jul. 2016.
[24] A. Žukauskas, I. Matulaitienė, D. Paipulas, G. Niaura, M. Malinauskas, and R. Gadonas, “Tuning the refractive index in 3D direct laser writing lithography: towards GRIN microoptics: Tuning the refractive index in 3D direct laser writing lithography,” *Laser Photonics Rev.*, vol. 9, no. 6, pp. 706–712, Nov. 2015.
[25] S. Dottermusch, D. Busko, M. Langenhorst, U. W. Paetzold, and B. S. Richards, “Exposure-dependent refractive index of Nanoscribe IP-Dip photoresist layers,” *Opt. Lett.*, vol. 44, no. 1, p. 29, Jan. 2019.
[26] K. M. Davis, K. Miura, N. Sugimoto, and K. Hirao, “Writing waveguides in glass with a femtosecond laser,” *Opt. Lett.*, vol. 21, no. 21, pp. 1729–1731, 1996.
[27] K. Miura, J. Qiu, H. Inouye, T. Mitsuyu, and K. Hirao, “Photowritten optical waveguides in various glasses with ultrashort pulse laser,” *Appl. Phys. Lett.*, vol. 71, no. 23, pp. 3329–3331, Dec. 1997.
[28] M. Beresna, M. Gecevičius, and P. G. Kazansky, “Ultrafast laser direct writing and nanostructuring in transparent materials,” *Adv. Opt. Photonics*, vol. 6, no. 3, p. 293, Sep. 2014.
[29] M. Thiel, J. Ott, A. Radke, J. Kaschke, and M. Wegener, “Dip-in depletion optical lithography of three-dimensional chiral polarizers,” *Opt. Lett.*, vol. 38, no. 20, p. 4252, Oct. 2013.
[30] S. Richter *et al.*, “Laser induced nanogratings beyond fused silica - periodic nanostructures in borosilicate glasses and ULE^{TM},” *Opt. Mater. Express*, vol. 3, no. 8, p. 1161, Aug. 2013.
[31] A. W. H. Lee and B. D. Gates, “Rapid Covalent Modification of Silicon Oxide Surfaces through Microwave-Assisted Reactions with Alcohols,” *Langmuir*, vol. 32, no. 29, pp. 7284–7293, Jul. 2016.
[32] N. F. Mott, S. Rigo, F. Rochet, and A. M. Stoneham, “Oxidation of silicon,” *Philos. Mag. B*, vol. 60, no. 2, pp. 189–212, Aug. 1989.
[33] Sigma-Aldrich, *Pentarythritol triacrylate*. .
[34] E. Shapiro, K. Panagiotidis, and T. Staffel, “Coated ammonium polyphosphate, its use and manufacture,” EP 2 808 358 A1.
[35] H. Ning *et al.*, “Transfer-Printing of Tunable Porous Silicon Microcavities with Embedded Emitters,” *ACS Photonics*, vol. 1, no. 11, pp. 1144–1150, Nov. 2014.
[36] Y. Lin, O. Gordon, M. R. Khan, N. Vasquez, J. Genzer, and M. D. Dickey, “Vacuum filling of complex microchannels with liquid metal,” *Lab. Chip*, vol. 17, no. 18, pp. 3043–3050, 2017.
[37] E. R. Blout, G. R. Bird, and D. S. Grey, “Infra-Red Microspectroscopy*,” *J. Opt. Soc. Am.*, vol. 40, no. 5, p. 304, May 1950.
[38] J. Mistrik, S. Kasap, H. E. Ruda, C. Koughia, and J. Singh, “Optical Properties of Electronic Materials: Fundamentals and Characterization,” in *Springer Handbook of Electronic and Photonic Materials*, S. Kasap and P. Capper, Eds. Cham: Springer International Publishing, 2017, pp. 1–1.
[39] Bahaa E. A. Saleh and Malvin Carl Teich, *Fundamentals of Photonics*. New York: Wiley, 1991.

[40] C. M. Focken, “The deviation produced by a biprism,” *J. Sci. Instrum.*, vol. 17, no. 2, pp. 42–42, Feb. 1940.
[41] R. K. Luneburg and A. L. King, “Mathematical Theory of Optics,” *Am. J. Phys.*, vol. 34, no. 1, pp. 80–81, Jan. 1966.
[42] A. Di Falco, S. C. Kehr, and U. Leonhardt, “Luneburg lens in silicon photonics,” *Opt. Express*, vol. 19, no. 6, pp. 5156–5162, Mar. 2011.
[43] A. Heifetz, S.-C. Kong, A. V. Sahakian, A. Taflove, and V. Backman, “Photonic Nanojets,” *J. Comput. Theor. Nanosci.*, vol. 6, no. 9, pp. 1979–1992, Sep. 2009.
[44] J. Zhu and L. L. Goddard, “Spatial control of photonic nanojets,” *Opt. Express*, vol. 24, no. 26, p. 30444, Dec. 2016.

CHAPTER 6

CONCLUSIONS

The projects presented in the previous chapters cover a broad range of topics. Here a summary of each will be provided.

6.1 Chapter Summaries

6.1.1. Summary of Chapter 2: Tunable Antireflection Coatings for Interference Lithography

Interference lithography is a technique commonly used to create 1D, 2D, and 3D periodic patterns in photoresist using the interference patterns of plane waves of light.[1] While it does not have the versatility of conventional lithography methods, the capability of interference lithography to create 3D patterns in a single exposure step and without a mask can be highly advantageous. For this reason, interference lithography is often used to create 3D photonic crystals. One issue with this method, though, is that while interference lithography in theory is capable of producing every Bravais lattice, some of these, such as simple cubic, are very difficult to achieve.[2] One reason for the difficulty in these geometries is that they require some of the interfering plane waves to have very steep angles of incidence, which leads to significant back-reflections from the substrate for even a tiny index mismatch, causing unwanted deviations in the interference pattern.

These backreflections can be eliminated using an antireflection coating. For this application, there unusual requirements for the antireflection coatings, including a very high uniformity, very low tolerance in refractive index, and the need to have a tunable refractive index, since the optimum refractive index changes with angle of incidence. We introduce the use of a polystyrene:poly(vinyl methyl ether) (PS:PVME) mixture as a material for an antireflection coating.[3] PS and PVME are special because it is one of the few pairs of homopolymers that are completely miscible for all compositions while having very different refractive indices.[4] PS:PVME mixtures thus have a highly uniform refractive index without phase separation and this refractive index is tunable across a wide range, making PS:PVME ideal as an antireflection coating material for a wide variety of substrates, from sapphire to CaF_2.

These antireflection coatings were used with interference lithography to fabricate simple cubic and body-centered cubic lattices. The interference fringes indicative of the backside reflections were not formed in the lattices fabricated with PS:PVME antireflection coatings, demonstrating the effectiveness of this method.

6.1.2. Summary of Chapter 3: Multilevel Phase Masks for Proximity-field Nanopatterning

Proximity-field nanopatterning (PnP) is variation of interference lithography whereby the interfering plane waves are created by sending a single plane wave through a diffraction grating to generate multiple beams with different propagation directions, powers and polarizations.[5] One particular benefit of this technique is that the diffracted beams have a phase difference defined by the diffracted mask, enabling the use of more than 4 interfering plane waves without the possibility of mismatched phases. A major difficulty with PnP is that there is no analytical method to come up with mask designs that are appropriate for creating a particular pattern.[6] Part of the issue is that only a small part of the complete design-space (sets diffraction efficiency, phase, and polarization for each diffracted beam) is accessible with conventional masks.

We investigated the conventional design-space and how to make changes to improve it. We find that conventional binary phase masks must diffract light such that opposite orders must have the same diffraction efficiency, as well as several other limitations in beam parameters. The origin of this symmetry in diffraction parameters is in certain symmetries in the binary masks. Multilevel phase masks, however, can break these symmetries, enabling designs that give very different diffraction efficiencies and opposite orders. We show in detail how the use of multilevel phase masks expands the design space of PnP.

The use of multilevel phase masks in PnP was also demonstrated experimentally. A mask to create a rod-connected diamond lattice was designed and fabricated by scribing a unit cell of the pattern into a diamond indentor tip using a focused ion beam. The tip was repeatedly indented into a photoresist film to form the conformal phase mask. After typical two-photon PnP exposure and development, SEM confirmed the rod-connected diamond

geometry. Given the time-consuming nature of the mask fabrication step, more scalable production methods of multilevel phase masks are needed.

6.1.3. Summary of Chapter 4: Proximity-field Nanopatterning of a Metallic Helix Array

Chapter 4 covers attempts to use proximity field nanopatterning to create an array of metallic helices that would function as a broadband circular polarizer. Though ultimately unsuccessful, these experiments lead to useful findings about the limitations of the PnP process.

Metallic helices have been shown to exhibit a strong circular dichroism, i.e. to absorb one handedness of circularly polarized light while transmitting the opposite handedness. These have long been used for radio antenna, but recently arrays of these elements been shown to be effective broadband circular polarizers.[7] These helical arrays have been created with direct laser writing (DLW) but a scalable technique for creating these arrays without a very high number of exposure steps has not been demonstrated. A PnP design to create helical arrays was generated, which was thought to resolve this issue. Implementing the design, however, proved difficult. Both generating the helical array pattern and metallizing it were not accomplished to the degree needed for adequate circular dichroism.

In investigating the cause of this difficulty, it was found that this particular design was especially sensitive to sources of noise in the lithography process. These sources of noise, concentration fluctuations of the photoinitiators and shot noise, have not been examined in interference lithography but are more commonly studied in extreme UV lithography.[8], [9] We combine the existing models of interference lithography with models of concentration fluctuation and shot noise to simulate the lithography process for these helical arrays. We find that even under ideal conditions, our design cannot yield a high enough signal to noise ratio without a very high concentration of photoinitiators, above the solubility limit for known photoinitiators. We recommend that the model developed here be used for feasibility studies before beginning the extensive experimental work to implement a challenging interference lithography design.

The metallization of porous SU8 templates as a later step in the creation of metallic helices was also studied. Electroless deposition of silver onto SU8 with good uniformity has been demonstrated using oxygen plasma to modify the surface chemistry of the SU8 to functional groups that serve as good silver electroless deposition initiation sites.[10] With our templates, however, we could not adequately perform the same modification of surface deep in the pores of SU8 due to the instability of plasma confined in the narrow pores of the photoresist template. Instead, we sought to achieve similar surface modification by wet chemical techniques that would not have this limitation. We demonstrated two techniques that provided fairly good initiation: a method using a low temperature, low concentration piranha etch that produces a wide variety of reactive surface groups and a method centering on epoxide ring opening followed by Jones oxidation to introduce carboxylic acid groups known to bond with silver ions. While we were successful in leading to a dense nucleation of silver electroless deposition, these methods still did not lead to uniform enough films for the designed metallic helix arrays even if the templates could be fabricated. Nevertheless, electroless deposition onto polymers is often desired but frequently challenging, and we hope these findings might prove useful.

6.1.4. Summary of Chapter 5: Direct Laser Writing of Gradient Refractive Index Optics in Porous Silicon and Porous Silicon Oxide

In a shift away from the topic of interference lithography, chapter 5 focuses on the use of porous silicon (PSi) to create novel optical elements. PSi is a nanoporous material created by an electrochemical etch into crystalline silicon.[11] The pores have diameters on the order of a few nanometers, making PSi an effective index medium in the visible and UV regime. The dimensions of the pores can be controlled by the current density of the electrochemical etch, so the effective refractive index can be tuned over a very wide range, from just above unity to around 4 (depending on the wavelength).[12] This has made porous silicon a frequent object of study for gradient refractive index (GRIN) optics.

An aspect of PSi that has not been so well used is its birefringence.[13] The pores of porous silicon follow the [1 0 0] family of directions and these pores lead to different amounts

of screening of the electric field for different polarizations, causing an optical anisotropy, or birefringence. Typically porous silicon optics are fabricated with the light propagating along the axis of the pores so that the light never 'sees' the birefringence. However, PSi can have a birefringence as high as 0.3, much higher than found in any uniform medium. We designed PSi elements to make use of this birefringence to give the element a strong polarization sensitivity: lenses that show a single focal point for one polarization and two focal points for the orthogonal polarization. The tunable birefringence of PSi is shown to have a great potential for unconventional optics.

The most exciting discovery we have made with regard to PSi is that it can function as a scaffold for underexposed photoresists. We've developed a technique whereby we fill the pores of PSi with a liquid crosslinking photoresist then expose it with DLW. I'm calling this technique STILUS (Shaped Tunable-Index Lithography Using Scaffolding). The PSi acts not only a support for macroscopic elements (e.g. a suspended lens not directly connected to the substrate) but also supports undercrosslinked photoresists, preventing total development in underexposed regions. After DLW, the porosity of the element can be locally controlled based on the local dosage: the pores can be completely filled with photoresist, completely empty, and everywhere in between. The local fill fraction of the photoresist also controls the local effective refractive index, meaning that the refractive refractive index can be tuned in 3D space practically independently. This opens up wide number of avenues for 3D optics.

We demonstrated the potential of STILUS to create 3D optical elements by defining a variety of optical elements. We first created cylindrical lenses with a uniform index, then gradient refractive index Luneburg lenses, then uniform index photonic nanojets for sub-diffraction limit focusing.[14], [15] One remaining issue is the characterization of the optical elements. These elements were examined with confocal microscopy and give results that match simulations, but theoretically there are an infinite number of 3D refractive index profiles that would give the same result. For the characterizing the photonic nanojet in particular, a sub-diffraction limited measuring tool is needed to test whether the element really does focus beyond the diffraction limit.

STILUS can also be used in conjunction with porosity control of PSi. In particular, we studied distributed Bragg reflectors (DBR's) with varying photoresist fill fractions.[16] As the fill fraction increases, the band-gap wavelength of the DBR becomes redshifted. We have found that we can use this to shift a DBR from the blue to the red parts of the visible spectrum. We have used this to embed images into the DBR that can be viewed by microscope, including the seal of the University of Illinois, a gray-scale portrait of George Washington that was converted to a blue-green scale, and an image of Charmander with accurate colors. We find that we can get feature sizes on the order of 1μm using this technique. Unfortunately, there are currently color limitations: one only has control over the hue of the color, not the value or saturation. Black, white, gray, purple and brown are not possible with the simple DBR's with uniform exposure.

6.2. Recommendations for Future Work

As the most exciting results have been on performing lithography within PSi and PSiO2, my recommendations will cover these areas. Work is currently being done on creating 3D focusing optics and embedded optical interconnects, so I will discuss two other branches of study: 1) expanding STILUS to work with conventional lithography instead of DLW and 2) making 3D rugate filters with interference lithography.

6.2.1. STILUS with Grayscale Lithography

A major limitation of STILUS is that it is not very scalable. This is due to the limitations of DLW, as rastering large volume optics would simply not be viable.[17] If can move to contact or projection lithography techniques, much larger elements could be made in a fraction of the time it takes to currently define a small element with DLW. This move would eliminate our capability of making 3D optics, but if we use gray-scale masks, our continuous shifting of bandgap will remain. Application of this technique to certain measurement techniques, such as hyperspectral imaging, would become possible.

Hyperspectral imaging is a measurement technique that collects both spatial and spectral data (e.g. forms an image at a wide number of wavelengths).[18] Conventional cameras usually collect spectral data along red, green, and blue channels, each weighted such that the image approximately matches what is seen by the human eye, or a few channels set for a particular kind of measurement (e.g. fluorescence imaging) defined by filters covering all the light. Unfortunately, the human eye leaves out a lot of information that is useful to know about in a research setting. STILUS can create a DBR array on top of a photodetector array such that each pixel has a spectral range, as shown in **Figure 6.1**, similar to a Bayer filter but with much more spectral information.[19] An array of 10x10 pixels repeated across the camera would still give spatial information but with 100 independent color channels. This method reduces the number of pixels corresponding to each channel but pixel density is not usually a limiting factor with 50 megapixel cameras being sold today as consumer products. The diffraction limit of the optics is more commonly the limiting factor in resolution than the pixel density of the camera.

I believe that easy hyperspectral imaging could revolutionize how microscopy is performed, especially in the biological realm. One could imagine performing fluorescence microscopy using a high number of dyes, each corresponding to different pieces of chemical information, being measured on the same sample simultaneously, enabling a much more precise chemical 'map' of the sample. Unfortunately, I am woefully underinformed in biological microscopy, so I will leave further speculation in this realm to those more knowledgeable.

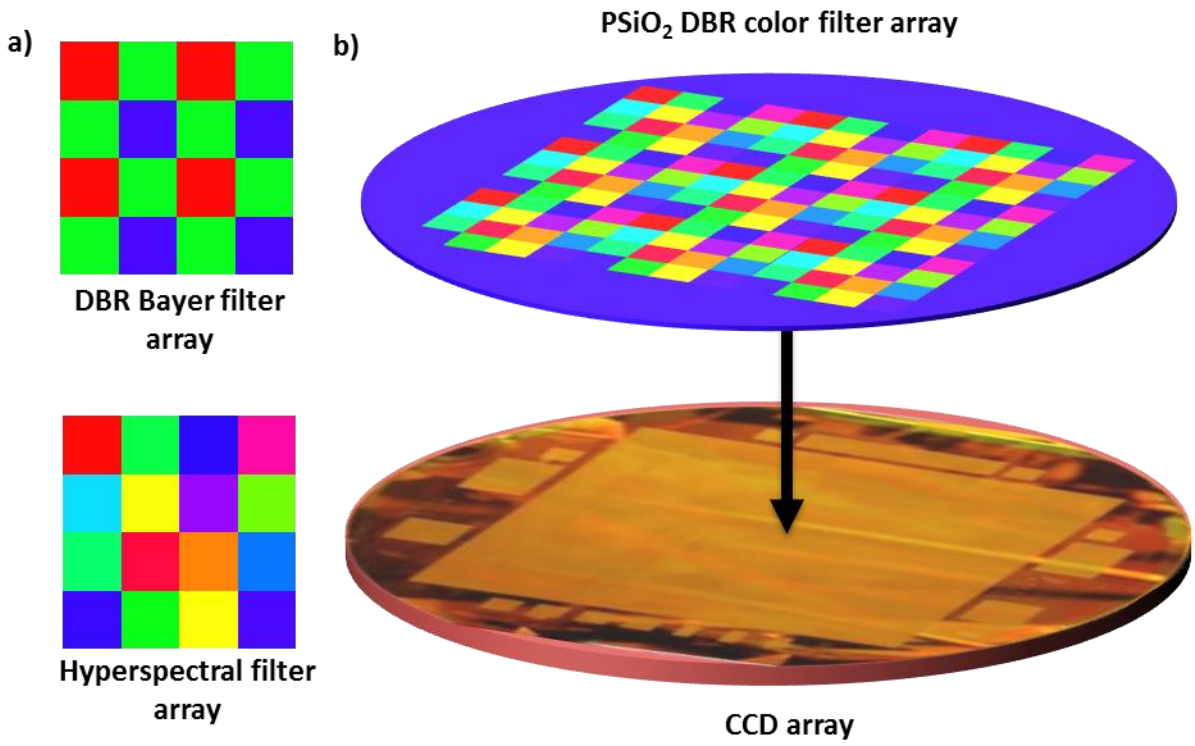

Figure 6.1. Hyperspectral imaging camera using STILUS. a) Comparison of color map of conventional red, green blue Bayer filter to a hyper filter array. b) Cartoon of fabrication of STILUS hyperspectral filter array with conventional CCD camera.

6.2.2. Higher Dimensional Rugate Filters with Interference Lithography

In addition to DLW and conventional lithography, interference lithography can be used for STILUS. As discussed in chapter 2, interference lithography can create 2D and 3D periodic patterns of photoresist and these patterns are commonly used to create 2D and 3D photonic crystals. If one performs this process within a PSi scaffold, then one should be able to create periodic patterns with a gradient refractive index basis. Photonic crystals with a gradient refractive index basis have been created for 1D bandgaps, and these are called rugate filters.[20] An interesting aspect of rugate filters is that (in the ideal case) there is only a single reflection mode. An FFT of a sinusoidally varying refractive index profile has only the 0 and ±1 orders, so coupling can only occur for the one wavenumber that matches the period. 2D and 3D interference patterns have an intensity profile that is like a summation of sinusoids going in different directions, so the FFT will similarly show a low number of discrete orders, removing the reflectance peak. Quick optical simulations of interference lithography applied inside of

PSiO2 are compared to conventional interference lithography in **Figure 6.2**. It can be seen that the higher order reflectance modes are indeed suppressed for 1D, 2D and 3D cases. In practice, producing this may be challenging due to the quandary of how to characterize the elements in PSi.

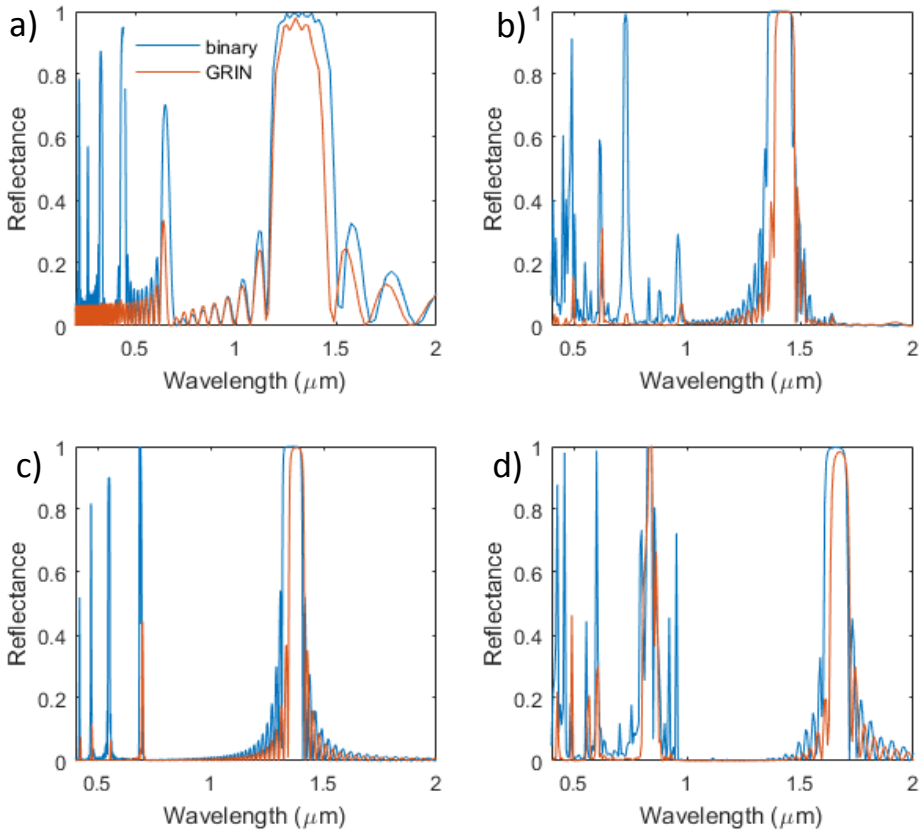

Figure 6.2. Simulated reflectance spectra of gradient refractive index photonic crystals (orange) and binary refractive index photonic crystals (blue). a) 1D sinusoidal rugate filter. b) 2D square interference pattern. c) 2D hexagonal interference pattern. d) 3D FCC interference pattern.

6.2.3. General Recommendations

In fact, the best path forward be very well be something I've not considered. I'm well aware of research paths that seem like a very good idea at the beginning of the project but that turns into a dead end, as well as chance discoveries that open up whole new exciting areas of research. We are in an age where the best advancements are interdisciplinary, so I encourage everyone to read widely, build collaborations, and try to solve other people's dilemmas as well

as your own. Every grad student must forge their own path, but I have one bit of advice I think applies to everyone: Never stop learning.

6.3. References

[1] C. Lu and R. H. Lipson, "Interference lithography: a powerful tool for fabricating periodic structures," *Laser Photonics Rev.*, vol. 4, no. 4, pp. 568–580, May 2009.
[2] L. Z. Cai, X. L. Yang, and Y. R. Wang, "All fourteen Bravais lattices can be formed by interference of four noncoplanar beams," *Opt. Lett.*, vol. 27, no. 11, pp. 900–902, 2002.
[3] D. A. Bacon-Brown and P. V. Braun, "Tunable Antireflection Coating to Remove Index-Matching Requirement for Interference Lithography," *Adv. Opt. Mater.*, p. 1701049, Feb. 2018.
[4] E. Jabbari and N. A. Peppas, "Use of ATR-FTIR to study interdiffusion in polystyrene and poly (vinyl methyl ether)," *Macromolecules*, vol. 26, pp. 2175–2175, 1993.
[5] S. Jeon, G. P. Wiederrecht, and J. A. Rogers, "Photonic systems formed by proximity field nanopatterning," 2005, pp. 187–195.
[6] J. W. Rinne, S. Gupta, and P. Wiltzius, "Inverse design for phase mask lithography," *Opt. Express*, vol. 16, no. 2, pp. 663–670, 2008.
[7] J. K. Gansel *et al.*, "Gold Helix Photonic Metamaterial as Broadband Circular Polarizer," *Science*, vol. 325, no. 5947, pp. 1513–1515, Aug. 2009.
[8] R. L. Brainard *et al.*, "Shot noise, LER, and quantum efficiency of EUV photoresists," 2004, pp. 74–85.
[9] E. Hassanein *et al.*, "Film quantum yields of EUV and ultra-high PAG photoresists," in *SPIE Advanced Lithography*, 2008, pp. 69211I–69211I.
[10] W. Dai and W. Wang, "Selective metallization of cured SU-8 microstructures using electroless plating method," *Sens. Actuators Phys.*, vol. 135, no. 1, pp. 300–307, Mar. 2007.
[11] Y. Watanabe, "Formation and Properties of Porous Silicon and Its Application," *J. Electrochem. Soc.*, vol. 122, no. 10, p. 1351, 1975.
[12] N. A. Krueger *et al.*, "Porous Silicon Gradient Refractive Index Micro-Optics," *Nano Lett.*, vol. 16, no. 12, pp. 7402–7407, Dec. 2016.
[13] L. A. Golovan', P. K. Kashkarov, and V. Y. Timoshenko, "Form birefringence in porous semiconductors and dielectrics: A review," *Crystallogr. Rep.*, vol. 52, no. 4, pp. 672–685, Jul. 2007.
[14] Y.-Y. Zhao, Y.-L. Zhang, M.-L. Zheng, X.-Z. Dong, X.-M. Duan, and Z.-S. Zhao, "Three-dimensional Luneburg lens at optical frequencies (Laser Photonics Rev. 10(4)/2016)," *Laser Photonics Rev.*, vol. 10, no. 4, pp. 533–533, Jul. 2016.
[15] J. Zhu and L. L. Goddard, "Spatial control of photonic nanojets," *Opt. Express*, vol. 24, no. 26, p. 30444, Dec. 2016.
[16] C. R. Ocier, N. A. Krueger, W. Zhou, and P. V. Braun, "Tunable Visibly Transparent Optics Derived from Porous Silicon," *ACS Photonics*, vol. 4, no. 4, pp. 909–914, Apr. 2017.
[17] L. Yuan and P. R. Herman, "Laser Scanning Holographic Lithography for Flexible 3D Fabrication of Multi-Scale Integrated Nano-structures and Optical Biosensors," *Sci. Rep.*, vol. 6, no. 1, Apr. 2016.

[18] L. Gao and R. T. Smith, “Optical hyperspectral imaging in microscopy and spectroscopy - a review of data acquisition,” *J. Biophotonics*, vol. 8, no. 6, pp. 441–456, Jun. 2015.
[19] Bryce E. Bayer, “Color imaging array,” US3971065A.
[20] B. G. Bovard, “Rugate filter theory: an overview,” *Appl. Opt.*, vol. 32, no. 28, pp. 5427–5442, Oct. 1993.

APPENDIX A

CALCULATION OF NON-CARTESIAN GRID FOR INTERFERENCE LITHOGRAPHY

It is sometimes useful to use a non-Cartesian lattice. For instance, the unit cell of a cubic lattice can be calculated directly, which enables it to be easily used for bandstructure calculations. For this purpose, the above code is unchanged, except for the calculation of the coordinate space. Assume that the ux_0, etc. (values of the u,v,w vectors) have been calculated and Nu, Nv, Nw (the number of cells to calculate along each lattice direction) have been defined

```
%Define periodicity vectors according to x,y,z coordinates
u_0 = [ux_0; uy_0; uz_0];
v_0 = [vx_0; vy_0; vz_0];
w_0 = [wx_0; wy_0; wz_0];

%Define uf, vf, and wf, which define the relative lattice coordinates
uf = linspace(0, 1 - 1/Nu,Nu) + offset(1);
vf = linspace(0, 1 - 1/Nv,Nv) + offset(2);
wf = linspace(0, 1 - 1/Nw,Nw) + offset(3);

%Create a grid of relative coordinate positions.  ufGrid contains the fraction of the lattice
        vector u to use for each and every point to be calculated
[ufGrid, vfGrid, wfGrid ] = ndmeshgrid(uf,vf,wf);

%Reshape the grid to a linear list of coordinates so that matrix multiplication can be used
ufGridR = reshape(ufGrid,1,[]);
vfGridR = reshape(vfGrid,1,[]);
wfGridR = reshape(wfGrid,1,[]);
r_ufvfwf = [ufGridR; vfGridR; wfGridR];

%Assemble the coordinate transformation matrix
M_xyz_uvw = [u_0, v_0, w_0];

%Perform matrix transformation and transpose so that is can be directly used in the
        above
r = (M_xyz_uvw * r_ufvfwf)';
```

The matrix ‘r’ can then be directly used in place of the ‘r’ described in section 2.3.

APPENDIX B

CODE FOR EFFICIENT CALCULATION OF 3D INTERFERENCE PATTERN

In Chapter 2, we covered the calculation of the 3D interference pattern for CW waves for multibeam interference lithography or PnP. The code sample presented there was an early method that is fairly easy to understand and is easily extensible but is not very computationally efficient. Any readers that need to perform a large number of these calculations are encouraged to use the code below, as it is a much faster algorithm.

```
function I = I_calc_efficient(E, k, r_limits, num_r_points, offset)

   %Arguments:
   %E is a set of electric field vectors [Ex1, Ey1, Ez1; Ex2, Ey2, Ez2;
         ...] for each order
   %k is a set of wave-vectors [kx1, ky1, kz1; kx2, ky2, kz2; ...] for
         each order
   %r_limits is the volume in which to do the calculation (of the form
         [xlim-,xlim+; ylim-, ylim+; zlim-, zlim+])
   %num_r_points is the number of points in each dimension: [Nx,Ny,Nz]
   %offset is a vector that moves the position of the unit cell [x, y, z]

   %Parameters:
   %I is the intensity (with arbitrary units)

   %List of all r-coordinates
   xcoord = linspace(r_limits(1,1) + offset(1),r_limits(1,2) + offset(1),
         num_r_points(1));
   ycoord = linspace(r_limits(2,1) + offset(1),r_limits(2,2) + offset(2),
         num_r_points(2));
   zcoord = linspace(r_limits(3,1) + offset(1),r_limits(3,2) + offset(3),
         num_r_points(3));

   %Allocate arrays for Ex, Ey, Ez values at each x, y, z
   E_x_r_tot = zeros(num_r_points(1), num_r_points(2), num_r_points(3),
         num_t_points);
   E_y_r_tot = zeros(num_r_points(1), num_r_points(2), num_r_points(3),
         num_t_points);
   E_z_r_tot = zeros(num_r_points(1), num_r_points(2), num_r_points(3),
         num_t_points);

   %Iterate through each beam
   for bi = 1:size(E,1)

      %Calculate the exp(kx * rx) etc. component for each 1D position
      expi_kx = exp(1i * k(bi,1) * xcoord);
      expi_ky = exp(1i * k(bi,2) * ycoord);
      expi_kz = exp(1i * k(bi,3) * zcoord);
```

```
        %Construct 4 grids corresponding to all x, y, z, t coordinates
        [expi_kx_mesh, expi_ky_mesh, expi_kz_mesh] = ndgrid( expi_kx,
              expi_ky, expi_kz);

        %Calculate exp(i*k*r - w*t) at each coordinate
        expi_r = expi_kx_mesh .* expi_ky_mesh .* expi_kz_mesh;

        %Calculate Ex, Ey, and Ez at each coordinate and add to the total
              for all beams
        E_x_r_tot = E_x_r_tot + E(bi,1) * expi_r;
        E_y_r_tot = E_y_r_tot + E(bi,2) * expi_r;
        E_z_r_tot = E_z_r_tot + E(bi,3) * expi_r;

    end

    %Calculate I at all coordinates
    I = E_total .* conj(E_total));

end
```